CRANFIELD UNIVERSITY

ANTONY NYOMBI

THERMAL AND CATALYTIC PROCESSING OF SOLID FUELS TO MINIMISE CARBON MONOXIDE EMISSIONS

CRANFIELD FORENSIC INSTITUTE

PhD Thesis
Academic Year: 2019 – 2020

Supervisors: Mr. Roland Wessling & Dr. Mike R. Williams
November 2019

CRANFIELD UNIVERSITY

CRANFIELD DEFENCE AND SECURITY
CRANFIELD FORENSIC INSTITUTE

PhD Thesis
Academic Year: 2019 – 2020

ANTONY NYOMBI

THERMAL AND CATALYTIC PROCESSING OF SOLID FUELS TO MINIMISE CARBON MONOXIDE EMISSIONS

Supervisors: Mr. Roland Wessling & Dr. Mike R. Williams
November 2019

This thesis is submitted in partial fulfilment of the requirements for the degree of Doctor of Philosophy

ABSTRACT

This research was conducted to evaluate the amount of carbon monoxide (CO) emissions from the incomplete combustion of solid fuels, the factors responsible for its release and methods to minimize its release and thus the human exposure to CO in different environments. Unintentional CO poisoning has resulted in many deaths, injuries and chronic ailments. Previous efforts to minimise exposure to CO include awareness campaigns, domestic CO alarms, improved designs for cooking stoves, space heating appliances, and post-combustion CO oxidation using catalysts. However, these methods have not fully solved the challenge of CO exposure.

In this study, different sold fuels were processed and analysed to investigate their behaviour under different oxidative environments and to establish ways to reduce the amount of CO released during combustion. Areas of solid fuel research of particular interest include physicochemical properties, reactivity and surface chemistry, CO emission properties, and catalyst impregnation on solid fuels to minimise CO emissions. This was achieved by using raw and pyrolysed wood biomass and coal.

The results reported in this thesis show that the degradation profile of wood sawdust involved a combination of mechanisms, including diffusion, geometrical contraction, nucleation, and reaction-order models. Pyrolysed charcoal was found be microporous with a low specific surface area. The charcoal contained high quantities of •C-C and •C-O free radicals, and low-temperature oxidation (< 200 °C) produced persistent peroxyl radicals. Mild-temperature (300 – 650 °C) oxidation showed that the charcoal was highly reactive, with low pre-exponential factors and activation energies. At temperatures < 550 °C, charcoal did not appear to glow to the naked eye. However, this temperature range was shown to correspond to the emission of large amounts of CO. In confined environments, the measured CO emissions increased with decrease in ventilation and increase in height above the floor.

Catalyst impregnation on charcoal reduced CO emissions by up to 97 % and increased the free active sites on the solid fuel surfaces, which decreased at temperatures > 500 °C possibly due to thermal deactivation of the catalyst.

Keywords:

Biomass; Charcoal; Coal; Pyrolysis; Free radicals; CO; CO_2; Pd-Sn/alumina; Cu-Mn/graphite; Thermal analysis; Confined environments

To my mother

Thank you for your everlasting love

ACKNOWLEDGEMENTS

I take this opportunity to thank everyone who has been there for me during my time as a PhD student. I thank my supervisors Mr. Roland Wessling and Dr. Mike Williams for entrusting me with this research. I also express my gratitude to my review team members Prof. David Lane and Dr. Nathalie Mai, for the fruitful advise.

This PhD would not have happened without funding. Thanks to the Gas Safety Trust of the United Kingdom, the Boat Safety Scheme of the United Kingdom and the Katie Haines Memorial Fund for sponsoring my PhD. I thank the Cranfield University Finance Department for providing funds whenever they were required. Thanks to the registry office, the student academic support, the entire Cranfield Forensic Institute (CFI) staff, and the entire Centre for Defence Chemistry (CDC) staff, the Barrington library, the Doctoral Community, Cranfield Student Association (CSA), the learning support services, and the IT department. All the individual persons who assisted in the experimental and analytical work are thanked in the acknowledgement sections of each chapter.

Throughout this PhD, I have met many people through external and internal meetings, conferences and seminars. Thanks to the Institute of Gas Engineers and Managers (IGEM), the CO^+ Safety Science and Technology (SciTech) group and the All-Party Parliamentary Carbon monoxide (APPCO) group for inviting me to conferences and meetings. I would like to thank Georgia Mcleod and Jessica Bolton for laying the foundation for this PhD through an MSc study on CO emissions from charcoal in 2013 and a CO^+ Impact study in 2014 – 2016, respectively.

Lastly, I thank my family for always encouraging, praying and believing in me. My mum and dad, brothers and sisters, Jantonia Nyombi, Joy-Wycliffe Nyombi, and Christine Namuyanja: thank you for being a wonderful family.

TABLE OF CONTENTS

LIST OF FIGURES

Chapter one

Chapter two

Chapter three

Chapter four

Chapter five

Chapter six

Chapter seven

Appendix B

Appendix C

Appendix D

LIST OF TABLES

Chapter two

Chapter three

Chapter four

Chapter five

Chapter seven

Appendix B

ABBREVIATIONS

A	Pre-exponential factor
a.u.	Arbitrary units
APPCO	All-Party Parliamentary Carbon monoxide group
A_T	Total area under the CO or CO_2 concentration time curve
BBQ	Barbecue
BET	Brunauer Emmett and Teller
BSS	Boat Safety Scheme
CAL	Clair Air Limited
CDC	Centre for Defence Chemistry
CFI	Cranfield Forensic Institute
cm	Centimetre
C_n	Concentration at the n^{th} time
ComC	Commercial Charcoal
CSA	Cranfield Student Association
CTCB	Catalyst Treated Charcoal Briquettes
CTL	City Technologies Limited
DAEM	Distributed activation energy model
DOI	Digital object identifier
DPPH	Diphenyl Picryl Hydrazine
DRIFT	Diffuse reflectance infrared Fourier transform
DSC	Differential scanning calorimetry
e	Exponent
E_a	Activation energy
EC	Electrochemical
E_i	Molar ratio (mole/mole) of emissions of CO or CO_2
EPR	Electron paramagnetic resonance
ESR	Electron spin resonance
$f(\alpha)$	Differential conversion function
FC	Fixed carbon
FCC	Fluid cracking catalyst

FTIR	Fourier transform infrared
FWO	Flynn-Wall-Onzawa
G	Gauss
g	Gram
$g(\alpha)$	Integral conversion function
GC	Gas chromatography
GHG	Greenhouse gas
GST	Gas Safety Trust
GUM	Guide for expression of uncertainty in measurements
HHV	High heating value
HMF	Hydroxymethyl furfural
ICD	International classification of disease
IGEM	Institute of Gas Engineers and Managers
In	Natural logarithm
IR	Infrared
J	Joule
K	Kelvin
k	Rate constant
KAS	Kissinger-Akahira-Sanose
kb	Stefan-Boltzmann constant
kg	Kilogram
kHz	Kilohertz
KIS	Kissinger
L	Avogadro's constant ($6.022140857 \times 10^{23}$)
L/min	Litre per minute
LCMs	Lamella constituent molecules
LGC	Laboratory for Government Chemist
log	Logarithm
LPG	Liquefied petroleum gas
M	Molarity
m^2	Square meter

m^3	Cubic meter
MAP	Microwave-assisted pyrolysis
MB	Methylene blue dye
MJ	Mega joule
mL	Millilitre
Mol	Mole
MS	Mass spectrometry
MSW	Municipal solid waste
mT	MilliTesla
MW	Microwave
mW	Milliwatt
NDIR	Non-distractive infrared
NMR	Nuclear magnetic resonance
PAH	Polycyclic aromatic hydrocarbon
PDF	Power Diffraction File
PE	Polyethylene
pH	Hydrogen ion concentration (-log[H^+])
PH	Peak height
PM	Particulate matter
PVC	Polyvinyl chloride
Q	Volumetric flow
R	Universal gas constant (8.314 J/mol.K)
R^2	Regression coefficient
RB	Reactive black dye
s	Second
SciTech	Science and Technology
SD	Standard deviation
SSA	Specific surface area
STP	Standard temperature and pressure
t_f	Final time
TGA	Thermogravimetric Analysis

TGA	Thermogravimetric analysis
t_n	n^{th} time
t_o	Initial time
UK	United Kingdom
USA	United States of America
UTCB	Untreated Charcoal Briquettes
UV	Ultraviolet
VM	Volatile matter
VOC	Volatile organic compound
V_{rtp}	Molar volume at room temperature and pressure
w/w	Weight per weight ratio
WHO	World Health Organization
X_c	Relative molecular mass of carbon
X_i	Moles of CO or CO_2
XRD	X-Ray Diffraction

NOTATIONS

α	Fractional conversion
π	Greek letter Pi
β	Heating rate (°C/min)
∞	Infinity
μ	Micro
φ	Molar recovery
$\sum$	Summation
•C-C	Carbon-carbon radical
•C-O	Carbon-oxygen radical
$•CH_3$	Methyl radical
θ_{CO}	Carbon monoxide coverage factor
ΔG	Change in Gibbs free energy
ΔH	Change in enthalpy
•H	Hydrogen radical
•O-O-	Oxygen-oxygen radical
•OH	Hydroxyl radical
ΔS	Change in entropy
%	Percent
°C	Degree Celsius
A	Pre-exponential factor (s^{-1})
Ag	Silver
Al	Aluminium
$Al(OH)_3$	Aluminium hydroxide
Al_2O_3	Aluminium oxide
$Alcl_3$	Aluminium chloride
Ar	Argon
Au	Gold
C	Carbon
C_2H_4	Ethene (ethylene)
C_3H_8	Propane

Ca	Calcium
Ce	Cerium
CH_4	Methane
CO	Carbon monoxide
Co	Cobalt
CO_2	Carbon dioxide
CO_c	Carbon monoxide from catalyst-treated charcoal
CO_o	Carbon monoxide from untreated charcoal
CO_{rT}	Residual carbon monoxide at any temperature
Cr	Chromium
Cu	Copper
Cu^+	Copper (I) ion
$Cu_{1.5}Mn_{1.5}O_4$	Hopcalite (most active phase)
Cu^{2+}	Copper (II) ion
Fe	Iron
Ga	Gallium
H_2O	Water
H_2O_2	Hydrogen peroxide
H_2S	Hydrogen sulfide
H_2SO_4	Sulfuric acid
He	Helium
HNO_3	Nitric acid
Ir	Iridium
K	Potassium
k	Rate constant (s^{-1})
K_2CO_3	Potassium carbonate
K_2O	Potassium oxide
La	Lanthanum
Mg	Magnesium
Mn	Manganese
Mn_2O_3	Manganese (III) oxide

Mn_3O_4	Manganese (II, III) oxide
Mn_5O_8	Manganese (II, IV) oxide
MnO	Manganese (II) oxide
MnO_2	Manganese (IV) oxide
Mo	Molybdenum
Mo_2C	Molybdenum Carbide
n	Reaction order
N_2	Molecular nitrogen
Na	Sodium
Na_2CO_3	Sodium carbonate
NaCl	Sodium chloride
NaOH	Sodium hydroxide
Nb	Niobium
Ni	Nickel
NO_2	Nitrogen dioxide
NO_x	Nitrogen oxides
O^-	Oxygen radical with filled orbital
O^+	Oxygen radical with unoccupied orbital
O_2	Molecular oxygen
^oC/min	Degrees centigrade per minute
P	Phosphorus
P_2O_5	Phosphorous pentoxide
Pd	Palladium
Pt	Platinum
R	Universal gas constant
Rh	Rhodium
Ru	Ruthenium
S	Sulfur
Si	Silicon
SiO	Silicon oxide
Sn	Tin

$SnCl_4$	Tin (IV) chloride
T	Thermodynamic temperature (K)
t	Time
Ta	Tantalum
Ti	Titanium
V	Char oxidation rate (mol/s)
V	Vanadium
W	Tungsten
W_2C	Tungsten Carbide
Y	Yttrium
Zn	Zinc
Zr	Zirconium

Chapter 1: INTRODUCTION

This PhD thesis is presented as a series of papers, either published, submitted for publication, or in preparation for publication. Each paper includes a brief review of the literature; thus, an extended review of the relevant literature is presented as a separate chapter to expand the coverage of previous and recent work. However, some aspects pertaining to the work in this thesis are presented in the introduction. The aim is to provide a full understanding of the project background and also to offer a context within which to place the individual papers and the work as a whole.

1.1 Impact of CO exposure to humans

Solid fuel emissions are dangerous to human health especially carbon monoxide (CO). It was observed that 5.2 % of suicide deaths in England and Wales were due to CO poisoning in 2001 – 2011. These numbers declined to a total of 53 deaths by 2015 with England accounting for 91 % of the total deaths [1]. Gas suicides cases reduced by 53 % for the year between 2001 to 2011. However, there was a 17-fold increase fatal cases due to helium for the two-year period 2001 – 2002 to 2010 – 2011. Barbecue charcoal gas fatalities increased from one (1) to eleven (11) in the same period [1], [2], *Table 1- 1*.

Table 1- 1: Number of deaths from accidental CO poisoning in England and Wales, deaths registered in 2011-2015. Adapted from the Office of National Statistics (UK) [1]

ICD 10 Code	Underlying cause[1,2,3]	England						Wales				
		2011	2012	2013	2014	2015		2011	2012	2013	2014	2015
V00-X59	All accidental carbon monoxide poisonings	75	58	57	52	48		4	7	3	3	5
X47	Accidental poisoning by other gases and vapours	33	23	22	25	24		1	2	2	1	1
X47.0	Occurrence at home	28	17	14	18	23		1	1	2	0	1

X47.1	Occurrence in residential institution	0	0	0	0	0	0	0	0	0	0
X47.2	Occurrence at school other institution/public admin area	0	0	0	0	0	0	0	0	0	0
X47.3	Occurrence at sports/athletics area	0	0	0	0	0	0	0	0	0	0
X47.4	Occurrence on street/highway	1	1	0	0	0	0	0	0	0	0
X47.5	Occurrence at trade/service area	1	0	0	1	0	0	0	0	0	0
X47.6	Occurrence at industrial/construction area	0	0	1	0	0	0	0	0	0	0
X47.7	Occurrence on farm	0	0	0	0	0	0	0	0	0	0
X47.8	Occurrence at other specified place	3	4	6	4	1	0	1	0	1	0
X47.9	Occurrence at unspecified place	0	1	1	2	0	0	0	0	0	0
V01-V99	Transport accident	0	0	0	0	1	0	0	0	0	0
X00-X09	Accidental exposure to smoke, fire and flames	42	35	34	27	23	3	5	1	2	4

[1]Cause of death was defined using the International Classification of Diseases, Tenth Revision (ICD 10). Deaths were selected where the underlying cause of death was accidental (ICD 10 codes V01-X59), and where the secondary cause of death was the toxic effect of carbon monoxide (ICD 10 code T58). The original underlying cause of death has been used. [2]Figures for England and Wales exclude deaths of non-residents based on boundaries as of November 2016. [3]Figures are for deaths registered, rather than deaths occurring in each calendar. Due to the length of time it takes to complete a coroner's inquest, it can take months or even years for a carbon monoxide poisoning death to be registered. More details can be found on the ONS website: www.ons.gov.uk/ons/guide-method/user-guidance/health-and-life-events/impact-of-registration-delays-on-mortality-statistics/index.html.

The Gas Safety Trust (GST) of the UK has also been compiling statistics on CO related death by fuel type [3] as well as other accidental death and injuries [4], [5] especially from 1995 to date [6], [7]. However, those are the incidents that have been reported to hospitals with well documented records. There are many other fatal incidents which are not captured.

1.2 Some aspects of solid fuel combustion

All solid fuels produce carbon monoxide (CO) during incomplete combustion [8]. Wood materials are sometimes used in their raw form for heating, warming in fireplaces [9], [10], or in semi-processed form as wood chips for use in boilers [11], [12] or for industrial applications. Wood can be carbonised or pyrolysed to form solid products such as charcoal/biochar, liquid products such as bio-oil, or flue gases [13]. On the other hand, coal is used in its processed form as a blended product with biomass or alone as pyrolysed coal both for home heating and industrial applications [14], [15]. An understanding of the physicochemical properties of these fuels is very important to determine their most suitable applications.

In some instances, it may be necessary to understand the chemical species on the surface of solid fuels that give rise to different pollutants [16]. Some of these species are 'free radicals' in nature, sometimes described as 'surface complexes' [17] [18], [19], [20], [21], whereas others are neutral with different functional groups that determine how these compounds behave.

A thorough investigation of the pollutants released by solid fuel combustion is important to assess their health and environmental impact when used for energy applications. The products of interest include CO, carbon dioxide (CO_2), methane (CH_4), particulate matter, aromatics, and polycyclic aromatic hydrocarbons (PAHs) [22], [23].

Carbon monoxide has continued to threaten human life despite several technologies invented for its detection. Scientists have therefore resorted to finding alternatives for converting CO into less harmful products. Much of the research thus far has addressed the use of transition metal compounds as catalysts [24] for the post-combustion oxidisation of CO.

This thesis therefore focuses on understanding solid fuel pyrolysis, the species that give rise to CO during combustion, CO evolution from charcoal and coal, and catalyst impregnation on charcoal to minimise CO emissions.

1.3 Inception of the project

1.3.1 The Hazel Woodhams incident

In July 2011, Roland Wessling's partner Hazel Woodhams died of CO poisoning in an incident that left Roland with severe injuries. These events were caused by taking a small, warm-to-the-touch charcoal barbeque grill into a tent before going to bed. Both partners were highly educated people, with MSc degrees in forensic science. Hazel worked as a Scene of Crime Officer for West Yorkshire Police and Roland is a lecturer in forensic science at Cranfield University, Shrivenham (the UK Defence Academy). Anyone would expect that with their educational background and work experience, they would have known that there was a risk of CO and other harmful gases from the charcoal, but they did not. They had a CO detector in their house but that was not enough to save Hazel's life.

Roland was arrested when the police arrived on the scene. What the police found was a couple, one dead, the other injured, and Roland appeared to be 'drugged'. However, Roland was released 6 hours later when the hospital confirmed the CO level in his blood.

CO can threaten in many different environments, such as tents, boats or at home. Without proper education, greater awareness and safer products, more and more people will die as the result of CO poisoning and some of these cases will not even be attributed to CO.

1.4 Aims and objectives

The aim of this PhD project was to find ways to reduce the emission of CO during solid fuel combustion. This was met through the following:

i. A review of the analysis and processing of solid fuels
ii. Understanding the principles of biomass pyrolysis
iii. An investigation of the combustion and surface chemistry of charcoal
iv. Determining the parameters responsible for the release of CO
v. Investigating the effect of impregnating charcoal with catalysts on the emissions released during combustion.

1.5 Thesis plan

Each research section has been structured into chapters based on papers that are published, submitted or in preparation, which together constitute this thesis. All chapters have been written by the first author, Antony Nyombi, and edited by Dr. Mike Williams and proofread by Mr. Roland Wessling. All laboratory work was undertaken by Antony Nyombi. The chapters are not exact copies of the published papers, some words have been added to make them more understandable in the thesis format.

The connection between the thesis chapters is shown in Figure 1-1. Chapter 2 reviews the solid fuel combustion kinetics and mechanisms during combustion and the methods used to minimise human exposure to CO. The current literatures on the impregnation of solid fuels with chemicals focus more on optimizing the desired products rather than minimising the emissions of CO. Hence further knowledge is required to minimise CO emissions. Chapter two also covers the main experimental techniques used in this work.

Chapter 3 deals with the kinetics and thermodynamics of slow pyrolysis in ash (*Fraxinus*) wood sawdust based on thermogravimetric analysis. Chapter 3 was published in *Energy Sources, Part A: Recovery, Utilization, and Environmental Effects* [25]. The physicochemical properties, kinetics, thermodynamics and pyrolysis mechanisms of ash (*Fraxinus*) had not been investigated in detail for potential bioenergy applications. A comprehensive analysis of this material should therefore add to the knowledge of other biomass materials used to generate energy. The deeper understanding of pyrolysis achieved in this chapter also facilitated the work described in Chapters 4–7.

Chapter 4 addresses the reactivity of charcoal during oxidation and the free radicals on the charcoal surface that form during pyrolysis/carbonisation as well as oxidation in air. Chapter 4 has been published in Energy and Fuels Journal [26].

Chapter 5 concerns CO emissions from wood sawdust and charcoal. Commercial charcoal and wood sawdust were tested to assess the amounts of CO released under different conditions. Furthermore, this chapter investigated the accumulation of CO in ISO container as a "model" for confined spaces. Chapter 5 was published in *Energy Sources, Part A: Recovery, Utilization, and Environmental Effects* [27].

Chapter 6 describes experimental work to minimise the release of CO from charcoal dust during combustion. Chemical compounds (catalysts) were mechanically impregnated into the charcoal and the residual CO produced during combustion was evaluated during isothermal combustion. This article considers CO oxidation at the pre-combustion stage (before CO is released from the charcoal surfaces) as opposed to post-combustion oxidation (after CO is released from the surface) which has been the focus of CO oxidation studies for many years. Chapter 6 was published in Chemical Physics Letters [28].

Chapter 7 further discusses impregnation of catalysts on solid fuels at an extended level. In this chapter, catalyst treated charcoal briquettes, untreated charcoal briquettes and coal briquettes were prepared using non-standard methods to optimize desired products. The real time emission of CO, CO_2, NO_x, and CH_4 was compared during a non-isothermal combustion study. Chapter 7 was published in Energy & fuels journal [29].

Chapter 8 is the general discussion of the thesis.

Chapter 9 has the general conclusions from this thesis.

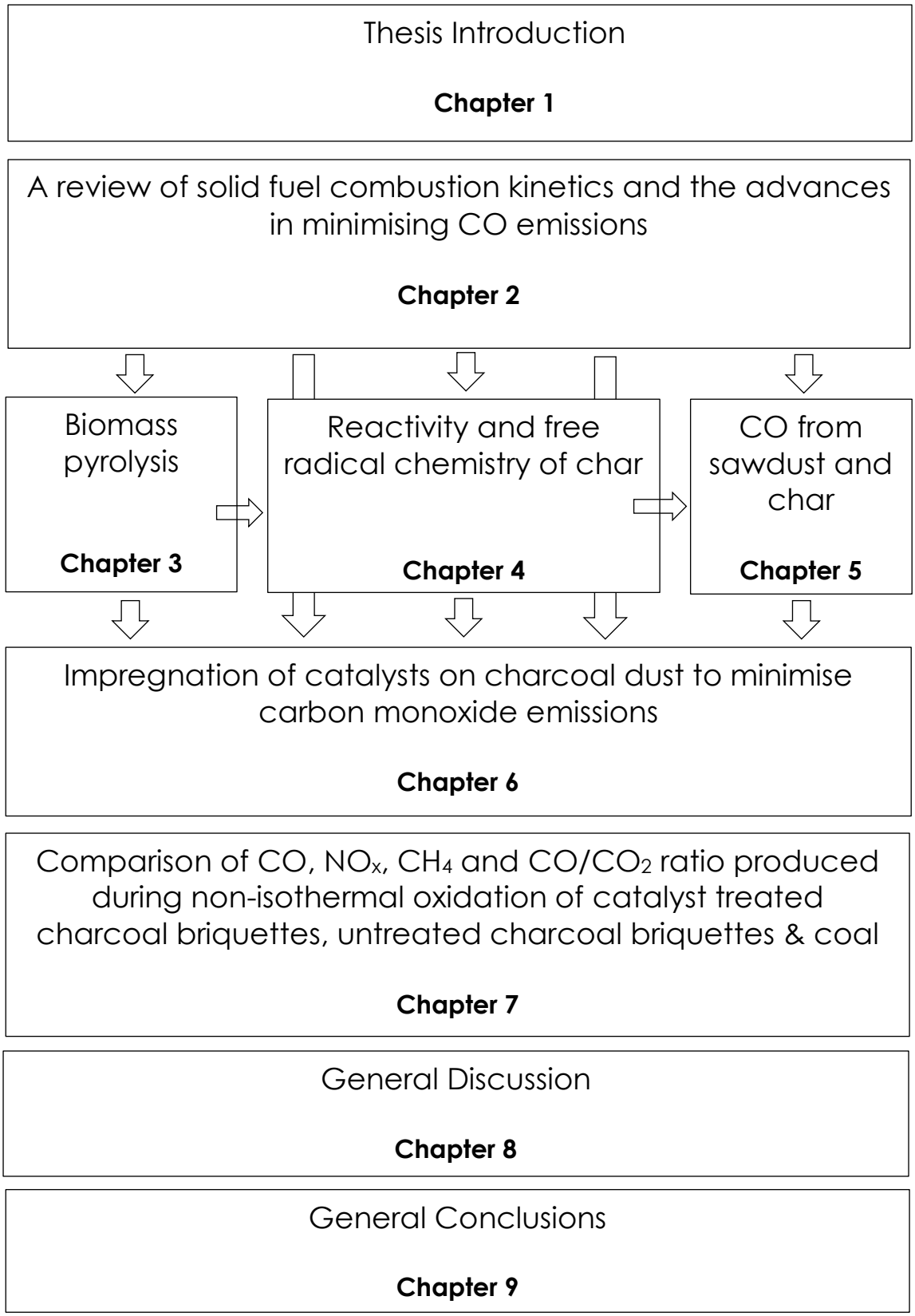

Figure 1-1: Connection between the chapters in this thesis.

Chapter 2 will discuss the kinetics of solid fuel combustion and the advances in minimizing CO emissions as well as the main methods used in this work.

Chapter 2: SOLID FUEL COMBUSTION: KINETICS, ADVANCES IN MINIMIZING CO EMISSIONS AND METHODS USED IN THIS WORK

2.1 Introduction

It is of great importance that the emission of toxic gases from the combustion of solid fuels is minimised while diversifying energy sources to supplement the declining fossil fuels. Wood and coal are regarded as the world's most used solid fuels in homes [30], [31]. It is estimated that 90 % of solid fuel (coal, crop residue, and woody materials) consumption is by developing countries. This population constitutes more than three billion people [32]. Biomass is the best foreseeable solid fuel to replace coal due to its ease of processing, friendliness to the environment and abundance.

In the UK, the main biomass materials include palm, soya and sunflower oils, sugarcane, and palm or coconut husks [33]. Other solid fuels may be formed from food waste which comprises approximately 10 million tonnes. Most of this is discarded annually in the UK of which only 18 % was recycled in 2016 [27]. Charcoal derived from pyrolysis of carbonaceous materials is widely used as a fuel for home, industrial and recreational energy generation purposes. Coal is one of the oldest carbon rich solid fuels. There are four types of coal: peat, lignite, bituminous, and anthracite, with anthracite being most desirable due to its high heat content [34].

High volatile matter content and moisture render biomass a low energy intensive fuel. Processing such solid fuels is necessary to enhance energy output, reduce toxic and ozone depleting emissions and to increase the share

of certain products in the outputs (i.e. gasification for increased gaseous products and bio-oil, torrefaction and low temperature pyrolysis for generating high quality solid products [35], etc.). During the processing of solid fuels, they undergo certain reaction mechanisms depending on the material properties and the controls used in the process. The data produced from controlled processing are used to determine the kinetic parameters for the processing or usage of solid fuels. The activation energies, pre-exponential factors, entropy, enthalpy and calorific value are used to assess a given solid fuels for bioenergy production [36], [37], [38].

During processing or usage of solid fuels, the main evolved gases are usually CO, CO_2, H_2O, CH_4, and C_2H_4 [39], [40]. The production of CO, H_2, and CO_2 is enhanced under CO_2 [41], over N_2, Ar, or air atmospheres. Pyrolysis enhances the carbon mass fraction while H_2, O_2, N_2 and S mass fractions are reduced [42].

The smoke from burning solid fuels especially coal contains fine particles, CO, benzene, polycyclic aromatic hydrocarbons (PAHs) among other pollutants which are associated with reduced intrauterine growth [43]. Carbon monoxide has always posed serious dangers to human life. The lungs of mummified bodies from the Paleolithic era are frequently black [44], a sign of heavy smoke which is indicative of poor combustion and thus CO production. In 1850's Claude Benard showed that CO blocked respiration in erythrocytes [45]. Even in ruminants, CO is reported to decrease the digestion of hemicellulose and cellulose by 40 and 27 % respectively.

In the effort to reduce toxic and greenhouse gas emissions, the EU through its European decarbonisation strategy 2050, has set targets including the 22 % of the energy share should come from renewables by 2030 and 42 % by 2050 up from 9 % in 2010 [46]. Furthermore, there are available technologies for

minimizing CO including sensors [47], improved cookstoves [48], better heating systems [49], catalytic systems [50], [51] among others.

2.2 Main methods used in this work

2.2.1 Specific Surface Area Analysis

The combustion of solids is a surface phenomenon, so knowledge of the surface area of samples is important. Surface area analysis gives a better idea of the topographic features than particle size as it includes surface irregularities and porosity.

The instrument used for this analysis was the ASAP 2020 Surface Area and Porosity Analyser. The sample was evacuated to remove moisture and atmospheric vapors by application of heat flushing with an inert gas (nitrogen), a process called degassing. Then the sample temperature was reduced to that of liquid nitrogen (77 K). Nitrogen was admitted to the sample (*Figure 2-1*) as a component in a flowing mixture with non-adsorbing helium. Plotting the accumulated gas quantity adsorbed versus gas pressure data at specified temperature generates an adsorption isotherm. The shape of this isotherm can be interpreted by a number of mathematical methods to give both specific surface area and, if the solid is microporous, a pore size distribution.

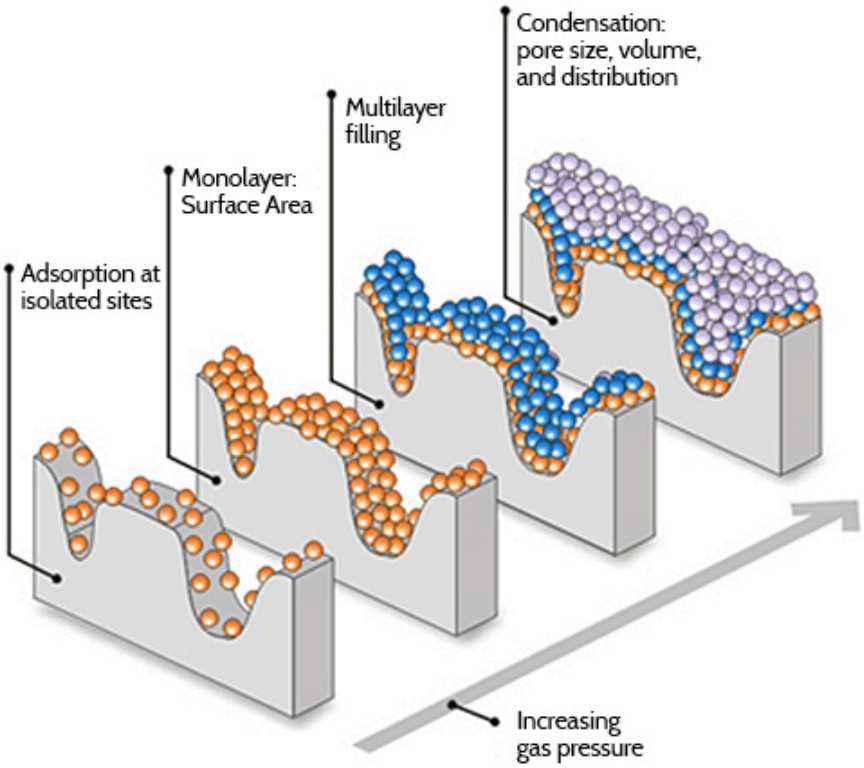

Figure 2-1: Principle of filling of pores within a sample

2.2.2 Electron spin resonance (ESR)

The process of surface combustion is thought to proceed by a free-radical mechanism and there will be a point during oxidation where free-radicals will exist on the solid surface. Free radicals contain unpaired electrons.

ESR is a method for observing the behavior of unpaired electrons within a molecule, and for analyzing various phenomena by identifying the electron environment. ESR was used particularly in chapter 4 for selectively measuring free radicals non-destructively in solid char but this method works for gases and liquids as well [52].

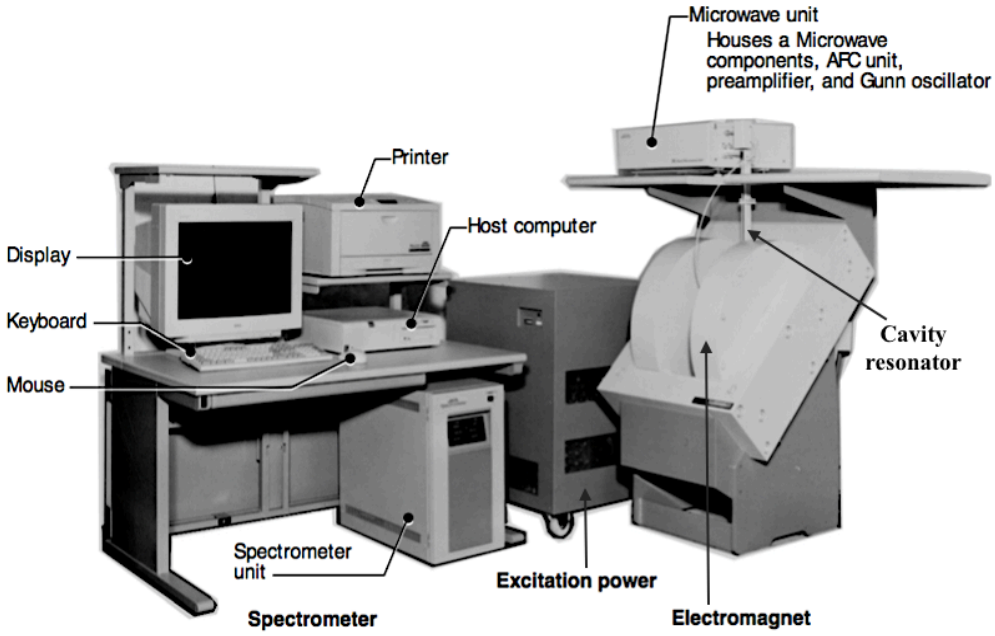

Figure 2-2: The JES-FA200 ESR spectrometer system

The ESR spectrometer system consists of a microwave unit, cavity resonator (*Figure* 2-3), electromagnet, excitation power supply and spectrometer.

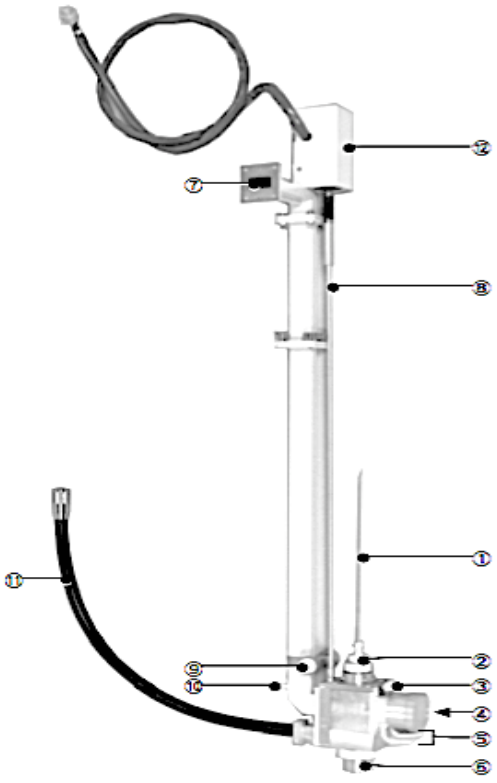

Figure 2-3: The ESR cavity resonator

The parts 1-12 are: (1) Sample tube - Sample tube made of quartz. The insertion position of the sample tube into the cavity is set using the sample-tube length setting gauge. (2) Sample tube collar - Holds the sample tube vertical. (3) ESR marker insertion port – where the ESR marker is inserted. (4) Irradiation window – Window for irradiating with ultraviolet radiation. (5) Cooling-water nozzles – Used when connecting the variable-temperature adapter. (6) Bottom cap – The double-walled tube is inserted from the bottom. The bottom cap is removed when the variable-temperature adapter is to be connected. (7) Waveguide – Transmits microwaves. (8) Coupling-adjustment rod – Shaft for adjusting coupling of the cavity resonator. (9) Cavity-resonator fixture – Supports the cavity resonator in the pole piece gap. (10) Nitrogen-gas nozzle – In low-temperature measurement, the air in the cavity is replaced by nitrogen gas, supplied through this nozzle, to prevent deterioration of Q due to dew condensation. (11) 100 kHz/50 kHz/25 kHz magnetic-field modulation cable – Supplies the signal for magnetic-field modulation. (12) Motor and cable for coupling adjustment – Rotates the coupling-adjustment rod, following instructions from the spectrometer.

With an ESR instrument, a sample is subjected to a varying magnetic field while a fixed microwave frequency is passed through it. When the magnetic field is of the strength that causes the gap between the lower spin state and upper spin state of an unpaired electron to match the energy of the frequency of the microwaves, electrons are promoted and some energy is adsorbed. The study of the magnetic field strength that causes the spin of the unpaired electrons in a sample to flip gives information about the nature of the atomic or molecular orbital containing the electrons and thus about the condition of the sample [52].

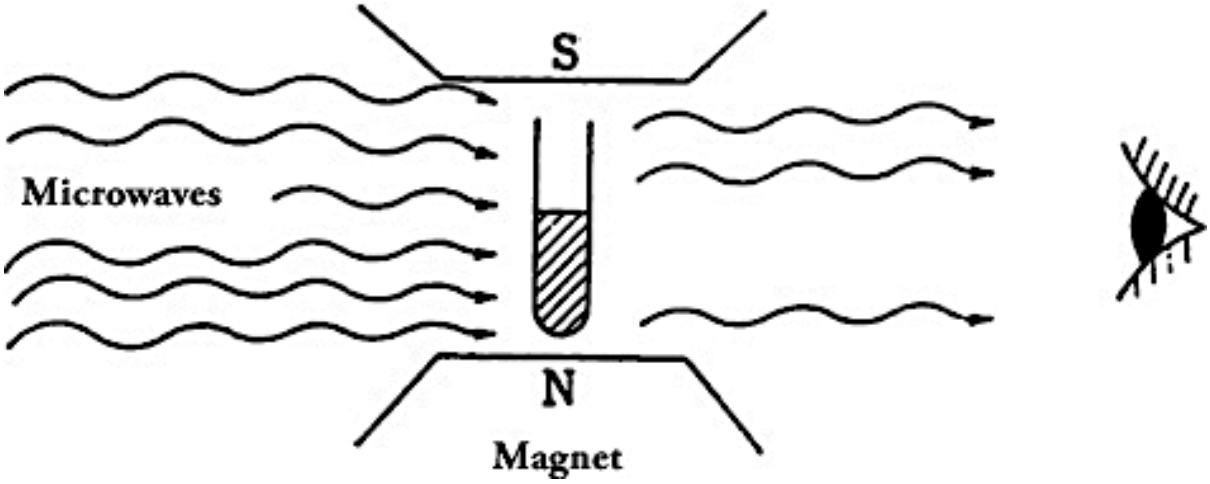

Figure 2-4: Observation of microwaves passing through a sample

ESR was used to observe and measure the absorption of microwave energy by unpaired electrons in a magnetic field.

2.2.3 X-Ray Diffraction (XRD)

XRD was used in this work to determine what happens to the crystalline parts of the solid fuels (charcoal and coal) and the catalysts (Pd-Sn/alumina and Cu-Mn/graphite) during the combustion process. This would give an indication of how CO oxidation would be affected since the different phases have unequal capabilities.

XRD analysis is based on constructive interference of monochromatic X-rays and a crystalline sample: The X-rays are generated by a cathode ray tube, filtered to produce monochromatic radiation, collimated to concentrate, and directed toward the sample (*Figure 2-5*). The interaction of the incident rays with the sample produces constructive interference (and a diffracted ray) when conditions satisfy Bragg's Law ($n\lambda=2d \sin \theta$). This law relates the wavelength of electromagnetic radiation to the diffraction angle and the lattice spacing in a crystalline sample [53].

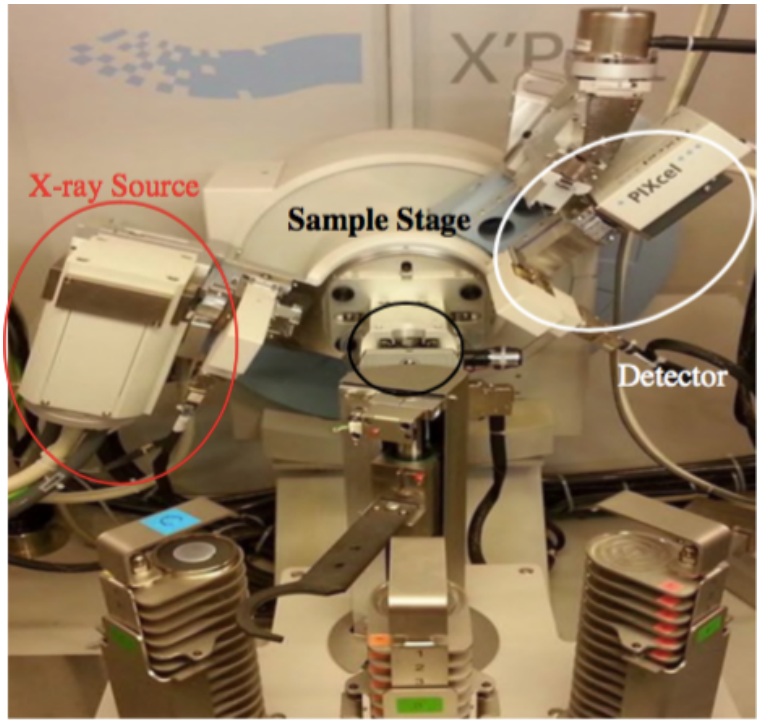

Figure 2-5: Photograph of the PANalytical X'pert powder diffractometer employed in Chapter 6 for characterising catalysts. The X-ray source, sample stage and X-ray detector are highlighted.

The characteristic x-ray diffraction pattern generated in a typical XRD analysis provides a unique "fingerprint" of the crystals present in the sample. When properly interpreted, by comparison with standard reference patterns and measurements, this fingerprint allows identification of the crystalline form.

2.2.4 Thermal analysis (TGA/DSC)

The effect of heating small samples of material in a controlled environment can not only give basic thermal stability information but can also be analysed to produce more fundamental information about the thermodynamics and kinetics of themal decomposition and combustion.

The Thermogravimetric Analyser (TGA) measures mass loss/gain of a sample as a function of temperature and time. Differential Scanning Calorimetry

measures the difference in heat flow rate between the sample and the inert reference as a function of temperature and time (Figure 2-6 to Figure 2-8).

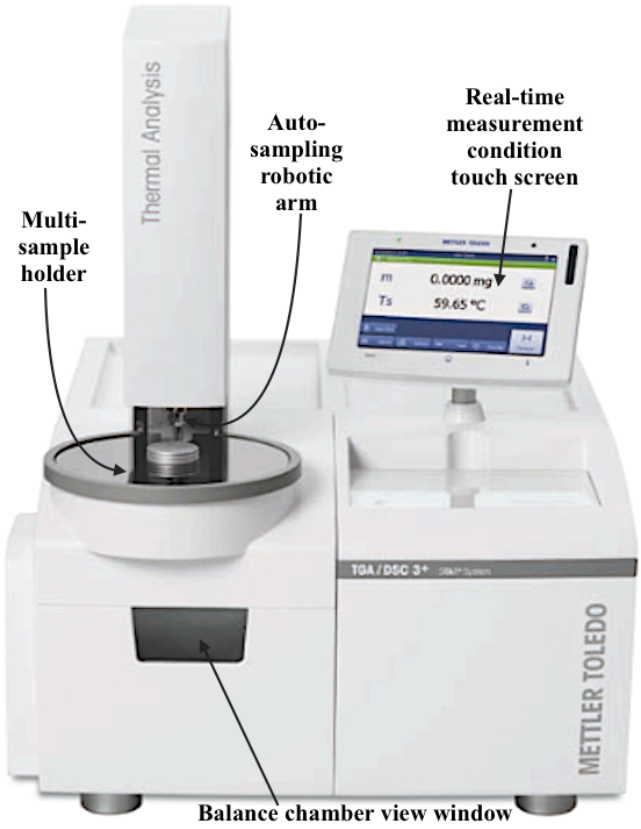

Figure 2-6: The TGA/DSC3+ instrument

The multi-sample holder and the auto-sampling robot are shown in detail in Figure 2-7. The measurement and heating unit are shown in Figure 2-8.

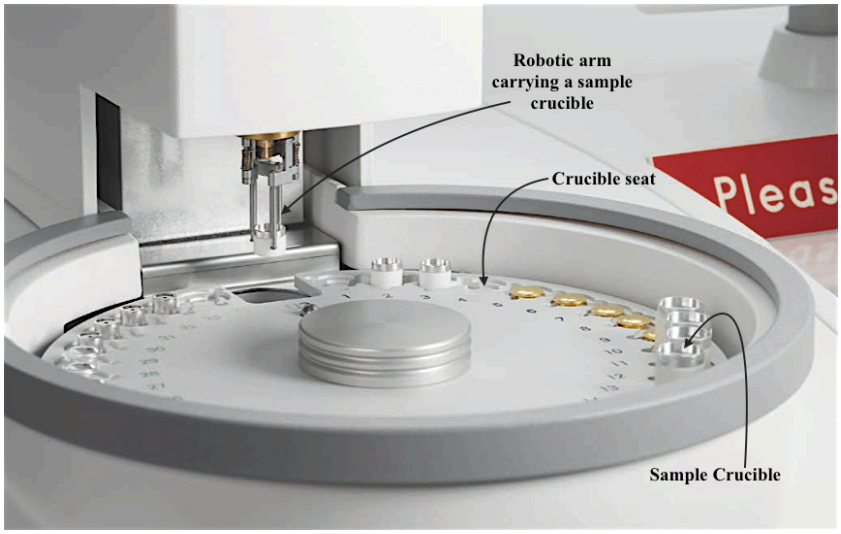

Figure 2-7: The TGA-DSC3+ auto-sampling unit

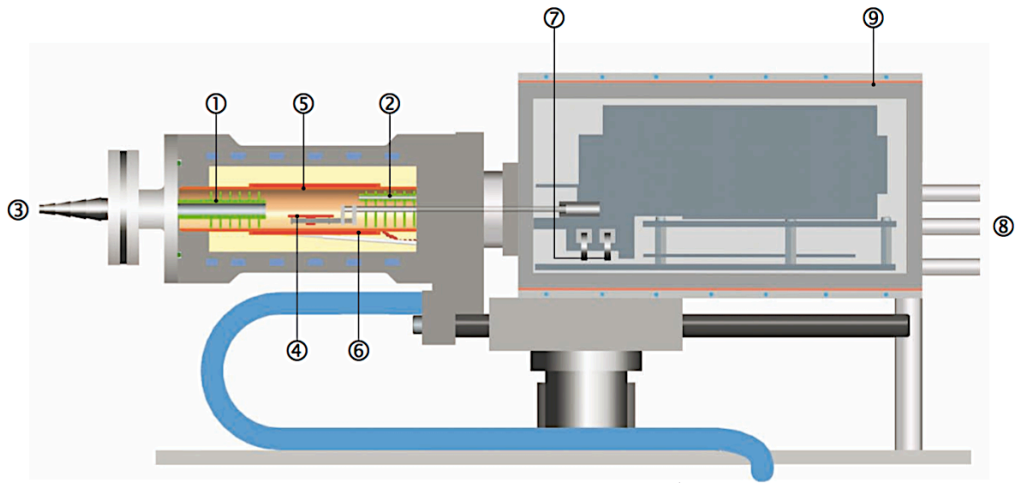

Figure 2-8: The TGA/DSC3+ measurement and heating unit

The parts 1-9 are: (1) Baffles, (2) Reactive gas capillary, (3) Gas outlet, (4) Temperature sensors, (5) Furnace heater, (6) Furnace temperature sensor, (7) Adjustment ring weights, (8) Protective and purge gas connector, and (9) Thermostatic balance chamber.

How the TGA balance works

The balance operates on a null-balance principle. At the zero, or "null" position equal amounts of light shine on the 2 photodiodes. If the balance moves out of the null position an unequal amount of light shines on the 2 photodiodes. Current is then applied to the meter movement to return the balance to the null position. The amount of current applied is proportional to the weight loss or gain [54].

Mechanisms of Weight Change in TGA

Weight change could be in form of weight Loss including decomposition (The breaking apart of chemical bonds), evaporation (The loss of volatiles with elevated temperature), reduction (Interaction of sample to a reducing

atmosphere (hydrogen, ammonia, etc), or desorption. On the other hand, weight change could be a weight gain in form of oxidation (Interaction of the sample with an oxidizing atmosphere) or absorption/aadsorption.

Information obtained from TGA

'Thermal Stability of Materials: Explicate decomposition mechanism, fingerprint materials for identification & quality control; Oxidative Stability of Materials: Oxidation of metals in air, Oxidative decomposition of organic substances in air/O_2, Thermal decomposition in inert atmosphere; Composition of Multi-component Systems: Behaviors sufficiently different on the temperature scale can be identified and reaction mechanism formulated; Estimated Lifetime of a Product: Related to thermal stability; Decomposition Kinetics of Materials: Rate of reaction, Activation Energy; The Effect of Reactive or Corrosive Atmospheres on Materials: Oxidation & Corrosion Studies; Moisture and Volatiles Content of Materials: Loss of moisture, drying, desorption' [54].

2.3 Kinetics and mechanisms for degradation of solid fuels

The rates of mass change and heat flow responses of substances to heating in TGA/DSC can be used to obtain fundamental parameters.

2.3.1 Determination of kinetic parameters

The first known kinetic studies were isothermal in nature and involved using models to fit the obtained data values. This method is still extensively used for kinetic analysis. However, this approach has challenges of not being able to determine a unique model for a particular reaction progress. Rather,

researchers fit the data to several models and draw conclusions based on one that which gives the best regression coefficient. These conclusions are not reliable even for isothermal data. With non-isothermal data, high uncertainties arise that make it difficult to compare reactions. The model free approaches for both isothermal and non-isothermal data avoids the ambiguous assignment of reaction models [55]. The kinetic parameters are dependent on the fractional conversion which can be determined with mini steps throughout the entire reaction progress. This allows reliable prediction of reaction rates and proper conclusions to be made.

Thermogravimetric analysis/differential scanning calorimetry (TGA/DSC) has been used for many years for determining thermal properties of solid fuels. TGA/DSC provides a controllable atmosphere and heating rates, with negligible thermal gradients and transport effects during oxidation of small solid samples [56]. The application of TG analysis is appropriate to obtain chemical kinetic parameters, such as activation energy.

The attainment of a proper and accurate description of the progress of thermal reactions (isothermal or non-isothermal) is the goal of any solid fuel material researcher. However, achieving this is often far from reach due to complex reactions, intermediate stages and mechanisms involved. Many times, oversimplifications are made to consider the (i) fractional conversion and (ii) temperature of reaction.

The decomposition rate of solid fuels can be modelled as:

$$\frac{d\alpha}{dt} = kf(\alpha) \qquad (2\text{-}1)$$

where α is the fractional conversion, namely the fraction of the solid fuel decomposed in time Δt, k is defined as the rate constant of the Arrhenius reaction equation, and $f(\alpha)$ is the reaction model function.

The activation energy (E_a) is related to the reaction rate constant by the Arrhenius expression, $k = Ae(\frac{-Ea}{RT})$ and reaction model function, f(α) – which may take different forms [56] , [57]. The fractional conversion is determined by comparing the original mass to the instantaneous and final mass [58], [59]. It takes the form shown in eqn. (2-2):

$$\alpha = \frac{W_o - W_t}{W_o - W_\infty} \qquad (2\text{-}2)$$

where W_o is the initial mass, W_t is the mass at any temperature and time, W_∞ is the mass at the end of the reaction. Hence, the kinetic equation for the assumption that the progress of reaction depends on temperature and fractional conversion can be written as:

$$\frac{d\alpha}{dt} = k(T).f(\alpha) \qquad (2\text{-}3)$$

Inserting the expression for the rate constant k, gives the main form of this equation as;

$$\frac{d\alpha}{dt} = Ae^{-\frac{Ea}{RT}}f(\alpha) \qquad (2\text{-}4)$$

Under non-isothermal conditions in which samples are heated at constant heating rates (β), the actual temperature under this condition can be expressed as;

$T = T_o + \beta t$ as described by [60].

where, T_o is the initial temperature, β is the linear heating rate (°C/min), and T is the temperature at time t. The following expression can be considered for non-isothermal conditions:

$$\frac{d\alpha}{dT} = \frac{d\alpha}{dt} \cdot \frac{dt}{dT} \qquad (2\text{-}5)$$

where, $\frac{d\alpha}{dT}$ is the non-isothermal reaction rate, $\frac{d\alpha}{dt}$ is the isothermal reaction rate and $\frac{dT}{dt}$ is the linear heating rate, β.

Combining equation (2-4) and (2-5) gives,

$$\frac{d\alpha}{dT} = \frac{A}{\beta}\, e^{-\frac{Ea}{RT}} f(\alpha) \qquad (2\text{-}6)$$

where, α is the fraction decomposed, A is the pre-exponential factor, E_a is the activation energy, R is the universal gas constant, T is the absolute temperature.

The determination of the equivalence temperature (T) at which the reaction rate is obtained is important at different heating rates (β) for all methods used for determining activation energy. The equivalence stage is the point at which a given fixed fraction of the initial mass is attained. Such methods are referred to as iso-conversional. Iso-conversional methods may be integral which rely on the temperature integral alone. These include the Starink, Kissinger-Akira-Sanose (KAS), and Flynn-Wall-Onzawa (FWO). The Kissinger method on the other hand is not iso-conversional because data values are taken from a single maximum temperature (T_m) to represent the entire reaction progress. Other methods do not use mathematical expressions but instead use the differential form at the equivalence stage of the reaction. These include the Friedman and Gupita methods.

2.3.1.1 Differential iso-conversional methods

The slopes of the changes in fractional conversion/time plots for isothermal/non-isothermal TGA give us the rate of fractional conversion. This can be described for the different isothermals by eqn. (2-4) above,

$$\frac{d\alpha}{dt} = Ae^{-\frac{Ea}{RT}}f(\alpha)$$

Taking natural logarithms on both sides of the above equation,

$$In\left(\frac{d\alpha}{dt}\right) = In[Af(\alpha)] - \left(\frac{Ea}{R}\right)\left(\frac{1}{T}\right) \qquad (2\text{-}7)$$

If the $In\left(\frac{d\alpha}{dt}\right)$ for all the data from the isothermals are plotted against the 1/T, a straight line is generated. For non-isothermal data obtained at different heating rates, β, the following equation is obtained:

$$In\left(\beta\frac{d\alpha}{dT}\right) = In[Af(\alpha)] - \left(\frac{Ea}{R}\right)\left(\frac{1}{T}\right) \qquad (2\text{-}8)$$

Again, plotting the $In\left(\beta\frac{d\alpha}{dT}\right)$ against 1/T gives straight lines. The slopes can be used to determine the activation energy. These methods do not require any knowledge of the f(α) function and hence are called model-free methods.

2.3.1.2 Integral iso-conversional methods.

These require the introduction of approximations to describe the temperature function, dα/dT accurately. We shall demonstrate this by deriving the Flynn-Wall-Onzawa (FWO) method. The FWO method was developed by Flynn – Wall [61] and Ozawa [62], based on Doyle's approximation [63]. From eqn. (2-6) above,

$$\frac{d\alpha}{dT} = \frac{A}{\beta}\exp\left(-\frac{Ea}{RT}\right)f(\alpha)$$

Integrating the function equation above, gives the following;

$$g(\alpha) = \int_0^{\alpha} \frac{d\alpha}{f(\alpha)} = \frac{A}{\beta}\int_{To}^{T} e^{-\left(\frac{E}{RT}\right)}\, dT \qquad (2\text{-}9)$$

The equation (2-9) does not have an analytical solution. Only approximations were proposed in the iso-conversion method of Flynn - Wall and Ozawa based on Doyle's approximation. Doyle calculated ln g(α) values for a wide range of (Ea/RT) values, and found that within the limits 20 ≤ (Ea/RT) ≤ 60 [64], the following approximation applies in eqn. (10) below after re-arranging;

$$In\beta = In\left(\frac{AEa}{R\, g(\alpha)}\right) - 5.331 - 1.052\left(\frac{Ea}{RT}\right) \qquad (2\text{-}10)$$

where g(α) is the integral conversion function (reaction model). The plot of lnβ versus 1/T gives a straight line whose slope $-1.052\left(\frac{Ea}{R}\right)$ can be used to determine the activation energy.

The Kissinger-Akahira-Sunose (KAS) method was based on the following equation:

$$In\left(\frac{\beta}{T^2}\right) = \left(-\frac{Ea}{R}\right)\left(\frac{1}{T}\right) + \frac{InAR}{Ea\, g(\alpha)} \qquad (2\text{-}11)$$

To arrive at more accurate results, the iso-conversional integral methods often include assumptions and approximations one of which was derived by Senum and Yang [65]. These are then referred to as iterative methods. When the 4th order Senum and Yang approximation is incorporated into the FWO and KAS, the following expressions are obtained:

$$In\left(\frac{\beta}{H_x}\right) = \left(\frac{0.0048A_\alpha E_\alpha}{g_{(\alpha)}R}\right) - \left(\frac{1.0516E}{R}\right)\left(\frac{1}{T}\right) \text{ for FWO} \qquad (2\text{-}12)$$

$$In\left(\frac{\beta}{h_x T^2}\right) = In\left(\frac{A_\alpha R}{g_{(\alpha)}E_\alpha}\right) - \left(\frac{E}{R}\right)\left(\frac{1}{T}\right) \text{ for KAS} \qquad (2\text{-}13)$$

where

$$H_{(x)} = \frac{(e^{-x})\, h_{(x)}/x^2}{0.0048\exp(-1.0516x)}$$

$$h_{(x)} = \frac{x^4 + 18x^3 + 86x^2 + 96x}{x^4 + 20x^3 + 120x^2 + 240x + 120}$$

This approximation gives an accuracy better than 10^{-5} % for x = E/RT ≥ 20, and $x = \frac{E}{RT}$. The iterative procedure performed involves: (i) Assume h(x) = 1 or H(x) = 1 to estimate the initial value of the activation energy E_1. The conventional iso-conversional methods stop at this step; (ii) using E_1, calculate a new value of E_2 for the activation energy from the plot of ln [β/H(x)] versus 1/T or ln [$\beta/h(x)T^2$] versus 1/T; (iii) repeat step (ii), replacing E_1 with E_2. When $E_i – E_{i-1}$ = 0.01 kJ/mol, then the last value of E_i is considered to be the exact value of the activation energy of the studied reaction.

Kissinger method

This was developed by Kissinger [66]. It is a model free method but it is not iso-conversional method because it assumes constant activation energy with the progress of conversion. At maximum temperatures (T_{max}), where the maximum rate of decomposition is reached, the second derivative of Eqn. (4) is equal to zero, as shown below;

$$\frac{d^2\alpha}{dt^2} = \left[\left(\frac{Ea\beta}{RT_{max}^2}\right) + Aexp\left(-\frac{Ea}{RT_{max}}\right)f'(\alpha)\right]\frac{d\alpha}{dt} = 0 \qquad (2\text{-}14)$$

where, f'(α) is the derivative form of f(α). Rearranging Eqn. (2-14), we obtain,

$$\left(\frac{\beta}{T_{max}^2}\right) = \left(\frac{AR}{Ea}\right)exp\left(-\frac{Ea}{RT_{max}}\right)f'(\alpha) \qquad (2\text{-}15)$$

Assuming that differential function f(α) follows a decelaratory model (explained in the next section) of the type $f(\alpha) = (1-\alpha)^n$, where *n* is the order of reaction, then its derivative $f'(\alpha) = n(1-\alpha)^{n-1}$. Taking natural logarithms on both sides of eqn. (2-15) and incorporating the f'(α), we obtain a linear function below;

$$In\left(\frac{\beta}{T_{max}^2}\right) = \left(-\frac{Ea}{R}\right)\left(\frac{1}{T_{max}}\right) + \left[In\left(\frac{AR}{Ea}n(1-\alpha)^{n-1}\right)\right] \qquad (2\text{-}16)$$

where, E_a and A are the apparent activation energy and pre-exponential factors at different conversions. Assuming that the rate of solid fuel oxidation followed first order kinetics although it may not be always the case, eqn. (2-16) may be re-written as;

$$In\left(\frac{\beta}{T_{max}^2}\right) = \left(-\frac{Ea}{R}\right)\left(\frac{1}{T_{max}}\right) + In\left(\frac{AR}{E_a}\right) \qquad (2\text{-}17)$$

Different heating rates ($\beta = \beta_1, \beta_2, \ldots..$) should be used during the measurements. The apparent activation energy is then determined from the plot of $In\beta/T^2_{max}$ Vs $1/T_{max}$.

2.3.1.3 Rate constant dependent methods

The time taken for complete oxidation of the sample determines the rate constant for the oxidation process. These are used for isothermal data. Assuming that the conversion of a solid fuel at the instant of oxidation is constant, eqn. (2-3), $\frac{d\alpha}{dt} = kf(\alpha)$, may be integrated such that;

$$\int_0^{\alpha} \frac{d\alpha}{f(\alpha)} = Constant\ (C) = k\int_0^t dt = kt \qquad (2\text{-}18)$$

Assuming that the kinetic rate constant follows an Arrhenius-type dependence on the combustion temperature,

$$k = Ae^{\left(-\frac{Ea}{RT}\right)} = \frac{C}{t}$$

Introducing natural logarithms;

$$Int = In\left(\frac{C}{A}\right) + \frac{Ea}{RT}\ or\ Ink = InA - \left(\frac{Ea}{R}\right)\left(\frac{1}{T}\right) \qquad (2\text{-}19)$$

The activation energy could be determined by plotting the natural logarithm of the rate constant against the inverse of the isothermal temperature [67], at different degrees of conversion from all the isothermals. The most common methods used for kinetic analysis are summarized in *Table 2-1*.

Table 2-1: Methods for determination of kinetic parameters

Method	Equation	Reference
Friedman	$In\left[\beta\left(\frac{d\alpha}{dt}\right)\right] = -\left(\frac{E_\alpha}{R}\right)\left(\frac{1}{T}\right) + InAf(\alpha)$	[68], [69]
Gupita	$In\left[\beta\left(\frac{d\alpha}{dt}\right)\right] = -\left(\frac{E_\alpha}{R}\right)\left(\frac{1}{T}\right) + InAf(\alpha)$	[70]
Freeman & Car-roll	$Y = -\frac{E}{R}X + n$ where, $Y = \frac{\Delta\, In\left(\frac{d\alpha}{dt}\right)}{\Delta\, In\,(1-\alpha)}$ and $X = \frac{\Delta\left(\frac{1}{T}\right)}{\Delta\, In\,(1-\alpha)}$	[71]

Kissinger-Akahira-Sanose (KAS)	$In\left(\frac{\beta}{T^2}\right) = -\left(\frac{Ea}{R}\right)\left(\frac{1}{T}\right) + In\left(\frac{A_\alpha R}{g_{(\alpha)}E_\alpha}\right)$	[72]
Flyn-Wall-Onzawa (FWO)	$In\beta = -1.052\left(\frac{Ea}{R}\right)\left(\frac{1}{T}\right) + In\left(\frac{AE_a}{R\,g(\alpha)}\right) - 5.331$	[62], [61]
Starink	$In\left(\frac{\beta}{T^{1.95}}\right) = -\left(\frac{Ea}{R}\right)\left(\frac{1}{T}\right) + In\left(\frac{A_\alpha R}{g_{(\alpha)}E_\alpha}\right)$ $In\left(\frac{\beta}{T^{1.92}}\right) = -1.008\left(\frac{Ea}{R}\right)\left(\frac{1}{T}\right) + In\left(\frac{A_\alpha R}{g_{(\alpha)}E_\alpha}\right)$	[68]
Boswel	$In\left(\frac{\beta}{T_{max}}\right) = -\left(\frac{Ea}{R}\right)\left(\frac{1}{T_{max}}\right) + constant$	[68], [73]
Coats and Redfern	$In\left(\frac{g(\alpha)}{T^2}\right) = -\left(\frac{Ea}{R}\right)\left(\frac{1}{T}\right) + In\left(\frac{AR}{\beta E}\right)$	[74]
ASTM-E698	$In\left[\beta\left(\frac{d\alpha}{dt}\right)\right] = -\left(\frac{E_\alpha}{R}\right)\left(\frac{1}{T}\right) + In[k_o(1-\alpha)]$	[75]
Karaosmanoglu & Cif	$In\left[\frac{-1}{\alpha_o-\alpha_f}\frac{d\alpha}{dt}\right] = In(A) - \frac{E_a}{RT} + n\,In\left(\frac{\alpha-\alpha_f}{\alpha_o-\alpha_f}\right)$	[76]
Isothermal method	$-In(t) = -\left(\frac{Ea}{R}\right)\left(\frac{1}{T}\right) + In\left[\frac{A}{g'(\alpha)}\right]$	[77]
FWO and KAS Iterative methods	$In\left(\frac{\beta}{H_{(x)}}\right) = \left(\frac{0.0048A_\alpha E_\alpha}{g_{(\alpha)}R}\right) - \left(\frac{1.0516E_\alpha}{R}\right)\left(\frac{1}{T}\right)$ $In\left(\frac{\beta}{h_{(x)}T^2}\right) = In\left(\frac{A_\alpha R}{g_{(\alpha)}E_\alpha}\right) - \left(\frac{E_\alpha}{R}\right)\left(\frac{1}{T}\right)$ where $H_{(x)} = \frac{(e^{-x})\,h_{(x)}/x^2}{0.0048\exp(-1.0516x)}$ and $h_{(x)} = \frac{x^4+18x^3+86x^2+96x}{x^4+20x^3+120x^2+240x+120}$ which is the 4th degree Senum and Yang approximation that gives an accuracy better than 10^{-5} % for x = E/RT ≥20.	[65], [78]
Vyazovkin	$\Phi(E_\alpha) = \sum_{i=1}^{n} * \sum_{j\neq 1}^{n} \frac{J[E_\alpha, T_i(t_\alpha)]}{J[E_\alpha, T_j(t_\alpha)]}$ Where the time integral: $J[E_\alpha, T_i(t_\alpha)] = \int_{t_{\alpha-\Delta\alpha}}^{t_\alpha} \exp\left[\frac{-E_\alpha}{RT_i(t)}\right] dt$ where, T(t) is the actual sample temperature, J is the integral with respect to T(t) and $T_i(t)$ is the temperature programs	[79], [55]
Kissinger	$In\left(\frac{\beta}{T_{max}^2}\right) = \left(-\frac{Ea}{R}\right)\left(\frac{1}{T_{max}}\right) + \frac{InAR}{Ea}$	[66], [80]

In the equations (the table above), α - is the fractional conversion, β - is the heating rate, A – is the pre-exponential factor, R – is the universal gas constant, and E_a is the activation energy.

2.3.2 Determination of reaction model

The functions, g(α) – the integral form, and f(α) – the differential form, are used to determine the reaction mechanisms [55], [81] as shown in Table 2-2. Reaction models for degradation of solid fuels can be generally categorized as: acceleratory, deceleratory, and sigmoidal. They all have specific fingerprint curves that describe their reaction path for the dependence of α or dα/dt on t or T. For isothermal data, such reaction path are easy to recognize since k(T) = constant (eqn. 3) making it easy to define the kinetic curves by the reaction models only. For non-isothermal data, both k(T) and f(α) change at the same time producing a sigmoidal type curve for α vs. T. This makes the identification of the reaction model difficult [82]. The isothermal reaction profiles for α vs. t are shown in *Figure 2-9*.

Acceleratory models are for processes with rates of reaction increasing with increase in fractional conversion reaching maximum values at the end of the reaction. Such models follow the Mampel power–law type. Decelaratory models have processes reaching their maximum at the start of the process and decrease with increase in fractional conversion. They are represented by phase boundary reactions and diffusion models. On the other hand, sigmoidal models are for processes whose initial and final stages are accelerating and decelerating so that the maximum rate is attained at some intermediate values of the fractional conversion. They are mostly represented by the Avrami–Erofeev models (Table 2-2).

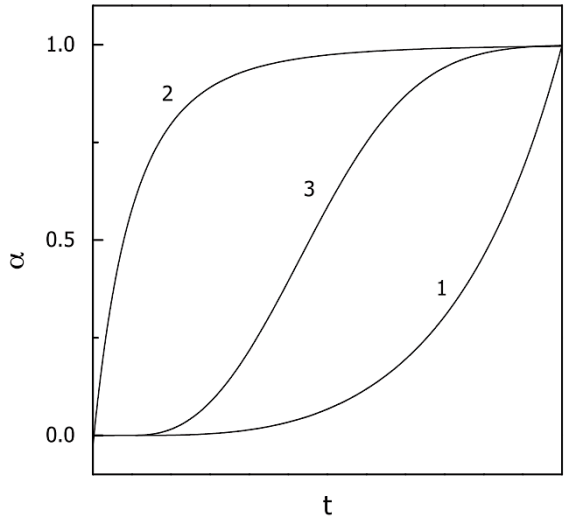

Figure 2-9: The α Vs. t, reaction profiles for (1) acceleratory, (2) deceleratory, and (3) sigmoidal models. Adapted from [82].

Table 2-2: Common mechanisms used during pyrolysis and degradation of solids. Adapted from [82].

No.	Symbol	Name of the Function	$g(\alpha)$	$f(\alpha)$	Rate-determining mechanism
1. Chemical process or mechanism non-invoking equations					
1	F1/3	One-third order	$1-(1-\alpha)^{2/3}$	$(3/2)(1-\alpha)^{1/3}$	Chemical reaction
2	F3/4	Three-quarters order	$1-(1-\alpha)^{1/4}$	$4(1-\alpha)^{3/4}$	Chemical reaction
3	F3/2	one and a half order	$[(1-\alpha)^{-1/2}-1]$	$2(1-\alpha)^{3/2}$	Chemical reaction
4	F2	Second order	$(1-\alpha)^{-1}-1$	$(1-\alpha)^2$	Chemical reaction
5	F3	Third order	$(1-\alpha)^{-2}-1$	$(1/2)(1-\alpha)^3$	Chemical reaction
2. Acceleratory rate equations					
6	P3/2	Mampel power law	$\alpha^{3/2}$	$(2/3)\alpha^{-1/2}$	Nucleation
7	P1/2	Mampel power law	$\alpha^{1/2}$	$2\alpha^{1/2}$	Nucleation
8	P1/3	Mampel power law	$\alpha^{1/3}$	$3\alpha^{2/3}$	Nucleation
9	P1/4	Mampel power law	$\alpha^{1/4}$	$4\alpha^{3/4}$	Nucleation
10	E1	Exponential law	$ln\alpha$	α	Nucleation
3. Sigmoidal rate equations or random nucleation and subsequent growth					
11	A1, F1	Avrami-Erofeev equation	$-\ln(1-\alpha)$	$(1-\alpha)$	Assumed random nucleation and its subsequent growth, n=1
12	A3/2	Avrami-Erofeev equation	$[-\ln(1-\alpha)]^{2/3}$	$(3/2)(1-\alpha)[-\ln(1-\alpha)]^{1/3}$	Assumed random nucleation and its subsequent growth, n=1.5
13	A2	Avrami-Erofeev equation	$[-\ln(1-\alpha)]^{1/2}$	$2(1-\alpha)[-\ln(1-\alpha)]^{1/2}$	Assumed random nucleation and its subsequent growth, n=2
14	A3	Avrami-Erofeev equation	$[-\ln(1-\alpha)]^{1/3}$	$3(1-\alpha)[-\ln(1-\alpha)]^{2/3}$	Assumed random nucleation and its subsequent growth, n=3
15	A4	Avrami-Erofeev equation	$[-\ln(1-\alpha)]^{1/4}$	$4(1-\alpha)[-\ln(1-\alpha)]^{3/4}$	Assumed random nucleation and its subsequent growth, n=4
16	Au	Prout-Tomkins equation	$Ln[\alpha/(1-\alpha)]$	$\alpha\ (1-\alpha)$	Branching nuclei
4. Deceleratory rate equations					
4.1 Phase boundary reactions					
17	R1, F0, P1	Power law	α	$(1-\alpha)^0$	Contracting disk
18	R2, F1/2	Power law	$1-(1-\alpha)^{1/2}$	$2(1-\alpha)^{1/2}$	Contracting cylinder (Cylindrical symmetry)
19	R3, F2/3	Power law	$1-(1-\alpha)^{1/3}$	$3(1-\alpha)^{2/3}$	Contracting sphere (spherical symmetry)
4.2 Based on the diffusion mechanism					
20	D1	Parabola low	α^2	$1/2\alpha$	One-dimensional diffusion

21	D2	Valensi equation	$\alpha+(1-\alpha)\ln(1-\alpha)$	$[-\ln(1-\alpha)]^{-1}$	Two-dimension diffusion
22	D3	Jander equation	$[1-(1-\alpha)^{1/3}]^2$	$(3/2)(1-\alpha)^{2/3}[1-(1-\alpha)^{1/3}]^{-1}$	Three-dimensional diffusion, Spherical symmetry
23	D4	Ginstling-Brounstein equation	$[1-2\alpha/3-(1-\alpha)^{2/3}$	$(3/2)[(1-\alpha)^{-1/3}-1]^{-1}$	Three-dimensional diffusion, Cylindrical symmetry
24	D5	Zhuravlev, Lesokin, Tempelman equation	$[(1-\alpha)^{-1/3}-1]^2$	$(3/2)(1-\alpha)^{4/3}[(1-\alpha)^{-1/3}-1]^{-1}$	Three-dimensional diffusion
25	D6	Anti-Jander equation	$[(1+\alpha)^{1/3}-1]^2$	$(3/2)(1+\alpha)^{2/3}[(1+\alpha)^{1/3}-1]^{-1}$	Three-dimensional diffusion
26	D7	Anti-Ginstling-Brounstein equation	$1+2a/3-(1+a)^{2/3}$	$(3/2)[(1+\alpha)^{-1/3}-1]^{-1}$	Three-dimensional diffusion
27	D8	Anti-Zhuravlev, Lesokin, Tempelman equation	$[(1+\alpha)^{-1/3}-1]^2$	$(3/2)(1+\alpha^{4/3}[(1+\alpha)^{-1/3}-1]^{-1}$	Three-dimensional diffusion
5. Another Kinetic equation with unjustified mechanism					
28	G1		$1-(1-\alpha)^2$	$½(1-\alpha)$	
29	G2		$1-(1-\alpha)^3$	$1/3(1-\alpha)^2$	
30	G3		$1-(1-\alpha)^4$	$1/4(1-\alpha)^3$	
31	G4		$[-\ln(1-\alpha)^2$	$(1/2)(1-\alpha)[1\ln(1-\alpha)]^{-1}$	
32	G5		$[-\ln(1-\alpha)^3$	$(1/3)(1-\alpha)[1\ln(1-\alpha)]^{-2}$	
33	G6		$[-\ln(1-\alpha)^4$	$(1/4)(1-\alpha)[1\ln(1-\alpha)]^{-3}$	
34	G7		$[1-(1-\alpha)^{1/2}]^{1/2}$	$4\{(1-\alpha)[1-(1-\alpha)^{1/2}\}^{1/2}$	
35	G8		$[1-(1-\alpha)^{1/3}]^{1/2}$	$6\{(1-\alpha)^{2/3}[1-(1-\alpha)^{1/3}\}^{1/2}$	

2.4 The formation and release of CO from solid fuels

The structures of functional groups that are present on the char or found on partially oxidized char surfaces are presented in Figure 2-10. These structures are responsible for the formation of CO in addition to the free-edge site reactions.

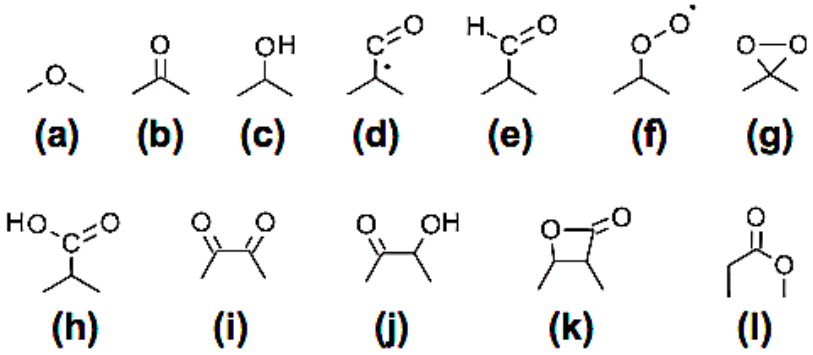

Figure 2-10: Several oxygenated functional groups present on partially oxidized PAHs or soot. (a) Pyrone (ether). (b) Ketone. (c) Hydroxyl. (d) Dangling CO (carbonyl). (e) Dangling HCO. (f) Peroxide. (g) Dioxyranyl. (h) Carboxylic. (i) Quinone. (j) Phenolic. (k) Lactone. (l) Oxypinyloxy. Adapted from [83], [26].

After the surface oxygenated functional groups are all oxidized, further reactions follow the "free edge site" reactions leading to formation of CO, a reaction similar to the breakdown of soot reported in the literature [84]. This follows a simplified mechanism, though numerous reactive sites can be present. As seen in Figure 2-11, free-edge sites and zig-zag sites on a polycyclic aromatic hydrocarbon (PAH) molecule react with oxygen to release CO and the formation of new edge-sites. This process is repeated until all the edge-sites are completed, after which, complete oxidation of the six-membered rings takes place until the entire structure is oxidised [84].

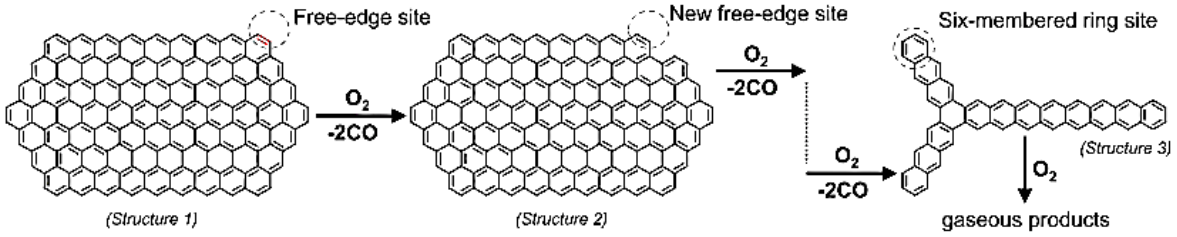

Figure 2-11: Free-edge oxidation of an example polycyclic aromatic hydrocarbon molecule comprising a soot particle. The oxidation of a free-edge on structure 1 leads to the generation of a new free-edge in this example on structure 2, thus causing chain oxidation through the reaction. Adapted from [84].

Further detailed complex reactions involve the breakdown of planar and curved PAHs which involves the formation of oxygenated free radicals that later desorb as CO or CO_2. Other carbon-centered free radicals react with oxygen forming CO as the main product [85], [86].

2.5 Methods for minimising human exposure to CO

There are various approaches used to minimize the CO emissions from solid fuel combustion, each of which is designed depending on the specific application. The main approaches include cooking systems, heating systems, catalytic

systems, and sensors/detectors. Some applications employ a combination of two or more depending on the complexity and desired outcomes. This work is particularly focusing on catalytic systems Figure 2-12.

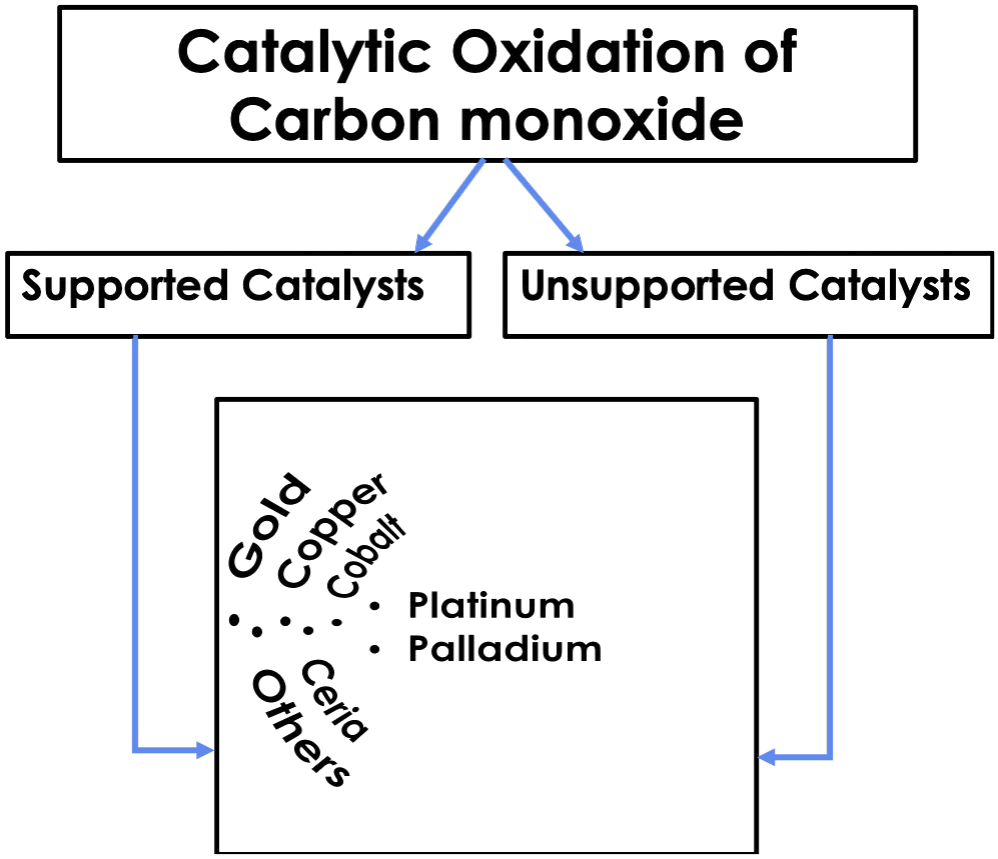

Figure 2-12: Catalytic systems for minimising CO

2.5.1 Catalytic oxidation of CO

2.5.1.1 Carbon monoxide and oxygen chemisorption on metals

Carbon monoxide

The adsorption and reactivity of carbon monoxide on oxides and metals is a result of CO having three resonance structures. By donating electrons through

the 5s orbital and accepting electrons through the antibonding 2p* orbital makes it possible for carbon monoxide to be coordinated to one or numerous species. Five spectral ranges of CO adsorption bands can be detected depending on the number species it is bonded to: 1700 – 1800, 1800 – 1920, 1860 – 2000, 2000 – 2130, and 2130 – 2200 cm^{-1}. The particle size and the nature of the metal site will determine the infrared band position. Platinum, rhodium, and palladium have been used to oxidise CO and have given infrared vibration bands at different positions depending on the orientations (mirror indices) of these metals. Chemisorption behavior of carbon monoxide on metals also varies considerably: for Pt, Rh, and Ru, the heat of chemisorption is directly proportional to the metal surface density. Also, the heats of chemisorption are inversely proportional to CO coverage (*q*CO) with platinum having the highest sensitivity [24].

Oxygen

For CO oxidation to be fully understood, the chemisorption of oxygen on catalyst surfaces must be understood as well. Unlike CO, adsorption of oxygen is dissociative. The heat of adsorption on most non-noble transition metals is mostly not affected by oxygen coverages. However, noble metals (Rh, Pd, and Pt) have inverse relations of the heat of chemisorption with oxygen coverage. This is due to differences in the metallic radius of the metals Figure 2-13.

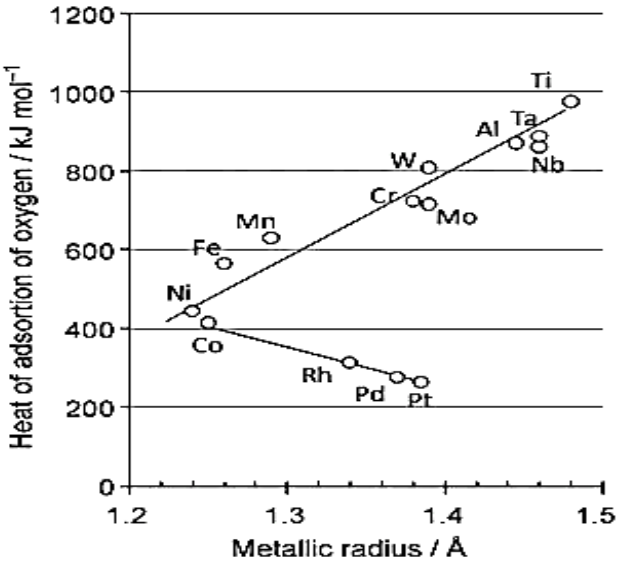

Figure 2-13: Heat of adsorption values of metals, as a function of their metallic radius. Adapted from [24].

2.5.1.2 Laboratory oxidation of CO over metals

Supported metal catalysts

The presence of catalyst support may have a significant effect on the catalyst activity and the overall reaction. The final reaction usually occurs on the catalyst or at the catalyst/support interface. Secondly, the oxidation/reduction state of the metal catalyst has a major implication on CO oxidation [24].

CO oxidation over simple oxide catalysts

Much as noble metals are very active for oxidation of CO, some oxides especially Cu and Co have shown remarkable activity as well for CO oxidation. The reactivity of noble metals and base metal oxides for oxidation of 1 % CO in excess oxygen and 300 °C follows the order; Pd > Pt > Co_2O_3 > CuO > CuO/Cr_2O_3 > $LaCoO_3$ > Au > MnO_2 > Fe_2O_3 > Cr_2O_3 > NiO [24].

Gold-based catalysts

The ability to change oxidation states by gold and ceria has played a great role during the catalytic oxidation of carbon monoxide [87]. This is also due to their oxygen vacancies, and high oxygen storage capacity of this catalyst system. However, the Au nanoparticles would agglomerate into sizable particles on ceria and this led to the decrease in activity of the catalyst. The shape of ceria as support also influences the catalytic activity of gold for CO oxidation. Carltonbird *et al*. [50], observed that the order of reactivity of gold catalyst in relation to the shape of ceria support was; rod-shaped > polyhedral > cube > octahedral shaped CeO_2. However, the addition of iron to the Au/CeO_2 system improved the catalytic activity for oxidation of CO and benzylamine compared to Au/CeO_2 alone [88].

A gold/titania-based catalyst is a unique combination in that on top of achieving 100 % conversion of CO at room temperature, it displayed remarkable CO oxidation at 120 K [89]. However, the titanate sites used must be amorphous for the cryogenic catalysis to happen. More so, the researchers were not able to establish the exact nature of the amorphous sites on the titanate based support. Other researchers have reported a gold catalyst supported on other supports for the oxidation of CO. Such systems included Au/activated carbon, Au/boron nitride, Au/titanium dioxide, and Au/mesoporous silicate-based (SBA-15) [90] in a fixed bed reactor at 120 ^{o}C. However, very low CO conversion (< 5 %) was achieved at this temperature. This was attributed to the inert silica support that had limited active sited for adsorption of CO and oxygen. Even after treatment of the catalyst with polyvinylpyrrolidone (PVP), only 12.8 % CO conversion was attained at 150 ^{o}C.

In other studies, perovskites ($LaMnO_3$, $LaFeO_3$, $LaCoO_3$, and $LaCuO_3$) have also worked excellently as supports for gold for oxidation of CO. With only 1 wt% of gold, superior activity was registered for CO oxidation [91] in a fixed bed flow

reactor. However, catalysts calcined at ≥ 800 °C showed no activity. Secondly, catalysts calcined at temperatures < 800 °C declined in activity for CO oxidation gradually. Gold supported on three dimensional Mn_2O_3 was used for CO, and toluene oxidation [92]. At only 15 °C, the researchers achieved up to 90 % conversion. This was attributed to its low-temperature reducibility, high oxygen adsorption capability, high porosity and the strong interaction between gold nanoparticles and the three-dimensional Mn_2O_3. The catalytic activity, however, declined slightly when the space velocity was increased, as well as introduction of water vapour, SO_2 and CO_2 into the system. In other studies, a gold-copper alloy supported on MgO or graphene [93] has been used for efficient oxidation of CO. This combination was preferred for its effectiveness and commercial affordability compared to other gold-based catalysts.

Copper-based catalysts

Water-resistant SnCu30 (30 wt% Cu) catalysts have been prepared and used for oxidation of CO [94]. The high activity was attributed to the lattice surface oxygen and the highly dispersed Cu^+ species within the Cu-SnO_2 catalyst matrix which provided active sites for adsorption of CO. Treatment with HNO_3 reduced the activity of the catalyst due to removal of active sites from the catalyst surfaces. Un-supported CuO uses the surface area advantage for oxidation of CO. A decrease in specific surface area of CuO from 90 to 8 m^2/g resulted in a four-fold increase in the specific catalytic rate [95]. However, a 20-fold decrease in the specific catalytic rate was observed when the catalyst specific surfaces area was reduced to 1 m^2/g. Activated-red-mud as support on CuO produces a well-structured porous and high surface area catalyst [96] for CO oxidation. However, the CO oxidation was dependent on CuO loading and the catalyst calcination temperature.

Copper-Manganese (commercially known as hopcalite) prepared by flame spray pyrolysis produced a superior hydrophobic catalyst that was resistant to humidity levels as high as 75 % [97]. This was achieved by applying 2-ethylhexanoate as precursors achieving a high specific surface area catalyst (180 m^2/g) composed of $Cu_{1.5}Mn_{1.5}O_4$ as the main phase. The most active catalyst was composed of Cu:Mn of 2 mol/mol achieving an 80 % CO conversion at room temperature. A more sophisticated Cu-based catalyst composed of Cu-Pd/CeO_2 [98] achieved excellent activity for CO oxidation. This was attributed to full oxidation of the Cu and Pd by the ceria support which dominated the catalyst system providing an excellent metal/support interaction. However, unlike the Cu–O_x–Ce and Pd–O_x–Ce, which interacted with the ceria support to produce excellent CO oxidation activity, there was no bond formation detected between the Cu–O_x–Pd. This was further verified by the lack of sufficient CO oxidation activity of the Cu-Pd oxide cluster.

Cobalt catalysts

The catalyst preparation method greatly impacts its performance. Dispersion–precipitation synthesis of Co_3O_4 produced a better catalyst for oxidation of carbon monoxide and propane than alkali-induced precipitation [99]. Dispersion–precipitation produced a more reducible Co_3O_4 catalyst with high numbers of active surface oxygen species. The activation energy for CO and C_3H_8 oxidation were reduced by 38 % and 31 % respectively with the dispersion–precipitation synthesised Co_3O_4 compared to alkali-induced precipitation synthesised Co_3O_4. Titania supported Co_3O_4 catalyst prepared by incipient wetness impregnation had a superior activity for CO and hydrocarbon oxidation in vehicle exhaust emissions compared to Co_3O_4/TiO_2 catalyst prepared by wet impregnation method [100]. Similarly, the activity of hollow type Co_3O_4 spheres prepared using silica templates for CO oxidation was dependent on calcination temperature with 623 K producing the best

activity [101]. These hollow sphere Co_3O_4 catalyst also showed superior activity compared to supported Co_3O_4 as well as Co_3O_4 nanoparticles. In a similar situation, Cao *et al.* [102] observed that the wormhole-like-mesoporous Co-Fe-O catalyst activity for CO oxidation was dependent on Co loading, the surface area, the pre-calcination temperature, and the particle size.

Platinum and Palladium catalysts

Being noble metals, a small concentration is needed in addition to a support for efficient CO catalytic activity. With only 0.5 wt% Pd/manganese oxide catalyst, maximum CO, toluene, and ethyl acetate oxidation were achieved at 55 °C compared to un-supported Pd catalyst. This excellent activity was attributed to high oxygen adsorption and low-temperature reducibility of the 0.5 wt% Pd/manganese oxide catalyst. With $LaMnO_3$ Perovskites, palladium loading was directly proportional to CO catalytic activity [103]. The activity was seen to increase with the temperature especially in the range 650 to 800 ^oC.

Pt/CeO_2 catalysts prepared by impregnation-reduction [51] had the best activity for complete oxidation of CO at room temperature compared to the same catalyst prepared by impregnation, and deposition-precipitation methods. The activity of the impregnation-reduction prepared Pt/CeO_2 catalyst was attributed to possessing highly numbers of negative Pt species for efficient adsorption of oxygen for CO oxidation. Similarly, acid treatment followed by thermal activation of palladium–copper complexes affected the catalyst's activity for CO oxidation [104]. The best results were obtained when the bimetallic Pd(II)–Cu(II) complexes were treated with 3M HNO_3 for 0.5 and heat-treated for 60 minutes.

Ceria based catalysts

Ceria being a base metal oxide works better with a support and at intermediate temperatures. It was reported that ceria/alumina could achieve complete oxidation of 7739 ppm of CO at 400 ^{o}C in excess oxygen compared to un-supported ceria [105]. The authors also observed a catalyst deactivation upon application of 3 % moisture. Additionally, thermal deactivation of the catalysts was another challenge encountered. Similarly, a ceria-zirconium catalyst system doped with low amounts of Nd (< 0.1 wt%) was reported to enhance the surface area of the catalyst thereby improving the catalytic activity for oxidation of CO [106]. However, high Nd content (0.2 – 0.3) promoted sintering and retarded the catalytic activity of Ce-Zr-Nd catalyst for CO oxidation.

Other catalysts

Aromatic organic chemical tetrapyrrole (commonly known as corrole) combined with transition metals (corX; X standing for the transition metal) have also been used for catalytic oxidation of CO. In one study, the metals Al, Ga, Si, Ge and As were tested [107]. The best results were obtained from the CorAl and CorGa while CorSi and CorGe formed very stable carbon-like intermediates that hindered CO oxidation. Other researchers have used Li_5FeO_4 and $LiFeO_2$ [108], V/graphene [109], Cr/graphene [110], and ZrO_2/MgO for oxidation of CO.

The ideal catalyst for CO oxidation should have high selectivity, high activity, thermally stable and long life, all of which come at a high cost. Noble metals are the best choice, but they are very expensive. Research into new materials such as Mn, Fe, Co, Ni, Cu or their combinations has been extensive [111], however, improving their stability is still a challenge. Even the reaction itself

between CO and O_2 on catalyst surfaces has had over 20 different proposed mechanisms with the Langumir–Hinshelwood (LH) being the best. Understanding the dynamic reactions at microscopic level on surface and the bulk of the catalyst under heating and cooling is the task at hand for researchers.

2.6 Catalyst impregnation on to solid fuels

2.6.1 Enhancing pyrolysis and char gasification

When secondary reactions are triggered during biomass pyrolysis by either alkali or alkali earth metals [112], the resulting char has varying reactivity. This could be due to blocking or deactivation of active sites for oxygen attack. Kirtania *et al.*, [113] observed that impregnation of sawdust with K_2CO_3, Na_2CO_3, NaOH and NaCl, followed by devolatilising, and pyrolysing the resulting char at different temperatures (750 – 900 °C) under CO_2, three classes of chars were produced. Those chars that were highly influenced by catalysts were swollen and had molten surfaces. The moderately influenced chars were wood-like while the least affected had salt deposits. Potassium carbonate (K_2CO_3) gave the best catalytic activity for gasification.

Leaching of biomass with water and HCl lead to a decrease in H_2 and CO_2 yields while the production of CO, CH_4, C_2H_4 and C_2H_6 increased [114]. This was attributed to the removal of alkaline and alkaline earth metals whose presence could enhance the homogeneous steam-tar reforming, hydrocarbon reforming, and water-gas shift reactions as well as the heterogeneous char gasification reactions. In a similar study, potassium impregnated biomass samples had high yields of CO_2 and H_2 while the release of CO and CH_4 declined [115]. This was due to the promotion of the cleavage of hydrogen

bonds, C-C, and C-H bonds and the promotion of the decomposition of the cellulose glucosidic bonds by the heterolytic mechanism. When iron or nickel were impregnated on cellulose, the yield and composition of fast pyrolysis products were different compared to un-catalysed cellulose [116]. With only1.5 wt% Fe or 1.7 wt% Ni catalyst loading, cellulose depolymerization was inhibited; char, moisture, and CO_2 yields were increased while tar and CO yields were reduced.

Yu *et al.,* [117], observed that bread waste could be turned into hydroxymethylfurfural (HMF) by impregnation of $SnCl_4$, $AlCl_3$, and $FeCl_3$ followed by pyrolysis. The highest HMF yield (30 mol%) was achieved using $SnCl_4$ as the catalyst. The polymerization-induced metal-impregnated high-porosity carbon was a possible precursor of the biochar-based catalyst.

Copper and lead impregnated on biomass had little effect on kinetic parameters that describe the pyrolysis process [118], [119]. However, silicon compounds resulted in glassy shelled char [120] when impregnated on rice husk biomass. The particle size and shape of the resulting chars were preserved. However, the reactivity of the char is more influenced by alkali content than the silicon oxides. The presence of K, in the raw biomass increases the reactivity and favoured the heat produced during low-temperature oxidation of the chars. This implies that the self-heating tendency of the char could be reduced by removal of inorganic matter through leaching of the biomass [121].

2.6.2 Improving char properties and removal of pollutants

Charcoal has been used as a support in several studies and has worked excellently. The addition of Co, Ni, and Fe to charcoal followed pyrolysis under helium enhanced the thermal stability of charcoal for catalytic combustion of

volatile organic compounds [122]. Cobalt gave the best results transforming the amorphous carbon into a graphite-like structure and also served as an active phase in the toluene and ethyl acetate oxidation reaction. Copper impregnated on activated carbon produced from oxytetracycline bacterial residue [123] gave excellent activity for adsorption and oxidation of sulphur dioxide than the activated carbon alone. Similarly, hydrated manganese oxide supported by biochar effectively sequestrate Pb(II) and Cd(II) than biochar alone [124]. The catalyst system could be regenerated and re-used several times. The catalyst activity was attributed to specific inner-sphere complexation of the manganese oxide and pre-enrichment and permeation of Pb(II) and Cd(II) cations into the pore channels of biochar enhanced by the oxygen-containing groups.

Coloured pigments are easily removed when char is impregnated with some metal catalysts. Park *et al.,* [125] observed that Fe-impregnated sugarcane biochar could achieve a 99.7 % azo dye Orange G (OG) removal efficiency from solution within 2 hours. The Fe- sugarcane-biochar is more economical, efficient, and recyclable. In similar studies, 96 % MB dye removal efficiency was achieved using Ni-impregnated powder activated carbon [126] while RB5 azo dye was completely degraded using grape marc activated carbon/TiO_2 hybrid [127] catalyst. The degradation species including carboxylic and sulfate groups were observed on the surfaces of the hybrid catalyst using FT-IR and UV-visible analysis.

Poggi and Singh [128] observed that impregnation of Fluid Cracking Catalyst (FCC) on modified biochar achieved a higher thermal degradation capability of acetic acid than FCC alone. With no catalyst, only 5.55 % conversion was achieved. With biochar-Ni, a 15.21 % conversion was achieved while FCC achieved a 12.41 % conversion. The modified bio-char (Biochar-Fe) showed the highest conversion of 40.66 %.

Summary of chapter 2

This work has reviewed solid fuel combustion kinetics, formation and release of CO, and the catalytic systems for minimizing human to exposure to CO. In summary;

- The main methods used to determine kinetic parameters for degradation of solid fuels include differential iso-conversional, and integral iso-conversional. The choice will depend on whether the investigations involve isothermal or non-isothermal analysis. It will also depend on whether the mechanism of decomposition has any particular relevance to the study or not.

- Carbon monoxide is released from oxygenated surface functional groups followed by free edge and zig-zag site reactions on PAHs molecules reacting with oxygen until the entire structure is oxidized.

- Carbon monoxide has been a silent killer since the paleolithic era and has continued to threaten human lives until today.

- Direct catalytic oxidations of post-combustion pollutants are highly efficient and can achieve 100 % CO conversion at ambient temperatures. They can be used in conjunction with other systems like cooking and heating. There are various combinations of catalysts available commercially and many more to be designed in the future. Their success is attributed to their high affinity for oxygen and toxic pollutants onto their surfaces. However, they are usually poisoned by moisture, SO_2, CO_2 and thermal deactivation. They are also affected by PH: low values reduce their active sites leading to reduced adsorption capabilities for CO and O_2. Effective systems also require high catalyst loading, specific preparation

methods, and material properties. Failure to achieve the stringent requirements means that the prepared system will not perform as required.

Although substantial safety from CO has been provided by the systems described above, there are still several CO related deaths recorded worldwide. All the systems used to minimize CO exposure are applied when the solid fuels are in their original form and during combustion; such solid fuels continue to release CO depending on the prevailing conditions. Should there be any malfunction, leakage or pathway for CO, such systems would still expose the user to toxic amounts that may be lethal or cause lifelong injuries.

Altering the composition of the solid fuels by impregnation of chemical catalysts has been used to trigger desired reactions and achieve target products (discussed in section 2-6). Using such an approach (while applying better chemical catalysts) on solid fuels used for cooking and heating systems would mean that the solid fuel would release minimal amounts of CO. Hence, the amounts of CO released would be rendered none lethal acutely.

The next five chapters (3 – 7) include the main details from the experimental work done during the PhD period. They are obtained from the journal published articles done during the period of the PhD whose content has been re-written to suit the Thesis format with minor changes to make a smooth flow of the entire story.

Chapter 3: DETERMINATION OF THE KINETIC AND THERMODYNAMIC BEHAVIOUR OF ASH (*FRAXINUS EXCELSIOR*) WOOD SAWDUST DURING SLOW PYROLYSIS BY THERMOGRAVIMETRIC ANALYSIS

The work contained in this chapter has been published in the journal *Energy Sources, Part A: Recovery, Utilization, and Environmental Effects*.

Citation: *Antony Nyombi, Mike Williams & Roland Wessling (2018) Determination of kinetic parameters and thermodynamic properties for ash (Fraxinus) wood sawdust slow pyrolysis by thermogravimetric analysis, Energy Sources, Part A: Recovery, Utilization, and Environmental Effects, 40:22, 2660-2670. DOI: https://doi.org/10.1080/15567036.2018.1502846*

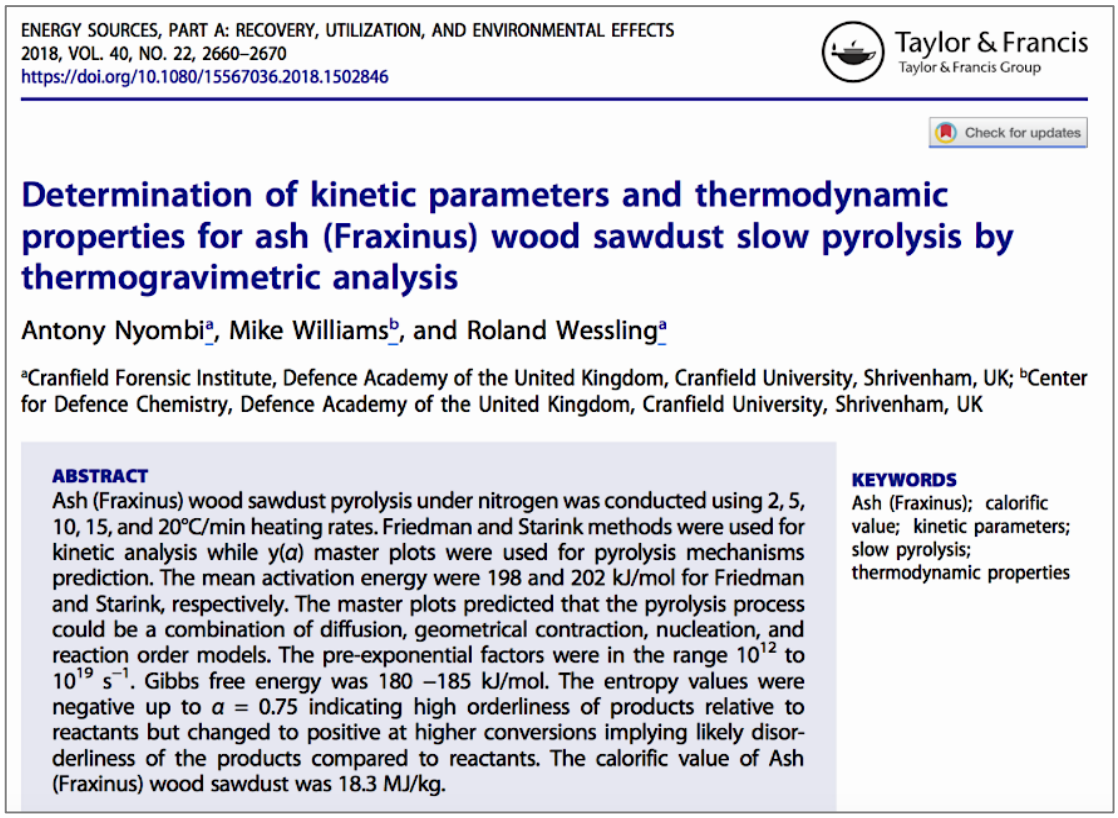

ENERGY SOURCES, PART A: RECOVERY, UTILIZATION, AND ENVIRONMENTAL EFFECTS
2018, VOL. 40, NO. 22, 2660–2670
https://doi.org/10.1080/15567036.2018.1502846

Taylor & Francis
Taylor & Francis Group

Check for updates

Determination of kinetic parameters and thermodynamic properties for ash (Fraxinus) wood sawdust slow pyrolysis by thermogravimetric analysis

Antony Nyombi[a], Mike Williams[b], and Roland Wessling[a]

[a]Cranfield Forensic Institute, Defence Academy of the United Kingdom, Cranfield University, Shrivenham, UK; [b]Center for Defence Chemistry, Defence Academy of the United Kingdom, Cranfield University, Shrivenham, UK

ABSTRACT

Ash (Fraxinus) wood sawdust pyrolysis under nitrogen was conducted using 2, 5, 10, 15, and 20°C/min heating rates. Friedman and Starink methods were used for kinetic analysis while y(α) master plots were used for pyrolysis mechanisms prediction. The mean activation energy were 198 and 202 kJ/mol for Friedman and Starink, respectively. The master plots predicted that the pyrolysis process could be a combination of diffusion, geometrical contraction, nucleation, and reaction order models. The pre-exponential factors were in the range 10^{12} to 10^{19} s^{-1}. Gibbs free energy was 180 –185 kJ/mol. The entropy values were negative up to $\alpha = 0.75$ indicating high orderliness of products relative to reactants but changed to positive at higher conversions implying likely disorderliness of the products compared to reactants. The calorific value of Ash (Fraxinus) wood sawdust was 18.3 MJ/kg.

KEYWORDS

Ash (Fraxinus); calorific value; kinetic parameters; slow pyrolysis; thermodynamic properties

Determination of kinetic parameters and thermodynamic properties for ash (Fraxinus) wood sawdust slow pyrolysis by thermogravimetric analysis

Highlights

- The slow pyrolysis of ash (*Fraxinus excelsior*) was investigated by kinetic and thermodynamic analysis
- Thermogravimetric/differential thermogravimetric analysis was used to determine the kinetic parameters of ash, and the results agreed with published biomass data
- The mechanisms of ash pyrolysis were determined using master plots
- Ash pyrolysis involved a combination of diffusion, geometrical contraction, nucleation, and reaction order models.

Abstract

Ash (*Fraxinus excelsior*) wood sawdust was pyrolysed under nitrogen at heating rates of 2, 5, 10, 15 and 20 °C/min. Friedman and Starink methods were used for kinetic analysis and y(α) master plots were used to predict the pyrolysis mechanisms. The mean activation energies were 198 and 202 kJ/mol for the Friedman and Starink methods, respectively. The master plots predicted that ash pyrolysis involves a combination of diffusion, geometrical contraction, nucleation, and reaction-order models. The pre-exponential factors fell within the range 10^{12} – 10^{19} s^{-1}. The Gibbs free energy was in the range 180 – 185 kJ/mol. The entropy values were negative up to α = 0.75 indicating the high

orderliness of products relative to reactants but changed to positive values at higher conversion rates implying disorderliness of the products compared to the reactants. The calorific value of ash wood sawdust was 18.3 MJ/kg.

3.1 Introduction

Energy sources have shifted from biomass to fossil fuels and back to biomass in less than 300 years due to economic and technological developments. The need for renewable resources is rising due to their environmental friendliness and sustainability. Globally, 19 % of the current energy needs are met by renewables, with 9 % contributed by biomass, but this is predicted to increase at a rate of 2.5 % per year [1]. However, the properties of such materials must be understood before they can be used to make biochar and other energy-rich products. Several biomass resources have been characterised in terms of their energy potential, including beech wood [2], pine wood [3], and bamboo [4]. Due to the abundant nature of biomass, many materials have not yet been investigated in detail, but they offer enormous potential for the production of bio-oil, biochar and other useful products.

Pyrolysis and torrefaction [5] are key methods used to process biomass materials for energy production. Thermogravimetric analysis (TGA) is widely used to study pyrolysis because it provides a controllable atmosphere and heating rate, with negligible thermal gradients and mass transport [2]. TGA can be used alone or combined with other techniques such as spectrometry to study biomass materials [6]. TGA can be used to determine chemical kinetic parameters, such as the activation energy, by employing differential and integral methods [7]. However, identifying the appropriate pyrolysis mechanism for processes with changing activation energies across a range of conversion rates requires the careful application of model-free and model-

fitting methods [8]. Master plots have been used extensively to determine the mechanisms of biomass pyrolysis [9].

In this study, we investigated the properties of sawdust from the perennial common ash tree (*Fraxinus excelsior*). Ash trees grow to 40 – 80 feet in height, are heavily branched, and are resistant to severe environmental conditions. We studied the physiochemical, kinetic and thermodynamic basis of pyrolysis using ash tree sawdust as the starting material. We highlight the benefits and potential applications of this plant material for energy generation, and our results add to the body of knowledge available for other biomass materials whose properties are already known.

3.2 Materials and methods

3.2.1 Sample preparation and characterisation

Sawdust samples from ash trees were ground to a fine powder using an Essa LM2 pulverising mill and were sieved to a particle size of < 200 µm before drying in an oven at 105 °C. Elemental analysis for carbon, hydrogen and nitrogen was carried out by the Cranfield University School of Water, Energy and Environment, following British standard BS EN 13654 – 2:2001 and BS7755, using a Vario EL elemental analyser. Oxygen levels were determined by difference analysis.

An automated thermogravimetric analyser (TGA/DSC3+ STAR system; Mettler Toledo, EAG.EID 304 model) was used to measure the moisture content, volatiles, fixed carbon and residual ash content as per the D7582-15 standard method (with slight modifications). Aliquots of dry sawdust (~ 8 mg) were pulverised to < 200 µm particle size in 70-mL alumina crucibles, loaded into the TGA instrument and heated in N_2 and air environments at 50 mL/min and at

heating rates of 25 °C/min. For moisture determination, the sample was heated from 303 to 383 K and held at that temperature for 10 min in N_2. For volatiles, the sample used for moisture analysis was heated further to 1073 K and held at that temperature for 10 min in N_2. For residual ash, the sample used for volatiles was heated at 1073 K for a further 40 min in air. Fixed carbon was determined by difference. This procedure was carried out in triplicate.

The TGA device used for proximate analysis was also used for pyrolysis (mass loss determination as a function of temperature and time). Approximately 5 mg of sawdust (< 200 µm particle size) was loaded into 70-mL alumina crucibles and heated at five different rates: 2, 5, 10, 15 and 20 °C/min. Samples were heated from 303 to 1073 K in a N_2 environment at 50 mL/min. Mass loss as a function of temperature and time was recorded automatically. This procedure was carried out in triplicate.

The calorific values were determined at Cranfield University, Bedfordshire Campus, using the 6400 Automatic Isoperibol Calorimeter. The calorimeter has a precision of 0.1 %, a temperature resolution of 273.1501 K, a calorie sample range of 5000 – 8000, and linearity across the operating range of 0.05 %. This procedure was carried out in triplicate.

3.2.2 Kinetic properties

The kinetic parameters were determined by considering the degradation mechanisms in ash tree sawdust. The reaction rate is related to the degree of conversion (α) according to eqn. 3-1:

$$\alpha = \frac{M_o - M_i}{M_o - M_\infty} \qquad (3\text{-}1)$$

where M_o, M_I and $M\infty$ are the initial mass, instantaneous mass and the final mass. The degradation kinetics [10] can be represented using the expression shown in eqn. 3-2:

$$\frac{d\alpha}{dt} = k(T)f(\alpha) \qquad (3\text{-}2)$$

The temperature dependence of the degradation rate is related to the Arrhenius equation (eqn. 3-3):

$$k = A\,exp\left(\frac{-E_a}{RT}\right) \qquad (3\text{-}3)$$

where A, E_a, R and T are the pre-exponential factor, activation energy, universal gas constant and absolute temperature, respectively. Substituting eqn. 3-3 into eqn. 3-2 gives eqn. 3-4:

$$\frac{d\alpha}{dt} = A\exp\left(\frac{-E_a}{RT}\right)f(\alpha) \qquad (3\text{-}4)$$

The isoconversional differential method of Friedman and the integral method of Starink were used to determine activation energy because both are considered more accurate than other available methods [11]. The Friedman and Starink methods take the forms shown in eqn. 3-5 and eqn. 3-6, respectively.

$$In\left[\beta_k\left(\frac{d\alpha}{dt}\right)_{\alpha,k}\right] = InA_\alpha f(\alpha) - \left(\frac{E_a}{R}\right)\left(\frac{1}{T_{\alpha,k}}\right) \qquad (3\text{-}5)$$

$$In\left(\frac{\beta_k}{T_{\alpha,k}^{1.92}}\right) = In\left(\frac{A_\alpha R}{g_{(\alpha)}E_a}\right) - 1.0008\left(\frac{E_a}{R}\right)\left(\frac{1}{T_{\alpha,k}}\right) \qquad (3\text{-}6)$$

where β_k is the kth heating rate, $T_{\alpha,k}$ is the temperature for a given α of kth heating rate, E_a is the apparent activation energy, and A_α is the pre-exponential factor of a given conversion.

A plot of $In\left[\beta_k\left(\frac{d\alpha}{dt}\right)_{\alpha,k}\right]$ or $In\left(\frac{\beta_k}{T_{\alpha,k}^{1.92}}\right)$ vs $\left(\frac{1}{T_{\alpha,k}}\right)$ can be used to estimate E_a from the slopes.

3.2.3 Master plots

The E_a values obtained by the Friedman method were used to determine experimental values for master plots. The approximate constant value of E_a was replaced by the average value $E_{a(o)}$ that was inserted into the $y(\alpha)$ function as shown in eqn. 3-7:

$$y(\alpha) = \left(\frac{d\alpha}{dt}\right)_{\alpha,k} \exp\left(\frac{E_{a(o)}}{RT_{\alpha,k}}\right) = \beta_k\left(\frac{d\alpha}{dT}\right)_{\alpha,k} \exp\left(\frac{E_o}{RT_{\alpha,k}}\right) = Af(\alpha) \qquad (3\text{-}7)$$

where $d\alpha/dT_{(\alpha,k)}$ is the differential conversion to temperature (T) at given α and a specified heating rate β, and $E_{a(o)}$ is the mean E_a. The experimental $y(\alpha)$ can be obtained by substituting the $E_{a(o)}$, β_k, R, $d\alpha/dT$ and T_α values into eqn. 3-7. The theoretical $y(\alpha)$ is obtained by substituting the given α into different $f(\alpha)$ functions as described elsewhere [12]. Because the pre-exponential factor (A) in eqn. 3-7 is still unknown, the experimental and theoretical $y(\alpha)$ values must be normalised [8] using eqn. 3-8.

$$y(\alpha)_{norm} = \frac{y(\alpha)}{y(0.5)} \qquad (3\text{-}8)$$

3.2.4 Thermodynamic parameters

The thermodynamic parameters, including pre-exponential factors (A), enthalpy (ΔH), Gibbs free energy (ΔG) and entropy (ΔS) were calculated using eqn. 3-9, 3-10, 3-11 and 3-12 [1].

$$A = \beta . Ea_\alpha \, exp\left(\frac{Ea_\alpha}{RT_m}\right) / R . T_m^2 \quad (3\text{-}9)$$

$$\Delta H = Ea_\alpha - RT \quad (3\text{-}10)$$

$$\Delta G = Ea_\alpha + R . T_m . In\left(\frac{K_b . T_m}{h . A}\right) \quad (3\text{-}11)$$

$$\Delta S = \frac{\Delta H - \Delta G}{T_m} \quad (3\text{-}12)$$

where kb = 1.38 x 10^{-23} J/K, h = 6.626 x 10^{-34} J.s, and T_m is the DTG peak temperature.

3.3 Results and discussion

3.3.1 Proximate, ultimate and heating values

Table 3-1 shows the proximate, ultimate and heating values of raw ash sawdust. These properties are comparable to and to some extent better than many biomass materials that have been investigated before [13]. The low moisture content of ash sawdust allows rapid heat transfer during pyrolysis [14] and achieves a high combustion yield. The comparison of several other biomass materials revealed a moisture content in the range 8.2 – 13.9 wt% [15] which is higher than the 5.7±0.04 wt% we observed for ash sawdust. The high content of volatile matter means the material can easily be devolatilised. The

residual ash content of ash tree sawdust was low (3.13±0.02 wt%) meaning that the removal of volatiles is unimpeded, resulting in less fouling and minimal residues, thus achieving a high thermal efficiency at low operating costs [16].

The calorific value of ash sawdust was 18.29±0.02 MJ/kg in its raw form. This value is higher than many other biomass fuels including moso bamboo (16.85 MJ/kg) [13], palm fibre (17.60 MJ/kg), palm sludge (13.80 MJ/kg) [19], cotton stalk (15.78 MJ/kg), wheat straw (17.90 MJ/kg), corn stalk (17.79 MJ/kg), grapevine chaff (16.68 MJ/kg), corn cobs (17.99 MJ/kg), sugar beet leaves (17.70 MJ/kg) and rice straw (12.13 MJ/kg) [20] but lower than wood (19.00 MJ/kg) [21]. Following torrefaction [22], ash sawdust was enhanced, making it suitable for co-firing or for industrial and domestic settings without the addition of other materials.

Table 3-1: Selected materials compared with raw ash sawdust.

Sample	HHV (MJ/kg)	Proximate analysis				Ultimate analysis					Reference
		M	V	FC	RA	C	H	N	S	O*	
Ash tree	18.29	5.66	70.14	21.07	3.13	49.12	6.64	0.35	-	43.89	This study
[α]Ash tree	17.23-22.06	7.6-4.2	86.8-69.3	12.3-26.1	0.9-0.4	48.9-57.3	5.9-5.8	<0.1-0.4	0.2-0.3	44.9-36.2	[17]
Moso bamboo	16.85	-	85.53	13.33	1.15	47.58	6.13	0.52	0.04	45.73	[13]
S. African coal	27.37	2.70	26.90	56.30	14.10	67.50	4.26	1.76	0.44	11.58	[18]

HHV = higher heating value; *determined by difference; M = moisture content, V = volatile matter, FC = fixed carbon, RA = residual ash; [α]values were taken before and after torrefaction at 300 °C.

3.3.2 Mass loss and conversion

Figure 3-1A and 3-1B show the mass loss and mass loss rate as a function of temperature. Ash sawdust underwent slow pyrolysis in three major phases at all heating rates. The first phase (50 – 200 °C) can be attributed to the loss of moisture, the second (200 – 450 °C) can be attributed to the degradation of hemicellulose and cellulose, and the last (450 – 800 °C) can be attributed to the degradation of lignin. There is a shift in the peak rate of mass loss for each heating rate: 325, 334, 348, 356, and 359 °C for rates of 2, 5, 10, 15, and 20 $^{\circ}$C/min, respectively.

The hydrophilic nature of sawdust, especially the non-crystalline parts and voids, allow water molecules to be accommodated in the structure. Sawdust is composed of α-cellulose, hemicellulose, lignin, pectin and waxes, with the first three representing up to 99 % of the sawdust by weight. Water is linked to the amorphous region of cellulose via intramolecular and intermolecular hydrogen bonds involving hydroxyl groups and free radicals on cellulose and hemicellulose [23]. During the first pyrolysis stage (50 – 200 °C), the main event is the dehydration of the sawdust. Dehydration reactions are both endothermic and potentially reversible, being based on interface reactions and diffusion. This may involve rapid initial nucleation on the surface followed by the spreading of the resulting coherent interface. Nucleation may occur at specific sites on the surface, in some but not all cases followed by growth. Structural re-organisation leads to the development of cracks, channels or pores via which moisture may escape from the interface [24].

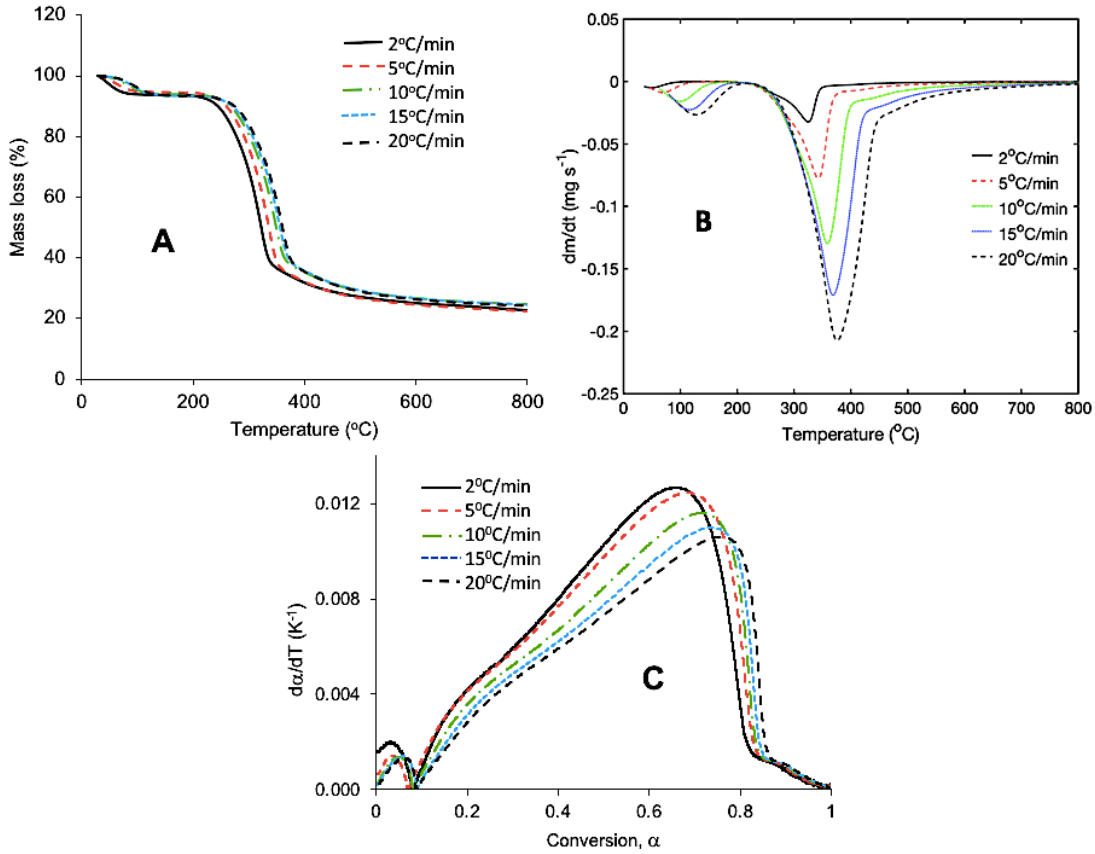

Figure 3-1: A - Mass loss. B - Mass loss rate. C - dα/dT as a function of conversion.

During the second pyrolysis stage (200 – 450 °C), the main reactions are the degradation of hemicellulose and cellulose. Hemicellulose is amorphous with a linear framework of xylan and glucomannan groups. Conversion occurs mainly in the 200 – 350 °C region and is catalysed by mineral matter, releasing moisture, CO_2 and other volatiles, and forming char [25]. Unlike hemicellulose, cellulose has both crystalline and amorphous phases. The conversion of cellulose mostly takes place at 300 – 450 °C. Decomposition reactions at about 300 °C are responsible for most of the lost mass as well as the release of CO, CO_2, and other organic compounds.

During the final pyrolysis stage (450 – 800 °C), lignin decomposition produces pyrolysis gases and tars that condense on the char wall surfaces [26]. Several

mechanisms describe this region including chemical reactions [27], random nucleation and growth, phase boundary mechanisms, and diffusion.

Figure 3-1C shows dα/dT as a function of conversion, with a sigmoidal curve as commonly observed in linear non-isothermal TGA [7], [28]. For 0 < α < 0.1, we observe a prominent peak corresponding to moisture loss. This is followed by a shoulder peak up to α ~ 0.3 corresponding to hemicellulose decomposition and a maximum peak at 0.6 < α < 0.75 corresponding to cellulose decomposition. At 0.85 < α < 1.0, we observe another shoulder peak corresponding to lignin decomposition. Furthermore, the 0 < α < 0.1 range (representing 50 < T < 220 °C at all heating rates) corresponds to the diffusion of moisture through the sawdust pores. The second conversion range (0.1 < α < 0.8) corresponds to 180 < T < 450 °C at all heating rates. For 0.80 < α < 1.00, the main reaction corresponds to lignin decomposition, which occurs in the range 360 < T < 800 °C for all heating rates. Figure 3-1C also shows the derivative dα/dT peak height declining with increasing heating rate, which can be attributed to the combined effects of heat and mass transfer within the sample [7].

3.3.3 Activation energy

Isoconversional methods were used to estimate activation energies at different degrees of conversion. Figure 3-2 A and 3-2 B show the Friedman and Starink plots that were used to calculate the activation energies. These methods gave similar and reasonable values at each degree of conversion, indicating they can be used to characterise the pyrolysis of ash tree sawdust. This is further strengthened by the high regression coefficients (0.999) within the 0.2 < α < 0.8 range, as shown in Figure 3-2C.

The observed activation energies could be divided into two main categories: 180 – 184 kJ/mol for 0.1 < α < 0.8 conversions and 195 – 350 kJ/mol for α > 0.8 conversions. The first category represents the breakage of relatively weak hemicellulose and cellulose bonds [29] whereas the second category represents the breakage of the stronger bonds of lignin [10].

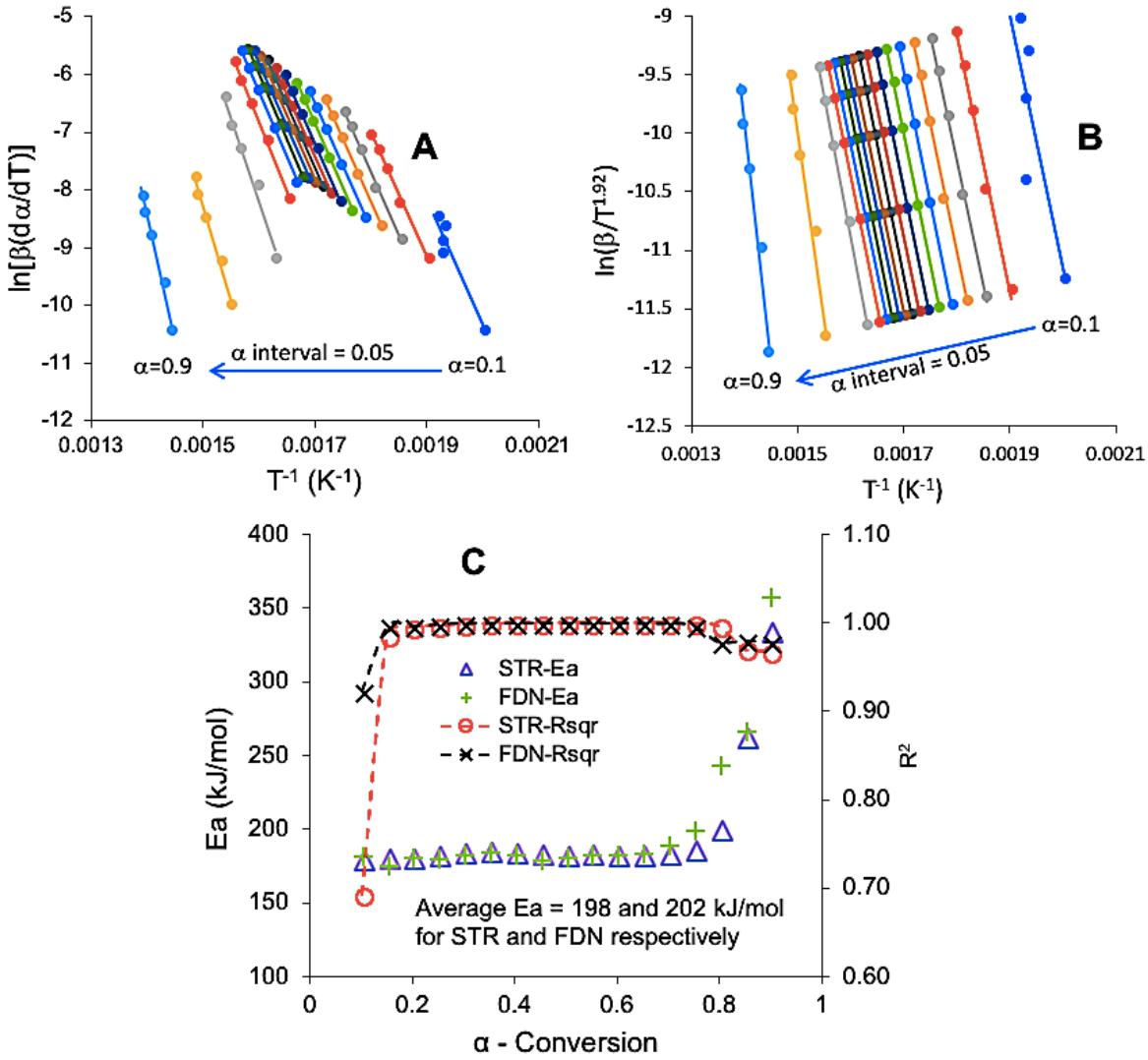

Figure 3-2: A – Friedman (FDN) plot, B – Starink (STR) plot, C – Activation energy and regression coefficients for STR and FDN.

The Ea of ash sawdust (198 – 202 kJ/mol) is similar to that of waste tea (208 – 223 kJ/mol) [30] and this indicates that ash sawdust is more difficult to pyrolyse than beech wood (147 – 174 kJ/mol) [2], moso bamboo (96 – 113 kJ/mol) [13], and other forms of biomass [31], [32], [33], [34]. However, the pyrolysis of ash

sawdust appears easier than *Corallina pilulifera* (248 kJ/mol), *Enteromorpha* spp. (228 kJ/mol) and rice husks (230 kJ/mol) [30].

3.3.4 Prediction of the reaction mechanism using master plots

When E_α values vary significantly with conversion, i.e. when the difference between the maximum and minimum E_α values exceeds 20 – 30 % of the average E_α, it is important to integrate over small segments (minimum α = 0.05 intervals) to avoid systematic errors [8].

In our experiments, we observed multi-step pyrolysis involving several mechanisms, and the deviation from $E_{\alpha(o)}$ exceeded 30 % once the conversion exceeded 0.8 for the Starink method and 0.75 for the Friedman method (Figure 3-3). These deviations may reflect secondary reactions between the volatiles and char [7].

Having excluded E_α values deviating by more than 30 %, we calculated $E_{\alpha(o)}$ using the Friedman method (because differential methods are considered more accurate than integral methods [8]) to give a value of 184 kJ/mol. The experimental $y(\alpha)$ master plot did not fit exactly to any of the theoretical master plots (Figure 3-4). However, the pyrolysis plots for ash sawdust were similar in shape to diffusion curves, especially D5 at lower conversions ($\alpha < 0.5$). In the same region, the ash sawdust pyrolysis master plot was similar to and intercepted several reaction-order master plots, especially n = 2 – 8.

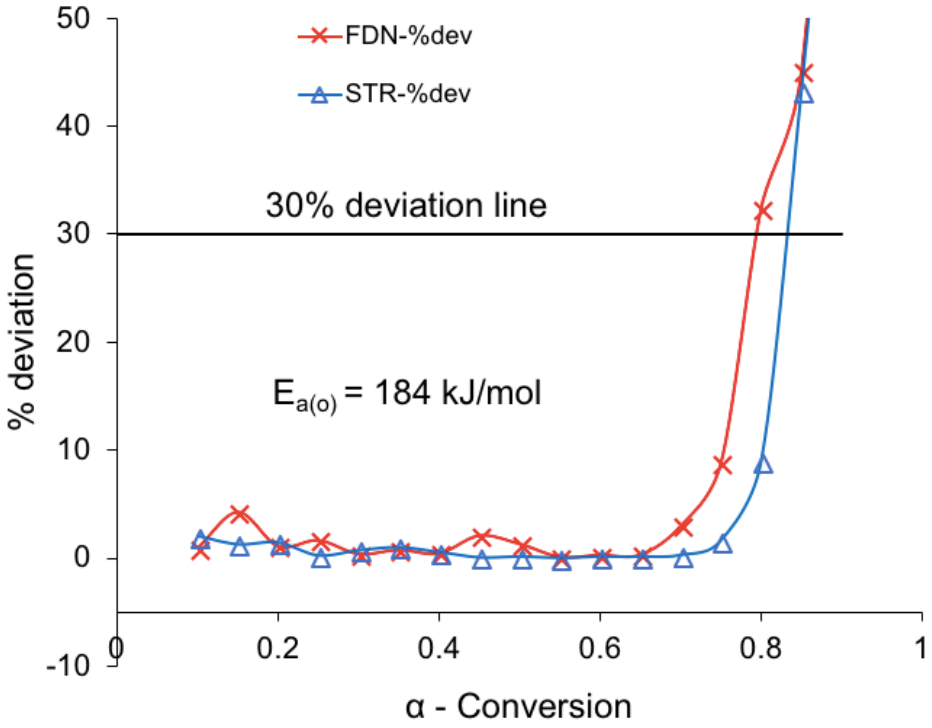

Figure 3-3: Deviation of E_a from $E_{a(o)}$.

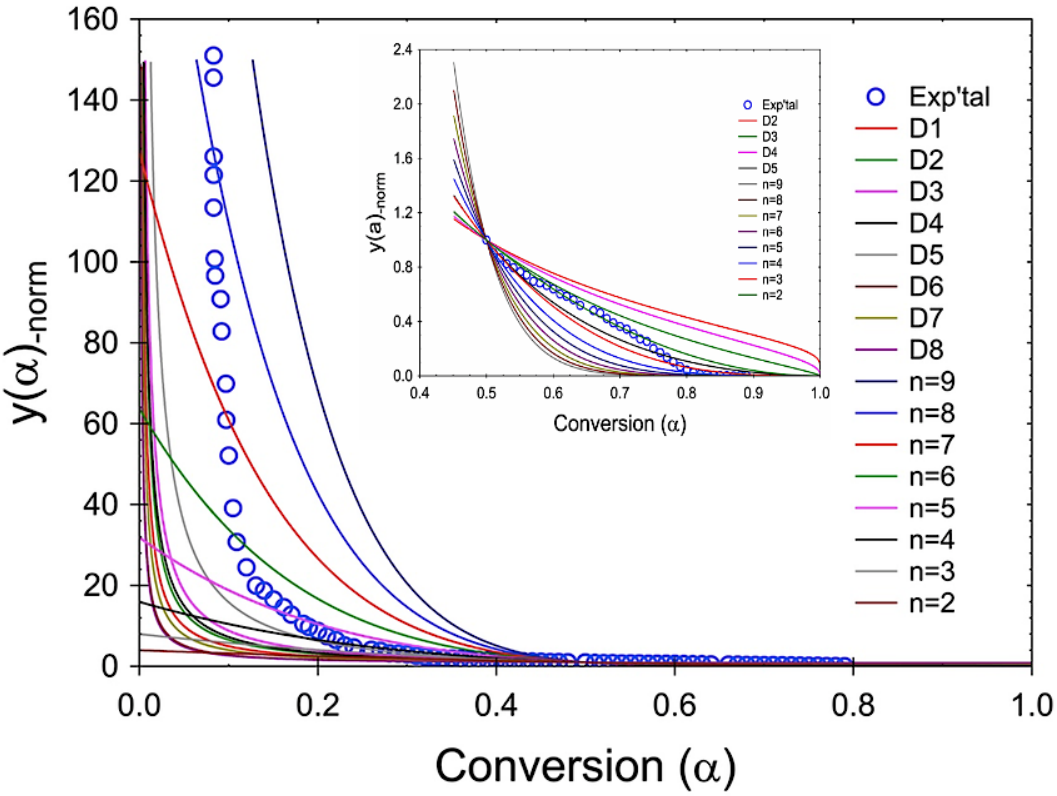

Figure 3-4: Generalised y(α) master plot, and master plot for α > 0.45 (insert).

At higher conversions (α > 0.5), the master plot for ash sawdust pyrolysis resembled the diffusion models D3 and D5, as well as reaction-order model n = 2 for 0.5 < α < 0.75. For α > 0.75, the master plot resembled diffusion model D5 and reaction-order models n = 2 – 9 (Figure 3-4-insert). However, the overall pyrolysis reaction may represent combinations of several mechanisms involving diffusion (D3 and D5), geometric contraction (G2 and G3), reaction-order models (n = 2 – 9), and/or nucleation [7].

3.3.5 Thermodynamic parameters

The pre-exponential factor (A), enthalpy (ΔH), Gibbs free energy (ΔG) and entropy (ΔS) were calculated using eqn. 3-9, 3-10, 3-11 and 3-12. The resulting A values fell between 10^{12} and 10^{19} except at α > 0.8. The ΔG values were constant at 185 kJ/mol and only decreased slightly at α > 0.8 (Table 3-2).

The A values for reactions in the solid state vary over six or seven orders of magnitude. Usually, the A value for first-order reactions ranges from 10^5 to 10^{18} s^{-1}. Low A values indicate surface reactions, but if the reactions are independent of the surface area, low A factors indicate that the activated complex is a 'sophisticated' one, whereas high A factors indicate a more straightforward complex [12]. The calculated changes in entropy were negative up to α = 0.7 for the Freidman method and up to α = 0.75 for the Starink method, indicating that the products were more ordered than the reactants [35]. The positive entropy values observed at high conversions indicate that the products were less ordered than the original materials [36].

Furthermore, entropy (ΔS) values are directly related to E_a and A: the higher the E_a and A values, the higher the ΔS [37]. The observation of both positive and negative ΔS values confirms the complexity of the pyrolysis reaction using ash tree sawdust as the starting material [1].

Table 3-2: Thermodynamic parameters for the pyrolysis of ash sawdust.

	Friedman				Starink			
α	A (s^{-1})	ΔH (kJ/mol)	ΔG (kJ/mol)	ΔS (J/mol)	A (s^{-1})	ΔH (kJ/mol)	ΔG (kJ/mol)	ΔS (J/mol)
0.10	7.29×10^{12}	176.80	185.29	-13.31	4.95×10^{12}	174.80	185.35	-16.53
0.15	2.21×10^{12}	170.66	185.48	-23.23	6.52×10^{12}	176.22	185.31	-14.25
0.20	6.85×10^{12}	176.48	185.30	-13.82	6.10×10^{12}	175.88	185.32	-14.80
0.25	5.70×10^{12}	175.53	185.33	-15.36	9.37×10^{12}	178.09	185.26	-11.23
0.30	8.83×10^{12}	177.79	185.27	-11.72	1.37×10^{13}	180.04	185.20	-8.09
0.35	1.37×10^{13}	180.06	185.20	-8.06	1.49×10^{13}	180.50	185.19	-7.35
0.40	8.68×10^{12}	177.70	185.27	-11.86	1.28×10^{13}	179.69	185.21	-8.66
0.45	4.88×10^{12}	174.74	185.35	-16.64	1.06×10^{13}	178.75	185.24	-10.17
0.50	6.34×10^{12}	176.08	185.32	-14.48	9.80×10^{12}	178.33	185.25	-10.85
0.55	9.72×10^{12}	178.28	185.25	-10.92	1.01×10^{13}	178.46	185.25	-10.64
0.60	9.10×10^{12}	177.95	185.26	-11.46	9.72×10^{12}	178.29	185.25	-10.92
0.65	1.18×10^{13}	179.30	185.22	-9.29	9.77×10^{12}	178.31	185.25	-10.88
0.70	3.08×10^{13}	184.24	185.08	-1.32	1.17×10^{13}	179.23	185.22	-9.40
0.75	2.44×10^{14}	194.92	184.79	15.88	1.88×10^{13}	181.69	185.15	-5.43
0.80	1.05×10^{18}	238.27	183.75	85.45	2.58×10^{14}	195.21	184.78	16.34
0.85	9.49×10^{19}	261.66	183.27	122.88	4.97×10^{19}	258.30	183.33	117.51
0.90	3.52×10^{27}	352.57	181.71	267.80	4.51×10^{25}	329.80	182.06	231.56

Summary & Conclusions

We investigated the kinetics and thermodynamics of ash wood sawdust during slow pyrolysis as parameters for measuring suitability for energy generation from a material. TGA/DSC3+ was used for sample preparation & analysis since this mehod gives the best environment for this kind of analysis. Friedman and Starink methods were used for kinetic analysis because these methods are more accurate than similar methods. The E_a values were 180 – 350 kJ/mol. Pyrolysis may have involved several mechanisms, including diffusion, geometrical contraction, reaction-order models and/or nucleation. The pre-exponential factors were between 10^{12} and 10^{19} s^{-1}. The change in entropy values remained negative up to α = 0.75, but became positive at higher conversions, implying greater disorder among the final products compared to the reactants. The calorific value of the ash wood sawdust was 18.3 MJ/kg which is comparable to other sources of biomass used for energy generation.

Acknowledgements

The authors thank the Hazel Woodhams Memorial, Gas Safety Trust, Boat Safety Scheme and Katie Haines of the United Kingdom for sponsoring this work.

References

[1] M. S. Ahmad, M. A. Mehmood, O. S. Al Ayed, G. Ye, H. Luo, M. Ibrahim, U. Rashid, I. Arbi Nehdi, and G. Qadir, "Kinetic analyses and pyrolytic behavior of Para grass (Urochloa mutica) for its bioenergy potential," Bioresour. Technol., vol. 224, pp. 708–713, 2017.

[2] Y. Ding, O. A. Ezekoye, S. Lu, and C. Wang, "Thermal degradation of beech wood with thermogravimetry/Fourier transform infrared analysis," Energy Convers. Manag., vol. 120, pp. 370–377, Jul. 2016.

[3] G. Mishra, J. Kumar, and T. Bhaskar, "Kinetic studies on the pyrolysis of pinewood," Bioresour. Technol., vol. 182, pp. 282–288, 2015.

[4] D. Chen, D. Liu, H. Zhang, Y. Chen, and Q. Li, "Bamboo pyrolysis using TG-FTIR and a lab-scale reactor: Analysis of pyrolysis behavior, product

properties, and carbon and energy yields," Fuel, vol. 148, pp. 79–86, 2015.
[5] D. Chen, Z. Zheng, K. Fu, Z. Zeng, J. Wang, and M. Lu, "Torrefaction of biomass stalk and its effect on the yield and quality of pyrolysis products," Fuel, vol. 159, pp. 27–32, 2015.
[6] X. Gu, C. Liu, X. Jiang, X. Ma, L. Li, K. Cheng, and Z. Li, "Thermal behavior and kinetics of the pyrolysis of the raw/steam exploded poplar wood sawdust," J. Anal. Appl. Pyrolysis, vol. 106, pp. 177–186, 2014.
[7] X. Wang, M. Hu, W. Hu, Z. Chen, S. Liu, Z. Hu, and B. Xiao, "Thermogravimetric kinetic study of agricultural residue biomass pyrolysis based on combined kinetics," Bioresour. Technol., vol. 219, pp. 510–520, 2016.
[8] S. Vyazovkin, A. K. Burnham, J. M. Criado, L. A. Pérez-Maqueda, C. Popescu, and N. Sbirrazzuoli, "ICTAC Kinetics Committee recommendations for performing kinetic computations on thermal analysis data," Thermochim. Acta, vol. 520, no. 1–2, pp. 1–19, 2011.
[9] J. E. White, W. J. Catallo, and B. L. Legendre, "Biomass pyrolysis kinetics: A comparative critical review with relevant agricultural residue case studies," J. Anal. Appl. Pyrolysis, vol. 91, no. 1, pp. 1–33, 2011.
[10] M. A. Islam, M. Asif, and B. H. Hameed, "Pyrolysis kinetics of raw and hydrothermally carbonized Karanj (Pongamia pinnata) fruit hulls via thermogravimetric analysis," Bioresour. Technol., vol. 179, pp. 227–233, 2015.
[11] M. J. Starink, "The determination of activation energy from linear heating rate experiments: A comparison of the accuracy of isoconversion methods," Thermochim. Acta, vol. 404, no. 1–2, pp. 163–176, 2003.
[12] L. Vlaev, N. Nedelchev, K. Gyurova, and M. Zagorcheva, "A comparative study of non-isothermal kinetics of decomposition of calcium oxalate monohydrate," J. Anal. Appl. Pyrolysis, vol. 81, no. 2, pp. 253–262, 2008.
[13] D. Chen, J. Zhou, and Q. Zhang, "Effects of heating rate on slow pyrolysis behavior, kinetic parameters and products properties of moso bamboo," in Bioresource Technology, vol. 169, Elsevier Ltd, 2014, pp. 313–319.
[14] A. K. Varma and P. Mondal, "Physicochemical characterization and pyrolysis kinetics of wood sawdust," Energy Sources, Part A Recover. Util. Environ. Eff., vol. 38, no. 17, pp. 2536–2544, 2016.
[15] Y. D. Singh, P. Mahanta, and U. Bora, "Comprehensive characterization of lignocellulosic biomass through proximate, ultimate and compositional analysis for bioenergy production," Renew. Energy, vol. 103, pp. 490–500, 2017.
[16] M. Peter, "Energy production from biomass (part 1): overview of biomass," vol. 83, no. July 2001, pp. 37–46, 2002.
[17] H. Haykiri-Acma, S. Yaman, and S. Kucukbayrak, "Combustion characteristics of torrefied biomass materials to generate power," in 2016 4th IEEE International Conference on Smart Energy Grid Engineering, SEGE 2016, 2016, pp. 226–230.

[18] D. Wu, M. Schmidt, X. Huang, and F. Verplaetsen, "Self-ignition and smoldering characteristics of coal dust accumulations in O2/N2 and O2/CO2 atmospheres," Proc. Combust. Inst., vol. 36, no. 2, pp. 3195–3202, 2017.
[19] Y. Y. Chong, S. Thangalazhy-Gopakumar, S. Gan, H. K. Ng, L.-Y. and Lee, and S. Adhikari, "Kinetics and mechanisms for co-pyrolysis of palm empty fruit bunch fibre (EFBF) with palm oil mill effluent (POME) sludge," Energy & Fuels, p. acs.energyfuels.7b00877, 2017.
[20] V. Skoulou and A. Zabaniotou, "Investigation of agricultural and animal wastes in Greece and their allocation to potential application for energy production," Renew. Sustain. Energy Rev., vol. 11, no. 8, pp. 1698–1719, 2007.
[21] T. Koyuncu and Y. Pinar, "The emissions from a space-heating biomass stove," Biomass and Bioenergy, vol. 31, no. 1, pp. 73–79, 2007.
[22] S. S. Daood, S. Munir, W. Nimmo, and B. M. Gibbs, "Char oxidation study of sugar cane bagasse, cotton stalk and Pakistani coal under 1% and 3% oxygen concentrations," Biomass and Bioenergy, vol. 34, no. 3, pp. 263–271, 2010.
[23] E. Manaila, M. D. Stelescu, G. Craciun, and D. Ighigeanu, "Wood sawdust/natural rubber ecocomposites cross-linked by electron beam irradiation," Materials (Basel)., vol. 9, no. 7, pp. 1–23, 2016.
[24] C. H. Bamford and C. F. H. Tipper, Reactions in the solid state, Volume 22. 1980.
[25] F. X. Collard and J. Blin, "A review on pyrolysis of biomass constituents: Mechanisms and composition of the products obtained from the conversion of cellulose, hemicelluloses and lignin," Renew. Sustain. Energy Rev., vol. 38, pp. 594–608, 2014.
[26] M. Brebu and C. Vasile, "Thermal degradation of lignin- a review," Cellul. Chem. Technol., vol. 44, no. 9, pp. 353–363, 2010.
[27] M. Jeguirim, J. Bikai, Y. Elmay, L. Limousy, and E. Njeugna, "Thermal characterization and pyrolysis kinetics of tropical biomass feedstocks for energy recovery," Energy Sustain. Dev., vol. 23, pp. 182–193, 2014.
[28] A. Khawam and D. R. Flanagan, "Solid-state kinetic models: Basics and mathematical fundamentals," J. Phys. Chem. B, vol. 110, no. 35, pp. 17315–17328, 2006.
[29] M. T. Reza, W. Yan, M. H. Uddin, J. G. Lynam, S. K. Hoekman, C. J. Coronella, and V. R. Vásquez, "Reaction kinetics of hydrothermal carbonization of loblolly pine," Bioresour. Technol., vol. 139, pp. 161–169, 2013.
[30] L. Tian, B. Shen, H. Xu, F. Li, Y. Wang, and S. Singh, "Thermal behavior of waste tea pyrolysis by TG-FTIR analysis," Energy, vol. 103, pp. 533–542, 2016.
[31] S. Ceylan, Y. Topcu, and Z. Ceylan, "Thermal behaviour and kinetics of alga Polysiphonia elongata biomass during pyrolysis," Bioresour. Technol., vol. 171, no. 1, pp. 193–198, 2014.
[32] S. Ceylan and Y. Topcu, "Pyrolysis kinetics of hazelnut husk using thermogravimetric analysis," Bioresour. Technol., vol. 156, pp. 182–188,

2014.
[33] K. Slopiecka, P. Bartocci, and F. Fantozzi, "Thermogravimetric analysis and kinetic study of poplar wood pyrolysis," Appl. Energy, vol. 97, pp. 491–497, 2012.
[34] T. Sonobe and N. Worasuwannarak, "Kinetic analyses of biomass pyrolysis using the distributed activation energy model," Fuel, vol. 87, no. 3, pp. 414–421, 2008.
[35] A. Alves, D. Maia, and L. C. De Morais, "Kinetic parameters of red pepper waste as biomass to solid biofuel," Bioresour. Technol., vol. 204, pp. 157–163, 2016.
[36] S. C. Turmanova, S. D. Genieva, A. S. Dimitrova, and L. T. Vlaev, "Non-isothermal degradation kinetics of filled with rise husk ash polypropene composites," Express Polym. Lett., vol. 2, no. 2, pp. 133–146, 2008.
[37] L. T. Vlaev, V. G. Georgieva, and S. D. Genieva, "Products and Kinetics of Non – Isothermal Decomposition of Vanadium (Iv) Oxide Compounds," vol. 88, pp. 805–812, 2007.

Chapter 4: REACTIVITY AND FREE RADICAL CHEMISTRY OF LILAC (*SYRINGA VULGARIS*) CHARCOAL

The work contained in this chapter has been published in Energy & Fuels Journal.

Citation: Nyombi A, Williams R M, Wessling R: Reactivity and free radical chemistry of lilac (Syringa vulgaris) charcoal.

DOI: http://doi.org/10.1021/acs.energyfuels.8b03665

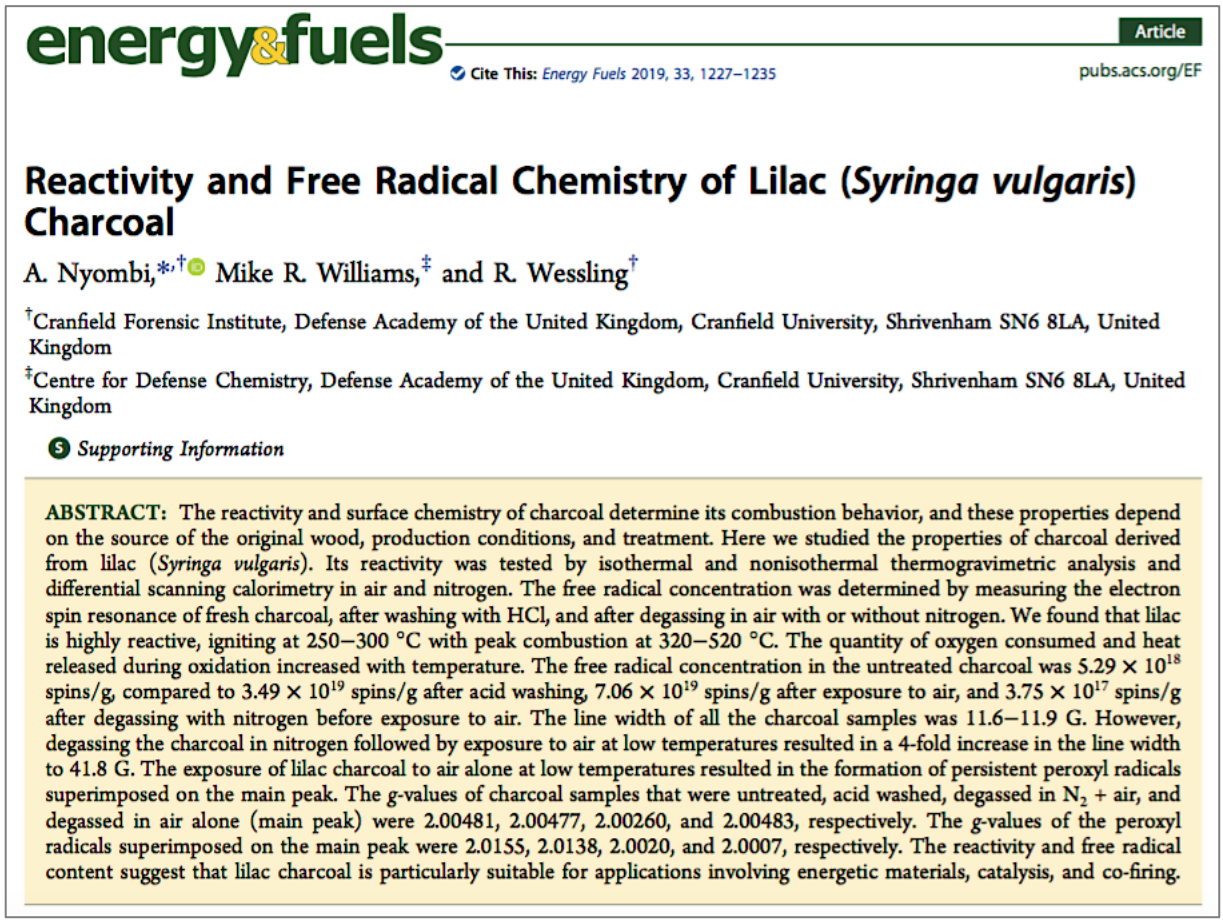

energy&fuels

Article

Cite This: *Energy Fuels* 2019, 33, 1227−1235

pubs.acs.org/EF

Reactivity and Free Radical Chemistry of Lilac (*Syringa vulgaris*) Charcoal

A. Nyombi,*,† Mike R. Williams,‡ and R. Wessling†

†Cranfield Forensic Institute, Defense Academy of the United Kingdom, Cranfield University, Shrivenham SN6 8LA, United Kingdom

‡Centre for Defense Chemistry, Defense Academy of the United Kingdom, Cranfield University, Shrivenham SN6 8LA, United Kingdom

Supporting Information

ABSTRACT: The reactivity and surface chemistry of charcoal determine its combustion behavior, and these properties depend on the source of the original wood, production conditions, and treatment. Here we studied the properties of charcoal derived from lilac (*Syringa vulgaris*). Its reactivity was tested by isothermal and nonisothermal thermogravimetric analysis and differential scanning calorimetry in air and nitrogen. The free radical concentration was determined by measuring the electron spin resonance of fresh charcoal, after washing with HCl, and after degassing in air with or without nitrogen. We found that lilac is highly reactive, igniting at 250−300 °C with peak combustion at 320−520 °C. The quantity of oxygen consumed and heat released during oxidation increased with temperature. The free radical concentration in the untreated charcoal was 5.29×10^{18} spins/g, compared to 3.49×10^{19} spins/g after acid washing, 7.06×10^{19} spins/g after exposure to air, and 3.75×10^{17} spins/g after degassing with nitrogen before exposure to air. The line width of all the charcoal samples was 11.6−11.9 G. However, degassing the charcoal in nitrogen followed by exposure to air at low temperatures resulted in a 4-fold increase in the line width to 41.8 G. The exposure of lilac charcoal to air alone at low temperatures resulted in the formation of persistent peroxyl radicals superimposed on the main peak. The *g*-values of charcoal samples that were untreated, acid washed, degassed in N_2 + air, and degassed in air alone (main peak) were 2.00481, 2.00477, 2.00260, and 2.00483, respectively. The *g*-values of the peroxyl radicals superimposed on the main peak were 2.0155, 2.0138, 2.0020, and 2.0007, respectively. The reactivity and free radical content suggest that lilac charcoal is particularly suitable for applications involving energetic materials, catalysis, and co-firing.

Reactivity and Free Radical Chemistry of Lilac (*Syringa Vulgaris*) Charcoal

Highlights

- Lilac ignites quickly (250 – 290 °C), and has a narrow combustion temperature range (300 – 520 °C),
- Lilac has C-C free radicals arising from carbonization,
- It forms peroxyl radicals on oxidation in air,
- Degassing in N_2 and acid washing removes the free radicals.

Abstract

The reactivity, and surface chemistry of charcoal determine its combustion behaviour, and these properties depend on the source of the original wood, production conditions and treatment. Here we studied the properties of charcoal derived from lilac (*Syringa vulgaris*). Its reactivity was tested by isothermal and non-isothermal thermogravimetric analysis and differential scanning calorimetry in air and nitrogen. The free radical concentration was determined by measuring the electron spin resonance of fresh charcoal, after washing with HCl, and after degassing in air with or without nitrogen. We found that lilac is highly reactive, igniting at 250 – 300 °C with peak combustion at 320 – 520 °C. The quantity of oxygen consumed and heat released during oxidation increased with temperature. The free radical concentration in the untreated charcoal was 5.29 x 10^{18} spins/g, compared to 3.49 x 10^{19} spins/g after acid washing, 7.06 x 10^{19} spins/g after exposure to air, and 3.75 x 10^{17} spins/g after degassing with nitrogen before exposure to air. The line width of all the radicals on the charcoal samples was 11.6 – 11.9 G. However, degassing

the charcoal in nitrogen followed by exposure to air at low temperatures resulted in a four-fold increase in the line width to 41.8 G. The exposure of lilac charcoal to air alone at low temperatures resulted in the formation of persistent peroxyl radicals superimposed on the main peak. The g-values of the free radicals on the charcoal samples that were untreated, acid washed, degassed in N_2 + air, and degassed in air alone (main peak) were 2.00481, 2.00477, 2.00260 and 2.00483, respectively. The g-values of the peroxyl radicals superimposed on the main peak were 2.0155, 2.0138, 2.0020 and 2.0007, respectively. The reactivity and free radical content suggest that lilac charcoal is particularly suitable for applications involving energetic materials, catalysis and co-firing.

4.1 Introduction

Charcoal is widely used for heating and cooking, but the properties of charcoal depend on its source, production conditions and treatment, which define its reactivity, and surface chemistry. Charcoal oxidation is a complex process which influences combustion and gasification. Oxidation rates are partially influenced by surface functional groups and reactions catalysed by mineral components, and such catalytic effects have also been observed during pyrolysis [1]. The oxidation of charcoal includes steps such as the adsorption of oxygen, the chemisorption of oxygen at carbon active sites to form complexes, migration to form low activation energy complexes, and the desorption of the complexes as gaseous products such as CO and CO_2 [2]. Physisorption is usually reversible, whereas chemisorption may involve free-site reactants and stable-oxide-site reactants. Together, these steps are affected by the properties of the char, the reaction temperature, the oxygen concentration, the char particle size, and the reactor type.

At low temperatures, oxygen almost completely penetrates the charcoal particle before the onset of significant oxidation [3]. The reactivity of char under both oxidizing and inert conditions has been studied by thermogravimetric analysis [4]. The free radicals generated during pyrolysis and carbonization can introduce considerable strain energy into the lattice. The cellulosic structure loses small molecules such as water and CO_2 together with more complex aliphatic acids, carbonyls, and alcohols. The resulting chemically-reactive lattice encloses the vacancies created by the loss of volatiles. The new lattice is continuously refined, but typically has high C/H and C/O ratios due to the preferential loss of hydrogen and oxygen. With increasing temperature, the unstable carbon network becomes more carbonaceous and more aromatic as the carbon atoms re-adjust their positions and approximate to the six-membered ring system comprising the building blocks of lamellar constituent molecules (LCMs). Further heat treatment removes more hydrogen, oxygen and nitrogen, causing the network to become more carbonaceous and aromatic.

Surface groups on the charcoal (including hydroxyl, carboxyl, carbonyl, ether and lactone structures) play a significant role during combustion [5] [6]. All these functional groups influence the reaction of charcoal and free radicals, the latter being responsible for the initiation and termination of chain reactions. The nature and content of these free radicals in charcoal must be characterized in order to understand the reactivity of charcoal in different environments.

Electron spin resonance (ESR) spectroscopy is often used to determine the organic free radical content of carbon materials [7], [8], [9]. However, peroxyl radicals do not form a defined ESR spectrum and are difficult to interpret [10], [11]. The primary bonding of peroxyl radicals results from Lewis acid-base reactions between diamagnetic R groups and O^+ or O^- radicals. The unoccupied π^* orbital in O_2^+ is an electron acceptor which acts as a Lewis σ

acid, whereas the filled level of O_2^- is an electron donor or Lewis σ base [12]. ESR spectroscopy is the most powerful technique for the structural characterization of paramagnetic systems because it is a non-invasive method hence the samples are not damaged. With free radicals as molecular probes, ESR spectroscopy is ideal for the analysis of the structural features of diamagnetic nanoscale and supramolecular structures and surfaces. Unlike other spectroscopic parameters, ESR transitions are characterized by tiny energy gaps (and consequently very long wavelengths). The small populations of the different energy levels (10^{-3} to 10^{-1} kJ/mol) limit the sensitivity of the technique, but it still outperforms nuclear magnetic resonance (NMR) spectroscopy [13]. For continuous wave ESR, some of the more important features include the position, separation, number of lines, line width, and intensity. The *g*-value determines the position, the separation is determined by the hyperfine coupling constant or *a*-value, and the number of lines in the hyperfine pattern is dictated by the nuclear spin *I*. The line width may be a consequence of dynamic effects or unresolved hyperfine interactions. The line intensities may be due to the multiplicity of the hyperfine lines caused by multiple interactions with nuclei of ≥½, or the anisotropy of the paramagnetic system [13].

Here we set out to determine the behaviour of lilac (*Syringa vulgaris*) charcoal in air under both isothermal and non-isothermal oxidative conditions. We also determined the free radical type and content for natural, pyrolyzed and oxidized charcoal with more emphasis on the peroxyl radical analysis and spectra simulation.

4.2 Methodology

4.2.1 Charcoal sample preparation

The charcoal used in this study was produced in the laboratory from lilac (*S. vulgaris*) wood. Lilac wood chips ~5 cm in length were inserted into the retort and covered with a lid *Figure 4-1*. The lid was sealed with fire cement and perforated with holes ~1 mm in diameter spaced at regular intervals to allow the escape of pyrolysis gases. The retort was inserted into a muffle furnace and heated to 500 °C for 4 h within an air atmosphere. The resulting charcoal was left to cool within the muffle retort overnight before storage and use. The charcoal samples were ground in an Essa LM2 pulverizing mill and sieved to <200 μm particle size. Portions of the ground charcoal were prepared on a Mettler Toledo TGA/DSC3+ device described in our previous work [14] under different conditions while others were prepared differently as shown in *Table 4-1*

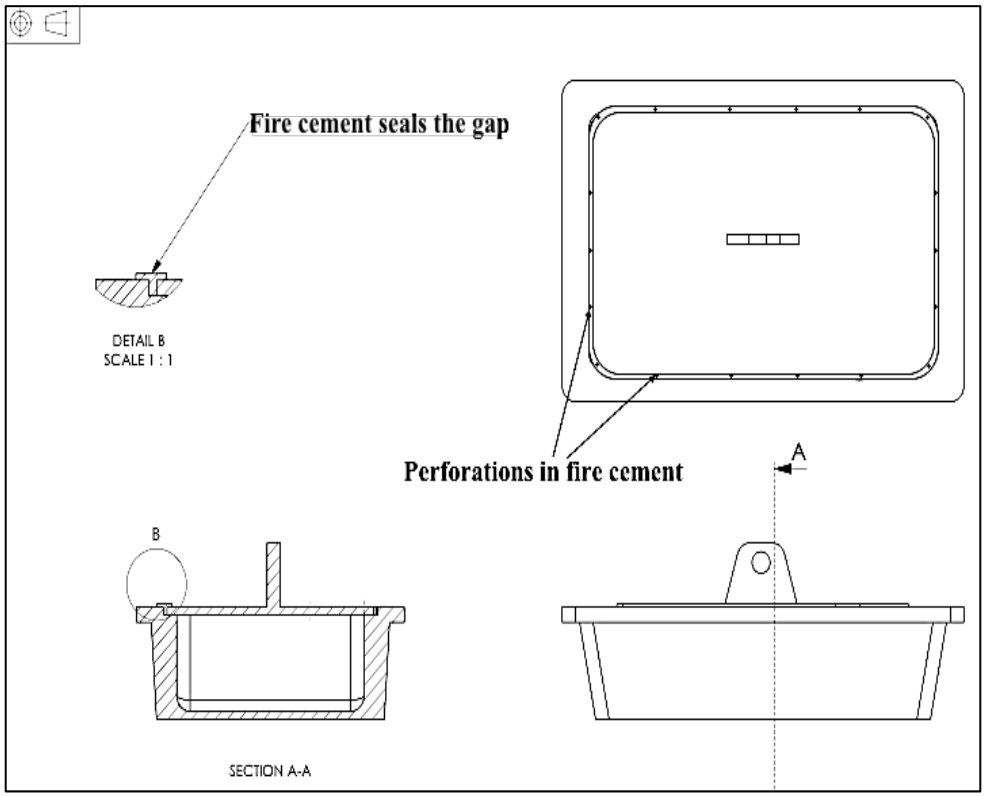

Figure 4-1: Schematic of the muffle retort used for laboratory charcoal making

4.2.2 Elemental and proximate analysis

Elemental analysis for carbon, hydrogen and nitrogen, and proximate analysis, were carried out as we previously described [14]. The quantities of elements present in the charcoal ash as oxides were analysed using a Seiko Instruments SEA6000VX bench-top X-ray fluorescence detector (Nanotechnology Incorporated) using a sample standard (RTC-CRM002-100G from LGC) and a rhodium tube as the target. The measurement time was 100 s with a collimator/spot size of 1.2 x 1.2 mm, a tube voltage of 50 kV, a tube current of 314 μA in auto mode, no filter and a helium purging environment.

Table 4-1: Sample preparation[a]

Sample	Preparation
A	5 – 10 mg of charcoal was pyrolyzed under N_2 (50 mL/min) at a heating rate of 20 °C/min from 30 °C to 750 °C, then cooled under N_2 to a desired test isothermal temperature and then exposed to air (50 mL/min) at that isothermal for 30 minutes.
B	5 – 10 mg of charcoal was pyrolyzed under N_2 (50 mL/min) at a heating rate of 20 °C/min from 30 °C to 750 °C, and then cooled under N_2 to 30 °C.
C	5 – 10 mg of charcoal was oxidized in air (50 mL/min) at 100 °C for 300 minutes.
D	5 – 10 mg of charcoal was oxidized under air (50 mL/min) at four different heating rates (2, 5, 10, and 15 °C/min) from 30 °C to 650 °C to evaluate its reactivity kinetics with air (oxygen).
E	5 – 10 mg of commercial activated carbon samples were also analysed with ESR for comparison.
F	40 – 50 g of charcoal were soaked in 1 M HCl overnight and rinsed afterwards with distilled-deionised water several times until the pH ≈ 7. Approximately 5-10 mg aliquots of the HCl washed charcoal was oxidized in air (50 mL/min) at 100 °C for 300 minutes.
G	Normal dry lilac charcoal (< 200 μm particle size) – no treatment performed

[a]All sample analysis were performed in triplicate in addition to blanks.

4.2.3 ESR spectroscopy

Continuous wave ESR was performed in the X-band of the microwave frequency and ESR spectra were recorded on a JES-FA Series ESR spectrometer (Jeol Ltd, Tokyo, Japan) as previously described [9]. Several runs were performed for samples A, B, C, E, F, and G (described in Table 4-1 above) to obtain enough material for this section. Samples (60 – 100 mg) were placed in a closed-bottom quartz capillary tube with a wall thickness of 0.75 mm and an outer diameter of 5 mm. The measurements were carried out at room temperature with a microwave power of 1 mW, a modulation width of 0.014 mT, a sweep width of 75 G, a sweep time of 2 min, and a time constant of 0.3 seconds. The spin concentrations (spins/g) of the samples were computed as described elsewhere [7]. Diphenyl Picryl Hydrazine (DPPH) was used as a standard to determine the spin concentration of the free radicals.

4.2.4 Oxidation/reactivity kinetics

4.2.4.1 Non-isothermal oxidation

The kinetics of non-isothermal oxidation in the air (using sample D – described in *Table 4-1*) was determined using the Kissinger, Kissinger–Akahira–Sunose (KAS), and Flynn–Wall–Ozawa (FWO) methods.

The Kissinger method [15] is model-free but it is not an iso-conventional method because it assumes constant activation energy during conversion. It was derived by assuming that the rate of oxidation follows first-order kinetics [16] although this may not always be the case, and it takes the form shown in eqn. 4-1.

$$In\left(\frac{\beta}{T_{max}^2}\right) = \left(-\frac{E_a}{R}\right)\left(\frac{1}{T_{max}}\right) + \frac{InAR}{E_a} \quad (4\text{-}1)$$

Different heating rates ($\beta = \beta_1, \beta_2, \ldots$) were used during the measurements. The apparent activation energy was determined from the plot of $In\beta/T^2_{max}$ versus $1/T_{max}$.

The Kissinger–Akahira–Sunose (KAS) method is based on eqn. 4-2;

$$In\left(\frac{\beta}{T^2}\right) = \left(-\frac{E_a}{R}\right)\left(\frac{1}{T}\right) + \frac{InAR}{E_a\, g(\alpha)} \quad (4\text{-}2)$$

where $g(\alpha)$ is the integral conversion function [17]. For constant conversion, the apparent activation energy was determined from the plot of $In\beta/T^2$ versus $1/T$.

The Flynn–Wall–Ozawa (FWO) method was developed by Flynn & Wall [18] and Ozawa [19], based on Doyle's approximation [20]. It was derived from the integral function shown in eqn. 4-3.

$$g(\alpha) = \int_0^{\alpha} \frac{d\alpha}{f(\alpha)} = \frac{A}{\beta}\int_{T_o}^{T} e^{-\left(\frac{E_a}{RT}\right)}\, dT \quad (4\text{-}3)$$

Equation 4-3 does not have an analytical solution. Doyle calculated ln $g(\alpha)$ values for a wide range of (E_a/RT) values, and found that within the limits $20 \leq (E_a/RT) \leq 60$ [21], the approximation shown in eqn. 4-4 can be derived by rearrangement.

$$In\beta = In\left(\frac{AE_a}{R\, g(\alpha)}\right) - 5.331 - 1.052\left(\frac{E_a}{RT}\right) \quad (4\text{-}4)$$

The plot of $In\beta$ versus $1/T$ gives a straight line whose slope $-1.052(Ea/R)$ is used to determine the activation energy.

4.2.4.2 Isothermal oxidation

Sample A and C (described in *Table 4-1*) were oxidised in air at temperatures in the range 50 – 600 °C. In both cases, samples were analysed by ESR spectroscopy for the presence of free radicals, and to determine the amount of oxygen adsorbed/consumed and the adsorption rates.

4.3 Results and Discussion

4.3.1 Proximate analysis, ultimate analysis and trace elements

The Proximate analysis, ultimate analysis and trace elements are shown in *Table 4-2*. The trace elements (oxides) are associated with the growth location, climate, and cropping [22]. The O/C and H/C atomic ratios were 0.158 and 0.033, respectively, similar to values obtained elsewhere [23]. The O/C ratio suggests that lilac charcoal is very reactive, which is consistent with the experimental observations discussed below. The H/C ratio correlated with the oxidative reactivity of the charcoal particles, reflecting the high probability of H abstraction by O_2 or the radicals present in the combustion environment such as $^{\bullet}H$, $^{\bullet}OH$, $^{\bullet}CH_3$ and $^{\bullet}C_3H_3$ to create radical sites on the charcoal to facilitate O_2 adsorption, thus increasing the oxidation rate [24].

4.3.2 Oxidation/reactivity

4.3.2.1 Non-isothermal oxidation

Figure 4-2, shows the conversion of charcoal (sample D) and its reactivity in the air at different heating rates. The conversion rates were unimodal at all heating

rates. The temperatures corresponding to 50 % conversion were 447.8, 428.8, 416.6 and 403.5 °C for 15, 10, 5 and 2 °C/min, respectively, and the temperatures corresponding to maximum conversion were 482.8, 458.8, 447.0 and 420.4 °C.

Table 4-2: The proximate analysis, ultimate analysis and trace elements as oxides presented as wt% and computed at one standard deviation

Proximate analysis, wt%		Ultimate analysis, wt%		Trace elements, wt%	
Moisture	3.46±0.01	C	83.44±0.46	FeO	0.9
[a]VM	11.71±0.01	H	2.74±0.14	SiO	43.8
[b]FC	80.88±0.03	O	13.21±0.48	CaO	29.8
[c]Ash	3.95±0.01	N	0.62±0.11	P_2O_5	13.8
				K_2O	10.6
				MgO	1.2
				Al_2O_3	0.7

[a]VM – Volatile matter, [b]FC – Fixed carbon, [c]Ash – Residual ash

Significant charcoal oxidation started at 250 – 300 °C. At temperatures < 250 °C, the remaining physically-bound and chemically-bound moisture as well as unstable volatiles are removed [23]. The oxidation took place in a narrow temperature range (mainly 330 – 520 °C) for all heating rates, suggesting that lilac charcoal is mostly composed of monomeric carbonaceous units, i.e. fragments of randomly curved carbon sheets containing pentagonal and heptagonal rings dispersed throughout a hexagonal network [25]. However, the reactivity could also reflect the size of the polycyclic aromatic hydrocarbon (PAH) units, the presence of oxygenated or aliphatic functional groups, the presence of active sites, the H/C ratio [23], the presence of free radicals, and the bonding between each unit. The high reactivity could also be due to the presence of many exposed carbon atoms on the surface and between the pores which are susceptible to oxidation.

The pre-exponential factor *A* is proportional to the frequency of collision between active sites on charcoal and oxygen. Low *A* values indicate complex active sites [24]. *Table 4-3* shows that the A values for lilac charcoal were in the range $10^2 – 10^7\ s^{-1}$, indicating that the active sites on charcoal may be complex,

possibly composed of PAHs with oxygen heteroatoms. The activation energy (E_a) values for oxidation in air were 110 – 145 kJ/mol, which is narrow compared to other carbons [26]. Also, we observed a drop in the E_a and A values during the progress of oxidation (*Figure 4-2* and *Table 4-3*) implying the progressive formation of weaker bonds [14]. However, the complexity of the active sites seems to increase with conversion, possibly due to pentagonal and hexagonal ring opening and the formation of reactive oxygen species which later form carbon oxides.

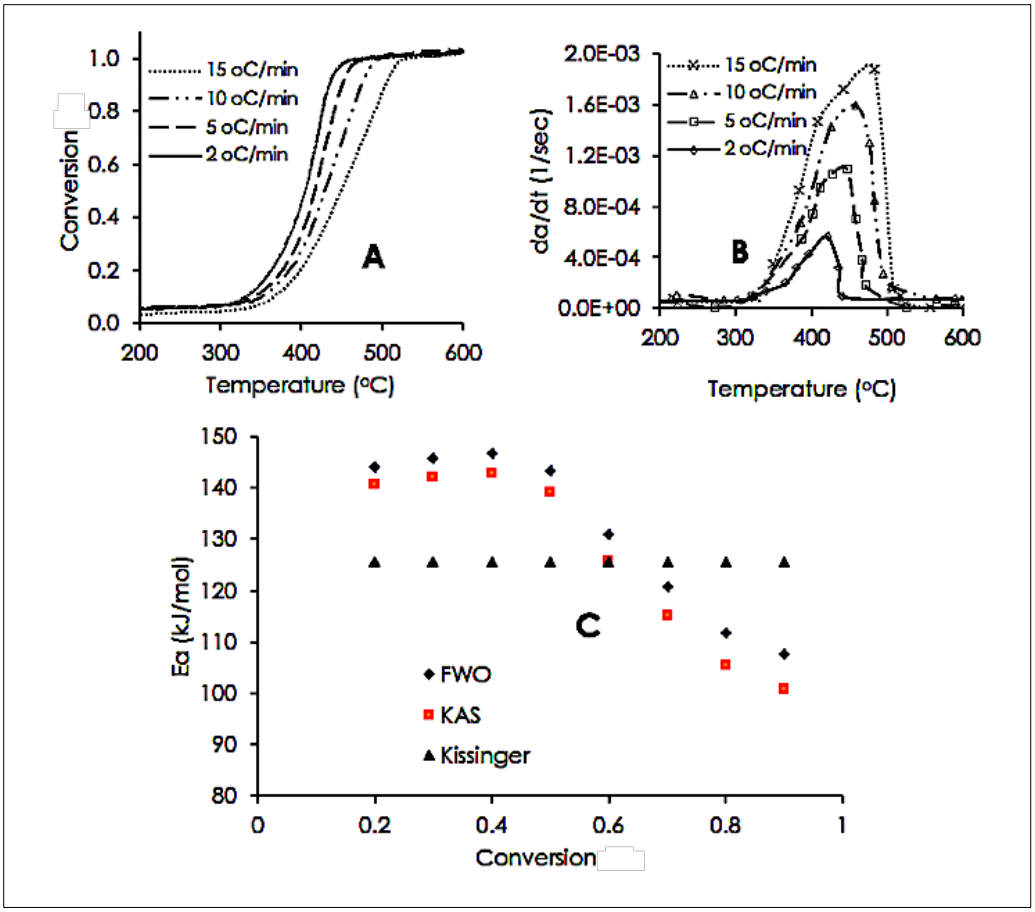

Figure 4-2: Conversion (A) and reactivity (B) and E_a (C) of lilac charcoal

4.3.2.2 Isothermal oxidation

When the charcoal was pyrolyzed in nitrogen, there was loss of moisture and volatiles (approximately the first 40 minutes of *Figure 4-3*). Cooling in nitrogen to the desired temperature, followed by exposure to air for 30 min, resulted in

a mass gain implying that oxygen was absorbed from the air (*Figure 4-3*). Fanning and Vannice [27] observed that activating carbon in argon and then oxidizing it with an oxygen/argon mixture yielded a diffuse reflectance infrared fourier transform (DRIFT) spectra indicating the formation of oxygen functional groups on the carbon surface. The functional groups were assigned to cyclic anhydrides, lactones, ethers, and phenols. The adsorption and reaction of ozone molecules on the surface of the carbon yields free radicals on the surface, which may be any oxygen-containing active species [28]. Similarly, the oxidation of carbon black with ozone and NO_2 forms carboxylic, phenolic, and lactonic groups on the carbon surface [29].

Table 4-3: Pre-exponential factors for the oxidation of charcoal

Conversion	Pre-exponential factors (s^{-1})		
α	FWO	KAS	Kissinger
0.2	7.77×10^{13}	3.55×10^{7}	4.79×10^{5}
0.3	4.29×10^{13}	1.89×10^{7}	4.79×10^{5}
0.4	2.45×10^{13}	1.05×10^{7}	4.79×10^{5}
0.5	7.45×10^{12}	2.92×10^{6}	4.79×10^{5}
0.6	4.82×10^{11}	1.51×10^{5}	4.79×10^{5}
0.7	4.79×10^{10}	1.23×10^{4}	4.79×10^{5}
0.8	5.47×10^{9}	1.16×10^{3}	4.79×10^{5}
0.9	1.02×10^{9}	1.0×10^{2}	4.79×10^{5}

Adsorption rate

Figure 4-4 shows that the initial adsorption rate is a steep gradient that follows zero-order kinetics at all temperatures, meaning that the amount adsorbed is dependent neither on the amount of carbon in the system nor the concentration of oxygen (air containing 21 % oxygen was used in all the experiments). The subsequent decay followed first-order kinetics, implying that the active sites on the carbon surface and the oxygen concentration both played a role. At low temperatures ≤ 250 °C, the decline could be attributed to the loss of active sites available for further adsorption.

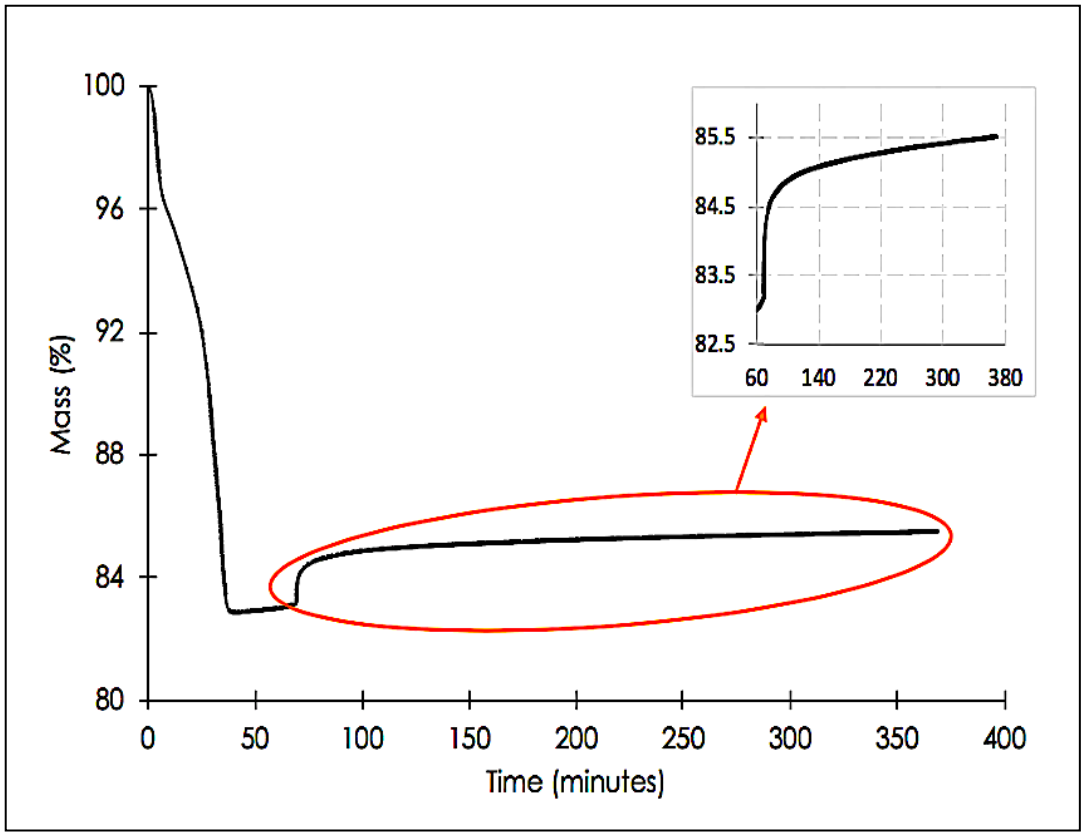

Figure 4-3: Mass gain of sample A exposed to air at 100 °C.

The area under the normalized oxygen adsorbed/consumed versus time curve gives the total amount of oxygen consumed at different temperatures. We found that the charcoal continued to adsorb/consume more oxygen as the temperature increased. *Figure 4-5* shows that the computed amounts of oxygen consumed increased exponentially as a function of temperature. This was previously observed during the oxidation of isomeric hexanes, and compounds with more tertiary C-H bonds showed a greater stability than those with more secondary C-H bonds due to the formation of ketone rather than aldehyde groups [30]. These observations are also in agreement with the data reported by Dollimore and colleagues [5].

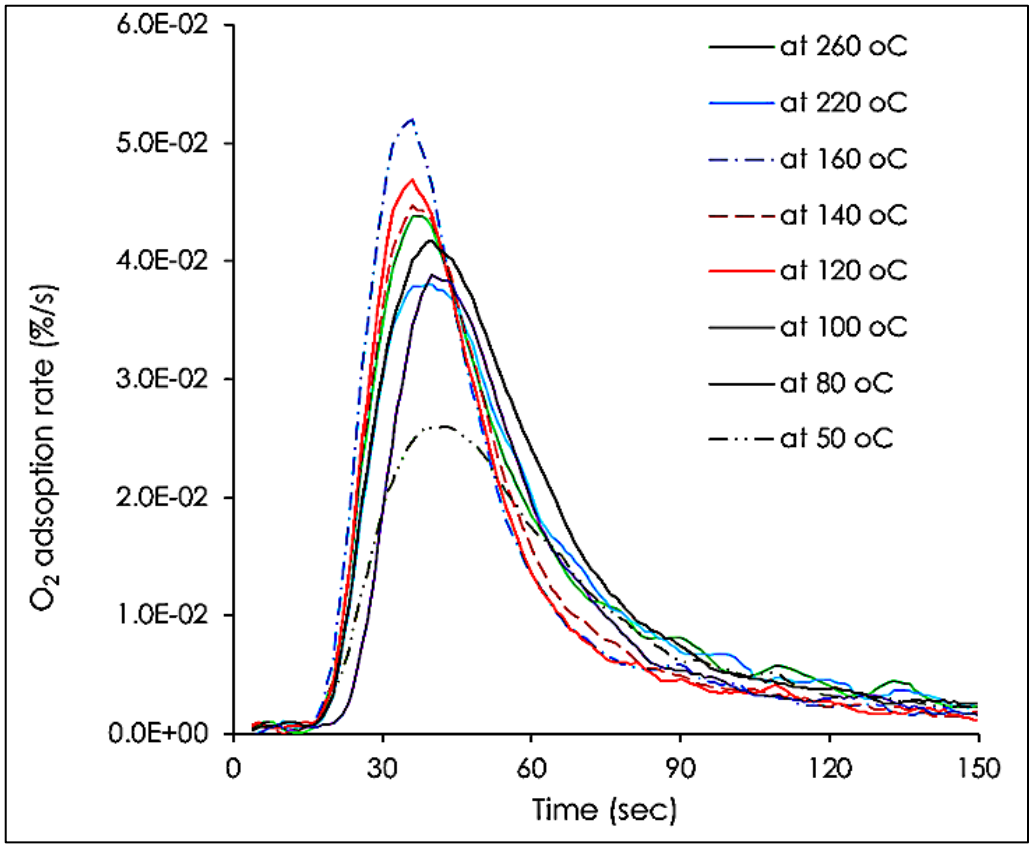

Figure 4-4: Rate of adsorption of oxygen on sample A over the temperature range 50 – 260 °C.

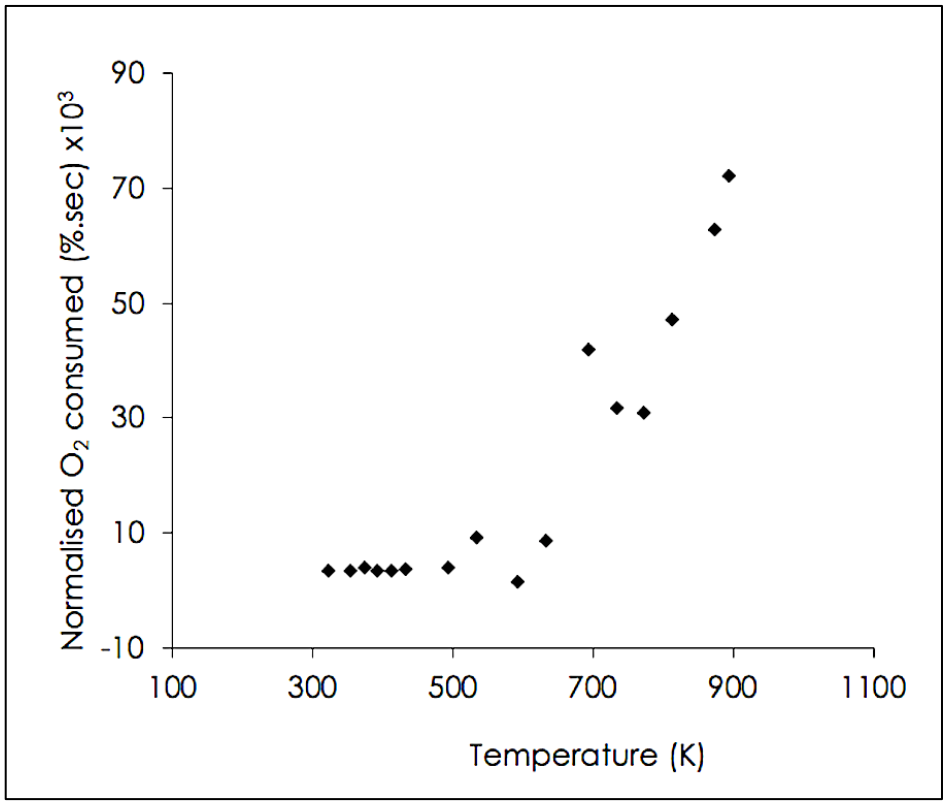

Figure 4-5: Amount of oxygen consumed at different temperatures by samples.

Exothermicity of isothermal oxidation

As expected, we found that the adsorption of oxygen to charcoal was an exothermic process. *Figure 4-6*A shows the integration of exotherms for oxygen adsorption at 50 and 160 °C to estimate the amount of liberated heat. The exothermicity of oxygen adsorption increased exponentially with temperature (*Figure 4-6*B). As discussed above, the amount of oxygen consumed also increased with temperature, and given that oxygen supports burning, the greater the consumption the more heat is generated.

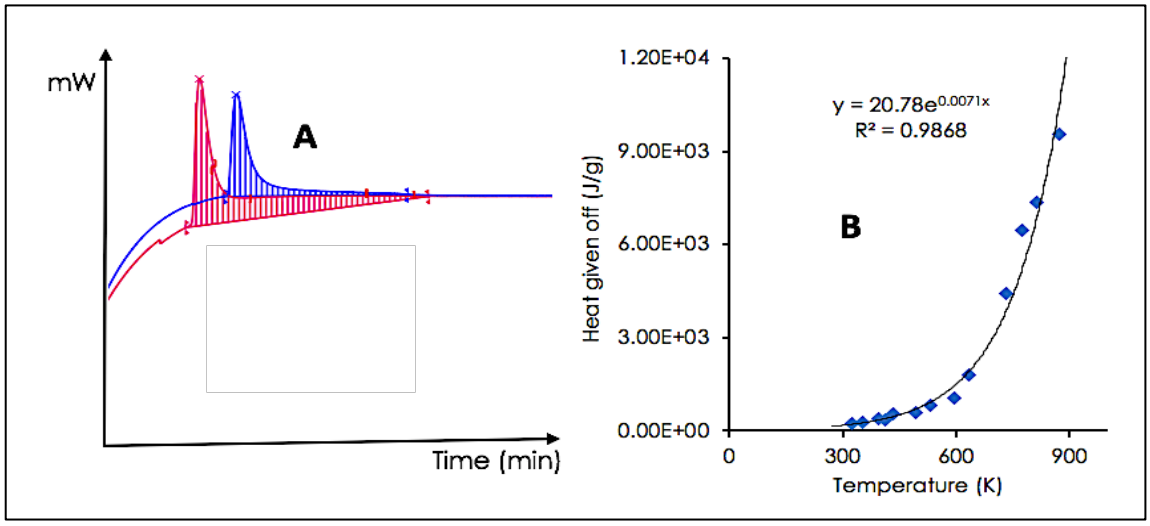

Figure 4-6: Exothermicity of oxygen adsorption. A – Peak integrals (blue at 50 °C and red at 160 °C). B – Heat given off at different temperatures.

4.3.3 Free radicals on the charcoal surface

4.3.3.1 Radicals on fresh and cleaned charcoal

Sample G was used in this section. Manufacturing charcoal at 500 °C makes it achieve maximum reactivity and free radicals [31]. Chang *et al* [8] observed that the normalized absorption peak area of the ESR spectrum of fossil coals increased with pyrolysis temperature (range 100 – 500 °C) due to the greater abundance of active sites available for oxidation and hence an increase in

the radical concentration. In the same study, the g-values decreased with temperature, implying that the complexity of the radicals formed during carbonization decreased with temperature [8]. High temperatures reduce the number of attached groups (oxygen and nitrogen among others) and the decreasing g-values coincide with a decrease in the number of hetero atoms for organic radicals. This in turn reduces the electron cloud, leading to a decrease in both the g-value and the spin concentration as temperature increases.

We observed a higher spin concentration for acid-washed charcoal (sample F) than untreated charcoal (sample G), but there were minor changes in the observed g-values (Table 4-4). Similarly, Silbernagel *et al* [32], observed that the electron density of acid-washed fossil coal was higher than that of untreated coal, coinciding with changes in g-value and line width attributed to the interaction between carbon radicals and paramagnetic inorganic constituents that make some carbon radicals unobservable [32].

Our trace element analysis (*Table 4-2*) revealed high levels of potassium, which can limit the concentration of radicals because potassium catalyses the conversion of bridges into char links during pyrolysis thus enhancing cross-linking and reducing char fluidity [9]. The formation of potassium-carbon bonds weakens the carbon-carbon bonds in aromatic rings and facilitates bond breaking at higher temperatures [9]. The line width of the nitrogen pyrolyzed charcoal subsequently exposed to air was 41.8 G because pyrolysis makes the carbon more ordered like graphite. Variations in line width can be caused by the formation of disorganized carbon (producing narrow signals) [9] and organized carbon with conductive electrons (producing broad signals) [7].

Table 4-4: ESR properties of the charcoal samples

Sample	Line width (G)	Spin conc. (spins/g)	g-value
Normal charcoal (G)	11.8	5.29×10^{18}	2.00481
Acid (HCl) washed (F)	11.9	3.49×10^{19}	2.00477
[a]Degassed with air (C)	11.6	7.06×10^{19}	2.00483
Degassed with N_2 and air (A)	41.8	3.75×10^{17}	2.00260

[a]The results are for the main peak.

An extraordinarily high concentration (~10^{20}/cm^3) of the oxygen radicals O^- and O_2^- were formed when ceramics were heated in a dry oxygen atmosphere [33]. The total radical concentration reached 1.7×10^{21}/cm^3 and the authors attributed this to the absorption of oxygen molecules which react with free oxygen to the radicals as follows in eqn. 4-5:

$$O_2 \text{ (atmosphere)} + O_2^- \text{ (system)} \rightarrow O^- \text{ (system)} + O_2^- \text{ (system)} \qquad (4\text{-}5)$$

As shown in *Figure 4-7*, we observed a similar phenomenon in which oxygen was adsorbed onto the charcoal surface, forming radicals with a concentration of 7.06×10^{19} spins/g.

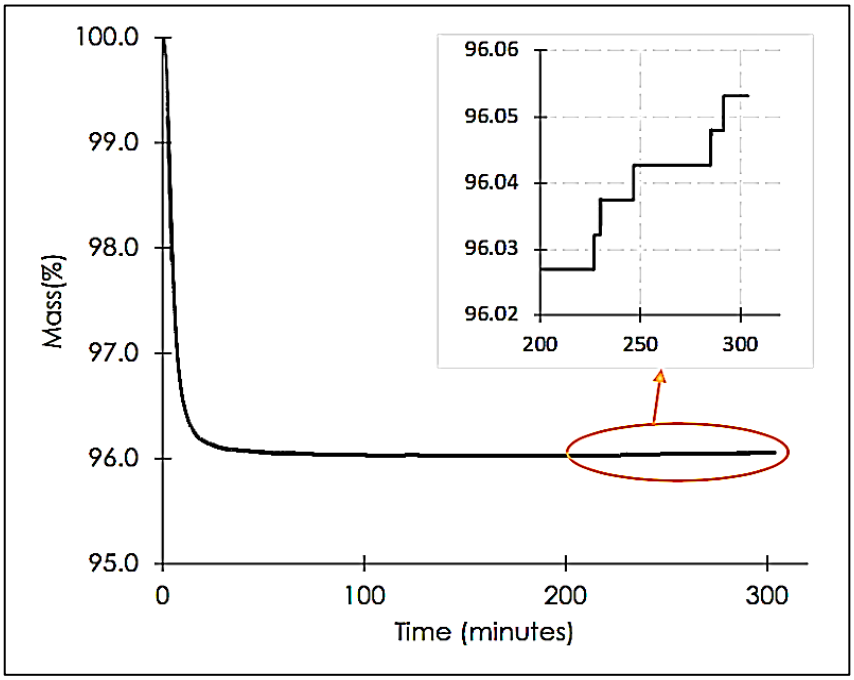

Figure 4-7: Mass gain of sample C following the exposure to air at 100 °C

The rate of adsorption reached its maximum immediately upon the initial exposure of sample A to air, which has previously been described as the early-peak phenomenon [34]. The adsorption rate then decreased with time at low temperatures, but nevertheless continued (*Figure 4-3*). The same observations have been reported by Heinz-Jurgen *at al* [35], for fossil coals and low-temperature wood chars, indicating that oxygen adsorption capacities depend on the time allowed for chemisorption. They observed that even after several days, the weight increase continued. We observed a similar behaviour at temperatures < 250 °C for lilac charcoal.

ESR analysis of sample G showed a single stable radical with a g-value of 2.00481 (*Figure 4-8*). Oxygen-centred radicals have g-values in the range 2.0038 – 2.0047 whereas carbon-centred radicals have g-values in the range 2.0025 – 2.003 [9] and peroxyl radicals have g-values in the range 2.038 – 2.003 [12].

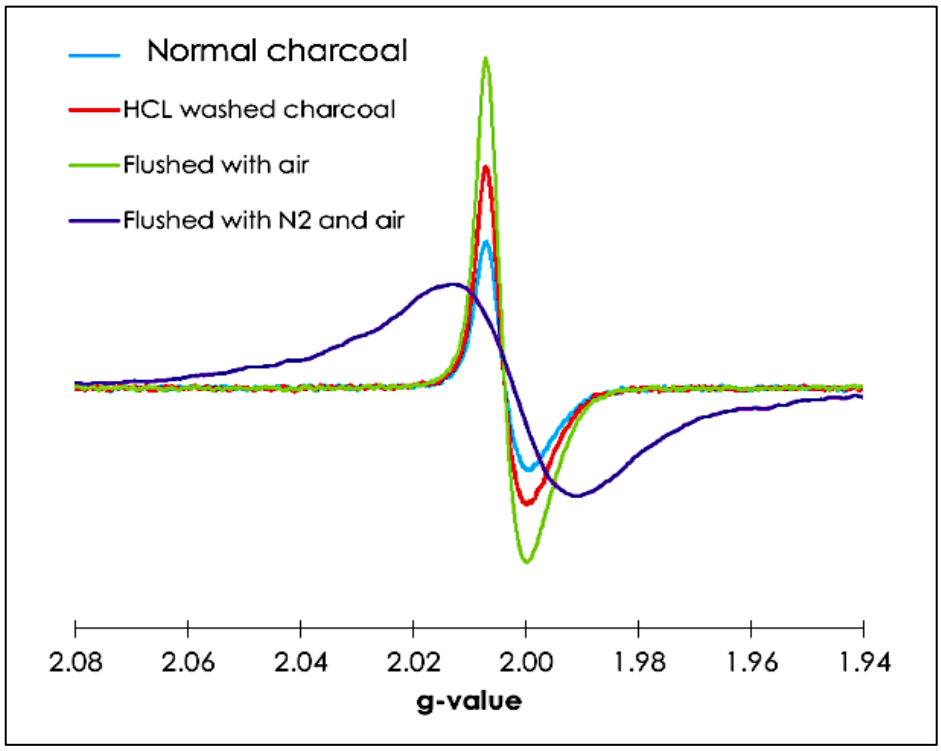

Figure 4-8: Free radical spectrum for normal charcoal (sample G), HCl-washed charcoal (sample F), charcoal flushed with air at 100 °C (sample C) and charcoal pyrolyzed in nitrogen and then flushed with air at 100 °C (sample A).

4.3.3.2 Peroxyl radicals

ESR analysis of normal charcoal (sample G) revealed a single radical which was no longer detected after degassing with nitrogen (sample B) (results not shown). Degassing the samples with nitrogen causes the radicals to be rearranged into non-radical species. However, exposure of the nitrogen-degassed charcoal to air at 100 °C (sample A) formed a different radical (g-value 2.0026), presumably carbon-centred with oxygen heteroatoms. This means that if normal charcoal (sample C) is exposed to air alone at 100 °C, we would expect to observe two radicals. The exposure of normal charcoal (sample C) to air resulted in a slight mass gain (*Figure 4-7*).

ESR analysis of sample C initially showed a single radical with g-value of 2.00483 (*Figure 4-8*), which is similar to the g-value obtained with normal charcoal (sample G). Reducing the noise of the ESR spectrum (by optimising the time constant) for sample C revealed four minor peaks superimposed on the major peak (*Figure 4-9*).

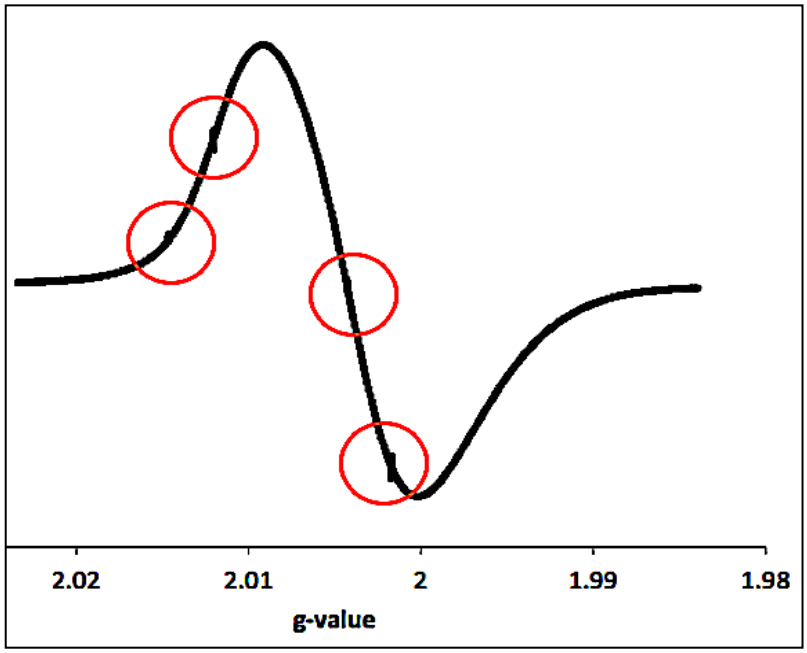

Figure 4-9: Peroxyl radicals (circled in red) detected in sample C are indicated by minor peaks superimposed on the major peak.

We initially assumed that the four peaks represented a single radical with multiple hyperfine line splitting, but this is unlikely according to the rules of hyperfine splitting and pascals triangle [13]. We therefore reduced the noise and magnified the spectrum further to observe the superimposed peaks more clearly (*Figure 4-10*).

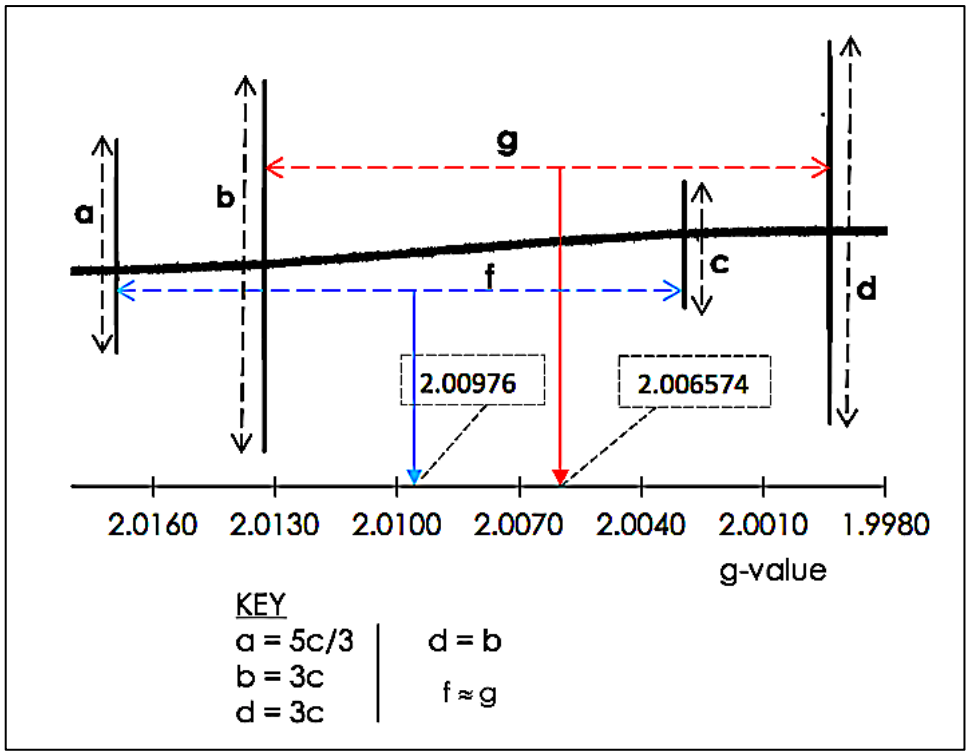

Figure 4-10: The ESR spectrum of the four peroxyl radicals

Assigning spectra to the radicals

Approach one: two peaks represent the same radical

A closer inspection of *Figure 4-10* revealed that the two high-intensity peaks appear to belong to one radical (g-value 2.00657) because they have approximately equal heights and constitute a 1:1 hyperfine split. Secondly, the peak-to-peak distance (hyperfine coupling constant) of the high-intensity peaks (average 2.142 mT) was similar to that of the low-intensity peaks (average 2.088 mT). This implies that the high-intensity radicals could be

precursors of the low-intensity radicals. The low-intensity radicals (g-value 2.00976) are likely to be complex diradicals with many oxygen heteroatoms. We also observed that the intensity of the peaks was not the same during replicate runs, even under the same experimental conditions, but they oscillated within a defined magnitude (Appendix B-1). This shows how difficult it can be to analyse the peroxyl radical spectrum. However, pulse oscillations of the microwave frequency in the kilohertz (kHz) range are likely to explain these spectral changes, because they cause pulsed changes in the intensities at reference points. Because the low-intensity peroxyl radicals were superimposed on the major peak, small changes in the normal pulse intensity affected the intensity of replicate runs under the same conditions, creating unevenness in the intensities of the peaks and distortions in the observed spectra (Figures B-2 to B-5, Appendix B).

Approach two: each peak is an independent radical

The difference in the average hyperfine coupling distances between the high-intensity peaks and the low-intensity peaks (see above) resulted in a standard deviation between these two values of 0.270 mT. A two-tailed t-test distribution comparing the replicate hyperfine coupling distance values for the high-intensity and low-intensity radicals returned a *p*-value of 0.00044525 with a 95 % confidence interval. This implies that the hyperfine coupling distances values are statistically different. Accordingly, each peak could represent a unique radical. The g-values and the peak heights of the peroxyl radicals are summarized in *Table 4-5*.

Table 4-5: Measurable parameters for the peroxyl radicals*

	Run	1	2	3	4	Mean±SD
Centre field (mT)	MW freq. (MHz)	8966.321	8966.308	8966.305	8966.303	
317.369	[α]PH ([γ]a.b)	1001	708	683	966	839.5±144.8
	g-value	2.015499	2.015502	2.015502	2.015507	2.015502±0.000003
318.105	PH (a.b)	1464	1187	1213	1373	1309.3±114.3
	g-value	2.013806	2.013777	2.013798	2.013783	2.013791±0.000011
319.984	PH (a.b)	775	1041	807	893	879±103
	g-value	2.002007	2.002015	2.002014	2.002016	2.002013±0.000003
320.679	PH (a.b)	1271	1480	1473	1262	1371.5±105.1
	g-value	2.000685	2.00067	2.000668	2.000642	2.000666±0.000015

*These values are based on the assumption that each peak belongs to an independent radical.
[γ]a.b – arbitrary value. [α]PH – Peak Height

Simulation of peroxyl radical spectra.

In several studies involving the analysis of peroxyl radicals [10] the authors did not produce clearly defined spectra, making interpretation difficult [11], [36]. Although we likewise found our spectra difficult to interpret, we attempted to reproduce them using the isotropic simulation software JEOL v2000, assuming that the low-intensity peaks represented one radical and the high-intensity peaks another. Having expanded the individual peaks as described above (Figures B-2 to B-5, Appendix B) we used the software to simulate the ESR spectrum for the low-intensity peroxyl radicals, revealing the 1:2:1 hyperfine splitting pattern shown in *Figure 4-11*. We assumed that the high-intensity radicals are precursors of the low-intensity radicals and that both have the same characteristic parent structure, with the low-intensity radicals having undergone further oxidation to gain further heteroatoms (hence the higher g-vale). The high-intensity peaks are formed by hyperfine interaction, i.e. simpler spectra combining to form a more complex spectrum (data not shown).

Reaction mechanisms forming peroxyl radicals

Charcoal contains multiple functional groups and heteroatoms linked either to the aromatic structure or bridges [37]. The general structure of lilac charcoal is likely to be similar to that proposed elsewhere [27], including the presence of aromatic groups, carbonyl carbonates, carboxylic acids, lactones (with four or five carbons), ether bridges, cyclic ethers, cyclic anhydrides (with five or six carbons), quinones, phenols, alcohols, and ketone groups, as shown in *Figure 4-12*.

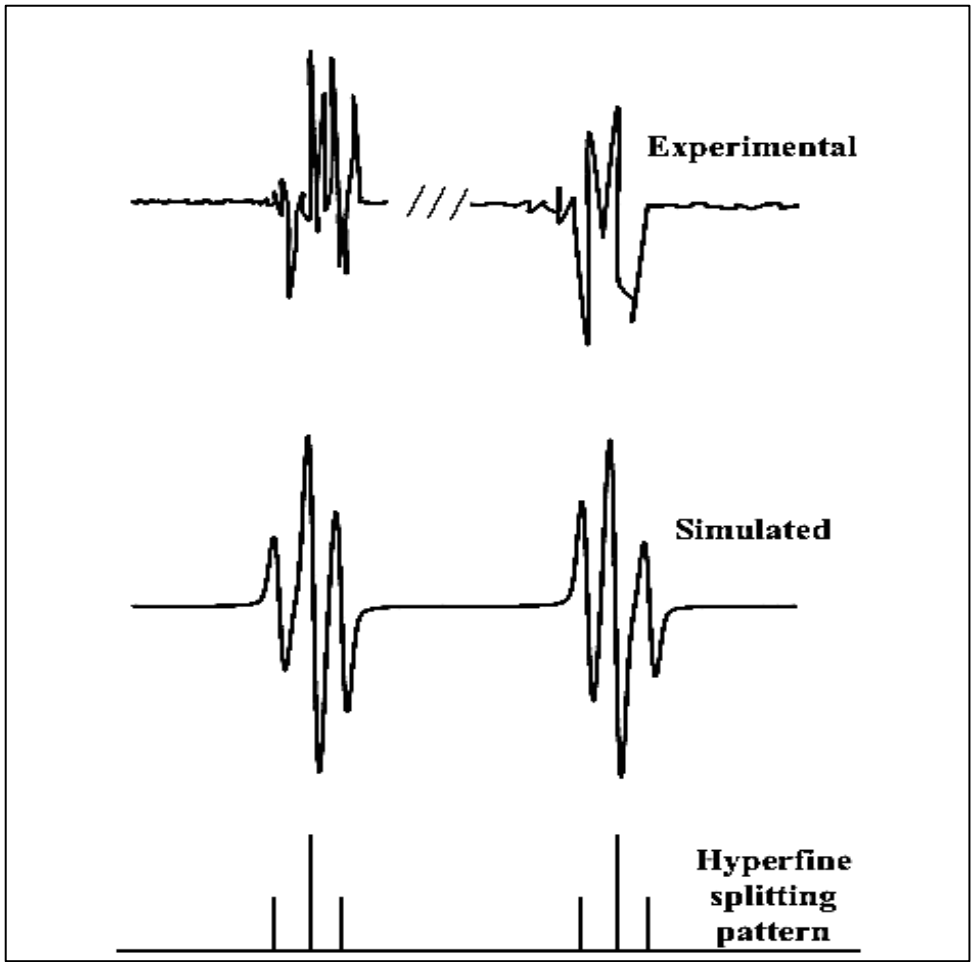

Figure 4-11: Simulation of the low-intensity peroxyl radicals

We found that peroxyl radicals do not form on activated carbons or cleaned carbon surfaces (i.e. carbon surfaces on charcoal that has been pyrolyzed in a nitrogen atmosphere to remove all the oxygen and nitrogen-containing functional groups as volatiles as well as converting free radicals into neutral groups). We cleaned the charcoal surfaces by pyrolysis in nitrogen and cooling in nitrogen to the desired temperature. Oxygen was adsorbed following exposure to air as explained above but ESR spectroscopy revealed radical species other than peroxyl radicals.

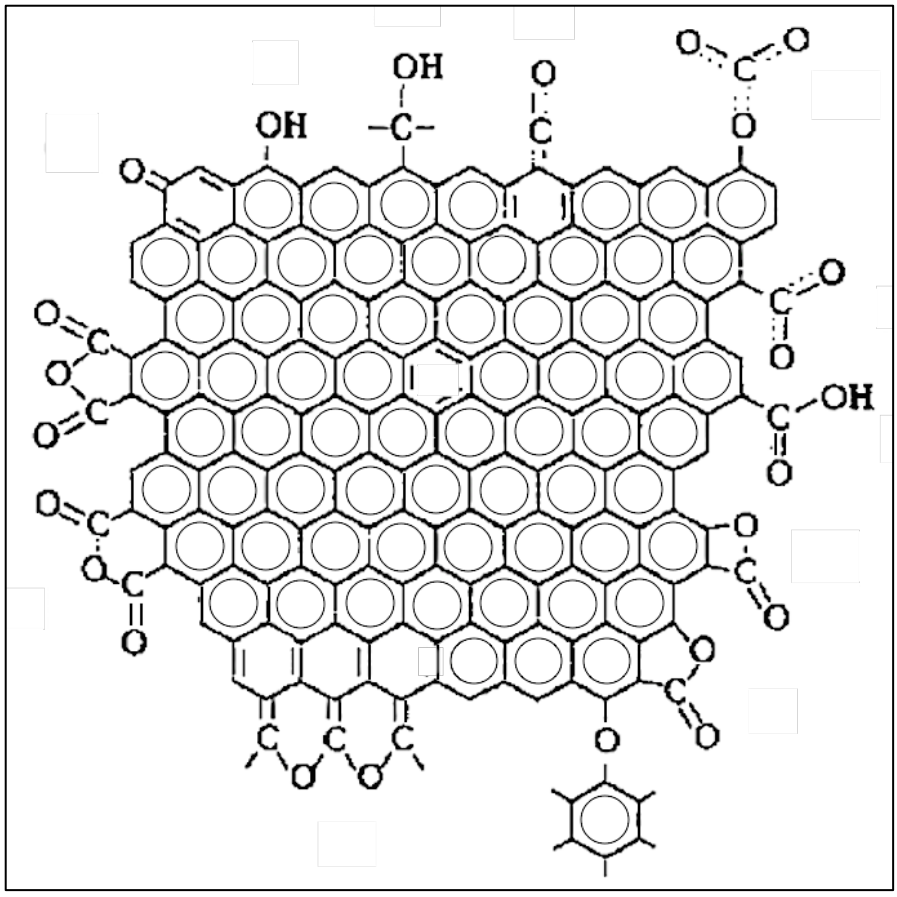

Figure 4-12: Structure of charcoal showing functional groups, adapted from [27].

We propose that the peroxyl radicals are formed by the abstraction of hydrogen from hydroxyl groups within the carbon matrix. These types of peroxyl radicals are formed from carboxylic acids, phenols and alcohols. Other peroxyl radicals are formed when oxygen reacts with carbon-centred free radicals or exposed active carbons attached to other functional groups such as ether bridges and cyclic ethers. Based on the general structure of charcoal presented in *Figure 4-12*, and the proposed functional groups discussed above, the plausible reactions in the solid state are summarized in *Figure 4-13*.

Oxygen can form complexes accompanied by a significant increase in the O-O interaction distance and a corresponding decrease in the v(O-O) vibrational stretching frequency. This may reflect the transfer of electrons from the carbon into the anti-bonding orbitals of O_2 to form the O-O bond [38].

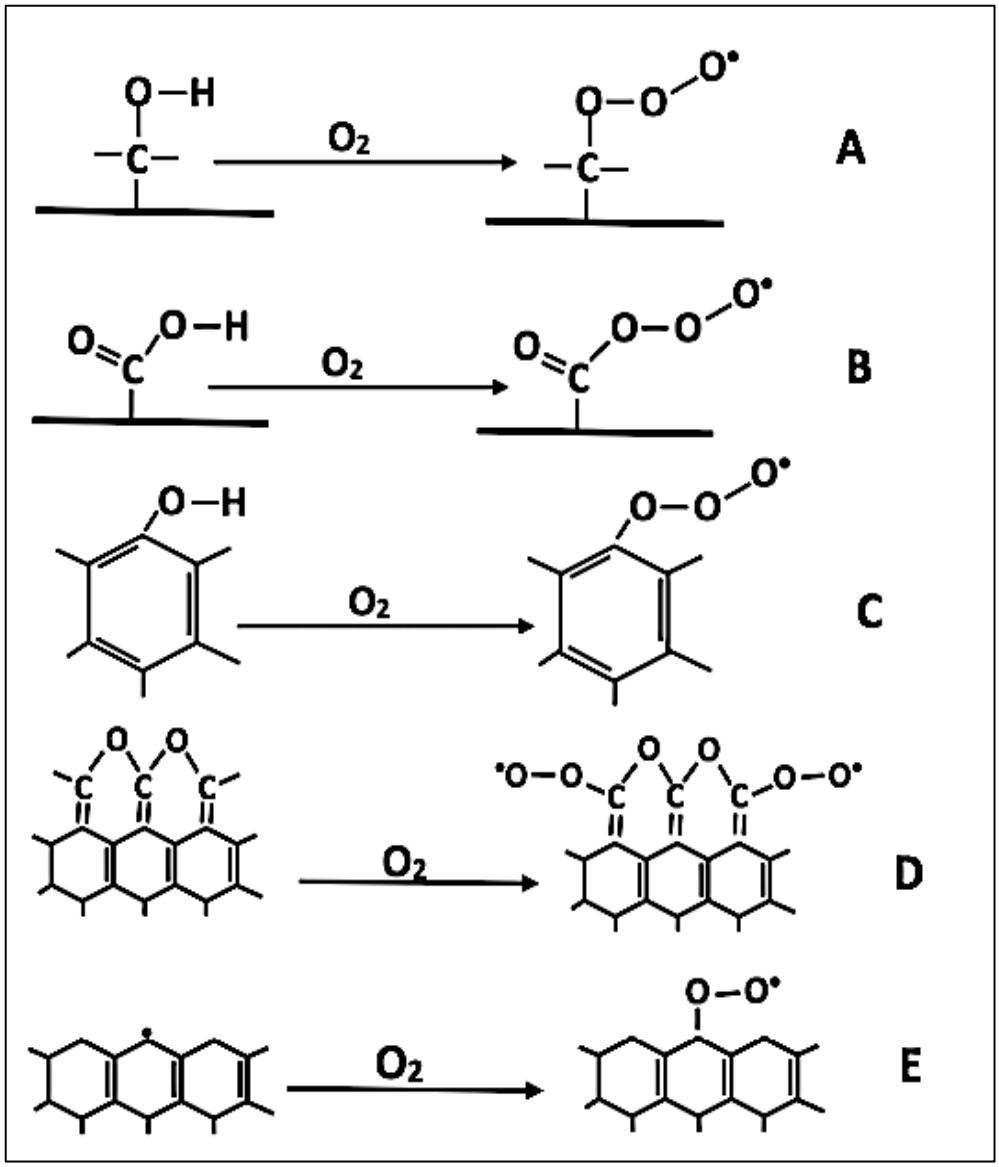

Figure 4-13: Proposed reaction for the formation of peroxyl radicals (potential intermediate steps omitted).

4.3.3.3 Activated and semi-activated carbons

The normal charcoal was degassed with nitrogen while heating from 30 to 750 °C and then cooled in nitrogen to 30 °C (sample B). ESR analysis of this sample (results not shown) did not reveal the presence of radicals. During the degassing process, oxygen and nitrogen species [27] are lost from the char surfaces as volatile gaseous products, and the carbon-carbon centred radicals recombine to form non-radical products [9]. Other volatiles that are

evolved include radicals such as •OH, •CH_3 and •OCH_3. During the loss of volatile matter, the volatile matter/fixed carbon ratio declines as aromaticity increases [37].

We analysed the activated carbons (sample E) by ESR spectroscopy for comparison and detected no signals at all, even after degassing in nitrogen and exposure to air for 30 min at 5 mL/min and 100 °C. The same results were observed when lilac charcoal was pyrolyzed in nitrogen to 750 °C and cooled in nitrogen to room temperature (sample B), confirming the unreactive nature of activated carbons in the presence of weak oxidants like air at low temperatures. Similarly, DRIFT spectroscopy revealed no bands even though gasification was occurring when Saran carbon (vinylidene chloride/vinyl chloride copolymer) was activated in hydrogen and then exposed to 20 % O_2, implying that no oxygen functional groups were formed [27]. Activating charcoal removes impurities and also removes oxygen from the carbon surface [27].

The adsorption of oxygen by the acid-washed charcoal (sample F) was limited compared to the un-acid-washed charcoal (sample G). When pyrolyzed in nitrogen and then exposed to air at 100 °C, the un-acid-washed charcoal (sample A), registered an ESR signal with a clear spectrum (after magnification). When the same treatment was applied to acid-washed charcoal no ESR signal was detected, implying a weaker adsorption capacity for oxygen in the air, leading to fewer radicals. Mineral elements appear to enhance the ability of charcoal to absorb materials that form radicals. For example, activated carbons washed with HCl did not absorb NO_2 and H_2S efficiently, possibly because the reaction between the molecules of the adsorbed gas and metal oxides in the mineral fraction led to the formation of nitrates and sulfides [39]. Our observation that fresh charcoal can adsorb more oxygen and form more radicals than acid-washed charcoal may reflect the

same phenomenon, involving the formation of mineral oxide linkages within the pore structure of the charcoal.

The summary of the free radical analysis is shown in *Table 4-6* below.

Table 4-6: Summary of free radical analysis

Sample	Normal radical	Peroxyl radical
A	[a]OK	[b]X
B	X	X
C	OK	OK
D	[c]N/A	N/A
E	X	X
F	OK	X
G	OK	X

[a]OK – radical detected, [b]X – no radical detected, [c]N/A – Not applicable

Summary & Conclusions

In this study, we characterized lilac charcoal to determine its reactivity, oxygen adsorption capacity, and ability to form free radicals:

- Lilac is a highly reactive material with low ignition temperatures (250 – 300 °C).
- It burns quickly within a narrow combustion temperature range (300 – 520 °C).
- The production of lilac charcoal from woody biomass via pyrolysis produces large amounts of free radicals, in the order of 10^{18} spins/g.
- However, acid washing (with HCl in our experiments) or flushing with nitrogen at high temperatures removes and/or inactivates the free radicals.
- Exposure of lilac charcoal to air forms persistent oxygen-centred free radicals.
- The ability of lilac charcoal to form persistent peroxyl radicals combined with the low ignition temperatures and narrow oxidation temperature range can be exploited for downstream applications such as carbon catalysis, the manufacture of highly reactive materials, and the

adsorption of specific target organic species. Lilac charcoal can also be used for co-firing applications.

Acknowledgments

The authors thank the Gas Safety Trust of the UK, the Boat Safety Scheme of the UK and Katie Haines Memorial Trust of the UK for sponsoring this work. We also acknowledge the experimental support provided by Nathan Flood, Ian Wilson, Peter Wilkinson, Nicola Darcy and Adrian Mustey.

References

[1] A. Zolin, A. Jensen, P. A. Jensen, F. Frandsen, and K. Dam-Johansen, "The Influence of Inorganic Materials on the Thermal Deactivation of Fuel Chars," *Energy & Fuels*, vol. 15, no. 5, pp. 1110–1122, Sep. 2001.

[2] R. E. Mitchell, P. A. Campbell, and L. Ma., "Characterization of coal and biomass conversion behaviors in advanced energy systems," in *GCEP Research Symposium*, 2005, pp. 1–13.

[3] M. Morin, S. Pécate, and M. Hémati, "Kinetic study of biomass char combustion in a low temperature fluidized bed reactor," *Chem. Eng. J.*, vol. 331, no. August, pp. 265–277, 2018.

[4] F. X. Collard and J. Blin, "A review on pyrolysis of biomass constituents: Mechanisms and composition of the products obtained from the conversion of cellulose, hemicelluloses and lignin," *Renew. Sustain. Energy Rev.*, vol. 38, pp. 594–608, 2014.

[5] J. Dollimore, C. M. Freedman, B. H. Harrison, and D. F. Quinn, "Surface complexes on carbon-I. A preliminary investigation of surface oxygen complex on a non-graphitic carbon," *Carbon N. Y.*, vol. 8, no. 5, pp. 587–596, 1970.

[6] M. J. Antal and M. Grønli, "The Art, Science, and Technology of Charcoal Production," *Ind. Eng. Chem. Res.*, vol. 42, no. 8, pp. 1619–1640, 2003.

[7] J. Bourke, M. Manley-Harris, C. Fushimi, K. Dowaki, T. Nunoura, and M. J. Antal, "Do all carbonized charcoals have the same chemical structure? 2. A model of the chemical structure of carbonized charcoal," *Ind. Eng. Chem. Res.*, vol. 46, no. 18, pp. 5954–5967, 2007.

[8] T. Chang, Q. Guo, H. Hao, B. Wu, and Y. Yang, "Formation of radicals in coal pyrolysis examined by electron spin resonance," *AIP Adv.*, vol. 7, no. 9, 2017.

[9] A. Trubetskaya, P. A. Jensen, A. D. Jensen, P. Glarborg, F. H. Larsen, and M. L. Andersen, "Characterization of free radicals by electron spin resonance spectroscopy in biochars from pyrolysis at high heating rates

and at high temperatures," *Biomass and Bioenergy*, vol. 94, pp. 117–129, 2016.
[10] K. U. Ingold, "Peroxy Radicals," *Acc. Chem. Res.*, vol. 2, no. 1, p. 5975, 1969.
[11] U. Molteni, F. Bianchi, F. Klein, I. El Haddad, C. Frege, M. J. Rossi, J. Dommen, and U. Baltensperger, "Formation of highly oxygenated organic molecules from aromatic\ncompounds," *Atmos. Chem. Phys. Discuss.*, no. December, pp. 1–39, 2016.
[12] D. C. McCain and W. E. Palke, "Theory of electron spin g-values for peroxy radicals," *J. Magn. Reson.*, vol. 20, no. 1, pp. 52–66, 1975.
[13] V. Chechik, E. Cater, and D. Murphy, *Electron Paramagnetic Resonance*. Oxford, U.K: Oxford University Press, 2016.
[14] A. Nyombi, M. Williams, and R. Wessling, "Determination of kinetic parameters and thermodynamic properties for ash (Fraxinus) wood sawdust slow pyrolysis by thermogravimetric analysis," *Energy Sources, Part A Recover. Util. Environ. Eff.*, vol. 40, no. 22, pp. 2660–2670, Aug. 2018.
[15] H. E. Kissinger, "Variation of peak temperature with heating rate in differential thermal analysis," *J. Res. Natl. Bur. Stand. (1934).*, vol. 57, no. 4, p. 217, 1956.
[16] S. S. Idris, N. A. Rahman, K. Ismail, A. B. Alias, Z. A. Rashid, and M. J. Aris, "Investigation on thermochemical behaviour of low rank Malaysian coal, oil palm biomass and their blends during pyrolysis via thermogravimetric analysis (TGA)," *Bioresour. Technol.*, vol. 101, no. 12, pp. 4584–4592, 2010.
[17] M. Heydari, M. Rahman, and R. Gupta, "Kinetic study and thermal decomposition behavior of lignite coal," *Int. J. Chem. Eng.*, vol. 2015, 2015.
[18] F. H. Joseph and W. A. Leo, "A quick, direct method for the determination of activation energy from thermogravimetric data," *Polym. Lett.*, vol. 4, no. 5, pp. 323–328, 1966.
[19] T. Ozawa, "A New Method of Analyzing Thermogravimetric Data," *Bull. Chem. Soc. Jpn.*, vol. 38, no. 11, pp. 1881–1886, 1965.
[20] J. Zsakó and H. E. Arz, "Kinetic analysis of thermogravimetric data," *J. Therm. Anal.*, vol. 6, no. 6, pp. 651–656, 1974.
[21] S. Mallakpour and M. Taghavi, "The Accuracy of Approximation Equations in the Study of Thermal Decomposition Behaviour of Some Synthesized Optically Active Polyamides," *Iran. Polym. J. (English Ed.*, vol. 18, no. 11, pp. 857–872, 2009.
[22] E. Apaydin-Varol and A. E. Pütün, "Preparation and characterization of pyrolytic chars from different biomass samples," *J. Anal. Appl. Pyrolysis*, vol. 98, pp. 29–36, 2012.
[23] K. Crombie, O. Mašek, S. P. Sohi, P. Brownsort, and A. Cross, "The effect of pyrolysis conditions on biochar stability as determined by three methods," *GCB Bioenergy*, vol. 5, no. 2, pp. 122–131, 2013.
[24] A. Raj, S. Y. Yang, D. Cha, R. Tayouo, and S. H. Chung, "Structural effects on the oxidation of soot particles by O2: Experimental and theoretical study," *Combust. Flame*, vol. 160, no. 9, pp. 1812–1826, 2013.

[25] P. J. F. Harris, "Fullerene-like models for microporous carbon," *J. Mater. Sci.*, vol. 48, no. 2, pp. 565–577, Jan. 2013.
[26] R. W. Froberg, P. Corporation, and R. Essenhigh, "Reaction order and activation energy of carbon oxidation during internal burning," *Symp. Combust.*, vol. 17, no. 1, pp. 179–187, 1979.
[27] E. P. Fanning and M. A. Vannice, "A Drifts Study of the Formation of Surface Groups on Carbon By Oxidation," *Carbon N. Y.*, vol. 31, no. 5, pp. 721–730, 1991.
[28] J. L. Figueiredo and M. F. R. Pereira, "The role of surface chemistry in catalysis with carbons," *Catal. Today*, vol. 150, no. 1–2, pp. 2–7, 2010.
[29] M. Ciobanu, A. M. Lepadatu, and S. Asaftei, "Chemical and Electrochemical Studies of Carbon Black Surface by Treatment with Ozone and Nitrogen Oxide," in *Proceedings of the International Conference on Diamond and Carbon Materials Chemical*, 2016, vol. 3, pp. S252–S257.
[30] K. C. Salooja, "Studies of combustion processes leading to ignition in hydrocarbons," *Combust. Flame*, vol. 9, no. June, pp. 121–129, 1965.
[31] T. Urbanski, S. Benbenek, S. Bedynski, and A. Wasilewski, "Free radicals in charcoal and the combustion of compositions containing charcoal," *Explosivstoffe*, vol. 1, pp. 9–11, 1970.
[32] B. G. Silbernagel, L. A. Gebhard, R. A. Flowers, and J. W. Larsen, "Demineralization effects on the EPR properties of Argonne premium coals," *Energy & Fuels*, vol. 5, no. 4, pp. 561–568, 1991.
[33] H. Hosono and H. Masahiro, "Functional Cultivation of Transport Oxides Utilising Natural and Artificial NAnostructures," in *Nanomaterials: From Research to Application*, 2006, pp. 27–30.
[34] P. A. Campbell and R. E. Mitchell, "The impact of the distributions of surface oxides and their migration on characterization of the heterogeneous carbon-oxygen reaction," *Combust. Flame*, vol. 154, no. 1–2, pp. 47–66, 2008.
[35] M. Heinz-Jurgen and H. van H. Karl, "Porosity and Thermal Reactivity," in *Porosity in Carbons*, 1st ed., London, 1995, pp. 131–148.
[36] S. Richters, H. Herrmann, and T. Berndt, "Different pathways of the formation of highly oxidized multifunctional organic compounds (HOMs) from the gas-phase ozonolysis of β-caryophyllene," *Atmos. Chem. Phys.*, vol. 16, no. 15, pp. 9831–9845, 2016.
[37] B. Miller and D. Tillman, *Combustion Engineering Issues for Solid Fuel Systems*, 1st ed. Califonia: Academic Press, 2008.
[38] N. Greenwood, N and A. Earnshaw, "Oxygen," in *Chemistry of the Elements*, 2nd ed., N. Greenwood, N and A. Earnshaw, Eds. London: Reed Educational and Professional Publishing, 1997, pp. 600–640.
[39] P. Nowicki, "The effect of mineral matter on the physicochemical and sorption properties of brown coal-based activated carbons," *Adsorption*, vol. 22, no. 4–6, pp. 561–569, 2016.

Chapter 5: TOXIC EMISSIONS FROM SMOULDERING COMBUSTION OF WOODY BIOMASS AND DERIVED CHAR WITH A CASE STUDY OF CO BUILD-UP IN AN ISO CONTAINER

The work contained in this chapter has been published in *Energy Sources, Part A: Recovery, Utilization, and Environmental Effects Journal*.

Citation: A. Nyombi, M R Williams & R. Wessling (2019): Toxic emissions from smouldering combustion of woody biomass and derived char with a case study of CO build-up in an ISO container. Energy Sources, Part A: Recovery, Utilization, and Environmental Effects.

DOI: https://doi.org/10.1080/15567036.2019.1623348

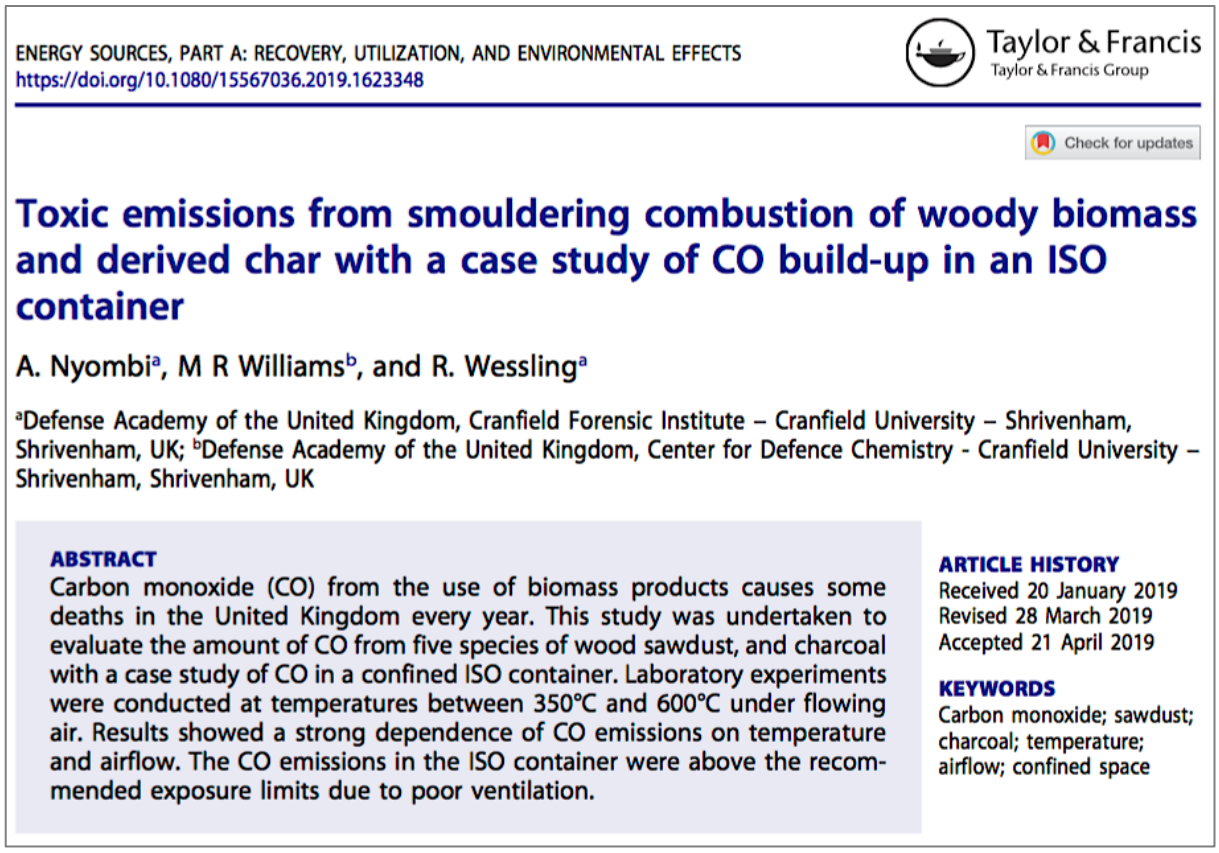

ENERGY SOURCES, PART A: RECOVERY, UTILIZATION, AND ENVIRONMENTAL EFFECTS
https://doi.org/10.1080/15567036.2019.1623348

Taylor & Francis
Taylor & Francis Group

Check for updates

Toxic emissions from smouldering combustion of woody biomass and derived char with a case study of CO build-up in an ISO container

A. Nyombi[a], M R Williams[b], and R. Wessling[a]

[a]Defense Academy of the United Kingdom, Cranfield Forensic Institute – Cranfield University – Shrivenham, Shrivenham, UK; [b]Defense Academy of the United Kingdom, Center for Defence Chemistry - Cranfield University – Shrivenham, Shrivenham, UK

ABSTRACT

Carbon monoxide (CO) from the use of biomass products causes some deaths in the United Kingdom every year. This study was undertaken to evaluate the amount of CO from five species of wood sawdust, and charcoal with a case study of CO in a confined ISO container. Laboratory experiments were conducted at temperatures between 350°C and 600°C under flowing air. Results showed a strong dependence of CO emissions on temperature and airflow. The CO emissions in the ISO container were above the recommended exposure limits due to poor ventilation.

ARTICLE HISTORY
Received 20 January 2019
Revised 28 March 2019
Accepted 21 April 2019

KEYWORDS
Carbon monoxide; sawdust; charcoal; temperature; airflow; confined space

Toxic Emissions from Smouldering Combustion of Woody Biomass and Derived Char with a Case Study of CO Build-Up in an ISO Container

Highlights

- CO emissions were quantified from wood sawdust and charcoal
- Accumulation of CO in confined spaces was simulated using an ISO container
- Temperature and airflow both affected the emissions of CO
- CO emissions from sawdust were in the range 98.8 to 258.0 mg/g
- CO emissions from charcoal were in the range 98.1 to 495 mg/g
- CO emissions in the ISO container increased with decrease in aeration and distance above the container floor.

Abstract

Carbon monoxide (CO) from the use of biomass solid fuels has caused several fatalities in the United Kingdom. This study was undertaken to evaluate the amount of CO from five species of wood sawdust, and charcoal with a case study of CO in a confined ISO container. Laboratory experiments were conducted at temperatures between 350 and 600 °C under flowing air. Results showed a strong dependence of CO emissions on temperature and airflow. Sawdust emitted CO levels as high as 298 mg/g while charcoal released 495 mg/g as highest. The CO emissions recorded in the ISO container were above the recommended exposure limits due to poor ventilation.

5.1 Introduction

Carbon monoxide (CO) produced by the combustion of carbonaceous solid fuels in air can accumulate in confined spaces and interfere with the human oxygen-carrying capacity of blood [1]. It is a potent yet odourless asphyxiant, with levels as low as 5000 ppm causing death in less than 30 min. In Denmark, between 2008 and 2012, there was approximately one accidental death per year from the burning of charcoal indoors [2]. In the UK, CO/gas safety records indicate that 3 % of the 719 deaths due to unintentional CO poisoning between 1995 and 2016 were caused by barbeques [3]. In 2012, a young girl died in a tent in The New Forest [4], and Nicholas Holmes also died in a camper van in the same area and year [5]. Hannah Thomas Jones died in Shropshire in 2013 from the same causes [6]. There have been several other reports of unintentional/suicide carbon monoxide poisoning in confined spaces from biomass usage [7] [8] [9] [10] [11] [12]. One of the authors of this article was the survivor of a similar accident, in which his partner died [13]. In this incident, the couple was convinced that the fire was out when they took the barbeque into their tent. This tragic accident was the event that prompted the studies described in this article.

Ideally, the combustion products of carbonaceous fuels would be entirely converted to CO_2, moisture and other harmless products at all temperatures because these are far less toxic than CO and the combustion reaction would be thermodynamically more efficient. The relative amounts of CO released by solid fuels during combustion can be influenced by the combustion temperature and by the amount of oxygen in the air. Solid fuels like sawdust and charcoal burn at their surfaces, where fuel-rich conditions predominate and the amount of air (oxygen) is likely to be insufficient for complete combustion [14]. The fuels generally reach temperatures of 700 – 800 °C during natural combustion. However, more literature and information is needed

about the effects of mid-level temperatures (300 – 600 °C) on the emission of CO from burning sawdust and charcoal.

Compressed sawdust briquettes have found wide applications in domestic and industrial applications as alternatives/supplements to wood logs, charcoal and fossil fuels [15], [16]. Derived from wood waste materials, wood sawdust briquettes are easy to make with simple technologies and low production costs [17], [18]. Wood waste in UK constituted 1.645 million tonnes in 2018 while packaging materials (paper & cardboard) constituted 4.749 million tonnes. Wood constituted 1.31 million tonnes in 2016 (Department for Environmental Food & Rural Affairs – DEFR - Government Statistical services) [19]. An estimated 10 million tonnes of 'post-farm gate' food waste is thrown out across the UK every year, of which only 1.8 million tonnes was recycled as per 2016 [19]. Forestry waste and agricultural wastes [20] are also good raw materials for making compressed sawdust logs/briquettes. Conversion of such carbonaceous materials to useful energy is a viable solution, to fill the energy gap left by the declining fossils as well as reducing the wastes sent to landfills and minimising deforestation.

The use of raw biomass materials for heating in fireplaces has been ongoing for many years since the invention of fire. The use of wood boilers since the 1970s and subsequent developments until today saw a remarkable stride in the utilisation of biomass materials in homes [21], [22]. However, the combustion of such carbonaceous materials emits several pollutants of which CO and CO_2 constitute over 80 % of the total emissions [23].

Quantifying the emissions from raw biomass combustion is vital to assess the burden against which sustainable solutions can be sought to minimise the danger of human intoxication especially from CO. Much as acute exposure to CO emissions from raw carbonaceous waste has been reported [24], [25], there is continuous exposure to chronic levels of pollutants [26]. Several studies

have analysed CO emissions from biomass materials: Bhattacharya *et al*. [27] compiled the data for emissions of CO from wood used in developing countries and the emission values were in the range 50 – 300 g/kg. However, some portable wood burning stoves [28] were reported to be efficient at minimising CO emissions to as low as 0.3 – 1.6 mg/g.

Much as wood and wood sawdust are used extensively, the derived product – charcoal, has found even more wide application due to high energy content, less smoke, easy of ignition and transport among other advantages. However, since the elemental carbon is more concentrated in charcoal than wood logs or wood sawdust, the amounts of CO emitted from incomplete combustion of charcoal are considerably higher. In one investigation of CO emissions from indoor barbecue charcoal, the authors tested temperatures in the range 450 – 550 °C with linear air flow rates of 10 and 20 L/s in a tube furnace [29]. In their study, temperature had no significant influence on CO emissions during the combustion of charcoal, but the effect of air flow was not discussed. A comparison of emissions from flaming and smouldering biomass and other solid fuels revealed that smouldering fuel produces more CO than flaming fuel [30]. An analysis of the emissions from coal braziers revealed that high ventilation rates reduce the levels of CO and other emissions from burning coal [31].

Several studies have been carried out to investigate CO emissions from charcoal under normal combustion conditions. Ojima [32] investigated the rate of CO generation from burning charcoal to determine the ventilation required in a room to maintain the CO levels below the Japanese national threshold. Evans and Emmons [33] produced an equation for burning charcoal which linked the CO/CO_2 ratio to temperature.

The desire to minimise heat loss in confined spaces has resulted in embracing double glazed window or door houses as a new fashion. This has its own

drawbacks: combustion pollutants easily build-up leading to chronic and sometimes acute exposures. For the case of CO, since it is colourless and odourless, the victims are taken unaware with feeling of tiredness, headache, and similar conditions which are related to other ailments. It is natural that when a person gets such feelings, they resort to resting/sleeping. In such a CO environment, the consequences may be fatal or sustaining serious injuries.

Confined spaces usually have incomplete mixing of air [34], [35] and hence pollutants from combustion form different layers with concentrations increasing with height depending on ambient temperature and air buoyancy within the confined space. The longer a solid fuel is burnt in a confined space, the higher the likelihood that CO levels will go beyond the set threshold limit values [36]. Burning barbecue charcoal with ignition enhancers usually produces smoke during the first stages which many users avoid due to unpleasantness, but it usually clears away soon. However, the maximum concentrations of CO are produced during the smouldering phase when there is no smoke [37].

Different organisations have set maximum exposure limits for CO; the WHO [38], [39] has established 100 mg/m^3 (90 ppm) for 15 minutes, 60 mg/m^3 (50 ppm) for 30 minutes, 30 mg/m^3 (25 ppm) for 1 hour, 10 mg/m^3 (10 ppm) for 8 hours. The Occupational Safety and Health Administration (OSHA) permissible exposure limit (PEL) for CO is 50 ppm parts of air (55 mg/m^3) as an 8-hour time-weighted average (TWA) concentration. The National Institute for Occupational Safety and Health (NIOSH) has established a recommended exposure limit (REL) for CO of 35 ppm (40 mg/m^3) as an 8-hour TWA and 200 ppm (229 mg/m^3) as a ceiling. The American Conference of Governmental Industrial Hygienists (ACGIH) has assigned CO a threshold limit value (TLV) of 25 ppm (29 mg/m^3) as a TWA for a normal 8-hour workday and a 40-hour workweek [40],[41].

The main goal of most recent studies has been to facilitate the design of more efficient cooking stoves [42], [43], [44] and ventilation systems [32], the development of standards for stoves [43] and biomass space-heating equipment [45], the comparison of solid fuel emissions [46], the design and building of air samplers, and the development of low-emission combustion technologies. In this study we investigated the effect of temperature and air flow on CO emissions during the mid-temperature smouldering combustion of wood sawdust and wood charcoal in a tube furnace system under flowing air. We also give a detailed case study of CO accumulation in confined space. The aim was to determine in more detail the role of temperature and airflow during the combustion of solid fuels, with the emphasis on CO emissions, during the smouldering phase and the factors influencing CO build-up in confined spaces and the appropriate preventive measures.

5.2 Methodology

5.2.1 Sawdust

The samples were obtained from five different wood species: ash (*Fraxinus Excelsior*), beech (*Fagus Sylvatica*), elder (*Sambucus Nigra*), lilac (*Syringa Vulgaris*), and Hazel (*Corylus Avellana*). These were crushed using a laboratory vibratory pulveriser and sieved through a 210 μm mesh. The samples were dried in an oven at 110 °C overnight and kept in sealed containers for subsequent analysis. The proximate and ultimate analysis for these samples are shown in *Table 5-1*. The calorific values were determined using a method described elsewhere [47]. For determination of carbon monoxide (CO) emissions, triplicates of 200 mg samples were pyrolysed under air at temperatures between 300 – 450 °C using a method described in our previous work [48]. The duration of the experiments varied between 5 – 7 minutes. The experiments were terminated when the data logger registered zero concentration for CO

meaning that the concentrations were below the detection limit of the sensor. The triplicates for each parameter were averaged to give a single data set.

5.2.2 Charcoal

The char samples were prepared in the laboratory in a furnace at 500 ◦C isothermal temperature for four hours. Upon cooling, the charcoal samples were ground to fine powder using an Essa LM2 pulverising mill and were sieved through a 210 µm mesh before drying in an oven at 105 °C and storing in a sealed container. The moisture content, volatile matter, fixed carbon and residual ash were determined as per the method described in our previous work [49].

For determination of carbon monoxide (CO) emissions, triplicates of 200 mg samples were heated under air at temperatures between 350 – 600 ◦C using a method previously described in our previous work [48].

Table 5-1: Ultimate, proximate analysis and heating values of the samples

Sample name	Ultimate analysis (wt%)				Proximate analysis (wt%)				HHV[e](MJ/kg)	Source
	N	C	H	O*	M[a]	VM[b]	FC[c]	RA[d]		
Lilac wood	0.30	49.19	6.63	43.87	5.8	73.2	19.5	1.5	19.15	This study
Ash wood	0.35	49.12	6.64	43.89	5.3	71.0	20.6	3.1	19.12	This study
Ash tree	<0.1	48.9	5.9	44.9	7.6	86.8	12.3	0.9	17.23	[50]
Hazel wood	0.51	48.41	6.60	44.48	4.9	75.7	18.2	1.2	18.75	This study
Elder wood	0.27	48.88	6.49	44.36	6.3	71.7	19.3	2.5	18.86	This study
Beech wood	0.35	49.07	6.67	43.92	5.8	75.8	17.7	0.8	19.12	This study
Lilac char	0.62	83.44	2.74	13.21	3.5	11.7	80.9	4.0	32.18	This study
Ash char	0.49	80.67	2.80	16.04	4.1	13.8	78.2	3.9	30.87	This study
Hazel char	1.08	83.11	2.81	13.00	3.8	12.0	80.5	3.7	32.13	This study
Hazel nut shell	-	75.00	5.50	40.60	-	20.6	77.1	2.3	-	[51]
Elder char	0.49	83.79	2.93	12.79	3.9	11.5	80.6	4.1	32.52	This study
Beech char	0.74	80.58	2.74	15.95	5.2	14.5	75.9	4.3	30.79	This study
Beech wood char	0.30	89.00	1.70	9.00	-	-	-	-	-	[52]
Beech char	-	80.00	2.00	18.00	-	-	-	-	-	[53]
Coal char	1.16	82.74	3.56	12.54	2.0	11.3	80.1	6.5	32.68	This study
Bituminous coal	1.60	81.30	5.30	10.80	14.6	35.2	46.2	4.0	-	[54]
Commercial char	0.25	84.02	2.15	13.58	4.3	9.5	60.4	25.9	31.86	This study
Bagasse char	0.47	79.40	3.60	16.60	-	27.0	64.0	10.5	-	[55]

*Determined by difference, [a]Moisture content, [b]Volatile matter, [c]Fixed carbon, [d]Residual ash, [e]Higher heating value

5.2.3 CO emission computation

The overall amounts of the CO were determined by first calculating the area under the concentration-time curve using eqn. 5-1, and then presenting the data in ppm.s,

$$A_T = \sum_{t_0}^{t_f} t_n \, C_n \qquad (5\text{-}1)$$

where A_T, t_o, t_f, t_n and C_n are the total area under the CO curves, initial time, final time, n^{th} time, and concentration at the n^{th} time, respectively. The total area was then used to calculate the total moles of CO evolved using eqn. 5-2, which involves the air flow rate and molar volume over the time of the experiment.

$$X_i = \frac{A_T Q}{60 V_{rtp} * 10^6} \qquad (5\text{-}2)$$

where X_i, Q and V_{rtp} are the moles of CO, air flow rate, and molar volume at room temperature and pressure, respectively. The CO emissions (mg/g) were calculated by determining the mass of CO (Moles x relative molecular mass x 1000) and dividing it by the dry basis mass (in grams) of the original sample.

5.2.4 A case study of CO in the ISO container

The experiments were carried out in a 33 m^3 ISO container with a double door (dimensions = L x H = 2.34 m x 2.28 m) and no windows (Figure F-1, Appendix F). However, the container was not air tight even in the fully closed position. One kilogram (1 kg) of barbecue charcoal in a paper bag was loaded on to a barbecue pan that was fixed on a 25 kg type load cell which had been calibrated prior to the experiments. Three K type thermocouples were inserted

into the charcoal before it was ignited. The thermocouples and load cell were connected to a Squirrel data logger that recorded the temperature and mass loss of the charcoal during the experiments. Two fans (10 cm diameter) were fixed one on each side of the barbecue (BBQ) pan blowing air at a velocity of 3.5 m/s towards the charcoal to allow uniform and quick distribution of combustion gases in the ISO container.

The CO emissions were recorded by auto-logging PHD6 instruments fitted with CO electrochemical sensors. The CO recording instruments were placed inside the container at 30 cm above the floor and near the door at 150 cm above the floor. These PHD6 instruments also recorded room temperature. For safety of the research team, another set of CO sensor was placed outside the container fitted with a suction pump to draw effluent gases from near the BBQ inside the container. This was connected to the data logger that was checked routinely to monitor the concentrations of CO. Once the CO concentrations went below 10 ppm, the experiment was terminated. Four domestic CO alarms (Kidde type, model 10LLDCO) were installed near the ceiling of the container. These were used to record the time when the alarm went off from the start of each experiment as they responded to time-weighted-average exposures and the maximum concentrations recorded during each run. Each set of experiments was repeated three times.

A portable weather station was installed just outside the container for monitoring wind speed, humidity, temperature, and dew point. The wind speeds were in the range 3.53 to 6.5 (m/s), the outside temperatures were in the range 17.3 to 19.6 (^{o}C), pressure of approximately 1020.7 mbar, and the dew point was in the range 12.2 to 15.2 (^{o}C). The mass of charcoal used per experiment was in the range 900 – 930 g. Each experiment lasted about 2 hours.

5.3 Results and discussion

5.3.1 Wood sawdust

5.3.1.1 Effect of temperature

The experiments were conducted for the temperature range 300 – 450 °C for two main reasons: (i) below 300 °C, the emissions of CO were too low to be detected; (ii) above 450 °C, the combustion process transformed from smouldering to flaming. Hence, any experiment in which no gaseous concentrations were detected within the first 5 minutes was terminated and disregarded. Likewise, for any experiment where the combustion system transformed from smouldering to flaming was also terminated and disregarded.

The tendency of combustion to transform from smouldering to flaming could be related to the concentration of volatiles within the sawdust samples. However, some studies suggest that some mineral elements, especially potassium, enhance the temperature of samples leading to enhanced combustibility [56].

The concentration of CO (mg/g) at each temperature can be seen in Table 5-2. The essential gases produced during smouldering are CO and CO_2 accounting for over 80 % [57] of the total gaseous emissions. Except for beech and ash (Fraxinus) (at 300 °C only), all samples registered CO values in the range $150 \leq CO \leq 250$ mg/g for all temperatures. These results are consistent with the 50 – 300 mg/g detected by Burnet *et al*. [58] from wood fire stoves but higher than the 0.3 – 1.6 mg/g detected by Cheng-Wei [28] emitted by portable household warming devices. The influence of temperature on emissions of CO from this study cannot be generalised. Beech and hazel

samples showed a general increase; lilac CO emissions remained almost constant, Ash (Fraxinus) CO emissions increased at 300 – 350 °C followed by a decrease to 450 °C. Elder showed a general decrease in CO emissions with temperature attributed to enhanced combustion efficiency [59]. Xiao *et al*. [60] determined the emissions of CO from a moving grate boiler to be in the range 49 – 56 mg/g. The amounts of CO emissions recorded in our study are high, and without sufficient ventilation, these values could lead to acute exposure symptoms in a healthy individual especially in a confined space.

5.3.1.2 Effect of airflow

There was a general decrease in CO emissions with airflow Table 5-2. This could be due to the increased turbulence created by the supply of increased air, which resulted in better combustion of volatile matter [61], [62]. This may also be due to the complete combustion of smaller particles and unburned carbon [59]. None the less the obtained values exceed the WHO limits. Casey et al. [63] determined the CO time-weighted averages in several homes in Navajo of Japan and found the values (> 40 ppm per eight hour weighted average) to exceed the recommended levels.

Table 5-2: Effect of temperature and airflow on emissions of CO ± STD (mg/g) from wood sawdust samples. The values were computed with one standard deviation.

Sample	Temperature (°C)				Airflow (L/min)			
	300	350	400	450	0.72	1.24	1.71	2.2
Lilac wood	122.7±3.4	124.0±7.8	117.5±6.6	128.3±5.6	129.5±12.8	125.6±4.5	123.4±8.5	114.1±4.0
Elder wood	172.3±3.9	167.2±6.8	162.4±4.5	161.8±14.1	165.6±8.2	176.6±7.8	167.2±5.9	159.1±7.8
Hazel wood	-	185.01±3.8	245.5±8.1	258.0±8.6	233.7±5.7	230.6±4.5	242.6±8.9	211.1±6.9
Ash wood	136.6±8.8	204.5±8.4	189.7±10.9	169.8±10.5	201.2±13.9	182.1±7.9	155.6±4.2	170.0±10.7
Beech wood	98.9±8.1	170.2±6.8	173.6±9.0	166.0±5.9	179.3±6.2	153.6±4.0	131.7±7.9	159.0±6.1

5.3.1.3 CO evolution profile from wood sawdust

Average data values were produced for each triplicate analysis. All CO evolution patterns followed a comparable trend similar to that reported elsewhere [23] and reached the minimum values at periods between 300 – 500 seconds for all samples. For this reason, lilac (Syringa vulgaris) was chosen to represent all the other sawdust samples Figure 5-1 for the evolution profiles. The key observations were: (i) the time required to attain the maximum CO concentration and the total time of the experiment decreased with increase in temperature across all airflows. This was attributed to the quick degradation of the cellulose, hemicellulose and lignin components with increase in temperature. (ii) There was a general increase in the maximum concentration of CO with an increase in temperature across all airflows. This was related to the early-peak-phenomena in which the concentration of products is directly proportional to temperature (iii) For a particular temperature, the maximum CO concentrations decreased with an increase in airflow. This was attributed to CO oxidation by oxygen in the air.

We also observed the appearance of a secondary peak towards completion of the emission profiles especially at low airflow rates and low temperatures. The second peak was attributed to CO emissions from devolatilised char which is rich in carbon.

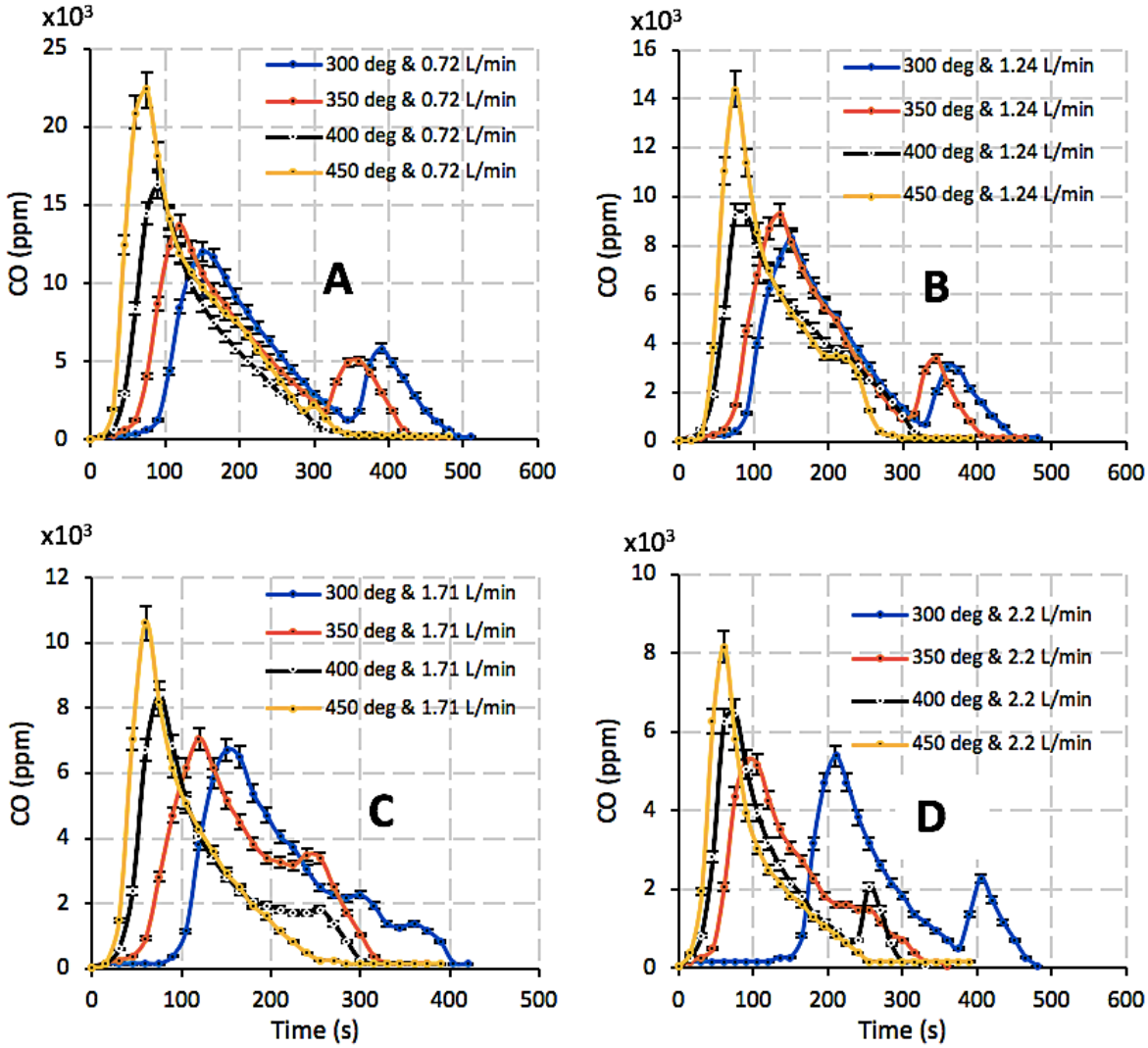

Figure 5-1: CO emission profile for lilac (Syringa vulgaris) representing the profiles for all sawdust samples in this study. A – at 0.72 L/min; B – at 1.24 L/min; C – at 1.71 L/min and D – at 2.2 L/min airflow rates.

5.3.2 Charcoal

The proximate and ultimate analysis values of charcoal shown in Table 5-1, are consistent with other studies [64], [65]. The low volatile matter content of commercial charcoal could be attributed to the temperature at which it was manufactured; high temperatures remove most of the volatiles [29].

5.3.2.1 Effect of temperature and air flow

There was a general decrease in CO emissions with temperature across all airflows Table 5-3. The CO evolution profile followed a general pattern shown in Figure 5-2 for all charcoal samples. The initial CO evolution is a typical zero order followed by a first order decay until most of the carbon is consumed. Apart from beech charcoal, the rest of the charcoal samples showed a general decrease in CO emissions with airflow Table 5-4.

The time-dependant decay of CO emissions is probably related to the turnover of surface complexes, their attachment (weak or strong) and subsequent loss. At any point on the decay curve, the rate of release (calculated from ppm data and flow rates as moles/s) can be related to the remaining mass of charcoal, and "rate constants" calculated.

Table 5-3: Effect of temperature on emissions of CO ± STD (mg/g) from charcoal samples. The values were computed with one standard deviation.

Sample	Temperature (°C)					
	350	400	450	500	550	600
Commercial charcoal	98.1±9.6	198.0±9.9	258.2±10.2	265.3±11.8	245.9±15.2	236.6±15.6
Lilac charcoal	303.9±10.2	287.5±3.2	275.4±7.0	257.5±13.9	251.3±10.3	296.47±5.5
Ash charcoal	299.0±12.8	286.6±13.6	300.6±17.7	291.3±11.7	273.0±16.0	272.2±10.2
Elder charcoal	301.9±14.5	331.8±7.0	324.4±14.7	305.4±19.9	272.2±10.5	275.7±13.2
Hazel charcoal	347.9±11.5	397.6±12.6	465.5±11.8	495.0±10.5	403.6±9.8	363.7±12.1
Beech charcoal	300.6±12.1	328.6±15.4	334.1±15.6	327.9±17.0	308.5±17.9	276.0±10.7

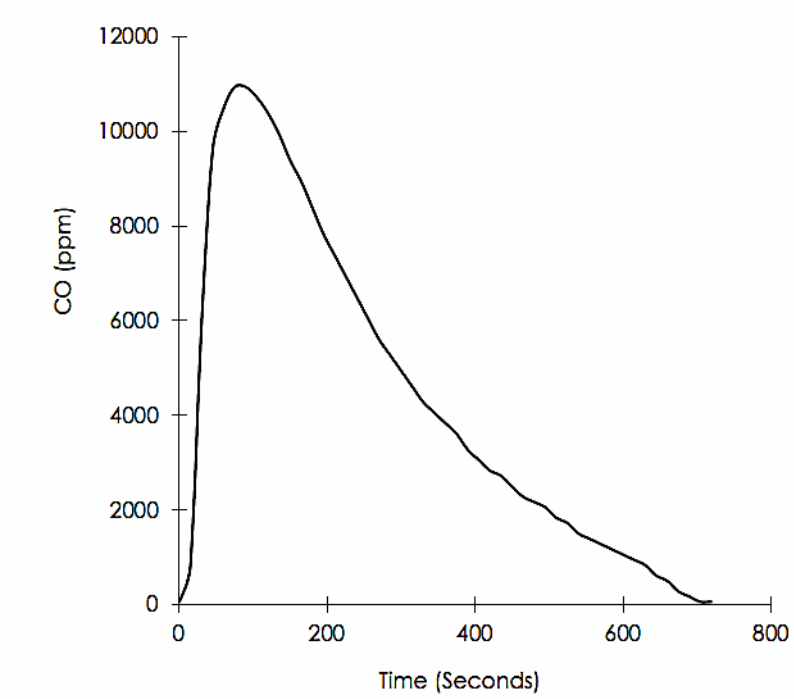

Figure 5-2: Typical profile for the release of CO from charcoal.

Table 5-4: Effect of airflow on emissions of CO ± STD (mg/g) from charcoal samples. The values were computed with one standard deviation.

Sample	Airflow (L/min)			
	0.72	1.24	1.71	2.2
Commercial charcoal	257.8±16.1	210.9±12.9	186.6±12.7	212.7±17.4
Lilac charcoal	265.4±13.4	292.6±17.7	282.7±12.9	273.9±13.3
Ash charcoal	264.0±16.1	306.7±10.2	291.2±14.1	286.6±14.3
Elder charcoal	318.8±17.3	297.7±12.7	286.7±18.2	304.3±13.6
Hazel charcoal	426.8±10.2	421.6±14.5	408.7±14.6	391.6±18.2
Beech charcoal	299.2±16.7	303.2±14.5	315.0±11.9	333.0±18.6

Although we did not measure the mass of charcoal continuously during the heating process, the number of moles remaining at any point can be estimated from the moles of CO and CO_2 released. The rate of CO production

was linearly dependent on the amount of carbon remaining for most part of each experiment, Figure 5-3.

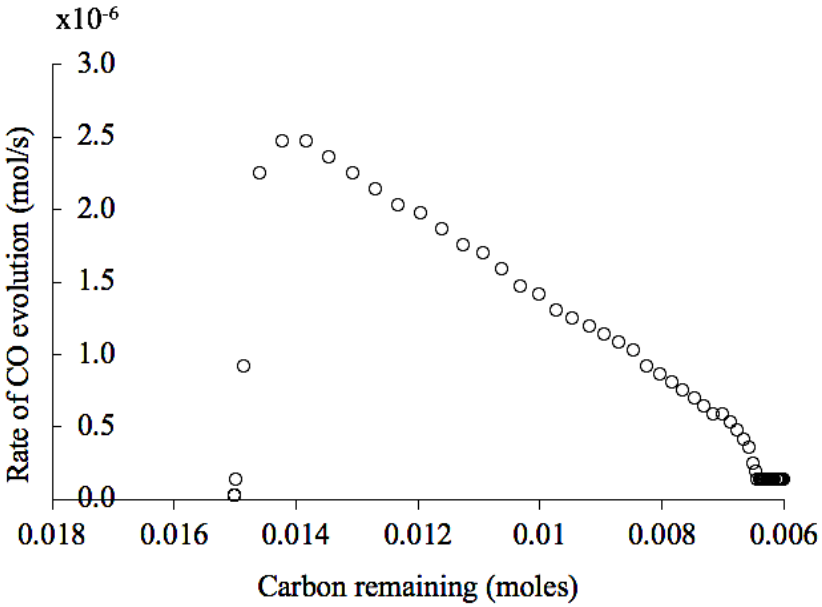

Figure 5-3: The rate of evolution of CO from char at 450 °C and 1.71 L/min air flow.

Rate constants (k_s in units of s^{-1}) can be derived if the linear data for CO in *Figure 5-3* are used in eqn. 5-3 which shows a simple pseudo first-order reaction assuming that the oxygen concentration is constant and the surface area of carbon decreases uniformly with mass. These data are shown in *Table 5-5*.

$$\frac{d[CO]}{dt} = k_s \,.\, [Carbon] \qquad (5\text{-}3)$$

Table 5-5: Values of ks (s^{-1}) for different temperatures and air flow rates

Temp (°C)	(Air flow±0.01) (L/min)			
	0.72	1.24	1.7	2.2
400	5.3 x10^{-4}	3.9 x10^{-4}	-	2.2 x10^{-4}
450	5.3 x10^{-4}	3.4 x10^{-4}	2.7 x10^{-4}	2.2 x10^{-4}
500	4.5 x10^{-4}	3.4 x10^{-4}	2.7 x10^{-4}	2.4 x10^{-4}
550	7.7 x10^{-4}	4.5 x10^{-4}	2.8 x10^{-4}	2.5 x10^{-4}4
600	8.8 x10^{-4}	6.8 x10^{-4}	3.6 x10^{-4}	2.3 x10^{-4}

We again observe an airflow effect, with low flows increasing the rate constant for CO evolution, and a temperature effect that is only manifested at the lower air flows.

Scanning electron microscopy, Figure 5-4, revealed that the wood char retains much of the micrometre-sized porous structure of the wood from which it was derived. Wood charcoal probably burns in much the same way on all surfaces similar to propellant grains [66] extruded with voids down their length so that as the external surface shrinks during burning, simultaneously the internal surface grows to maintain the overall surface area thus conferring a near constant burn rate. Hence, the assumption that surface area depends on the mass of charcoal could be true.

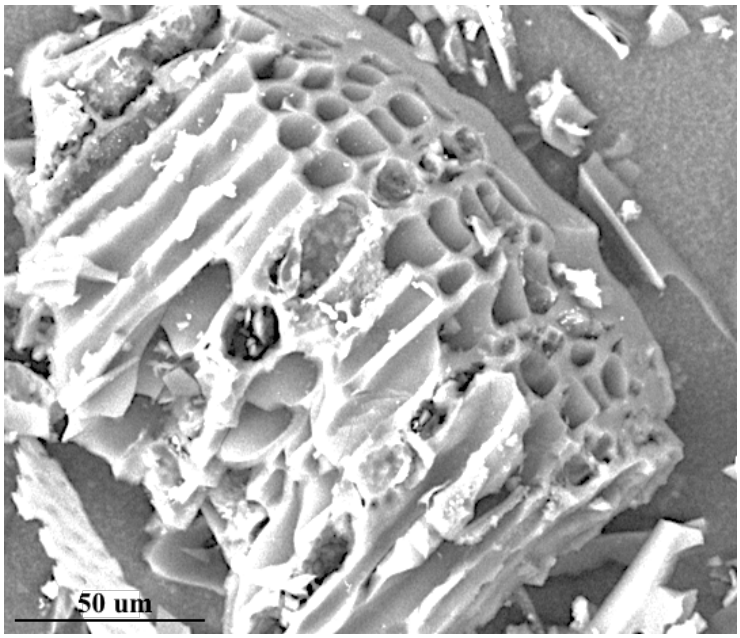

Figure 5-4: Scanning electron microscopy image for wood charcoal

5.3.2.2 ΔG as a predictor of reaction feasibility

Several reactions may take place during char combustion leading to production of CO, including the following:

$$2C_{(s)} + O_{2\,(g)} \rightarrow 2CO_{(s)} \quad (5\text{-}4)$$

$$CO_{(s)} \rightarrow CO_{(g)} \quad (5\text{-}5)$$

$$C_{(s)} + CO_{2(g)} \rightarrow 2\,CO_{(g)} \quad (5\text{-}6)$$

We predict that reactions 5-4 become less favourable as the temperature increases, whereas 5-5 become more favourable because the former involve a decrease in gas-phase species and the latter an increase. Reaction 5-6 does not occur at temperatures below 973 K [67].

There are many other factors to consider. The product ratios (CO/CO_2) may reflect the different active sites present on each char surface associated with cationic trace metal impurities that act as catalysts [68]. Although our experiments involved isothermal combustion, the actual char temperatures could have been higher because metal impurities can enhance the burning temperature of char [69]. There is evidence for CO conversion to CO_2 at the char surface by the catalytic action of the char mineral matter [70]. It is also possible that the decrease in CO amounts with temperature are due to secondary processes taking place in the charcoal pores, promoting the conversion of CO to CO_2.

Our results highlight the dangerous assumption that charcoal fires do not produce CO merely because they are not glowing red hot. Radiant heat should be an indicator of continuing combustion. Initial results with this charcoal sample suggest that there are steps that could be taken to encourage secondary conversion of CO to CO_2 in these systems and that this may be as simple as selecting the most suitable wood for charcoal preparation.

5.3.3 Case study of CO in the ISO container

5.3.3.1 CO at different positions in the container

The results clearly show that the CO values recorded at 150 cm above floor (near the door) were higher than those recorded at 30 cm above floor (extreme end inside the container), Figure 5-5. This could be explained by the movement of heavy, moist and fresh air from the outside displacing dry, warm and polluted air from charcoal combustion to the upper parts of the container [71].

Secondly, the buoyant air movement and the temperature difference within the ISO container was a major factor contributing for movement of CO to the upper parts of the ISO container [72]. This emphasises two very important considerations during cooking/heating: (i) to keep the door and windows open to allow entry of fresh air [73] and (ii) to move at the lower side as possible (in a crawling position) as we exit any confined space on fire. As expected, the amounts of CO emissions relative to the door position were in the order; fully closed > half open > fully open. Even in the fully closed-door position, fresh air could enter since the door was not air tight [74].

There was a steady decline in charcoal temperature recorded during the fully closed-door session reaching its lowest value (159 °C) at the end of the experiment compared to the fully open and half open-door positions which had the lowest charcoal temperature as 442 and 500 °C respectively. This could be attributed to low air flow within the container during the fully closed-door position, hence, residual ash built-up on charcoal surfaces and could not be easily removed due to low airflow rates. This also explains the high amounts of CO recorded during the fully closed-door experiment due to low purging compared to the fully open and the half open door positions. Additionally, due to constant blowing of air, the temperature during the fully open and half open

experiments was maintained above 440 °C [75] throughout the experiment compared to the fully closed-door position where the charcoal temperature declined continuously to as low as 159 °C.

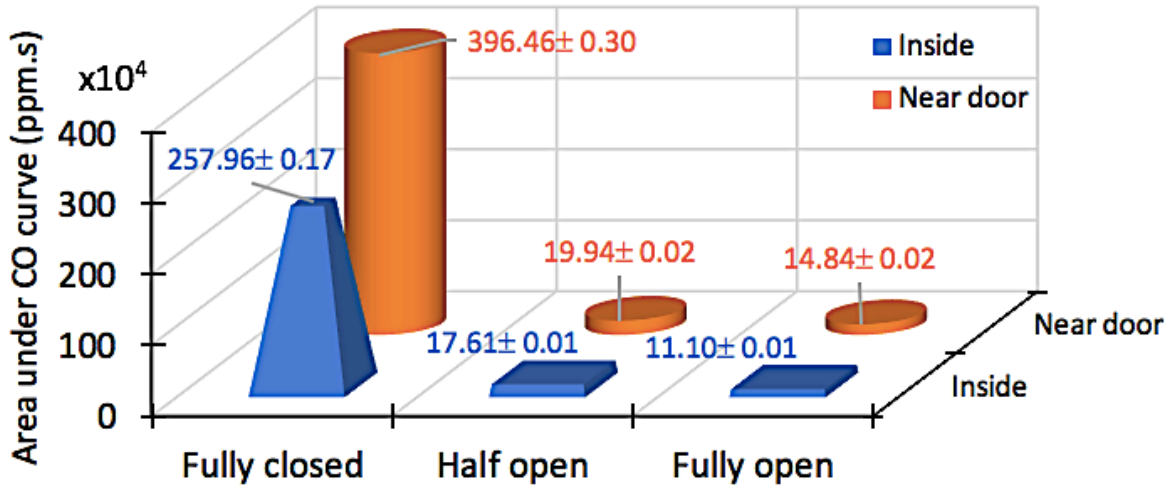

Figure 5-5: Area under the CO curves for the different door positions during the ISO container experiments.

The fully open-door experiment took about 110 minutes, the half open experiment took about 120 minutes while the fully closed-door experiment took the longest time of close to 140 minutes. This could be due the oxidation of charcoal by incoming air: the higher the airflow, the faster the oxidation [76].

Even when charcoal looks to be out of fire, it is not recommended to take it to any confined space. The best practice would be to empty the charcoal remaining into a waste/hot charcoal safety bin before storage of the BBQ grill. In the 33 m^3 ISO container experiment described above, CO values as high as 70 ppm were recorded from only 270 g of (charcoal + residual ash) which had remained after the 1 kg charcoal sample was burnt from the outside – this was done to simulate what some CO poisoning victims do after a BBQ meal. This implies that, any confined space smaller than the ISO container used in this study could have registered very high CO concentrations [77].

The domestic alarms also provided very important information. In the fully open position, the alarms went off at 22 to 25 minutes within the experiment. Once checked at the end of the experiments, they recorded maximum CO concentrations as 125 to 130 ppm. In the half open door position, the alarms went off at 15 to 20 minutes within the experiment and they recorded 820 to 900 ppm as maximum CO concentrations. In the fully closed-door position, the alarms went off at 2 to 6 minutes and they recorded 999 ppm as maximum CO concentrations during those experiments. With the charcoal burnt from the outside and then taken inside the ISO container, the CO alarms went off after 40 minutes. According to the manufacturers of Kidde alarms [78], the alarm response times and CO concentration are shown in Table 5-6.

Table 5-6: CO concentrations and Kidde alarm response times

Carbon Monoxide Level	Alarm Response Time
40 ppm	10 hours
50 ppm	8 hours
70 ppm	1 to 4 hours
150 ppm	10 to 50 minutes
400 ppm	4 to 15 minutes

The experimental alarm response values (CO concentration and time) agree with the guide from the manufacturers of Kidde alarms. In the fully open-door position, the alarm response time was within the 15-minute allowable limits but outside the 1-hour limits of UK/EU/WHO [39] guideline. In the half open and fully closed-door positions, the recorded values all exceed the UK/EU/WHO guideline values for 15 minutes (100 mg/m^3 or 87.3 ppm) and 1-hour (35 mg/m^3 or 30.6 ppm) indoor exposures.

5.3.3.2 CO levels in relation to recommended exposure limits

In the fully closed-door position, the overall time-weighted-average (TWA) CO concentration for the entire experiment (2 hours and 20 minutes) at 150cm was

497 ppm. This level is said to cause mild headache, fatigue, nausea and dizziness [79]. However, the one-hour time weighted average CO value was 751 ppm. This value is close to 800 ppm established by OSHA that causes serious headache and may trigger other symptoms that are life threatening. In the sitting position (at 30 cm), the one-hour time weighted average was 481 ppm. These CO levels would cause mild headache, fatigue, nausea and dizziness (OSHA, WHO) [38].

In the half open door position, the overall time-weighted-average (TWA) CO concentration for the entire experiment (2 hours) at 150 cm was 28 ppm. According to WHO and OSHA, this level would not cause any immediate symptoms. However, the one hour TWA was 47 ppm which is lower than the dangerous levels set by UK-EU-WHO-OSHA) [38] for 60 minutes CO exposures. In the sitting position height, (at 30 cm), the 2hour TWA was 25 ppm. However, the one hour TWA was 37 ppm which is higher than the 25 ppm level set by UK-EU-WHO-OSHA) [38] for 60 minutes CO exposures.

In the fully open-door position, the overall time-weighted-average (TWA) CO concentration for the entire experiment (110 minutes) at 150 cm was 22 ppm-TWA. According to WHO and OSHA, this level would not cause any immediate symptoms. However, the one hour TWA was 30 ppm which is lower than the dangerous levels set by UK-EU-WHO-OSHA) [38], [80] for 60 minutes CO exposures (set in 2011, and 2005). In the sitting position (at 30 cm), the overall TWA CO concentration was 17 ppm for the entire experiment (1 hour 50 minutes). However, the one hour TWA was 22 ppm which is lower than the levels set by UK-EU-WHO-OSHA) [38] for 60 minutes CO exposure. This CO level is also lower than the levels set by UK-EU-WHO-OSHA for the 60 minutes (set in 2015) CO exposures in the standing position. However, low levels of CO exposure have been linked neurodevelopment disorders [81].

However, all the recorded CO values in this case study are higher than 20 ppm – long term exposure (8 hours) and the 100 ppm – short term exposure (15 minutes) set by the UK Health and Safety Executive 2018 [82].

Summary & Conclusions

In this study, the emissions of CO from wood sawdust and charcoal from the same wood species were evaluated. Sawdust emitted less CO than charcoal. Secondary, a case study of CO accumulation in a confined space was simulated using an ISO container. CO emission from wood sawdust were in the range 98.8 mg/g as lowest to 258.0 mg/g as highest across all temperatures and airflows. On the other hand, the CO emission from charcoal were in the range 98.1 mg/g as lowest to 495 mg/g as highest across all temperatures and 186.6 mg/g as lowest to 426.8 mg/g as highest across all airflows.

There was a general decrease in CO emissions across all temperatures and airflows for both sawdust and charcoal except wood sawdust for which the CO emissions from each sample was affected differently by temperature. The amounts of CO emissions recorded in the ISO container increased with decrease in airflow within the container. Higher amounts of CO were recorded at the upper parts of the container compared to the lower parts. The ISO container case study elaborates the build-up of CO in enclosed environments and the importance of aeration.

Acknowledgements

The authors thank the Gas Safety Trust (UK), the Boat Safety Scheme (UK) and the Katie Haines memorial Trust (UK) for sponsoring this work. Gratitude for the experimental support provided by Adrian Mustey.

References

[1] I. Blumenthal, "Carbon Monoxide Poisoning," *J. R. Soc. Med.*, vol. 94, pp. 270–272, 2001.

[2] P. R. Nielsen, A. Gheorghe, and N. Lynnerup, "Forensic aspects of carbon monoxide poisoning by charcoal burning in Denmark, 2008-2012: An autopsy based study," *Forensic Sci. Med. Pathol.*, vol. 10, no. 3, pp. 390–394, 2014.

[3] Gas Safety Trust - UK, "UK deaths caused by accidental Carbon Monoxide (CO) poisoning," Isle of Wight, 2017.

[4] A. Whelan, "Camping site tragedy girl 'gassed by a BBQ': 'She was our whole world,' say devastated parents after rescue attempt," *Mail Online*, 2012. [Online]. Available: http://www.dailymail.co.uk/news/article-2126693/Holmsley-campsite-tragedy-Isabelle-Harris-poisoned-BBQ-New-Forest-Hampshire.htm. [Accessed: 20-Aug-2018].

[5] BBC-Online-News, "Nicholas Holmes: Camper van death caused by barbecue," *BBC News*, 2012. [Online]. Available: http://www.bbc.co.uk/news/uk-england-hampshire-19506458.htm. [Accessed: 20-Aug-2018].

[6] BBC-Online-News, "Bucknell tent death: Hannah Thomas-Jones died from carbon monoxide poisoning," *BBC News*, 2013. [Online]. Available: https://www.bbc.co.uk/news/uk-england-21059594.htm.

[7] E. Yoshioka, S. J. B. Hanley, Y. Kawanishi, and Y. Saijo, "Epidemic of charcoal burning suicide in Japan," *Br. J. Psychiatry*, vol. 204, no. 4, pp. 274–282, 2014.

[8] I. M. Madani, S. Khalfan, H. Khalfan, J. Jidah, and M. Nabeel Aladin, "Occupational exposure to carbon monoxide during charcoal meat grilling," *Sci. Total Environ.*, vol. 114, no. C, pp. 141–147, 1992.

[9] G. Y. Huh, G. R. Jo, K. H. Kim, Y. W. Ahn, and S. Y. Lee, "Imitative suicide by burning charcoal in the southeastern region of Korea: The influence of mass media reporting," *Leg. Med.*, vol. 11, no. SUPPL. 1, pp. S563–S564, 2009.

[10] Y. Y. Chen *et al.*, "Suicide by burning barbecue charcoal in England," *J. Public Heal. (United Kingdom)*, vol. 35, no. 2, pp. 223–227, 2013.

[11] F. R. Fisher DS, Bowskill S, Saliba L, "Unintentional domestic non-fire related carbon monoxide poisoning: Data from media reports, UK/Republic of Ireland 1986-2011," *J. Emerg. Med.*, vol. 45, no. 2, p. 312, 2013.

[12] D. P. Betten, D. J. Castle, L. L. Bales, and M. J. Hughes, "Effect of fuel type on carbon monoxide accumulation in tents of varied design," *Wilderness Environ. Med.*, vol. 24, no. 3, pp. 280–284, 2013.

[13] L. Stewart and C. Health, "My partner 'was killed by a barbecue,'" *BBC World News*, 2015. [Online]. Available: https://www.bbc.co.uk/news/health-33976414. [Accessed: 12-Oct-2018].

[14] R. C. Flagan and J. H. Seinfeld, "Combustion fundamentals," in

Fundamentals of Air pollution engineering, no. 1–2, I. WordCrafters Editorial Services, Ed. Prentice Hall: Englewood Cliffs, NJ, 1988, pp. 59–163.

[15] Eduardo A. Sánchez, Milagros B. Pasache, and Marcos E. García, "Development of Briquettes from Waste Wood (Sawdust) for Use in Low-income Households in Piura, Peru," *World Congr. Eng.* , vol. 2, no. 4, pp. 1–6, 2014.

[16] S. K. Chembukulam, A. S. Dandge, N. L. K. Rao, K. Seshagiri, and R. Vaidyeswaran, "Smokeless fuel from carbonized sawdust," *Ind. Eng. Chem. Prod. Res. Dev.*, vol. 20, no. 4, pp. 714–719, Dec. 1981.

[17] H. Hosseinizand, S. Sokhansanj, and C. J. Lim, "Co-pelletization of microalgae Chlorella vulgaris and pine sawdust to produce solid fuels," *Fuel Process. Technol.*, vol. 177, pp. 129–139, 2018.

[18] M. Zamorano, V. Popov, M. L. Rodríguez, and A. García-Maraver, "A comparative study of quality properties of pelletized agricultural and forestry lopping residues," *Renew. Energy*, vol. 36, no. 11, pp. 3133–3140, 2011.

[19] UK - DEFRA, "UK Statistics on Waste - Department for Environmental Food & Rural Affairs (DEFRA) - Government Statistical services," 2018.

[20] G. Lazaroiu *et al.*, "Biomass combustion with hydrogen injection for energy applications," *Energy*, vol. 127, pp. 351–357, 2017.

[21] Tarm Biomass, "Wood Boiler Evolution," 2018. [Online]. Available: https://www.woodboilers.com/tarm-biomass-wood-boilers-distributor-intelligently-engineered-wood-boiler-systems/resources/wood-boiler-evolution-wood-boiler-history/. [Accessed: 27-Nov-2018].

[22] D. Josua and Wood Pellet Boiler Solutions, "Wood Pellet Boilers – A Brief History," 2012. [Online]. Available: http://woodpelletsolutions.co.uk/wood-pellet-boilers-a-brief-history/. [Accessed: 27-Nov-2018].

[23] C. J. Lupa, S. R. Wylie, A. Shaw, A. Al-Shamma'a, A. J. Sweetman, and B. M. J. Herbert, "Gas evolution and syngas heating value from advanced thermal treatment of waste using microwave-induced plasma," *Renew. Energy*, vol. 50, pp. 1065–1072, 2013.

[24] L. P. Naeher *et al.*, "Woodsmoke health effects: A review," *Inhal. Toxicol.*, vol. 19, no. 1, pp. 67–106, 2007.

[25] A. Muala *et al.*, "Acute exposure to wood smoke from incomplete combustion - indications of cytotoxicity," *Part. Fibre Toxicol.*, vol. 12, no. 1, pp. 1–14, 2015.

[26] E. Green, S. Short, L. K. Shuker, and P. T. C. Harrison, "Carbon monoxide exposure in the home environment and the evaluation of risks to health - A UK perspective," *Indoor and Built Environment*. 1999.

[27] S. C. Bhattacharya and P. Abdul Salam, "Low greenhouse gas biomass options for cooking in the developing countries," *Biomass and Bioenergy*, vol. 22, no. 4, pp. 305–317, 2002.

[28] C.-W. Fan and J. (Jim) Zhang, "Characterization of emissions from portable household combustion devices: particle size distributions, emission rates and factors, and potential exposures," *Atmos. Environ.*,

vol. 35, no. 7, pp. 1281–1290, 2001.
[29] H. L. Huang, W. M. G. Lee, and F. S. Wu, "Emissions of air pollutants from indoor charcoal barbecue," *J. Hazard. Mater.*, vol. 302, pp. 198–207, 2016.
[30] E. J. S. Mitchell, A. R. Lea-Langton, J. M. Jones, A. Williams, P. Layden, and R. Johnson, "The impact of fuel properties on the emissions from the combustion of biomass and other solid fuels in a fixed bed domestic stove," *Fuel Process. Technol.*, vol. 142, pp. 115–123, 2016.
[31] M. Tafadzwa, Daniel M. Masekameni, Harold J. Annegarn, Patricia Forbes, "Emission factors of domestic coal-burning braziers," *S. Afr. J. Sci.*, vol. 113, no. 3, pp. 1–11, 2017.
[32] J. Ojima, "Generation rate of carbon monoxide from burning charcoal.," *Ind. Health*, vol. 49, no. 3, pp. 393–395, 2011.
[33] D. D. Evans and H. W. Emmons, "Combustion of wood charcoal," *Fire Saf. J.*, vol. 1, no. 1, pp. 57–66, 1977.
[34] E. M. Barber and J. R. Ogilvie, "Incomplete mixing in ventilated airspaces. Part 1 Theoretical considerations," *Can. Agric. Eng.*, vol. 24, pp. 25–29, 1982.
[35] American Conference of Governmental Industrial Hygienists (ACGIH), *Industrial Ventilation Manual*, 23rd ed., vol. 552. Ohio: ACGIH, 1998.
[36] P. W. Francisco, J. R. Gordon, and B. Rose, "Measured concentrations of combustion gases from the use of unvented gas fireplaces," *Indoor Air*, vol. 20, no. 5, pp. 370–379, 2010.
[37] R. J. Crewe, S. P. Andrews, T. R. Hull, P. N. Birbeck, and A. A. Stec, "Combustion and Toxic Gas Production from Disposable Barbecues in Enclosures," *J. Forensic Sci.*, vol. 59, no. 1, pp. 127–138, 2014.
[38] WHO, "Carbon Monoxide," in *Air Quality Guidelines*, 2nd ed., Copenhagen, Denmark: WHO Regional Office for Europe, 2011, pp. 1–8.
[39] WHO, "WHO Guidelines for Indoor Air Quality: Selected Pollutants," 2010.
[40] American Conference of Governmental Industrial Hygienists (ACGIH), *Documentation of the Threshold Limit Values and Biological Exposure Indices*, 7th ed. Ohio: ACGIH, 2013.
[41] DHHS-NIOSH, *NIOSH Pocket Guide to Chemical Hazards*. National Institute for Occupational Safety and Health (NIOSH)., 2004.
[42] S. C. Bhattacharya, D. O. Albina, and P. A. Salam, "Emission factors of wood and charcoal-fired cookstoves," *Biomass and Bioenergy*, vol. 23, pp. 453–469, 2002.
[43] J. Jetter *et al.*, "Pollutant emissions and energy efficiency under controlled conditions for household biomass cookstoves and implications for metrics useful in setting international test standards," *Environ. Sci. Technol.*, vol. 46, no. 19, pp. 10827-10834., 2012.
[44] V. Tanetsakunvatana and V. I. Kuprianov, "Experimental study on effects of operating conditions and fuel quality on thermal efficiency and emission performance of a 300-MW boiler unit firing Thai lignite," *Fuel Process. Technol.*, vol. 88, no. 2, pp. 199–206, 2007.
[45] T. Koyuncu and Y. Pinar, "The emissions from a space-heating biomass stove," *Biomass and Bioenergy*, vol. 31, no. 1, pp. 73–79, 2007.

[46] K. R. Smith, M. a K. Khalil, R. A. Rasmussen, S. A. Thorneloe, F. Manegdeg, and M. Apte, "Greenhouse Gases from Biomass and Fossil-Fuel Stoves in Developing-Countries - a Manila Pilot-Study," *Chemosphere*, vol. 26, pp. 479–505, 1993.
[47] G. Toscano and E. Foppa Pedretti, "Calorific Value Determination of Solid Biomass Fuel By Simplified Method," *J. Agric. Eng.*, vol. 40, no. 3, pp. 1–6, 2009.
[48] A. Nyombi, M. R. Williams, and R. Wessling, "Mechanical impregnation of Pd-Sn/alumina and Cu-Mn/graphite on charcoal to minimise carbon monoxide emissions," *Chem. Phys. Lett.*, vol. 715, pp. 181–185, Jan. 2019.
[49] A. Nyombi, M. R. Williams, and R. Wessling, "Determination of Kinetic Parameters and Thermodynamic properties of Ash (fraxiuns) sawdust slow pyrolysis using Thermogravimetric Analysis," *Energy Sources, Part A Recover. Util. Environ. Eff.*, vol. 40, no. 22, pp. 2660–2670, 2018.
[50] A. Nyombi, M. Williams, and R. Wessling, "Determination of kinetic parameters and thermodynamic properties for ash (Fraxinus) wood sawdust slow pyrolysis by thermogravimetric analysis," *Energy Sources, Part A Recover. Util. Environ. Eff.*, vol. 40, no. 22, pp. 2660–2670, Aug. 2018.
[51] A. Demirbas and A. Demirba, "Properties of charcoal derived from hazelnut shell and the production of briquettes using pyrolytic oil," *Energy*, vol. 24, pp. 141–150, 1999.
[52] W. Klose and M. Wölki, "On the intrinsic reaction rate of biomass char gasification with carbon dioxide and steam," *Fuel*, vol. 84, no. 7–8, pp. 885–892, 2005.
[53] M. J. Antal and M. Grønli, "The Art, Science, and Technology of Charcoal Production," *Ind. Eng. Chem. Res.*, vol. 42, no. 8, pp. 1619–1640, 2003.
[54] F. Scala, "A new technique for the measurement of the product CO/CO_2 ratio at the surface of char particles burning in a fluidized bed," *Proc. Combust. Inst.*, vol. 32 II, no. 2, pp. 2021–2027, 2009.
[55] S. Katyal, "Effect of Carbonization Temperature on Combustion Reactivity of Bagasse Char," *Energy Sources, Part A Recover. Util. Environ. Eff.*, vol. 29, no. 16, pp. 1477–1485, 2007.
[56] J. M. Jones *et al.*, "Low temperature ignition of biomass," *Fuel Process. Technol.*, vol. 134, pp. 372–377, 2015.
[57] C. J. Lupa, S. R. Wylie, A. Shaw, A. Al-Shamma'a, A. J. Sweetman, and B. M. J. Herbert, "Experimental analysis of biomass pyrolysis using microwave-induced plasma," *Fuel Process. Technol.*, vol. 97, pp. 79–84, 2012.
[58] P. G. Burnet, N. G. Edmisten, P. E. Tiegs, J. E. Houck, and R. A. Yoder, "Particulate, Carbon Monoxide, and Acid Emission Factors for Residential Wood Burning Stoves," *J. Air Pollut. Control Assoc.*, vol. 36, no. 9, pp. 1012–1018, Sep. 1986.
[59] F. Duan, J. Liu, C. S. Chyang, C. H. Hu, and J. Tso, "Combustion behavior and pollutant emission characteristics of RDF (refuse derived fuel) and sawdust in a vortexing fluidized bed combustor," *Energy*, vol. 57, pp. 421–426, 2013.
[60] Z. Xiao *et al.*, "Energy recovery and secondary pollutant emission from

the combustion of co-pelletized fuel from municipal sewage sludge and wood sawdust," *Energy*, vol. 91, pp. 441–450, 2015.
[61] S. Rao and V. Reddy, "Effect of secondary air injection on the combustion efficiency of sawdust in a fluidized bed combustor," *Brazilian J. Chem. Eng.*, vol. 25, no. 01, pp. 129–141, 2008.
[62] F. Duan, C. Chyang, Y. Wang, and J. Tso, "Effect of secondary gas injection on the peanut shell combustion and its pollutant emissions in a vortexing fluidized bed combustor," *Bioresour. Technol.*, vol. 154, pp. 201–208, 2014.
[63] J. G. Casey, J. Ortega, E. Coffey, and M. Hannigan, "Low-cost measurement techniques to characterize the influence of home heating fuel on carbon monoxide in Navajo homes," *Sci. Total Environ.*, vol. 625, pp. 608–618, 2018.
[64] V. Strezov, M. Patterson, V. Zymla, K. Fisher, T. J. Evans, and P. F. Nelson, "Fundamental aspects of biomass carbonisation," *J. Anal. Appl. Pyrolysis*, vol. 79, no. 1-2 SPEC. ISS., pp. 91–100, 2007.
[65] X. Cao *et al.*, "Characterization of Wood Chars Produced at Different Temperatures Using Advanced Solid-State 13 C NMR Spectroscopic Techniques," *Energy & Fuels*, vol. 26, no. 9, pp. 5983–5991, 2012.
[66] A. Bailey and S. G. Murray, *Explosives, Propellants & Pyrotechnics*, Volume 2. London: Brassey's (UK) Ltd, 1989.
[67] J. Dollimore, C. M. Freedman, B. H. Harrison, and D. F. Quinn, "Surface complexes on carbon-I. A preliminary investigation of surface oxygen complex on a non-graphitic carbon," *Carbon N. Y.*, vol. 8, no. 5, pp. 587–596, 1970.
[68] L. Tognotti, J. . Longwell, and F. Sarofim, "The products of the high temperature oxidation of a single char particle in an electrodynamic balance," in *Twenty-Third Symposium (International) on Combustion/The Combustion Institute*, 1990, pp. 1207–1213.
[69] J. H. Pohl, "Influence of Mineral Matter on the Rate of Coal Char Combustion," in *Mineral Matter and Ash in Coal*, 1986, pp. 430–436.
[70] D. P. Mccollor, M. L. Jones, S. A. Benson, and B. . Young, "Promotion of char oxidation by inorganic constituents," in *Twenty-second Symposium (international) on combustion/The Combustion Institute*, 1988, pp. 59–67.
[71] N. De Nevers, *Air Pollution Control Engineering*, vol. 1. Totowa, New Jersey: Humana Press, 2004.
[72] L. Zhigang, "Characteristics of Byoyancy Driven Natural Ventilation Through Horizontal Openings," Aalborg University, Copenhagen, 2006.
[73] B. R. Hughes and C. M. Mak, "A study of wind and buoyancy driven flows through commercial wind towers," *Energy Build.*, vol. 43, no. 7, pp. 1784–1791, 2011.
[74] M. F. Hekal and W. M. El-maghlany, "Experimantal Study of Fabric Air duct," *Int. J. Adv. Sci. Tech. Res.*, vol. 1, no. 7, pp. 106–121, 2017.
[75] C. J. T. Spence, N. A. Buchmann, and M. C. Jermy, "Airflow in a Domestic Kitchen Oven measured by Particle Image Velocimetry," in *16th Australasian Fluid Mechanics Conference.*, 2007, no. December, pp. 1364–1368.

[76] J. P. A. Neeft, T. X. Nijhuis, E. Smakman, M. Makkee, J. A. Moulijn, "Kinetics of the oxidation of diesel soot," *Fuel*, vol. 76, no. 12, pp. 1129–1136, 1997.
[77] U. R. A. Svedberg, H. E. Högberg, J. Högberg, and B. Galle, "Emission of hexanal and carbon monoxide from storage of wood pellets, a potential occupational and domestic health hazard," *Ann. Occup. Hyg.*, vol. 48, no. 4, pp. 339–349, 2004.
[78] Kidde-United-Technologies, *Carbon monoxide levels that will set off your alarm*. 2018.
[79] S. Euan and B. Nicholas, "Carbon monoxide," *Medicine (Baltimore).*, vol. 44, no. 3, pp. 151–152, 2016.
[80] Health and Safety Executive, "UK - EH4O/2005 Workplace exposure limits," 2011.
[81] R. J. Levy, "Carbon monoxide pollution and neurodevelopment: A public health concern," *Neurotoxicol. Teratol.*, vol. 49, pp. 31–40, 2015.
[82] Health and Safety Executive, "EH40/2005 Workplace exposure limits," 2018.

Chapter 6: MECHANICAL IMPREGNATION OF Pd-Sn/ALUMINA AND Cu-Mn/GRAPHITE ON CHARCOAL TO MINIMISE CARBON MONOXIDE EMISSIONS

The work contained in this chapter has been published in Chemical Physics Letters.

Citation: Nyombi A, Williams R. Mike, Wessling R: Mechanical Impregnation of Pd-Sn/alumina and Cu-Mn/graphite on charcoal to minimise carbon monoxide emissions. DOI: https://doi.org/10.1016/j.cplett.2018.11.041

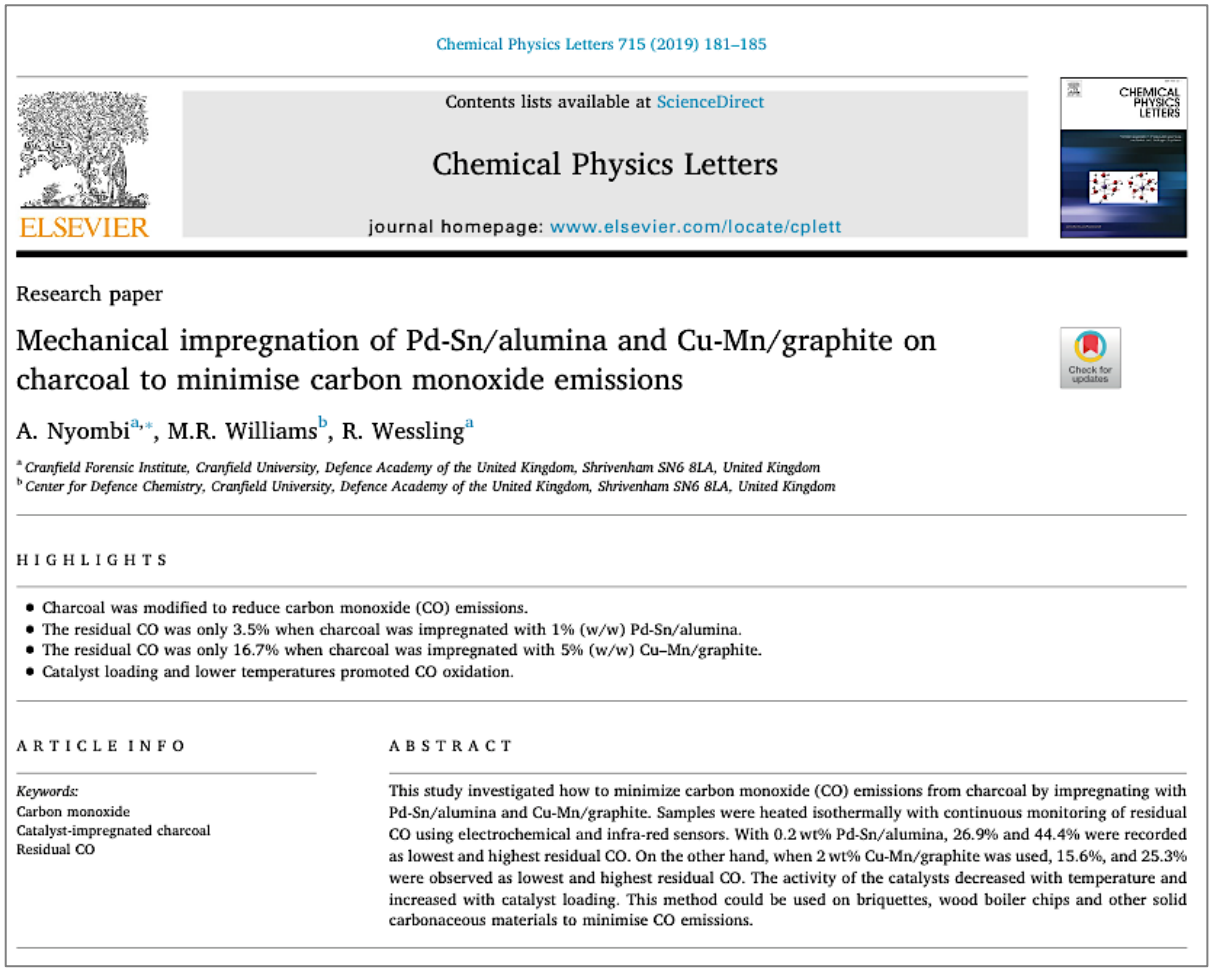

Chemical Physics Letters 715 (2019) 181–185

Contents lists available at ScienceDirect

Chemical Physics Letters

journal homepage: www.elsevier.com/locate/cplett

Research paper

Mechanical impregnation of Pd-Sn/alumina and Cu-Mn/graphite on charcoal to minimise carbon monoxide emissions

A. Nyombi[a,*], M.R. Williams[b], R. Wessling[a]

[a] Cranfield Forensic Institute, Cranfield University, Defence Academy of the United Kingdom, Shrivenham SN6 8LA, United Kingdom
[b] Center for Defence Chemistry, Cranfield University, Defence Academy of the United Kingdom, Shrivenham SN6 8LA, United Kingdom

HIGHLIGHTS

- Charcoal was modified to reduce carbon monoxide (CO) emissions.
- The residual CO was only 3.5% when charcoal was impregnated with 1% (w/w) Pd-Sn/alumina.
- The residual CO was only 16.7% when charcoal was impregnated with 5% (w/w) Cu–Mn/graphite.
- Catalyst loading and lower temperatures promoted CO oxidation.

ARTICLE INFO

Keywords:
Carbon monoxide
Catalyst-impregnated charcoal
Residual CO

ABSTRACT

This study investigated how to minimize carbon monoxide (CO) emissions from charcoal by impregnating with Pd-Sn/alumina and Cu-Mn/graphite. Samples were heated isothermally with continuous monitoring of residual CO using electrochemical and infra-red sensors. With 0.2 wt% Pd-Sn/alumina, 26.9% and 44.4% were recorded as lowest and highest residual CO. On the other hand, when 2 wt% Cu-Mn/graphite was used, 15.6%, and 25.3% were observed as lowest and highest residual CO. The activity of the catalysts decreased with temperature and increased with catalyst loading. This method could be used on briquettes, wood boiler chips and other solid carbonaceous materials to minimise CO emissions.

Mechanical Impregnation of Pd-Sn/Alumina and Cu-Mn/Graphite on Charcoal to Minimise Carbon Monoxide Emissions

Highlights

- Charcoal was modified to reduce carbon monoxide (CO) emissions
- The residual CO was only 3.5 % when charcoal was impregnated with 1 wt% Pd-Sn/alumina
- The residual CO was only 16.7 % when charcoal was impregnated with 5 wt% Cu-Mn/graphite
- Catalyst loading and lower temperatures promoted oxidation

Abstract

The burning of charcoal can release dangerous levels of carbon monoxide (CO). Here we investigated methods to reduce CO emissions by impregnating the charcoal with Pd-Sn/alumina and Cu-Mn/graphite. Samples were heated isothermally with continuous monitoring of residual CO using electrochemical and infra-red sensors. With a Pd-Sn/alumina content of 0.2 wt%, the highest and lowest residual CO levels were 44.4 % and 26.9 %, respectively. However, with a Cu-Mn/graphite content of 2 wt%, the highest and lowest residual CO levels were 25.3 % and 15.6 %, respectively. The activity of the catalysts decreased at higher temperatures but increased with catalyst loading. Such catalysts could be applied to briquettes, wood boiler chips and other solid carbonaceous materials to minimise CO emissions.

6.1 Introduction

Charcoal from woody biomass is a high-energy material (calorific value ≈ 30 MJ/kg) used for cooking and heating. As it burns, charcoal releases several by-products that are dependent on its properties and the prevailing conditions. Complete combustion yields mainly carbon dioxide (CO_2) and moisture, whereas incomplete combustion yields carbon monoxide (CO), CO_2, particulate matter, volatile organic compounds and carbonyls [1]. The use of charcoal has led to unintentional CO poisoning, resulting in many deaths and also near misses and chronic injuries [2], [3], [4], [5]. CO emissions from charcoal have also been used as a suicide method [6], [7], [8], [9].

Equipment has been designed to achieve the near-complete combustion of charcoal for maximum CO oxidation [10], [11], [12], [13], [14]. However, such systems are largely unsuccessful, because they still expose users to high concentrations of CO. The oxidation of CO is favoured by using metal/metal oxide catalysts or combinations thereof. However, the chemisorption of CO by metals varies according to the catalyst, with the heat of chemisorption increasing commensurate with the density of the metal surface for Pt, Rh and Ru catalysts, whereas Pd and Ir show the opposite profile. The heat of chemisorption can be ranked as follows: Pd ≈ Ir > Pt > Rh > Ru ≈ Ni > Co >> Cu. The heat of chemisorption on metal surfaces also declines with CO and O_2 coverage. Oxygen is chemisorbed in a dissociative manner on metal surfaces, with the heat of dissociative chemisorption ranked as follows: W > Mo > Fe > Co > Ir ≈ Ru > Rh ≈ Ni > Cu > Pt > Pd > Ag > Au [15].

The activity of metal and metal oxide catalysts is influenced by the presence or absence of a supporting material. For example, copper (ii) oxide (CuO) is unstable when unsupported, and the oxidation state of copper usually varies depending on temperature and the CO/O_2 ratio. The three oxidation states (Cu^{2+}, Cu^{+} and Cu^{0}) may coexist during a reaction. However, the presence of

a support such as zirconia or alumina increases the activity of CuO by up to 200-fold. Supported CuO catalysts are also more tolerant of inhibitors such as sulfur dioxide (SO_2). The support enhances the co-existence of Cu^{2+}, Cu^{+} and Cu^{0} species, especially when appropriate pre-treatments are applied or when the optimal set of supports is used, but the catalyst is deactivated by moisture [15].

Manganese and its oxides work best with other elements, such as copper, cobalt, nickel and lanthanum, forming manganites. This combination enhances the ability of Mn to catalyse the oxidation of CO. It forms three principal oxides: MnO_2, Mn_2O_3 and Mn_3O_4, with Mn_2O_3 showing the highest stability and activity. MnO_2 has four polymorphs (α, β, γ and δ) with α and δ achieving the most efficient CO oxidation. This is attributed to the strength of the Mn–O bond ($\beta > \gamma > \alpha > \delta$), with the strongest Mn-O bond associated with the weakest catalytic activity [15].

Fuchs *et al*. [16] found that the rate of CO adsorption onto a Pd catalyst was dependent on the oxidation of CO. The adsorption on the metal surface follows the Langmuir-Hinshelwood mechanism [17], [18]. Bi *et al*. [19] found that the efficiency of CO oxidation by Pd/NaZSM-5 declined at higher calcination temperatures and increased at higher Pd concentrations. The lower activity associated with calcination could reflect the greater crystallinity of the support and the less efficient metal/support interaction [20].

Kondrat *et al*. [21] found that the ability to control phase formation (Cu and Mn oxides) in a heated Cu-Mn/support catalyst allowed the catalytic potential for CO oxidation to be assessed. The presence of the Cu-Mn_2O_4 phase within the catalyst mix was associated with efficient CO oxidation. Both the retention of CO_2 as a by-product and contact with moisture poisoned the catalyst, but expelling the moisture at moderate temperatures restored its catalytic activity [22]. The catalytic activity of Cu-Mn generally decreases with temperature

[23]. Greater catalytic activity was also associated with more homogeneous catalysts during the oxidation of CO at ambient temperatures [24].

In all the studies cited above, CO was oxidised by passing the gas through or over a catalyst in either a fixed bed or a reactor. These studies did not attempt to improve the safety of charcoal by impregnating it with catalysts. Accordingly, we mixed the catalysts with charcoal to form a homogeneous product. Commercial Pd-Sn/alumina and Cu-Mn/graphite were used at different concentrations, and the catalyst activity was tested by heating the product isothermally at different temperatures in the range 300 – 600 °C with residual CO measurement and recording. The catalyst activity was tested by monitoring the residual CO evolved as a function of temperature and catalyst concentration.

6.2 Methodology

6.2.1 Materials

The charcoal used in this study was produced by the pyrolysis of wood in a sealed retort heated for 4 h at 500 °C using a controlled laboratory muffle furnace (the method is described in detail in Chapter 4). The charcoal was ground in an Essa LM2 pulverising mill and sieved through a 210-µm mesh. Commercial Pd-Sn/alumina and Cu-Mn/graphite catalysts purchased from Molecular Products Limited were mechanically mixed with the charcoal in different proportions 0.2, 1.0, 2.0, and 5.0 (wt%) using a mortar and pestle to achieve a homogeneous product.

6.2.2 Material characterisation

The commercial catalysts Pd-Sn/alumina and Cu-Mn/graphite as well as the catalyst-treated charcoal were characterised by thermogravimetric analysis (TGA), X-ray diffraction (XRD), and X-ray fluorescence (XRF). TGA was performed using a Mettler Toledo DSC/TGA3+ instrument in an air environment at 50 mL/min, in non-isothermal mode. Diffraction patterns were recorded with a Panalytical XPert diffractometer using Cu-Kα radiation. The powdered catalyst was loaded onto low-background-scattering (off-cut silicon) XRD holders. A PIXcel strip detector was used to collect data as stepped scans across an angular range of 10 to 80 2θ ($^{\circ}$). The quantities of elements present in the residual ash were determined using an SEA6000VX bench-top X-ray fluorescence instrument manufactured by Seiko Instruments (Nano Technology Inc) with a sample standard (RTC-CRM002-100G from LGC) and a Rh tube as the target. The measurement time was 100 s, with a 1.2 x 1.2 mm collimator/spot size, a tube voltage of 50 kV, a tube current of 314 µA in auto mode, no filter and He purging.

6.2.3 Testing catalyst activity

Approximately 200 mg of the catalyst-impregnated charcoal was tested for residual CO evolution. Charcoal samples were weighed (on an HF-300G analytical balance with an accuracy of ±0.002 g) into a quartz boat and loaded into a quartz tube (diameter = 35 mm, length = 550 mm) in a horizontal Carbolite tube furnace, which had been pre-heated to a set temperature with a regulated constant air flow. The experiments were conducted isothermally, and the temperature of the furnace was controlled using a Eurotherm CTFI-1200 controller. Samples were heated at 300, 320, 340, 360, 380, 400, 420, 440, 460, 480, 500, 520, 540, 560, 580 and 600 °C (±5 °C) and at an air flow rate of 2.0±0.1 L/min. Air flow was controlled using a calibrated (R^2 = 0.99) Platon

rotameter flow meter. The CO was passed through a 0.8 µm cellulose membrane filter to remove any smoke particles and fed into a CO sensor which gave an output to a Squirrel 1200 data logger and recorded voltages at a rate of four data points per minute. The logger display was regularly inspected during the heating period until the reading had fallen to zero CO (indicating emissions were below the detection limit for the sensor). The sensor was calibrated by injecting measured volumes of pure CO from a gas-tight syringe into several Tedlar bags which had been filled with air from a cylinder at a known flow rate for a known length of time. Calibration graphs were constructed to cover the range of concentrations that the sensors could measure. The calibration graph (R^2 = 0.99) was used to calculate the concentrations of CO.

6.2.4 Percentage residual CO

The residual amount of CO was computed using eqn. (6-1).

$$CO_{rT}\ (\%) = 100 - \frac{CO_0 - CO_c}{CO_0} * 100 \qquad (6\text{-}1)$$

where CO_{rT}, CO_0 and CO_c are the residual CO at any temperature T, CO from untreated charcoal and CO from catalyst-treated charcoal, respectively.

6.3 Results and discussion

The emission of CO from charcoal can be limited by impregnating the charcoal matrix with Cu-Mn and Pd-Sn catalysts. We investigated the decomposition profiles of the catalysts in air by TGA, and the phase composition of the as-received and heat-treated catalysts by using XRD. The composition of the resulting ash after combustion was analysed by XRF. The

residual CO levels are presented for catalyst-treated-charcoal samples as a function of temperature.

6.3.1 Thermogravimetric analysis of catalysts

Figure 6-1, shows the thermogravimetric and differential thermogravimetric (TG/DTG) data for the Cu-Mn/graphite and Pd-Sn/alumina catalysts in air (50 mL/min) at a heating rate of 10 °C/min. The first peak on the Pd-Sn/alumina profile at 114 °C corresponds to the loss of physically-bound moisture whereas the second peak at 272 °C corresponds to the loss of chemically-bound moisture from $Al(OH)_3$ to form AlOOH. The third peak at 467 °C corresponds to the final loss of chemically-bound moisture from AlOOH to form Al_2O_3. Similarly, the first peak on the Cu-Mn/graphite profile at 114 °C corresponds to the loss of physically bound moisture, but the remaining peaks involve the redox interactions among the catalyst metals. The second peak at 450 °C corresponds to the conversion of Cu^{2+} to Cu^{+}, the third peak at 500 °C corresponds to the conversion of $Mn^{2.7+}$ to $Mn^{3.2+}$, the forth peak at 550 °C corresponds to the conversion of $Mn^{3.2+}$ to $Mn^{3+,}$ and the peak at 660 °C may reflect the formation of copper metal from its ions [23]. The phase transformations were supported by XRD analysis of the as-received catalyst samples and after heat treatment at 600 °C as discussed below.

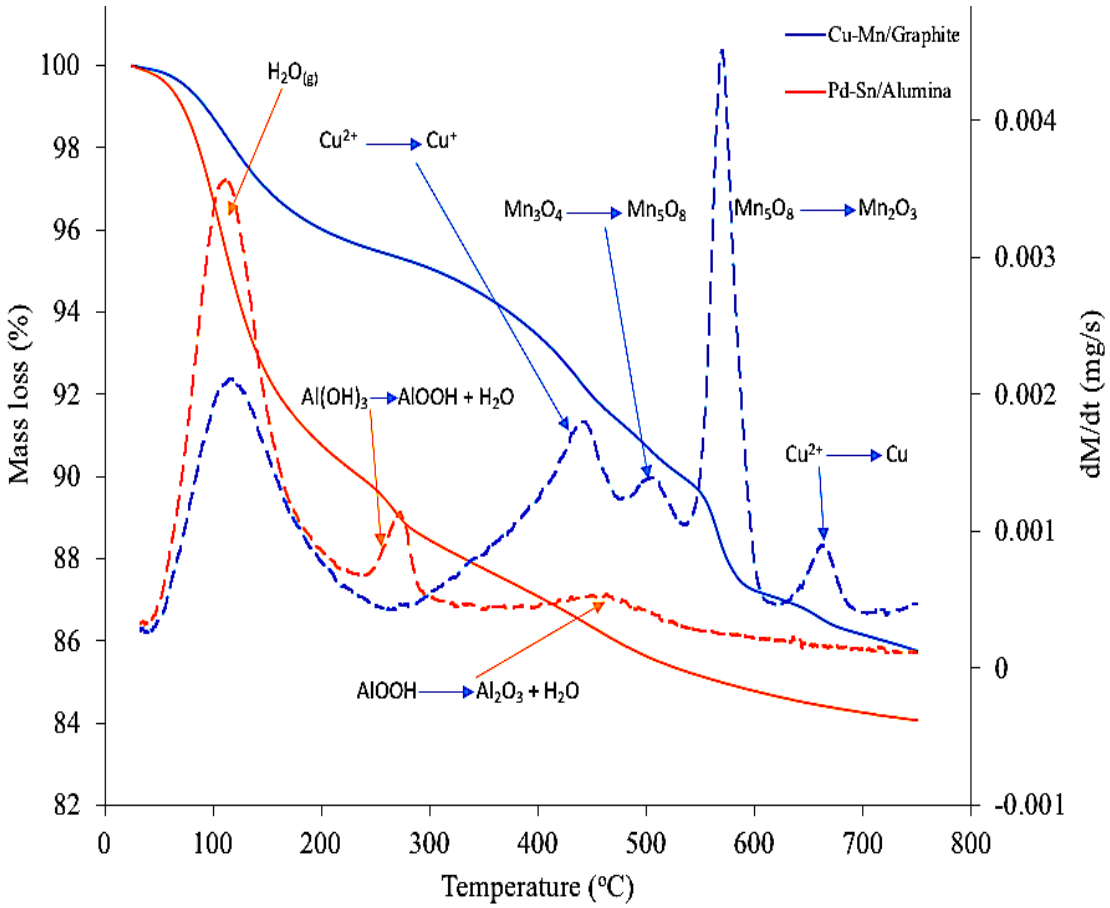

Figure 6-1: TG and DTG curves for the Pd-Sn/alumina and Cu-Mn/graphite catalysts in air (50 mL/min) at a heating rate of 10 °C/min.

6.3.2 X-ray diffraction

Figure 6-2(1) and (2) show the XRD data of the Cu-Mn/graphite and Pd-Sn/alumina catalysts. The phases MnO_2 (PDF 30-820), $CuMn_2O_4$ (PDF 74-2422) and graphite (PDF 23-64) were identified in the as-received Cu-Mn/graphite catalyst, but after heat treatment at 600 °C for 3 h, we identified the phases $Cu_{1.5}Mn_{1.5}O_4$ (PDF 35-1030), Mn_5O_8 (PDF 20-718), Mn_2O_3 (PDF 2-898) and graphite (PDF 23-64). The presence of Mn_5O_8 and Mn_2O_3 in the heat-treated catalyst is consistent with previous observations of Mn oxide phase transitions during the *in situ* calcination of Mn(II) glycolate [25]. The authors reported that Mn_3O_4 at 18.0 (°) was formed at ~185 °C after the Mn(II) glycolate peaks had disappeared. The decreasing intensity of Mn_3O_4 peaks was accompanied by an increase in the intensity of Mn_5O_8 at ~350 °C. At 550 °C, the peaks assigned

to Mn_5O_8 disappeared after the appearance of the more stable α-Mn_2O_3 reflection at 23.2 (°). The presence of $Cu_{1.5}Mn_{1.5}O_4$/CuO after the calcination of a Cu-Mn catalyst at 550 °C has also been reported [23].

In the as-received Pd-Sn/alumina catalyst, we observed the phases AlO(OH) (PDF 83-2384), $Al_2O_3.3H_2O$ (PDF 1-287) and Al_2O_3 (PDF 4-880), but after heat treatment as above we observed Al_2O_3 (PDF 4-880) and PdO (PDF 882434). Alumina (Al_2O_3) is manufactured mainly from its hydroxide. If the mother material remains in the final product, it undergoes dehydration to form more crystalline phases by calcination until the most stable phase is formed. The dehydration of aluminium hydroxide to form alumina is shown in eqn. (6-2) and eqn. (6-3).

$$Al(OH)_{3\,(s)} \rightarrow AlOOH_{(s)} + H_2O_{(g)} \qquad (6\text{-}2)$$

$$2AlOOH_{\,(s)} \rightarrow Al_2O_{3\,(s)} + H_2O_{(g)} \qquad (6\text{-}3)$$

The masking of the Pd-Sn peaks in the background of the XRD profile before heat treatment may reflect the low concentrations of Pd and Sn in the catalyst mixture relative to the alumina support. However, the AlO(OH) peaks disappeared after heat treatment, revealing the PdO phase, as previously suggested [19].

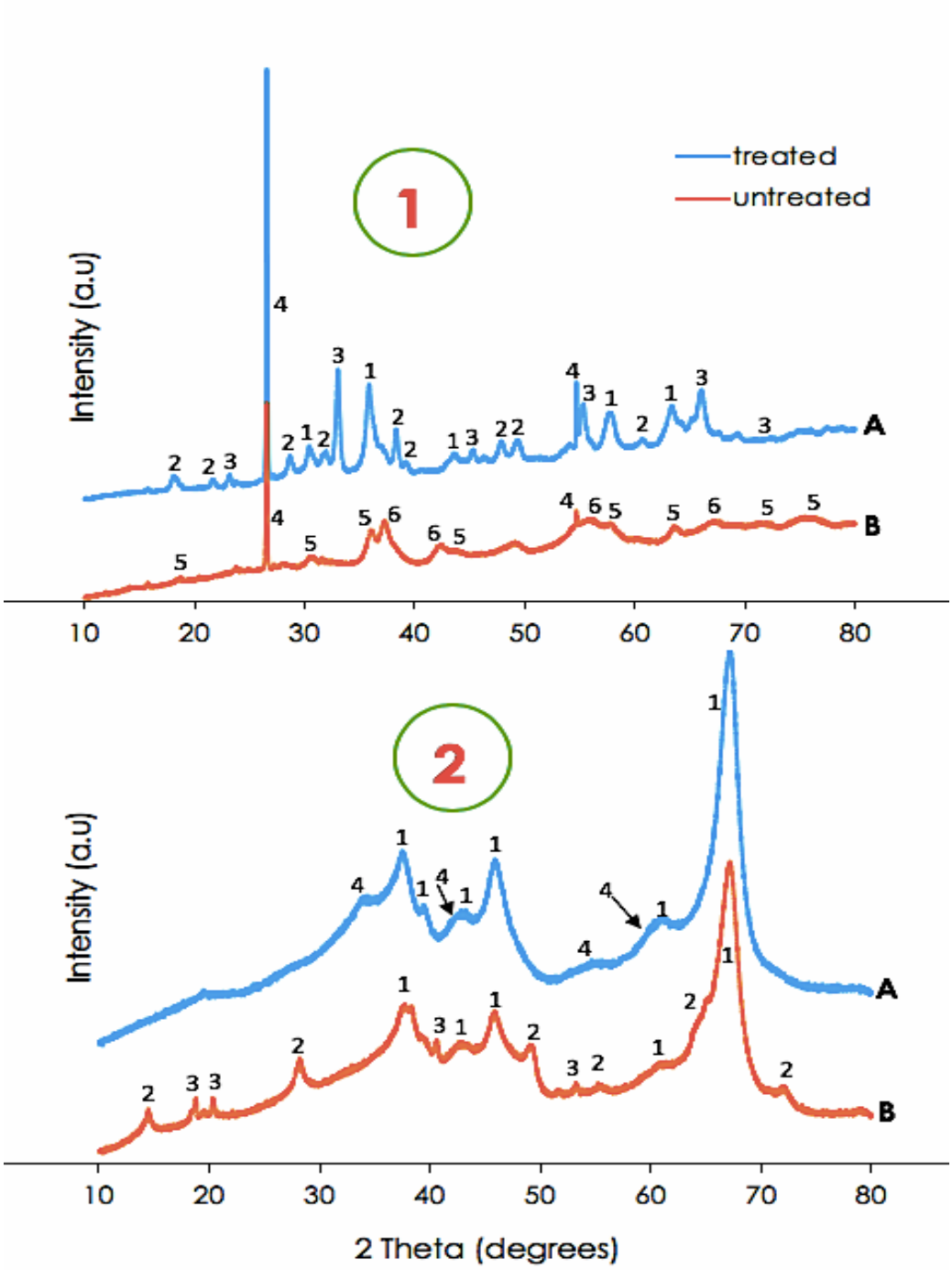

Figure 6-2: (1) - XRD profile of the Cu-Mn/graphite catalyst: A - after heat treatment at 600 °C for 3 h, and B – before heat treatment. The numbers 1, 2, 3, 4, 5 and 6 represent the phases $Cu_{1.5}Mn_{1.5}O_4$, Mn_5O_8, Mn_2O_3, C (graphite), $CuMn_2O_4$, and MnO_2 respectively. (2) - XRD profile of Pd-Sn/alumina: A - after heat treatment at 600 °C for 3 h, and B – before heat treatment. The numbers 1, 2, 3 and 4 represent the phases Al_2O_3, AlO(OH), $Al_2O_3.3H_2O$ and PdO respectively.

6.3.3 X-ray fluorescence

The concentrations of trace elements in the ash as percentages by weight were 43.8 % SiO, 29.8 % CaO, 13.8 % P_2O_5, 10.6 % K_2O, 0.9 % FeO, 1.2 % MgO and 0.7 % Al_2O_3. The concentrations of trace elements in charcoal could affect the activity of the catalysts by reacting with and/or poisoning the catalyst, e.g. S and P can inhibit Pd catalysts [26]. Secondly, the build-up of product gases from combustion also deactivates Pd catalysts, although they can be regenerated using organic polar solvents. Sulphur also poisons Cu catalysts during methanol synthesis, which involves the reaction of CO with H [26]. However, the impact of these trace elements on catalyst activity was not investigated in the current study.

6.3.4 The activity of Cu-Mn/graphite & Pd-Sn/alumina for CO oxidation

Catalysts act by physically or chemically adsorbing reactants onto their surfaces where the reaction is subsequently facilitated. CO is adsorbed onto Pd at four binding sites (Atop, Bridge, FCC and Hcp), and higher catalytic efficiency correlates with lower CO saturation coverage and lower CO binding energies [27]. Furthermore, adsorbed CO can be observed on the Mn catalyst, where Mn doping facilitates oxygen vacancy formation and Mn adatoms inhibit this process [28]. Oxygen (O) atoms on the Pd surface increase the binding energy due to mutual lateral repulsion [29]. The interaction between O and Pd causes strong electrostatic repulsion between adsorbates which reduces the adsorption energy with increasing coverage. There is a general decrease in the heat of chemisorption on transition metal surfaces with CO and O_2 coverage that could be linked to the metallic radius of the catalysts [15].

Figure 6-3 shows the residual amounts of CO detected for catalyst-treated charcoal heated to 300 – 600 °C in air at a flow rate of 2 L/min. The amount of residual CO was related to temperature, but the relationship was non-linear. Argyle *et al*. [26] showed that Pd and Cu catalysts are denatured at high temperatures via a sintering process, and proposed that reaction temperatures should be restricted to 33 – 50 % of the melting point of the metal catalysts to prevent sintering, consistent with earlier reports [19],[23],[30] .

When we impregnated the charcoal with 5 wt% Cu-Mn/graphite catalyst, the residual CO levels ranged from 16.7 % to 41.7 %, whereas the equivalent values for the 2 wt% Cu-Mn/graphite catalyst were 15.6 % to 25.3 %. On the other hand, the charcoal mixed with Pd-Sn/alumina released less CO than the charcoal mixed with Cu-Mn/graphite. When we impregnated the charcoal with 1 wt% Pd-Sn/alumina catalyst, the residual CO levels ranged from 3.5 % to 31.6 %, but when the quantity of catalyst was reduced to 0.2 wt% the residual CO levels ranged from 26.9 % to 44.4 %. The increase in activity with catalyst loading is consistent with earlier observations [15], [19].

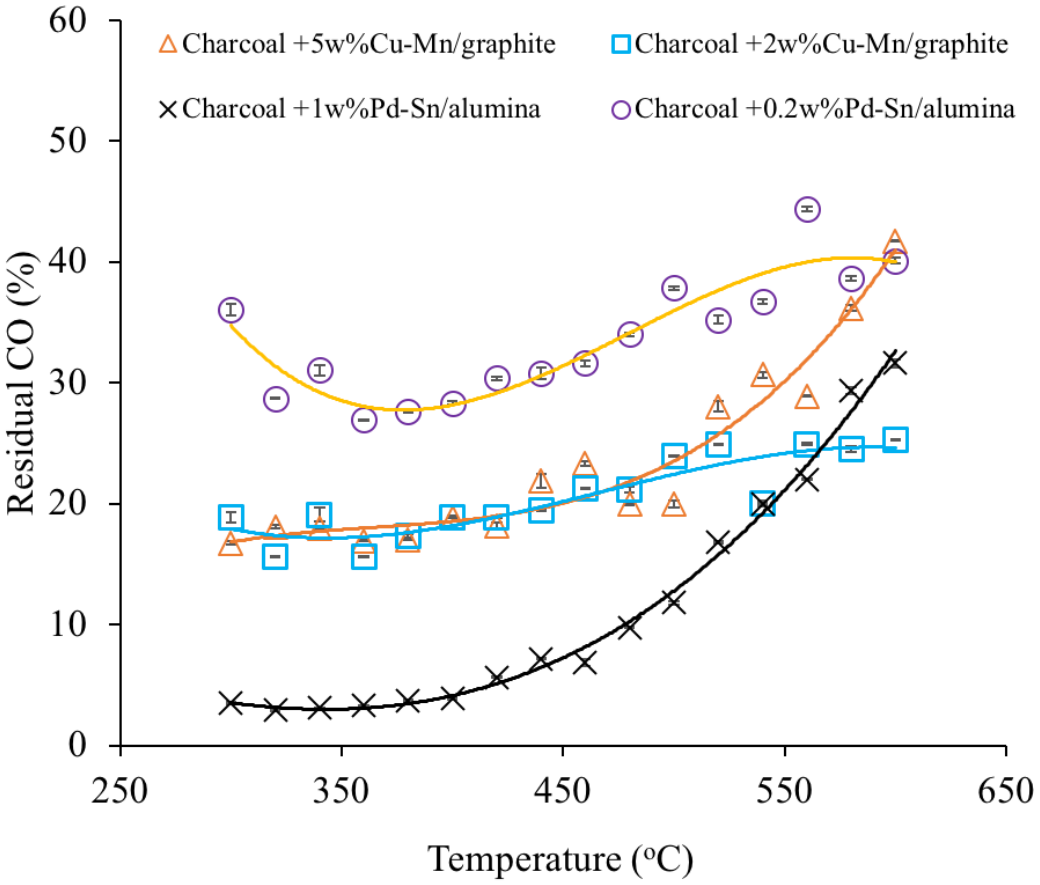

Figure 6-3: Residual CO levels recorded for catalyst-treated charcoal.

Summary & Conclusions

In this study, charcoal was mechanically impregnated with catalysts to minimise the CO levels released during isothermal combustion. Two commercial catalysts were used: Pd-Sn/alumina and Cu-Mn/graphite. When 1 wt% Pd-Sn/graphite was used as the catalyst, the lowest residual CO level in the charcoal was 3.5 %, but this increased to 26.9 % when 0.2 wt% Pd-Sn/graphite was present. On the other hand, when 5 wt% Cu-Mn/graphite was used as the catalyst, the lowest residual CO level in the charcoal was 16.7 %, and this fell slightly to 15.6 % when 2 % Cu-Mn/graphite was present. Pd-Sn/alumina was a better catalyst for CO oxidation in this study. In all cases of catalyst testing, the activity decreased with temperature. The lower activity of the catalysts may have reflected a combination of fewer active phases,

thermal deactivation, and the presence of trace elements in the charcoal ash. However, the effect of trace elements was not investigated in this study. The catalysts used in this study could be scaled-up for the commercial production of catalyst-treated charcoal that is safer for domestic and industrial applications. The method could also be used to produce catalyst-treated sawdust briquettes, wood boiler chips and other solid materials to minimise the amounts of CO released from combustion reactions.

Acknowledgments

The authors thank the Hazel Woodhams Memorial Fund, Gas Safety Trust, Boat Safety Scheme and Katie Haines for sponsoring this work. We also thank Charlene Greenwood, Peter Wilkinson and Nicola Darcy for assisting at some stages of the experimental work.

References

[1] H.L. Huang, W.M.G. Lee, F.S. Wu, Emissions of air pollutants from indoor charcoal barbecue, J. Hazard. Mater. 302 (2016) 198–207. doi:10.1016/j.jhazmat.2015.09.048.

[2] D. Bosch, Unintentional domestic non-fire related carbon monoxide poisoning: Data from media reports, UK/Republic of Ireland 1986-2011: Fisher DS, Bowskill S, Saliba L, Flanagan RJ. Clin Toxicol (Phila) 2013;51:409-16., J. Emerg. Med. 45 (2013) 312. doi:10.1016/j.jemermed.2013.06.014.

[3] I. Dianat, J. Nazari, Characteristics of unintentional carbon monoxide poisoning in Northwest Iran--Tabriz., Int. J. Inj. Contr. Saf. Promot. 18 (2011) 313–20. doi:10.1080/17457300.2011.589006.

[4] J. Nazari, I. Dianat, A. Stedmon, Unintentional carbon monoxide poisoning in northwest iran: A 5-year study, J. Forensic Leg. Med. 17 (2010) 388–391. doi:10.1016/j.jflm.2010.08.003.

[5] L. Bennetto, L. Powter, N.J. Scolding, Accidental carbon monoxide poisoning presenting without a history of exposure: a case report., J. Med. Case Rep. 2 (2008) 118. doi:10.1186/1752-1947-2-118.

[6] Y.Y. Chen, O. Bennewith, K. Hawton, S. Simkin, J. Cooper, N. Kapur, D. Gunnell, Suicide by burning barbecue charcoal in England, J. Public Heal. (United Kingdom). 35 (2013) 223–227.

doi:10.1093/pubmed/fds095.
[7] P.R. Nielsen, A. Gheorghe, N. Lynnerup, Forensic aspects of carbon monoxide poisoning by charcoal burning in Denmark, 2008-2012: An autopsy based study, Forensic Sci. Med. Pathol. 10 (2014) 390–394. doi:10.1007/s12024-014-9574-3.
[8] A.C.W. Lee, Y. Ou, S.Y. Lam, K.T. So, C.W. Kam, Non-accidental carbon monoxide poisoning from burning charcoal in attempted combined homicide-suicide, J. Paediatr. Child Health. 38 (2002) 465–468. doi:10.1046/j.1440-1754.2002.00019.x.
[9] E. Yoshioka, S.J.B. Hanley, Y. Kawanishi, Y. Saijo, Epidemic of charcoal burning suicide in Japan, Br. J. Psychiatry. 204 (2014) 274–282. doi:10.1192/bjp.bp.113.135392.
[10] J.J. Jetter, P. Kariher, Solid-fuel household cook stoves: Characterization of performance and emissions, Biomass and Bioenergy. 33 (2009) 294–305. doi:10.1016/j.biombioe.2008.05.014.
[11] K.R. Smith, M. a K. Khalil, R.A. Rasmussen, S.A. Thorneloe, F. Manegdeg, M. Apte, Greenhouse Gases from Biomass and Fossil-Fuel Stoves in Developing-Countries - a Manila Pilot-Study, Chemosphere. 26 (1993) 479–505. doi:10.1016/0045-6535(93)90440-G.
[12] Q. Li, J. Jiang, J. Qi, J. Deng, D. Yang, J. Wu, L. Duan, J. Hao, Improving the Energy Efficiency of Stoves to Reduce Pollutant Emissions from Household Solid Fuel Combustion in China, Environ. Sci. Technol. Lett. 3 (2016) 369–374. doi:10.1021/acs.estlett.6b00324.
[13] M. Ezzati, B.M. Mbinda, D.M. Kammen, Comparison of emissions and residential exposure from traditional and improved cookstoves in Kenya, Environ. Sci. Technol. 34 (2000) 578–583. doi:10.1021/es9905795.
[14] M.A. Johnson, R.A. Chiang, Quantitative guidance for stove usage and performance to achieve health and environmental targets, Environ. Health Perspect. 123 (2015) 820–826. doi:10.1289/ehp.1408681.
[15] S. Royer, D. Duprez, Catalytic Oxidation of Carbon Monoxide over Transition Metal Oxides, ChemCatChem. 3 (2011) 24–65. doi:10.1002/cctc.201000378.
[16] S. Fuchs, T. Hahn, H.G. Lintz, Oxidation of carbon monoxide by oxygen over platinum, palladium and rhodium catalysts from 10^-10 to 1 bar, Chem. Eng. Process. 33 (1994) 363–369. doi:10.1016/0255-2701(94)02007-8.
[17] Y. Li, Y. Yu, J.G. Wang, J. Song, Q. Li, M. Dong, C.J. Liu, CO oxidation over graphene supported palladium catalyst, Appl. Catal. B Environ. 125 (2012) 189–196. doi:10.1016/j.apcatb.2012.05.023.
[18] M.D. Esrafili, P. Nematollahi, R. Nurazar, Pd-embedded graphene: An efficient and highly active catalyst for oxidation of CO, Superlattices Microstruct. 92 (2016) 60–67. doi:10.1016/j.spmi.2016.02.006.
[19] Y. Bi, G. Lu, Catalytic CO oxidation over palladium supported NaZSM-5 catalysts, Appl. Catal. B Environ. 41 (2003) 279–286. doi:10.1016/S0926-3373(02)00166-2.
[20] F. Wang, Y. Xu, K. Zhao, D. He, Preparation of Palladium Supported on Ferric Oxide Nano-catalysts for Carbon Monoxide Oxidation in Low

Temperature, Nano-Micro Lett. 6 (2014) 233–241. doi:10.1007/BF03353787.
[21] S.A. Kondrat, T.E. Davies, Z. Zu, P. Boldrin, J.K. Bartley, A.F. Carley, S.H. Taylor, M.J. Rosseinsky, G.J. Hutchings, The effect of heat treatment on phase formation of copper manganese oxide: Influence on catalytic activity for ambient temperature carbon monoxide oxidation, J. Catal. 281 (2011) 279–289. doi:10.1016/j.jcat.2011.05.012.
[22] E.C. Njagi, C.-H. Chen, H. Genuino, H. Galindo, H. Huang, S.L. Suib, Total oxidation of CO at ambient temperature using copper manganese oxide catalysts prepared by a redox method, Appl. Catal. B Environ. 99 (2010) 103–110. doi:10.1016/j.apcatb.2010.06.006.
[23] S.N. Basahel, E.H. El Mossalamy, M. Mokhtar, Preparation and physicochemical characterisation of thermally stable nano-sized hopcalite catalysts, Int. J. Nanomanuf. 4 (2009) 159. doi:10.1504/IJNM.2009.028122.
[24] T.J. Clarke, T.E. Davies, S.A. Kondrat, S.H. Taylor, Mechanochemical synthesis of copper manganese oxide for the ambient temperature oxidation of carbon monoxide, Appl. Catal. B Environ. 165 (2015) 222–231. doi:10.1016/j.apcatb.2014.09.070.
[25] M. Augustin, D. Fenske, I. Bardenhagen, A. Westphal, M. Knipper, T. Plaggenborg, J. Kolny-Olesiak, J. Parisi, Manganese oxide phases and morphologies: A study on calcination temperature and atmospheric dependence, Beilstein J. Nanotechnol. 6 (2015) 47–59. doi:10.3762/bjnano.6.6.
[26] M. Argyle, C. Bartholomew, Heterogeneous Catalyst Deactivation and Regeneration: A Review, Catalysts. 5 (2015) 145–269. doi:10.3390/catal5010145.
[27] R. Chen, Z. Chen, B. Ma, X. Hao, N. Kapur, J. Hyun, K. Cho, B. Shan, CO adsorption on Pt (111) and Pd (111) surfaces: A first-principles based lattice gas Monte-Carlo study, Comput. Theor. Chem. 987 (2012) 77–83. doi:10.1016/j.comptc.2011.07.015.
[28] L.-C. Hsu, M.-K. Tsai, Y.-H. Lu, H.-T. Chen, Computational Investigation of CO Adsorption and Oxidation on Mn/CeO_2 (111) Surface, J. Phys. Chem. C. 117 (2013) 433–441. doi:10.1021/jp310457g.
[29] J. Shah, S. Kansara, S.K. Gupta, Y. Sonvane, Oxygen adsorption on palladium monolayer as a surface catalyst, Phys. Lett. Sect. A Gen. At. Solid State Phys. 381 (2017) 3084–3088. doi:10.1016/j.physleta.2017.07.024.
[30] K.I. Ivanov, E.N. Kolentsova, D.Y. Dimitrov, Alumina Supported Copper-Manganese Catalysts for Combustion of Exhaust Gases : Effect of Preparation Method, Int. J. Chem. Mol. Nucl. Mater. Metall. Eng. 9 (2015) 298–307.

Chapter 7: CATALYTIC EFFECTS ON THE NON-ISOTHERMAL OXIDATION OF SOLID FUELS BY OXYGEN: AN EXPERIMENTAL STUDY

The work contained in this chapter has been published in Energy & Fuels journal.

Citation: Antony Nyombi, Mike Williams, Roland Wessling (2019): Catalytic Effects On The Non-Isothermal Oxidation Of Solid Fuels By Oxygen: An Experimental Study. DOI: https://doi.org/10.1021/acs.energyfuels.9b02514

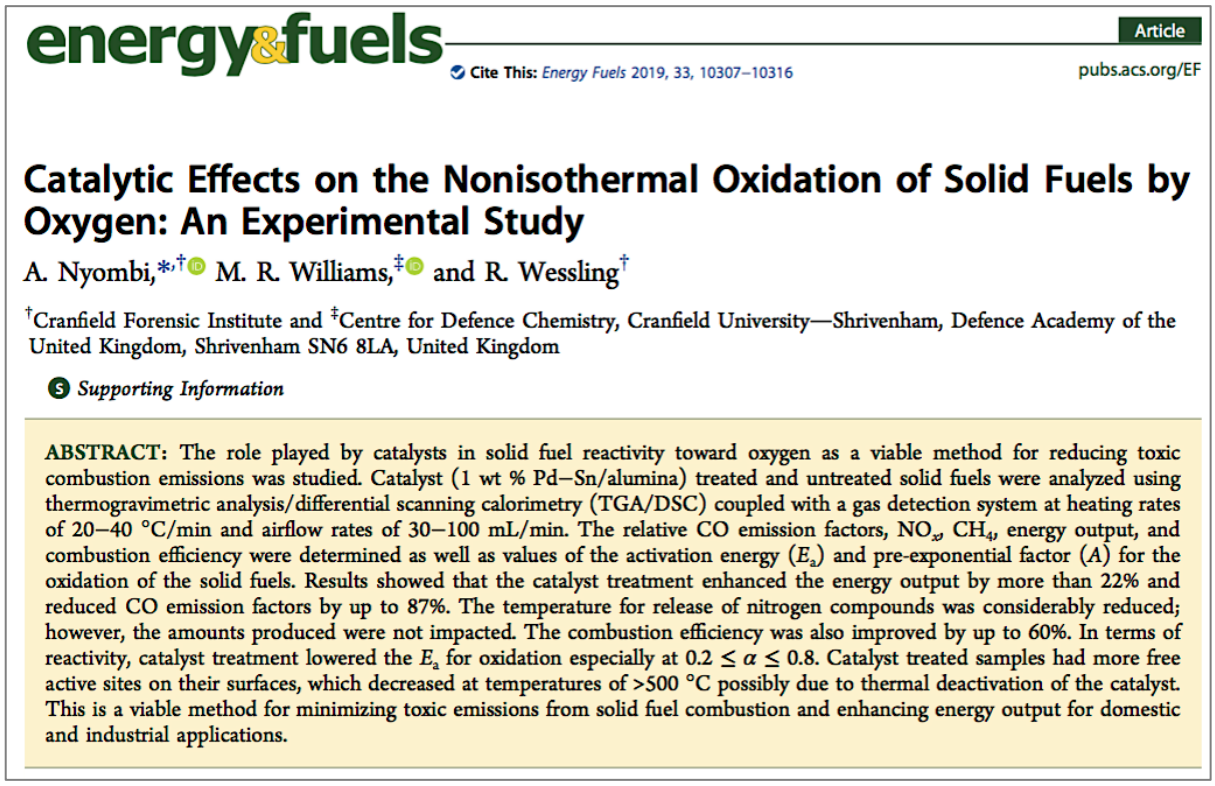

energy&fuels

Article

Cite This: *Energy Fuels* 2019, 33, 10307−10316

pubs.acs.org/EF

Catalytic Effects on the Nonisothermal Oxidation of Solid Fuels by Oxygen: An Experimental Study

A. Nyombi,*,† M. R. Williams,‡ and R. Wessling†

†Cranfield Forensic Institute and ‡Centre for Defence Chemistry, Cranfield University—Shrivenham, Defence Academy of the United Kingdom, Shrivenham SN6 8LA, United Kingdom

Supporting Information

ABSTRACT: The role played by catalysts in solid fuel reactivity toward oxygen as a viable method for reducing toxic combustion emissions was studied. Catalyst (1 wt % Pd−Sn/alumina) treated and untreated solid fuels were analyzed using thermogravimetric analysis/differential scanning calorimetry (TGA/DSC) coupled with a gas detection system at heating rates of 20−40 °C/min and airflow rates of 30−100 mL/min. The relative CO emission factors, NO_x, CH_4, energy output, and combustion efficiency were determined as well as values of the activation energy (E_a) and pre-exponential factor (A) for the oxidation of the solid fuels. Results showed that the catalyst treatment enhanced the energy output by more than 22% and reduced CO emission factors by up to 87%. The temperature for release of nitrogen compounds was considerably reduced; however, the amounts produced were not impacted. The combustion efficiency was also improved by up to 60%. In terms of reactivity, catalyst treatment lowered the E_a for oxidation especially at $0.2 \leq \alpha \leq 0.8$. Catalyst treated samples had more free active sites on their surfaces, which decreased at temperatures of >500 °C possibly due to thermal deactivation of the catalyst. This is a viable method for minimizing toxic emissions from solid fuel combustion and enhancing energy output for domestic and industrial applications.

Catalytic Effects on The Non-Isothermal Oxidation of Solid Fuels by Oxygen: An Experimental Study

Highlights

The reactivity of Pd-Sn/alumina treated and untreated solid fuels were compared. With catalyst treatment;

- CO emissions factors reduced by 87 %,
- Reduced CO/CO_2 ratio by 7-fold
- Increased combustion efficiency by 60 %,
- Increased free active sites on solid fuel surfaces and
- Reduced the temperature for release of NO_x emissions

Abstract

The role played by catalysts in solid fuel reactivity towards oxygen as a viable method for reducing toxic combustion emissions was studied. Catalyst (1 wt% Pd-Sn/alumina) treated, and untreated solid fuels were analysed using thermogravimetric analysis/differential scanning calorimetry (TGA/DSC) coupled with a gas detection system at heating rates 20 – 40 °C/min and airflow rates 30 – 100 mL/min. The relative CO emission factors, NO_x, CH_4, energy output, and combustion efficiency were determined as well as the activation energies (E_a) and pre-exponential factors (A) for the oxidation of the solid fuels. Results showed that the catalyst treatment enhanced the energy output by more than 22 % and reduced CO emission factors by up to 87 %. The temperature for release of nitrogen compounds was considerably reduced;

however, the amounts produced were not impacted. The combustion efficiency was also improved by up to 60 %. In terms of reactivity, catalyst treatment lowered the E_α for oxidation especially at $0.2 \leq \alpha \leq 0.8$. Catalyst treated samples had more free active sites on their surface, which decreased at temperatures > 500 °C possibly due to thermal deactivation of the catalyst. This is a viable method for minimising toxic emissions from solid fuel combustion and enhancing energy output for domestic and industrial applications.

7.1 Introduction

Solid fuels (coal, lump charcoal, and charcoal briquettes) are extensively used for home and recreational cooking applications. Due to insufficient oxygen availability during combustion, fuel-rich conditions that produce toxic emission are created at mid-to-high temperatures (300 – 800 °C). The toxic emissions (carbon monoxide, nitrous oxide, etc.) from incomplete solid fuel combustion have caused several fatalities and chronic illnesses [1], [2], [3], [4], [5], [6].

To reduce the emissions of toxic gases from solid fuel combustion systems, technologically advanced/improved cookstoves [7], [8], [9], that use forced draft systems, with electric fans [10] and chimneys have been used. These enhance the air circulation around the fuel improving the air-to-fuel ratio hence reducing the combustion emissions, as well as drawing out any released pollutant through the stack. Other stoves use a catalyst layer/mesh just above the solid fuel [11] to oxidise the toxic emissions during combustion while other fix the catalyst mesh in the stack of an improved cookstove [12] for the same purpose.

In domestic heaters and boilers, air-staging/two-stage combustion has been used as an effective way to reduce toxic emissions [13]. This involves supplying secondary air to aid further oxidation of flue gases from primary combustion

hence reducing toxic gases [14], [15]. Others use a combination of air staging and catalyst layers [16] in stacks to further oxidise unreacted toxic emissions.

The use of CO detectors/alarms [17] for warning against lethal combustion emissions has been embraced extensively. Some sensors are colorimetric [18], forming colored complexes as the concentrations of pollutants change [19]. Others are electrochemical which work by converting CO to CO_2 that is detected using an electrolyte [20] between a working and a counter electrode. Semi-conductor sensors have been the most used [21], [22], [23] employing transition metal oxides like SnO combined with other metal oxides. The above-mentioned methods for reducing combustion emissions work in the post-combustion mode (reducing already released emissions); hence a more robust method that minimises toxic emissions from the source is needed.

To develop a unique product that releases reduced toxic gases during cooking operations, this work draws motivation from several studies that were performed to enhance desired products during solid fuel pyrolysis / combustion / gasification. These involved the addition of catalysts on solid fuels. Inorganic mineral salts [24] particularly potassium (K) salts [25] decreased the temperature at which maximum degradation occurs. Char yields are also increased upon impregnation of K [26].

Potassium also reduced torrefaction time by over 28 % [27]. Tungsten carbide (W_2C/alumina) [28], molybdenum carbide Mo_2C/support [29] have been impregnated on biomass as effective hydrodeoxygenation agents of biomass-derived small oxygenates, phenolics and furan derivatives. This method has been used for the selective production of aromatic hydrocarbons from lignocellulosic biomass *via* catalytic fast-hydropyrolysis by removing sulfur, nitrogen, oxygen, and metals. In another study, waste ashes containing Al, Ca, Mg, Cu and Fe, K, Na, and Zn were impregnated with 10 % Ni to enhance hydrogen-rich gas yield by over 15 % from biomass [30]. Catalyst impregnation

works in real-time (in heterogeneous reactions) to effect desired products hence; using such a method will ensure that the cooking products (char) are safer from toxic emissions regardless of where they are used.

The objectives of this study, therefore, were to investigate and quantify the difference in reactivity of catalyst (Pd-Sn/alumina) treated charcoal briquettes (CTCB) in comparison to untreated charcoal briquettes (UTCB), commercial lump charcoal (ComC) and coal in the air (21 % oxygen). Experimental studies were conducted to compare the emission of carbon monoxide, carbon dioxide, nitrogen oxides, and methane as well as the energy released from combustion and the combustion efficiency. All the experiments were carried out at different heating rates (20, 25, 30, and 40 °C/min) and airflow rates (30, 50, 80 and 100 mL/min), with temperatures ranging from 50 – 800 °C.

The difference in reactivities was quantified at different conversion levels of the solid fuels in terms of activation energies, and pre-exponential factors. This study expands on our previous work [31] in which catalyst impregnation was done on charcoal but the experiments were done isothermally in a tube furnace, yet real-life combustion occurs non-isothermally. Secondly, only CO emissions were quantified, and the temperature range was 300 – 600 °C, and thirdly, this study uses laboratory manufactured charcoal briquettes similar to products on the market.

7.2 Materials & methods

7.2.1 Materials

The CTCB and UTCB were prepared in the laboratory using non-standard recipes developed to maximise the desired product. The recipes contained: (i)

charcoal fines (< 400 μm particle size) as the main fuel, wood sawdust (< 400 μm particle size) as an ignition enhancer, and cassava flour as the binder for UTCB (ratio: 20:2:1). (ii) Charcoal fines (< 400 μm particle size) as the main fuel, wood sawdust (< 400 μm particle size) as an ignition enhancer, cassava flour as the binder and 1 wt% Pd-Sn/alumina as the catalyst for CTCB (ratio: 20:2:1:0.25). The charcoal used for these recipes was prepared by laboratory pyrolysis of wood as per our previous method [32]. Appropriate amounts of water were added to the solid components and mixed thoroughly with an auto blender to form a paste that was extruded with a mould, dried and stored for subsequent analysis. Figure 7-1, shows the extruded dry charcoal briquettes. The ComC and coal used in this study were obtained from sales stores.

Figure 7-1: Charcoal briquettes

7.2.2 Experimental set-up

The experimental set-up is as shown in Figure 7-2. Four samples were analysed: CTCB, UTCB, ComC, and coal. Dried powdered sample aliquots of 3 – 5 mg were inserted into alumina crucibles and loaded onto the Mettler Toledo TGA/DSC3+. The outlet from the chamber of the TGA/DSC was connected to a MultiRae lite gas analyser calibrated for CO, CO_2, NO_x, and CH_4. The resolution of the gas analyser is 1 ppm for CO, 0.1 ppm for NOx and 100 ppm

for CO_2. The gas analyser uses a pumped model operation to suck gases on to its sensors at a rate of 2 liters per minute. The MultiRae lite gas analyser was programmed to auto-log data at a rate of a single data point per minute.

Combustion experiments were carried out non-isothermally (in triplicate) at 20, 25, 30 and 40 °C/min heating rates from 50 to 800 °C and airflow rates of 30, 50, 80 and 100 mL/min. The proximate analysis was performed as per the methods described elsewhere [33]. Since the gas analyser pump required 2 L/min of air, a connection to dry air from a cylinder was added to top-up the total flow during each experiment. The gas analyser is equipped with filters at the inlet for volatile organic compounds (VOCs), particulate matter and moisture to avoid damage to the sensors and ensuring accuracy and reproducibility of results. Blank runs with dry air only were performed every after a sample runs for 30 minutes to ensure the MultiRae lite gas analyser was fresh for the next sample.

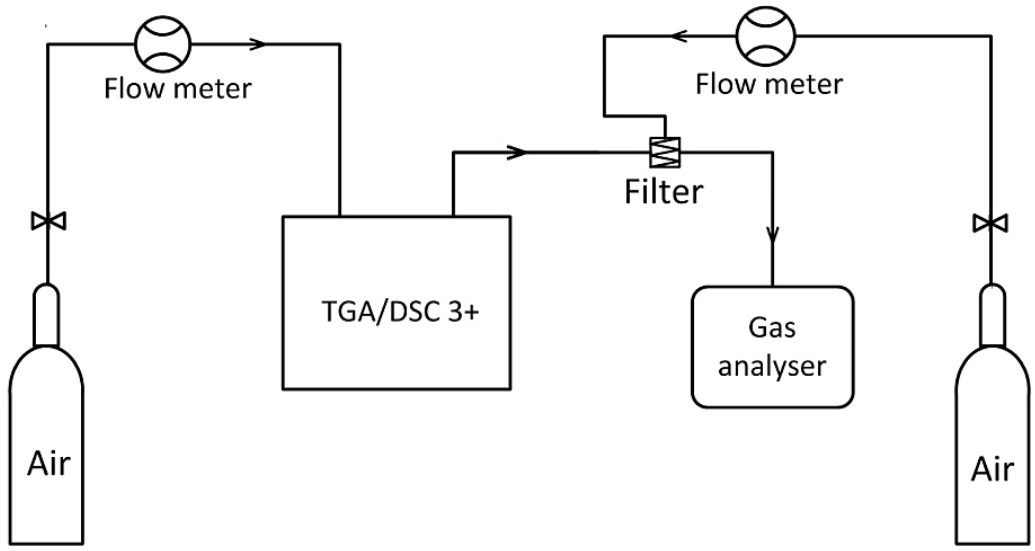

Figure 7-2: Experimental set-up for the combined TGA/DSC and evolved gas analysis

The computation of CO emission factors was performed as per the method described in our previous work [34].

Specific surface area (SSA) was determined using the ASAP2020 Micromeritics Surface Area and Porosity Analyser instrument. Samples (0.5 – 1.0 g) were degassed at 200 °C for 120 minutes. SSA analysis was done using nitrogen and helium gases. The following steps were performed:

i. The surface of a known mass of sample (0.5 – 1.0 g) was cleared of all adsorbed gases and moisture by vacuuming, heating, and purging with nitrogen gas (a process called "degassing").
ii. The sample was then cryogenically cooled, with liquid nitrogen (77 K).
iii. The adsorbate gas, (nitrogen) was then dosed into the system at a series of reduced pressures (p/p_0), where p is the pressure of the adsorbate gas and p_0 is its saturation pressure.
iv. The gas was then adsorbed and the system was allowed to equilibrate, after which time the resultant pressure over the sample was measured.
v. The amount of gas adsorbed by the sample at each reduced pressure point was then used to construct an isotherm.
vi. The Brunauer-Emmett-Teller (BET) theory was then applied to the raw data, which gave the SSA of the sample.

The procedure above was performed for both the reference standard and the sample whose SSA was required.

7.3 Results and discussions

7.3.1 General properties of the solid fuels

The energy released from the combustion of CTCB, UTCB, ComC, and coal as well as the proximate analysis and SSA are shown in Table 7-1. The energy produced from each solid fuel was calculated from integrals of the exotherm peaks for each run and expressed as kJ/g. This energy increased with airflow

due to increased oxygen availability and decreased with the heating rate. Secondly, CTCB produced up to 6.7 % more energy compared to UTCB; up to 22.3 % more energy compared to ComC and 14.8 % more energy than commercial coal. In general, the high energy output from CTCB was attributed to enhanced combustion facilitated by oxygen adsorbed on the catalyst surfaces. The energy output of fuels analysed was directly linked to their volatile matter (VM) content: the higher the VM, the higher the energy released. ComC had the highest SSA while coal had the lowest *SSA*. The low SSA for coal could be attributed to its lack of sufficient porosity.

Table 7-1: Energy released from combustion, proximate analysis and Specific surface area (SSA)

	kJ/g	M (wt%)	FC (wt%)	VM (wt%)	RA (wt%)	SSA (m^2/g)
CTCB	25.33±0.48	1.52±0.11	2.71±0.20	91.8±0.69	3.88±0.87	67.3
UTCB	23.64±1.26	1.64±0.24	3.04±0.50	91.0±0.69	4.32±0.08	78.3
ComC	19.70±0.25	1.09±0.24	4.8±0.19	68.15±1.29	25.96±1.00	82.2
Coal	21.57±1.22	0.95±0.06	3.54±0.48	88.58±0.33	6.93±0.43	27.0

CTCB-Catalyst treated charcoal briquettes; UTCB-Untreated charcoal briquettes; ComC-Commercial charcoal; M-Moisture content; FC-Fixed carbon; VM-Volatile matter; RA-Residual ash; SSA – Specific surface area

7.3.2 CO emissions trends

The emission of CO from the solid fuels took different patterns during the combustion process:

i. CTCB underwent four CO emission stages, Figure 7-3A. The first positive steep phase between 290 – 350 °C (CO values reaching 15 ppm as lowest and 25 ppm as highest) was attributed to release of CO from pyrolysis as a result of enhanced temperatures in sawdust and cassava binder due to the impregnated metal catalyst. Previous research has proved that metal impurities enhance the combustion temperature during combustion [35].

The second low gradient phase happened between 370 – 450 °C, in which maximum adsorption of oxygen and CO onto the catalyst surface took place resulting to maximum oxidation of CO to CO_2 (CO values increased by 2 ppm as lowest and 5 ppm as highest). The third stage happened between 470 – 500 °C where the catalyst continuously lost activity due to sintering as temperature increased until most of the charcoal was burnt (CO values increased by 5 ppm as lowest and 15 ppm as highest). The last phase occurred between 500 – 570 °C when the remaining carbon was decomposed as well as the decay of the accumulated CO.

ii. The UTCB (Figure 7-3B) had an initial slow release of CO between 290 – 370 °C from pyrolysis of hemicellulose, cellulose, and breakdown unstable surface oxide complexes from sawdust and cassava binder (CO values reached about 25 ppm). The second phase was a positive steep gradient from 380 – 500 °C attributed to the decomposition of the main char matrix (CO values increased by 120 ppm as lowest and 230 ppm as highest). The last stage between 530 – 620 °C involved the breakdown of any remaining carbon as well as wash-out of accumulated CO.

iii. The ComC (Figure 7-3C) had an initial slow release of CO between 340 – 430 °C from the breakdown of unstable surface oxide functional groups (CO values increased to 20 ppm as lowest and 50 ppm as highest). The second positive steep stage from 440 – 500 °C corresponded to the decomposition of the main char material (CO values increased by 110 ppm as lowest and 150 ppm as highest). The last stage between 530 – 700 °C involved breakdown of any remaining lignin in charcoal as well as decay of accumulated CO.

iv. Coal (Figure 7-3D) had an initial slow release of CO between 350 – 500 °C from the breakdown of unstable surface oxide complexes (CO values increased to 50 ppm as lowest and 110 ppm as highest). The second CO

release was from 510 – 590 °C corresponding to degradation of the main carbon structure (CO values increased by 180 ppm as lowest and 300 ppm as highest). The last stage between 600 – 790 °C corresponded to the breakdown of the remaining stable lignin structures and decay of accumulated CO.

v. The emission profiles took a general similar shape for all solid fuels, however, there was a general increase in peak height with an increase in airflow rate. There was also an observed shift in the peak CO emission values to higher temperatures with a decrease in airflow rates. Similarly, there was a shift of the mass loss profile to higher temperatures (Figure C-2 – Appendix C) with a decrease in airflow rates. This behavior could be explained by the slow decomposition rates of samples at low airflows creating a shift in the attainment of the peak mass loss and CO emissions. Of all the solid fuels analysed, ComC had the highest ash content. In terms of thermal stability (resistance to decomposition at high temperature), coal > ComC > UTCB ≥ CTCB.

Other figures showing the variation of mass loss and CO emissions at different heating rates and airflows are shown in Figures C-1 to C-3 of Appendix C.

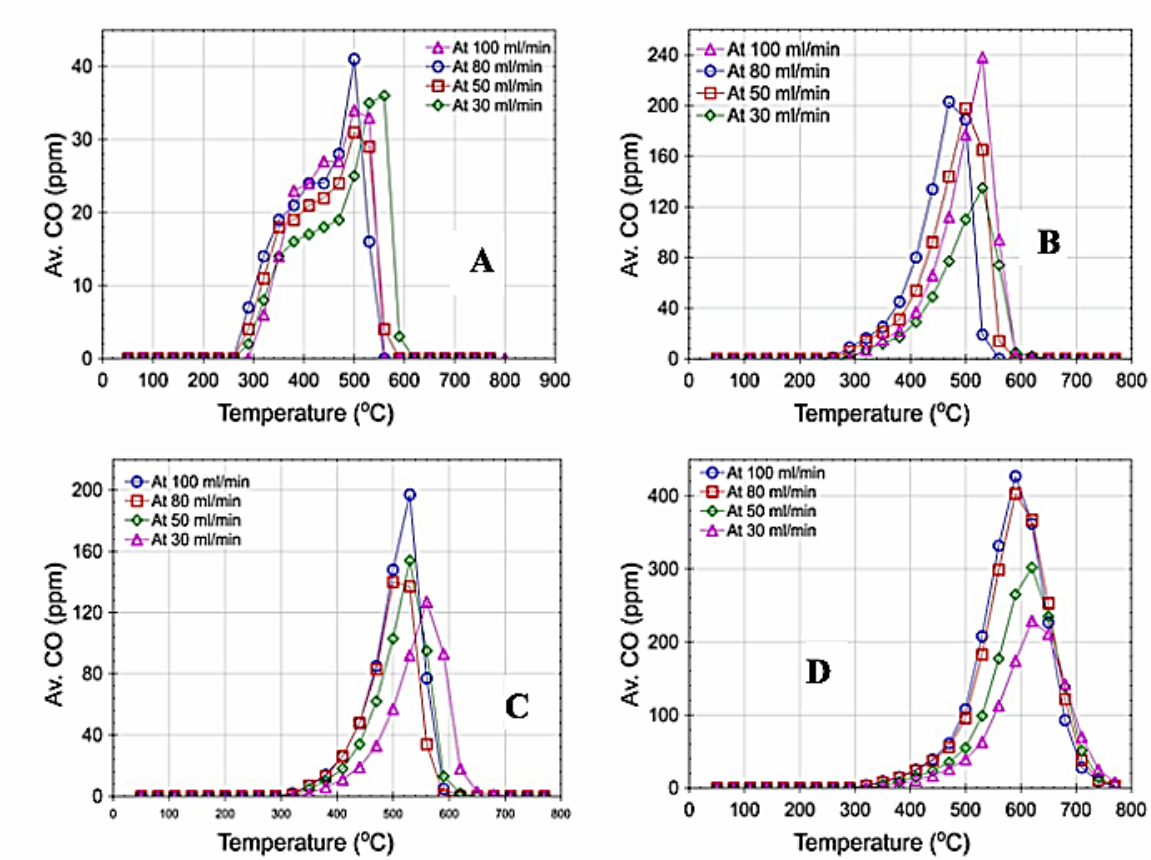

Figure 7-3: Average CO emissions (Av. CO) at different airflows and 30 °C/min heating rate. (A) – CTCB; (B) – UTCB; (C) – ComC; (D) – Coal

Figure 7-4 shows a summary of the ratios of the CO emissions (CO emissions from one solid fuel divided by CO emissions from CTCB) from the different solid fuels at 20 °C/min. We observed that UTCB emitted up-to 8 times more CO than CTCB at its peak/maximum degradation stage. Even at high temperatures > 500 °C when the catalyst activity had reduced, UTCB still emitted more CO than CTCB. The same analogy applies to ComC and coal. But one point to note is that at the temperatures shown in Figure 7-4, coal was just in the initial phase of oxidation. Coal's maximum emissions occurred in the range from 570 – 620 °C at which point, the average CO ratio was up to 300 times more compared to that of CTCB.

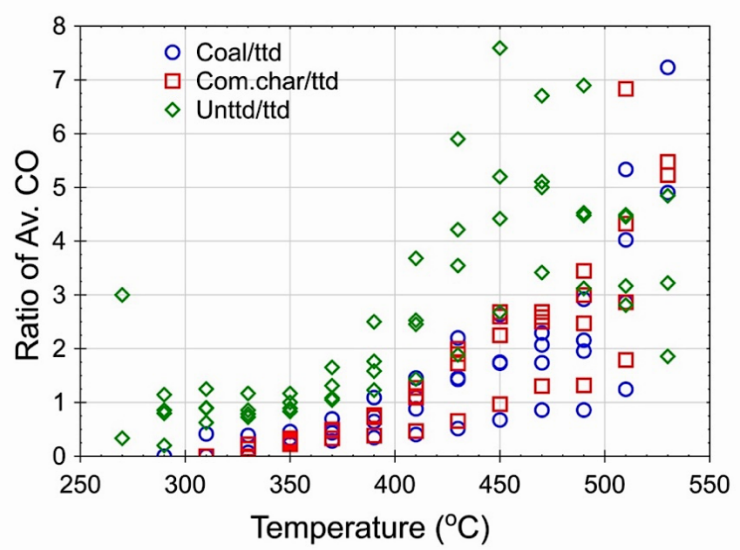

Figure 7-4: Ratios of Average CO emissions (Av. CO) for Coal/CTCB, ComC/CTCB and UTCB/CTCB at 20 °C/min. The acronym "ttd" means treated charcoal briquettes or CTCB.

7.3.3 CO emission factors

Figure 7-5, shows the trend of CO emission factors (the average emission rate of CO relative to the initial amount of solid fuel used) calculated for different airflow rates. Three points are shown at each airflow representing different heating rates per sample. Apart from coal at 100 mL/min, all the values for each sample showed no significant differences in CO emission factors at a single airflow. However, the CO emission factors increased exponentially with an increase in airflow. Coal had the highest CO emission factors with a maximum of 155 mg/g at 100 mL/min and 20 °C/min. CTCB had the lowest CO emission factors with 2.8 mg/g at 30 mL/min and 20 °C/min. WU *et al.* [36], reported that the catalyst treatment of coal tremendously reduced the combustion emissions.

The UTCB and ComC emitted almost similar values though the former had slightly higher values (highest of 52 mg/g at 100 mL/min and lowest of 13 mg/g at 30 mL/min). From our previous work [34], the emission factors for ComC were 257.8 mg/g at 720 mL/min, 210.9 mg/g at 1240 mL/min, 186.6 mg/g at 1710

mL/min and 212.7 mg/g at 2200 mL/min. This trend shows that CO emission factors were generally decreasing with airflow. However, these values were obtained at isothermal temperatures ranging between 300 – 600 °C in a tube furnace and at relatively high airflows. In another study, [31], mechanically impregnated catalysts were used to minimise CO emissions from charcoal. CO emissions were reduced but the catalyst lost activity with an increase in temperature. However, that study was also performed at isothermal temperatures yet real-life combustion takes place non-isothermally. In the present study, non-isothermal temperatures (50 – 800 °C) were used with different heating rates (20 – 40 °C/min) and low airflows (30 – 100 mL/min).

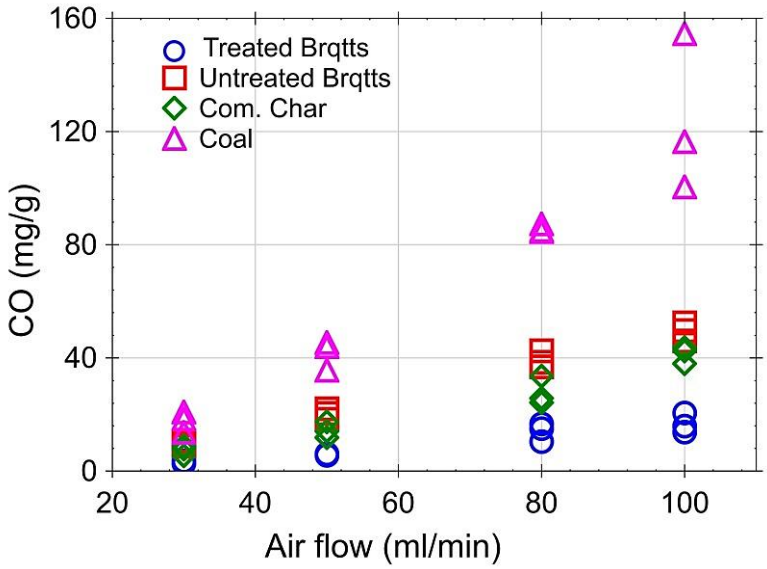

Figure 7-5: Overall CO emission factors as a function of airflow for Pd-Sn/alumina CTCB, UTCB, ComC, and coal

7.3.4 CO/CO_2 ratio

The CO/CO_2 ratio is a very important property during combustion of solid fuels. High ratios are usually associated with incomplete combustion. CTCB Figure 7-6A, showed a slight increase CO/CO_2 between 300 – 370 °C, reaching the maximum ratio of ≈ 0.12 with a few spikes close to ≈ 0.23 and a continuous decline to 0.02 until all the char was burnt above 550 °C. The initial increase was due to pyrolysis reactions in sawdust and cassava flour binder as well as the breakdown of unstable carbon oxide surface complexes and other

functional groups. The subsequent decline was due to increased oxidation of CO as a result of strong adsorption of Oxygen and CO on catalyst surfaces resulting in enhanced reactions forming CO_2 until the final decay of accumulated combustion products from the TGA/DSC chamber.

UTCB Figure 7-6B showed a slight increase in CO/CO_2 ratio initially to ≈ 0.25 at 400 °C which declined gently to 0.1 at 500 °C and then dropped sharply due to completion of char oxidation and then washing-out of accumulated CO from the reaction chamber.

ComC Figure 7-6C showed a steep rise in CO/CO_2 ratio to about 0.25 especially at 80 mL/min followed by a decline until 600 °C. Coal had a continuous increase in CO/CO_2 ratio reaching the highest recorded value in this study of slightly above 0.5 at 600 °C, Figure 7-6D.

In general, coal had more than twice as much of the CO/CO_2 ratio compared to the other solid fuels. The impact of airflow on the CO/CO_2 was not significant. In our previous study, [34] the low CO/CO_2 was linked to secondary reactions occurring in the pores of the charcoal promoting the conversion of CO to CO_2 which pores are minimal in coal. This is also reflected by the low specific surface area of coal compared to other solid fuels Table 7-1. Other figures showing the variation of CO/CO_2 at different heating rates and airflow rates are given in Figures C-4 to C-6 of Appendix C.

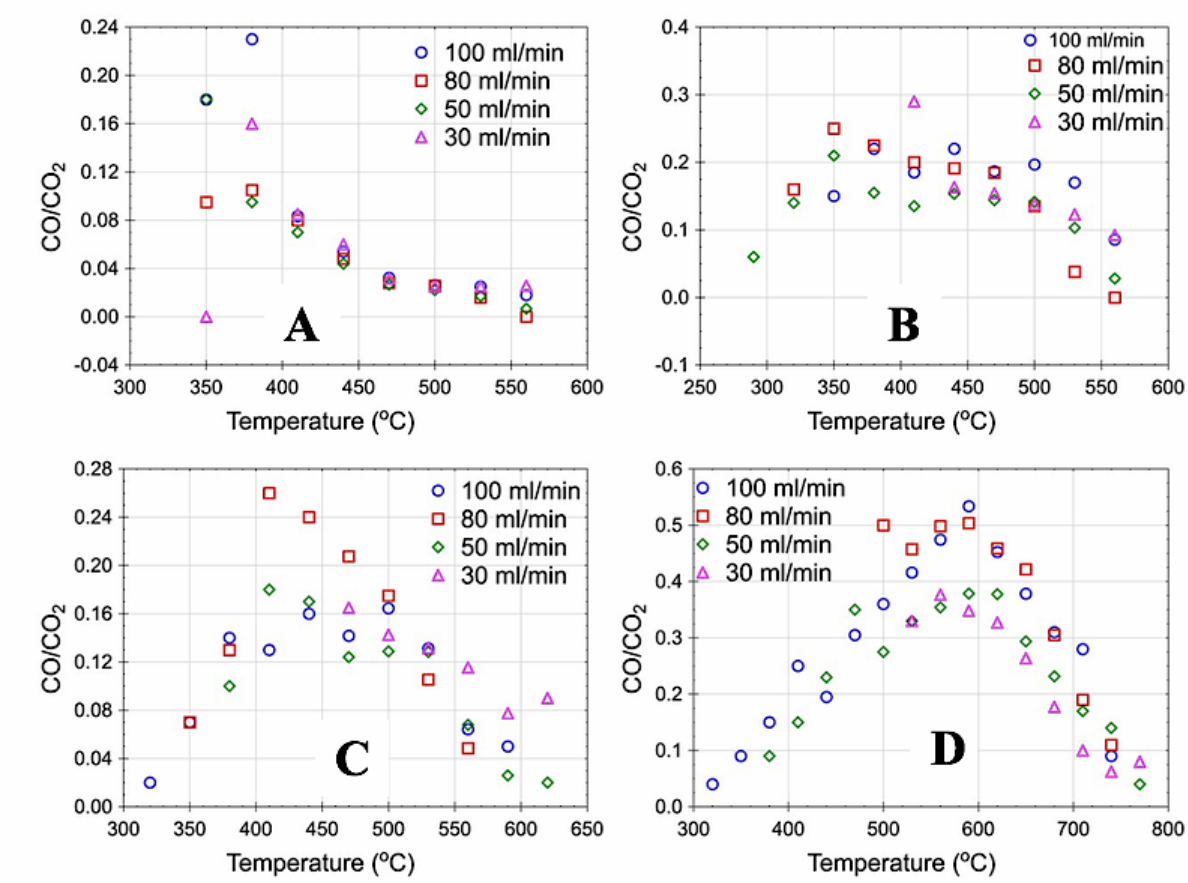

Figure 7-6: CO/CO_2 ratio at different airflows and 30 °C/min heating rate. A – CTCB; B – UTCB; C – Commercial barbecue charcoal; and D – Commercial coal

The actual CO/CO_2 ratio was also predicted by manipulating experimental data using the relationship analogous to the Arrhenius equation, i.e. $\frac{CO}{CO_2} = A_\alpha \exp\left(-\frac{B}{T_\alpha}\right)$, where A, is a constant independent of temperature and the parameter B, is analogous to an activation energy [37], [38]. We developed a relationship that was used for evaluation of constants B and A at dynamic heating experiments by incorporating a heating rate, β = dT/dt. Hence, the relationship became; $\left(\frac{CO}{CO_2}\right)\left(\frac{dt}{dT}\right) = \left(\frac{dt}{dT}\right)\left(\frac{A_\alpha}{\beta}\right)\exp\left(-\frac{B}{T_\alpha}\right)$. Introducing natural logarithms and re-arranging, $In\left[\beta\left(\frac{CO}{CO_2}\right)\right]_{\alpha,k} = InA_{\alpha,k} - B_{\alpha,k}\left(\frac{1}{T_{\alpha,k}}\right)$. A plot of the left-hand side against $1000/T_{\alpha,k}$ at several k^{th} heating rates and particular conversion - α, yields straight lines Figure 7-7(A), that were used to determine the constants B and A. In a similar study, Hu *et al.*, [37], expressed the CO/CO_2

ratio with a universal gas constant (R = 8.314 J/mol.K) so that the constants A and B could be interpreted as relationships to pre-exponential factors and activation energy respectively.

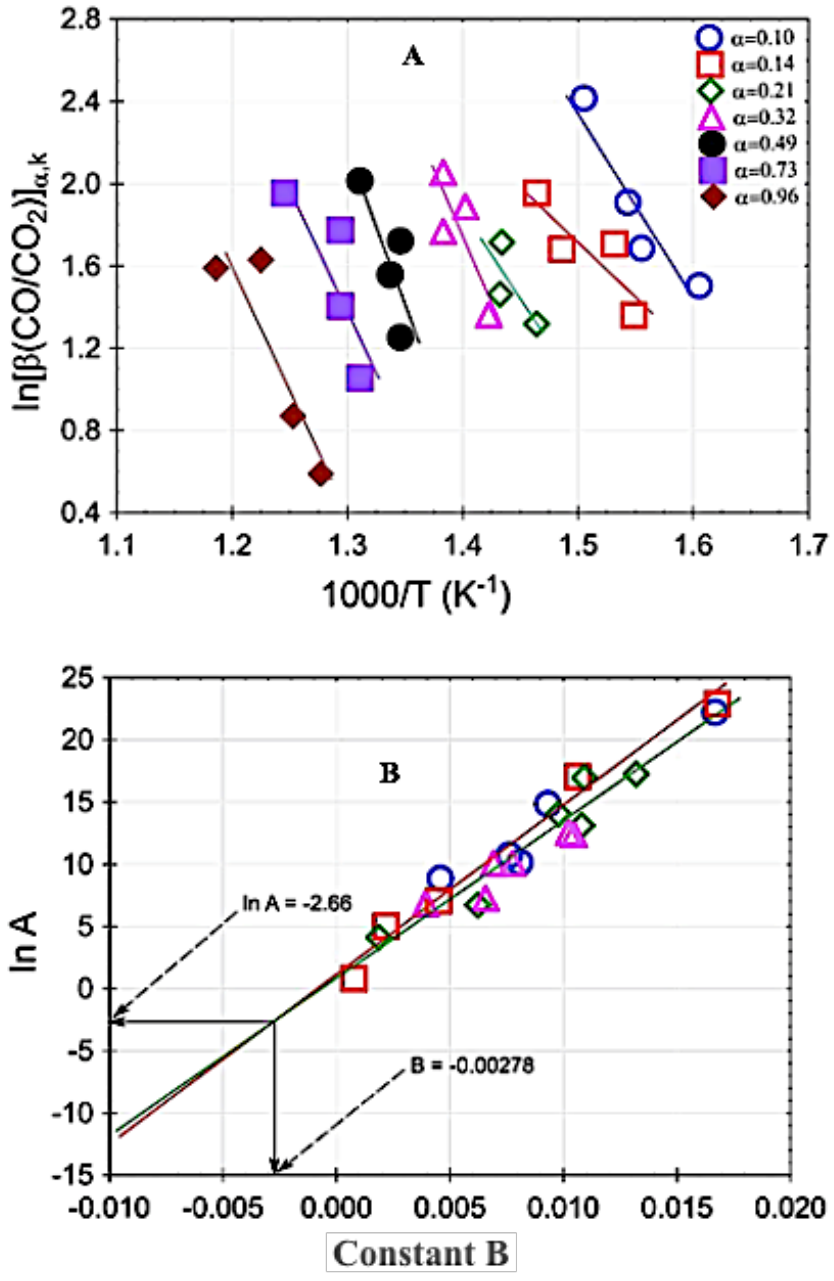

Figure 7-7: (A) the CO/CO_2 function against 1000/T for determination of B and A at different conversions for UTCB. A similar plot was used for CTCB. (B) lnA against constant B for CTCB for determination of the true values of constants A and B that were used to predict the CO/CO_2 ratios

Tables 1 and 2 of Appendix C show the values obtained for the constants A and B at different conversions and airflow rates. To obtain the true values that would be used to predict the CO/CO_2 relationships for CTCB and UTCB, the

natural logarithms of A (i.e. ln A) were plotted against constants B for the different airflows Figure 7-7(B). The point of intersection of the respective lines on the plot is the true value of ln A and constant B.

Hence, the general CO/CO_2 relationship obtained for CTCB was $CO/CO_2 = 0.07\exp(0.00278/T)$ and $CO/CO_2 = 0.2314\exp(0.00229/T)$ for UTCB. The predicted equations over-estimate the CO/CO_2 though they are close to the experimental values with minimal error margins. The general trend is a decline in the ratio with an increase in temperature similar to experimental data, and the predicted UTCB values are more than 3-fold compared to CTCB. Morin et al., [38], obtained the relationship $^{n}CO/^{n}CO_2 = 6308.8\exp(-6724/T)$ for beech stick char obtained by pyrolysis at 923 K in a fluidised bed reactor. Their ratio showed an increase in CO/CO_2 ratio with temperature; the opposite of what we have obtained for CTCB. However, the ratio depends on the material being investigated [37] among other factors.

7.3.5 Mass loss rate

As shown in Figure 7-8, the mass-loss rate followed one main segment with a few exceptions. CTCB (A) had the first peak at 350 °C (maximum at ≈ |3.9| %/min) attributed to the breakdown of hemicellulose, and cellulose components in sawdust and cassava binder during pyrolysis forming char. The same peak was observed with UTCB (B) though it was relatively shorter. The decomposition of the main char and lignin components happened at 530 °C for CTCB, reaching the highest mass loss rate of |29| %/min at 80 mL/min as also observed elsewhere [36]; |27| %/min at 100 mL/min while 30 mL/min had the lowest maximum peak mass loss rate of |24| %/min. The completion of degradation of CTCB occurred at 650 °C.

UTCB reached a maximum mass loss rate of |27| %/min at 100 mL/min while 30 mL/min still registered the lowest maximum peak of 23.5 %/min. ComC peak breakdown occurred at 560 °C, with |23| %/min as the maximum mass loss rate at 100 mL/min while 50 and 30 mL/min tied on the maximum peak value of |20.7| %/min and its completion of oxidation happened at 710 °C.

Coal peak decomposition happened at 620 °C and it registered the lowest peak mass loss rate among all the samples at |18| %/min for 100 mL/min while its complete degradation occurred at 800 °C. There was a shift in the attainment of the main decomposition peak to higher temperatures with a decrease in airflow rate and an increase in heating rate.

Other figures showing the variation of mass-loss rate with temperature are shown in Figures C-7 to C-9 of Appendix C. This variation in mass loss rate was attributed to complex reactions, mass transfer, and heat transfer during the char oxidation reactions and the interaction of the char with the metal catalyst [39] in case of CTCB.

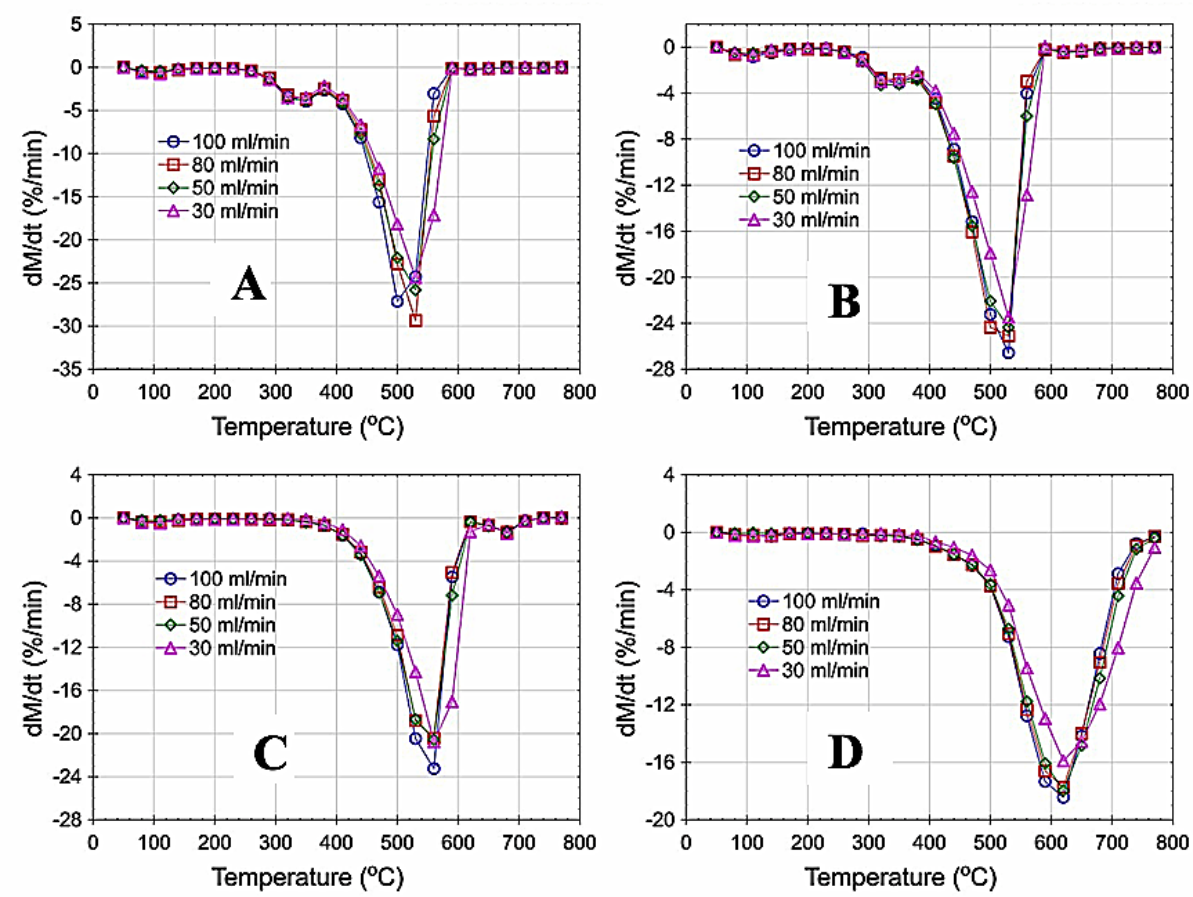

Figure 7-8: Mass loss rate at different airflows and 30 °C/min heating rate. A – CTCB; B – UTCB; C – Commercial barbecue charcoal; and D – Commercial coal

7.3.6 Kinetic parameters

Four different heating rates were used for determination of activation energy and pre-exponential factors with the Friedman equation. The selection of the best fit was based on the highest regression coefficient possible. The computed values are shown in the subsequent figures and tables. From now onwards, more emphasis will be put on CTCB and UTCB as these have the same recipe only that CTCB has the added 1 wt% Pd-Sn/alumina catalyst. More so, the study was focused on comparing catalyst treatment on the oxidation behavior of solid fuels used for cooking purposes. ComC and commercial coal are also compared and discussed intermittently.

7.3.6.1 Ea and A based on the conversion rate from mass loss data

The Friedman equation [40] for determination of E_a and A was developed from $d\alpha/dt = k(T)f(\alpha)$, where $k = A\,exp((-E\_a)/RT)$, and takes the general form;

$$\frac{d\alpha}{dt} = A_\alpha \exp\left(\frac{-E_\alpha}{RT_\alpha}\right) f(\alpha) \qquad (7\text{-}1)$$

Introducing a heating rate β = dT/dt and re-arranging

$$\beta_k \left(\frac{d\alpha}{dT}\right)_{\alpha,k} = A_\alpha \exp\left(\frac{-E_\alpha}{RT_\alpha}\right) f(\alpha) \qquad (7\text{-}2)$$

Introducing natural logarithms;

$$In\left[\beta_k \left(\frac{d\alpha}{dT}\right)_{\alpha,k}\right] = In[A_\alpha f(\alpha)] - \frac{E_\alpha}{R}\left(\frac{1}{T_\alpha}\right) \qquad (7\text{-}3)$$

where, f(α), is the reaction model function at a particular k^{th} heating rate, and a is the conversion. A plot of the left-hand side against $1000/T_\alpha$ should yield straight lines with gradient, $-E_a/R$ and intercept $\ln[A_\alpha f(\alpha)]$, Figure 7-9(A).

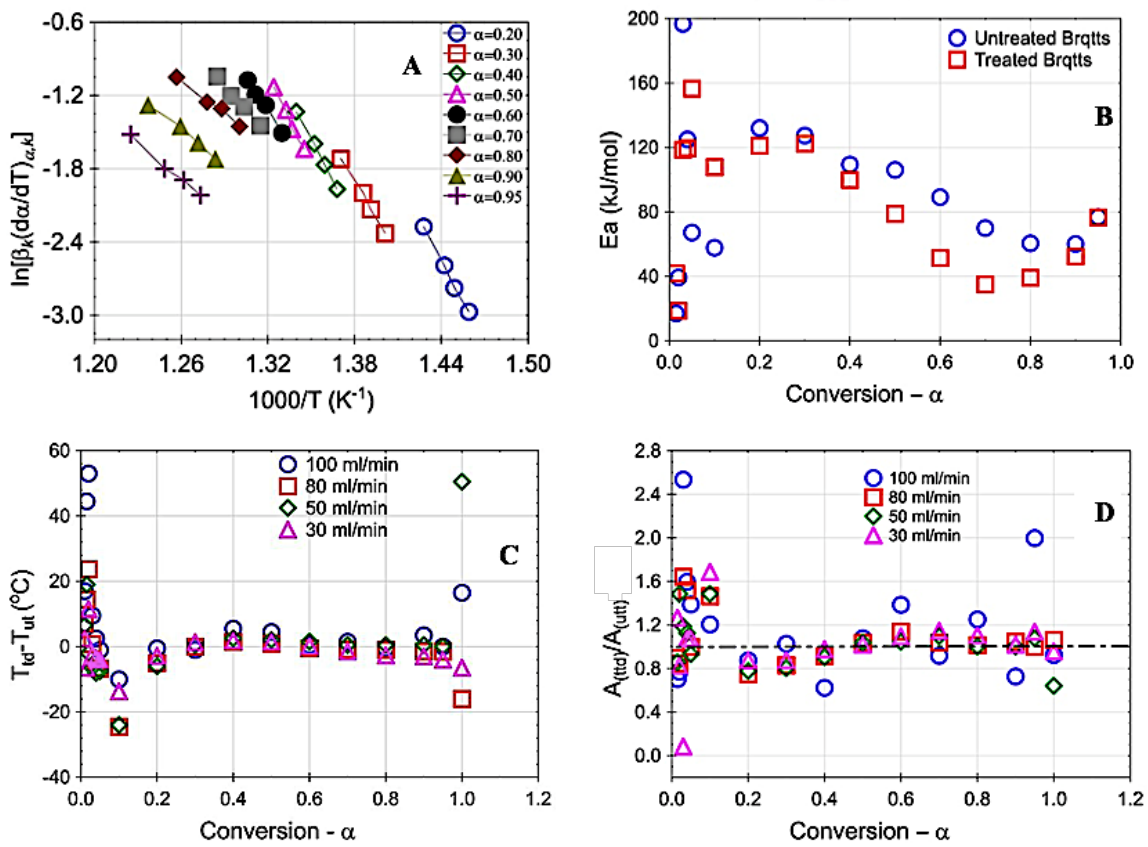

Figure 7-9: Plots of: (A) Friedman function against 1000/T for data obtained at 100 mL/min and different heating rates for CTCB. (B) activation energy for CTCB and UTCB at different conversions. (C) temperature difference between CTCB and UTCB at each degree of conversion for different airflow rates. (D) ratio of pre-exponential factors for CTCB ($A_{(ttd)}$) to UTCB ($A_{(utt)}$).

Figure 7-9(B), show the variation of the activation energies with conversion for UTCB and CTCB. We observed that at low conversions $\alpha < 0.1$ (and low temperatures T < 300 °C) the Ea were similar for UTCB and CTCB. This implied that the attainment of the activated complex during CTCB pyrolysis was the same as that of UTCB. At higher conversions $0.2 < \alpha < 0.8$, the Ea for CTCB continued to be lower than that for UTCB (with statistical significance) due to the catalytic action [36]. However, at high conversions $\alpha > 0.9$, the Ea for both solid fuels was almost the same. At this conversion (and high temperatures T > 500 °C), the catalyst continuously lost activity due to thermal sintering and agglomeration [41].

At low temperatures (< 300 °C) and lower conversions (α < 0.1), the major reactions involved loss of physically and chemically bound moisture and other weakly attached functional groups in endo/exothermic reactions. The addition of a catalyst enhanced the temperature and the exothermicity of the system at lower conversions (with statistical significance) and hence the positive temperature difference Figure 7-9(C). The temperature difference dT oscillated between negative and positive (0.0±5 °C) at 0.2 < α < 1 but was kept more to the negative side meaning that catalyst treatment lowered the temperature for heterogenous reactions during oxidation.

Assuming both the CTCB and UTCB followed similar reaction mechanism, f(α), at a particular k^{th} heating rate, and α – conversion, then, the ratio of pre-exponential factors can be determined as follows;

$$\frac{A_{Tt,\alpha,k}}{A_{Utt,\alpha,k}} = \frac{\left(\frac{d\alpha}{dT}\right)_{Tt,\alpha,k}}{\left(\frac{d\alpha}{dT}\right)_{Utt,\alpha,k}} * \exp\left[\left(\frac{E_\alpha}{RT_\alpha}\right)_{Utt,\alpha,k} - \left(\frac{E_\alpha}{RT_\alpha}\right)_{Tt,\alpha,k}\right] \qquad (7\text{-}4)$$

where A_{Tt} and A_{Utt} are the pre-exponential factors for the CTCB and UTCB at a k^{th} heating rate, and conversion (α). Using the expression Eqn. 7-4, the ratio of pre-exponential factors can be deduced at different airflow rates. The same equation was customised for the ComC and coal.

Except for 100 mL/min airflow whose A ratios kept fluctuating up and below unity (1.0), there were general trends in A ratios for all airflows Figure 7-9(D). At α < 0.1, the A ratios were mostly > 1.0. Between 0.2 < α < 0.5, the A ratios were < 1, while at 0.5 < α < 0.9, the A ratios were > 1.0. At α > 0.9, the A ratios were generally close to unity (1.0). In regions where A ratios were > 1.0 (which are the majority – with statistical significance), the active sites on the CTCB were more compared to UTCB. This was attributed to adsorptive sites provided by the catalyst and these sites allowed faster and quick turn-over of reactions.

7.3.7 Methane and combustion efficiency

Methane is a common by-product of solid fuel combustion. The quantity obtained of which depends on the C/H ratio of the solid fuel and the sensitivity of the analysis system. From all the samples analysed, methane was not detected, possibly due to very low concentration.

The combustion efficiency or selectivity to CO_2 is the measure of the total emission of CO_2 as a ratio/percentage to the total carbon oxides $(CO_2/(CO+CO_2))*100$. This was computed for CTCB, UTCB, ComC, and coal Figure 7-10. We observed that coal had a decreasing CO_2 selectivity due to increased production of high amounts of CO as temperature increased. The CTCB had low selectivity at temperatures < 400 °C due to low oxidation of CO. At temperatures > 400 °C, CTCB had rapidly increasing CO_2 selectivity due to enhanced oxygen adsorption on catalyst surfaces that promoted the conversion of CO to CO_2.

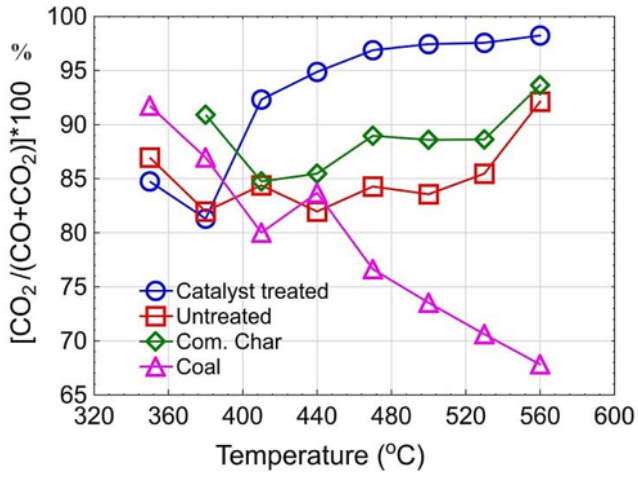

Figure 7-10: Plot of combustion efficiency for different solid fuels as a function of temperature.

7.3.8 Nitrogen oxides

The combined nitrogen oxides, commonly known as NO_x, were also analysed in this study and are presented in Figure 7-11. The NO_x arising from the nitrogen in the fuel are termed as fuel-nitrogen. Fuel-nitrogen is found in plants, animal proteins, and nitrogen-rich bacteria. Reactions of amines with carboxylic groups or aldehyde groups give rise to nitrogenous species present in solid fuels which are typically bound to organic matter. Nitrogen content in solid fuels usually ranges from 0.2 % to 2 % [42]. Biomass fuels usually contain < 1 % nitrogen while coal typically contains 1 % to 2 % of nitrogen with bituminous coals usually containing 1.5 – 1.75 % and anthracites mostly containing less than 1 % [43].

The NO_x emissions were observed starting from 440 °C for CTCB and above 500 °C for the rest of the samples. This is because nitrogen forms strong triple bonds that are not easy to break at low temperatures compared to carbon-carbon and carbon-oxygen bonds. Secondly, catalyst treatment reduced the temperature at which NO_x emissions were produced. We observed that except for ComC, the areas under the curves (giving total amount of NO_x) were not distinguishable implying that catalyst treatment did not increase the amounts of NO_x produced. The low NO_x emissions produced by ComC could be related to its low nitrogen content as observed in our previous study [34]. However, in one study [44], it was observed that metal impurities in biomass solid fuels enhanced NO_x emissions during combustion.

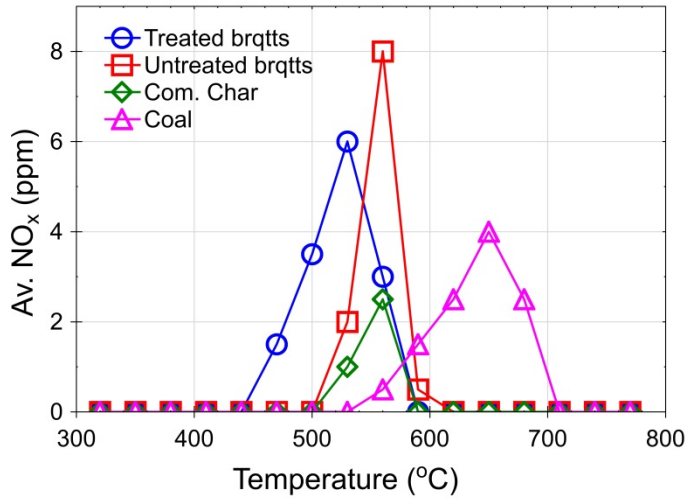

Figure 7-11: Scatter plot for NO_x emissions for different solid fuels

Summary & Conclusions

The effect of catalyst treatment on solid fuel reactivity in an oxidative environment was studied and quantified experimentally. Two laboratory prepared biomass briquette types: catalyst (1 wt% Pd-Sn/alumina) treated charcoal briquettes (CTCB) and untreated charcoal briquettes (UTCB) were studied in addition to commercial charcoal (ComC) and coal. CO emissions and NO_x usually affected by oxygen supply and thermal reactivity. To study how these factors affect solid fuels reactivity, non-isothermal thermogravimetric analysis in the air (21 % oxygen) coupled with evolved gas analysis with a robust online multi-sensor gas analyser was performed. The outputs from the experiments were used to determine and compare energy output, CO emission factors, NO_x, combustion efficiency, activation energy (from mass loss and CO-CO_2 emissions) as well as pre-exponential factors. It has been demonstrated that catalyst treatment of solid fuels enhanced their energy output by more than 22 % and reduced CO emission factors by 87.1 %, 63.6 %, and 55.6 % compared to coal, UTCB, and ComC respectively. Catalyst treatment lowered the temperature at which NO_x emissions were produced but did not affect their quantity. The combustion efficiency was also improved by up to 60 % compared to coal and up to 20 % compared to UTCB and

ComC. Treatment of solid fuels with catalyst lowered the activation energy for oxidation especially at 0. 2 ≤ α ≤ 0.8. CTCB had more free active sites for reactions evidenced by an increased ratio of pre-exponential factors, however, the active sites decreased at temperatures > 500 ^{o}C possibly due to thermal deactivation of the catalyst. Overall, this is a very promising method for minimising toxic emissions from the combustion of solid fuels and enhancing energy output for domestic and industrial applications. However, more research is needed for thermally stable catalysts at high temperatures.

Acknowledgments

The authors thank the experimental support provided by Adrian Mustey and Karl Norris.

References

[1] D. Chakraborty, N. K. Mondal, and J. K. Datta, "Indoor pollution from solid biomass fuel and rural health damage: A micro-environmental study in rural area of Burdwan, West Bengal," *Int. J. Sustain. Built Environ.*, vol. 3, no. 2, pp. 262–271, 2014.

[2] Y. Y. Chen *et al.*, "Suicide by burning barbecue charcoal in England," *J. Public Heal. (United Kingdom)*, vol. 35, no. 2, pp. 223–227, 2013.

[3] N. B. Hampson, C. C. Kramer, R. G. Dunford, and D. M. Norkool, "Carbon Monoxide Poisoning From Indoor Burning of Charcoal Briquets," *JAMA*, vol. 271, no. 1, pp. 52–53, Jan. 1994.

[4] C. Winder, "Carbon monoxide-induced death and toxicity from charcoal briquettes," *Med. J. Aust.*, vol. 197, no. 6, pp. 349–350, Sep. 2012.

[5] P. R. Nielsen, A. Gheorghe, and N. Lynnerup, "Forensic aspects of carbon monoxide poisoning by charcoal burning in Denmark, 2008-2012: An autopsy based study," *Forensic Sci. Med. Pathol.*, vol. 10, no. 3, pp. 390–394, 2014.

[6] J. R. Lyness and J. Crane, "Carbon Monoxide Poisoning From Disposable Charcoal Barbeques," *Am. J. Forensic Med. Pathol.*, vol. 32, no. 3, 2011.

[7] N. MacCarty, D. Still, and D. Ogle, "Fuel use and emissions performance of fifty cooking stoves in the laboratory and related benchmarks of performance," *Energy Sustain. Dev.*, vol. 14, no. 3, pp. 161-171., 2010.

[8] M. Njenga *et al.*, "Gasifier as a cleaner cooking system in rural Kenya," *Clean. Prod.*, vol. 121, pp. 208-217., 2016.
[9] M. Njenga *et al.*, "Quality of charcoal produced using micro gasification and how the new cook stove works in rural Kenya," *Environ. Res. Lett.*, vol. 12, no. 9, p. art. no. 095001, ., 2017.
[10] F. Yip *et al.*, "Assessment of traditional and improved stove use on household air pollution and personal exposures in rural western Kenya," *Environ. Int.*, vol. 99, pp. 185–191, 2017.
[11] D. O. Obada, M. Peter, D. M. Kulla, N. O. Omisanya, A. Y. Atta, and D. Dodoo-Arhin, "Catalytic abatement of CO species from incomplete combustion of solid fuels used in domestic cooking," *Heliyon*, vol. 4, no. 8, pp. e00748–e00748, Aug. 2018.
[12] A. D. Paulsen *et al.*, "Gaseous and particulate emissions from a chimneyless biomass cookstove equipped with a potassium catalyst," *Appl. Energy*, vol. 235, no. October, pp. 369–378, 2018.
[13] K. Nuutinen, J. Jokiniemi, O. Sippula, H. Lamberg, and J. Sutinen, "Effect of air staging on fine particle , dust and gaseous emissions from masonry heaters," *Biomass and Bioenergy*, vol. 67, pp. 167–178, 2014.
[14] H. Lamberg *et al.*, "Operation and Emissions of a Hybrid Stove Fueled by Pellets and Log Wood," *Energy & Fuels*, vol. 31, no. 2, pp. 1961–1968, 2017.
[15] F. Sher, M. A. Pans, T. A. Daniel, C. Sun, and H. Liu, "Experimental investigation of woody and non-woody biomass combustion in a bubbling fluidised bed combustor focusing on gaseous emissions and temperature profiles," *Energy*, vol. 141, pp. 2069–2080, 2017.
[16] S. Bensaid, F. A. Deorsola, D. Fino, and N. Russo, "After-treatment of household wood-fired stove emissions: From catalyst formulation to full-scale system," *Catal. Today*, vol. 197, no. 1, pp. 76–89, 2012.
[17] M. Zhi, A. Koneru, F. Yang, A. Manivannan, J. Li, and N. Wu, "Electrospun La0.8Sr0.2MnO3 nanofibers for a high-temperature electrochemical carbon monoxide sensor," *Nanotechnology*, vol. 23, no. 30, 2012.
[18] C. Lin *et al.*, "High Performance Colorimetric Carbon Monoxide Sensor for Continuous Personal Exposure Monitoring," *ACS Sensors*, vol. 3, no. 2, pp. 327–333, 2018.
[19] C. Pannek, K. R. Tarantik, K. Schmitt, and J. Wöllenstein, "Investigation of gasochromic rhodium complexes towards their reactivity to CO and integration into an optical gas sensor for fire gas detection," *Sensors (Switzerland)*, vol. 18, no. 7, pp. 1–15, 2018.
[20] G. Alberti, M. Casciola, and R. Palombari, "Amperometric sensor for carbon monoxide based on solid state protonic conduction," *Solid State Ionics*, vol. 61, no. 1–3, pp. 241–244, 1993.
[21] C. T. Wang and M. T. Chen, "Vanadium-promoted tin oxide semiconductor carbon monoxide gas sensors," *Sensors Actuators, B Chem.*, vol. 150, no. 1, pp. 360–366, 2010.
[22] P. Van Geloven, M. Honore, J. Roggen, S. Leppavuori, and T. Rantala, "The influence of relative humidity on the response of tin oxide gas sensors to carbon monoxide," *Sensors Actuators B. Chem.*, vol. 4, no. 1–

2, pp. 185–188, 1991.
[23] M. Anastasescu *et al.*, "Nanostructured SnO2–ZnO composite gas sensors for selective detection of carbon monoxide," *Beilstein J. Nanotechnol.*, vol. 7, pp. 2045–2056, 2016.
[24] P. R. Patwardhan, J. A. Satrio, R. C. Brown, and B. H. Shanks, "Influence of inorganic salts on the primary pyrolysis products of cellulose," *Bioresour. Technol.*, vol. 101, no. 12, pp. 4646–4655, 2010.
[25] Q. Lu, Z.-X. Zhang, X. Wang, H.-Q. Guo, M.-S. Cui, and Y.-P. Yang, "Catalytic Fast Pyrolysis of Biomass Impregnated with Potassium Phosphate in a Hydrogen Atmosphere for the Production of Phenol and Activated Carbon," *Front. Chem.*, vol. 6, p. 32, Feb. 2018.
[26] L. Zhou, Y. Jia, T. Nguyen, A. A. Adesina, and Z. Liu, "Hydropyrolysis characteristics and kinetics of potassium-impregnated pine wood," *Fuel Process. Technol.*, vol. 116, pp. 149–157, 2013.
[27] M. Safar *et al.*, "Catalytic effects of potassium on biomass pyrolysis, combustion and torrefaction," *Appl. Energy*, vol. 235, pp. 346–355, 2019.
[28] K. Venkatesan, S. He, K. Seshan, P. Selvam, and R. Vinu, "Selective production of aromatic hydrocarbons from lignocellulosic biomass via catalytic fast-hydropyrolysis using W2C/γ-Al2O3," *Catal. Commun.*, vol. 110, pp. 68–73, 2018.
[29] M. A. Machado, S. He, T. E. Davies, K. Seshan, and V. Teixeira da Silva, "Renewable fuel production from hydropyrolysis of residual biomass using molybdenum carbide-based catalysts: An analytical Py-GC/MS investigation," *Catal. Today*, vol. 302, pp. 161–168, 2018.
[30] A. S. Al-Rahbi and P. T. Williams, "Waste ashes as catalysts for the pyrolysis–catalytic steam reforming of biomass for hydrogen-rich gas production," *J. Mater. Cycles Waste Manag.*, 2019.
[31] A. Nyombi, M. R. Williams, and R. Wessling, "Mechanical impregnation of Pd-Sn/alumina and Cu-Mn/graphite on charcoal to minimise carbon monoxide emissions," *Chem. Phys. Lett.*, vol. 715, pp. 181–185, Jan. 2019.
[32] R. W. A. Nyombi, M. Williams, "Reactivity and Free Radical Chemistry of Lilac (Syringa) Charcoal," *Energy & Fuels*, vol. 33, no. 2, pp. 1227–1235, 2019.
[33] R. García, C. Pizarro, A. G. Lavín, and J. L. Bueno, "Biomass proximate analysis using thermogravimetry," *Bioresour. Technol.*, vol. 139, pp. 1–4, 2013.
[34] A. Nyombi, M. R. Williams, and R. Wessling, "Toxic emissions from smouldering combustion of woody biomass and derived char with a case study of CO build-up in an ISO container," *Energy Sources, Part A Recover. Util. Environ. Eff.*, pp. 1–18, May 2019.
[35] L. Febrero, E. Granada, A. Regueiro, and J. L. Míguez, "Influence of Combustion Parameters on Fouling Composition after Wood Pellet Burning in a Lab-Scale Low-Power Boiler," *Energies*, vol. 8, pp. 9794–9816, 2015.
[36] Z. Wu, Z. Yu, W. Zhu, and R. Zhou, "Energy Saving and Pollution Reducing Effects of Coal Combustion Catalysts," *Tsinghua Sci. Technol.*, vol. 6, no. 2, 2001.

[37] W. Hu, E. Marek, F. Donat, J. S. Dennis, and S. A. Scott, "A thermogravimetric method for the measurement of CO/CO2 ratio at the surface of carbon during combustion," *Proc. Combust. Inst.*, vol. 37, no. 3, pp. 2987–2993, 2019.
[38] M. Morin, S. Pécate, and M. Hémati, "Kinetic study of biomass char combustion in a low temperature fluidized bed reactor," *Chem. Eng. J.*, vol. 331, no. August, pp. 265–277, 2018.
[39] K. B. Larionov and A. A. Gromov, "Non-isothermal oxidation of coal with Ce(NO3)3 and Cu(NO3)2 additives," *Int. J. Coal Sci. Technol.*, vol. 6, no. 1, pp. 37–50, 2019.
[40] Y. J. Rueda-Ordóñez and K. Tannous, "Isoconversional kinetic study of the thermal decomposition of sugarcane straw for thermal conversion processes," *Bioresour. Technol.*, vol. 196, pp. 136–144, 2015.
[41] Q. Zheng, R. Farrauto, and M. Deeba, "Part II: Oxidative Thermal Aging of Pd/Al2O3 and Pd/CexOy-ZrO2 in Automotive Three Way Catalysts: The Effects of Fuel Shutoff and Attempted Fuel Rich Regeneration," *Catalysts*, vol. 5, no. Part II, pp. 1797–1814, 2015.
[42] P. Glarborg, J. A. Miller, B. Ruscic, and S. J. Klippenstein, "Modeling nitrogen chemistry in combustion," *Prog. Energy Combust. Sci.*, vol. 67, pp. 31–68, 2018.
[43] J. Leppdahti and T. Koljonen, "Review Nitrogen evolution from coal , peat and wood during gasification : Literature review," *Fuel Process. Technol.*, vol. 43, pp. 1–45, 1995.
[44] S. Fournel, J. H. Palacios, S. Godbout, and M. Heitz, "Effect of Additives and Fuel Blending on Emissions and Ash-Related Problems from Small-Scale Combustion of Reed Canary Grass," *Agriculture*, vol. 5, no. x, pp. 561–576, 2015.

Chapter 8: DISCUSSION & LIMITATIONS

8.1 Introduction

This chapter discusses the feasibility of a new product, i.e. solid fuels that emit less carbon monoxide (CO) which has been investigated thoroughly in terms of raw material properties, the production process and cost–benefit analysis. CO needs to be addressed and given equal if not more attention than other emissions from solid fuel combustion because exposure to levels as low as 5000 ppm can kill in less than 30 minutes. CO poisoning claimed 75, 58, 57, 52 and 48 lives in the years 2011, 2012, 2013, 2014 and 2015, respectively in the United Kingdom [1]. These are the incidents that have been confirmed with reference to CO victims in hospitals with clear symptoms. However, many other deaths are not recognised as CO poisoning because the symptoms are similar to other ailments. Although the fatalities show a downward trend, ideally it should be possible to prevent CO poisoning all together. The situation is even worse in developing countries, where CO awareness, domestic CO alarms and other CO minimisation strategies are not well enforced. This has promoted research aiming to reduce CO emissions by developing advanced cook stoves [129], cleaner fuels for better energy efficiency less CO emission [130], and the post-combustion catalytic conversion of CO [24] among other strategies. However, none of these technologies have fully addressed the challenge, and solid-fuel consumers continue to suffer CO exposure. Furthermore, the post-combustion catalytic oxidation of CO is not compatible with simple technologies like charcoal barbeques, simple cook stoves, or open-fire cooking.

The research described in this thesis involved the preparation of charcoal samples by customised pyrolysis (Chapter 3 & 4), assessing the chemical species on the charcoal surface responsible for CO release during combustion (Chapter 4), evaluating the relationship between combustion conditions

(temperature and airflow) and the emission of CO (Chapter 5), and the mechanical impregnation of charcoal and briquettes with catalysts as a strategy to minimise CO emissions from charcoal (Chapter 6 & 7).

8.2 The choice of samples

The initial laboratory investigations involved commercial samples of charcoal and coal. The challenge with charcoal and similar biomass materials is feedstock variability, because the mineral content is associated with the growth location, climate and cropping of the trees from which the charcoal is prepared [131]. We observed from preliminary studies that the commercial charcoal samples were mixtures from different tree species. We therefore prepared our own samples from known tree species (Chapter 4) using the knowledge obtained in Chapter 3.

The emission of CO and CO_2 as a function of temperature and airflow was investigated using these laboratory-prepared samples as well as sawdust and commercial samples (Chapter 5). Although the laboratory samples gave more consistent results, the commercial samples represent the actual product used by consumers, hence several runs were performed, and averages values were reported. To make more comparisons, briquettes were prepared (Chapter 7) and a more thorough analysis of emissions was done. This involved CO, CO/CO_2 ratio, NO_x and CH_4.

8.3 The nature of charcoal & coal and CO emissions

The research involved the determination of the reactivity and free radicals on the surface of lilac charcoal prepared in the laboratory under controllable conditions to achieve consistent results (Chapters 4 and 5). The data improved

our understanding of the nature and behaviour of charcoal under different conditions and formed the basis of experiments involving the impregnation of charcoal with catalysts to minimise CO emissions. Elemental analysis of lilac charcoal revealed an O/C ratio of 0.158, suggesting it is highly reactive. Indeed, oxidative pyrolysis showed that significant oxidation started at temperatures as low 250 – 300 °C with most char oxidation taking place within a narrow temperature range (mainly 330 – 520 °C) for 2, 5, 10 and 15 °C/min heating rates, consuming 80 % of the char. This further implies that lilac charcoal is mostly composed of monomeric carbonaceous units. The H/C ratio was 0.033, suggesting a high probability of H abstraction by O_2 [85]. This was shown when lilac charcoal was exposed to pressurised air (21 % oxygen) in a TGA/DSC3+ instrument at 100 °C resulting in the formation of peroxyl radicals by hydrogen abstraction from hydroxyl groups within the carbon matrix. Based on the general proposed structure of charcoal presented in Chapter 4, the peroxyl radicals were most likely formed from carboxylic acids, phenols and alcohols.

Pyrolysis also showed that the kinetic pre-exponential factor *A*, indicating the frequency of collision between active sites on charcoal with oxygen, had A values ranging from 10^2 to10^{13} (s^{-1}) consisting of complex active sites possibly comprising polycyclic aromatic hydrocarbons with oxygen heteroatoms [85]. Analysis of the fresh lilac charcoal samples by electron spin resonance (ESR) spectroscopy showed the presence of stable free radicals with *g*-values in the range 2.00477 – 2.00483, typical for free radicals with oxygen heteroatoms [132]. The free radical spin concentration of lilac ranged from 10^{17} to 10^{19} spins/g, possibly reflecting the charcoal production temperature of 500 °C. This temperature produces large quantities of free radicals [133]. Also, we observed a drop in the E_a values from 145 to 110 kJ/mol and in the *A* values from 10^{13} to 10^2 (s^{-1}) with increasing conversion, implying the progressive formation of weaker bonds [134].

Pyrolysis of lilac charcoal in N_2 resulted in the removal of oxygen and nitrogen oxides as volatile gaseous products [135], and the re-arrangement of the carbon-carbon centred radicals to form non-radical products [132]. This was confirmed by the ESR spectroscopy of pyrolysed charcoal and no free radicals were detected. Activated carbons were analysed for comparison and no ESR signals were detected. In fact, activated charcoal remained unreactive even in pressurised air, with no ESR signals observed after it was exposed to air at 5 mL/min and 100 °C for 30 min [135]. However, pyrolysed lilac charcoal registered an ESR signal after it was exposed to pressurised air at 100 °C, implying that lilac had not fully been graphitised like commercial activated charcoal.

The removal/deactivation of radicals from the charcoal surface was also observed with hydrochloric acid (HCl)-treated lilac charcoal, which showed no ESR signals. Additionally, acid-washed charcoal had a weaker oxygen-adsorption capacity than untreated charcoal. This may show the synergistic effect between carbon atoms and mineral matter within the charcoal for attracting and forming partial or full bonds with oxygen and other species. A similar result was reported when activated carbons washed with HCl did not absorb NO_2 and H_2S efficiently, which was attributed to the removal of metal oxides which could have reacted with the molecules of the adsorbed gas to form nitrates and sulfides [136].

Chapter 5 examined the effect of temperature and airflow on the emission of CO from sawdust and charcoal and the accumulation of CO in an ISO container. The production of CO was inversely proportional to the temperature of the sawdust and charcoal. We could not confirm the proportions of CO and CO_2 produced by one-stage and two-stage processes. Dollimore *et al.* [18] suggested a mechanism based on a transient surface complex followed by a more stable surface oxide which then broke down. There were many other factors to consider including the product ratios, which could reflect the

different active sites present on each char surface associated with cationic trace metal impurities that act as catalysts [137]. Although our experiments involved isothermal combustion, the actual temperatures of sawdust and char could have been higher because metal impurities increase the burning temperature of solid fuels [138] as evidenced by CO_2 production at the char surface by the catalytic action of the char mineral matter [139].

In the ISO container experiments (Chapter 5), CO emissions accumulated more in less aerated conditions. There was also a net movement of polluted air to the upper parts of the container. The buoyant air movement and the temperature difference within the ISO container was a major factor contributing for movement of CO to the upper parts of the ISO container [140].

Nitrogen adsorption (Chapter 7) showed that the laboratory prepared charcoal briquettes were microporous with a specific surface area (SSA) of 67 – 78 m^2/g. Commercial charcoal had slightly high SSA of 82.2 m^2/g while coal had the lowest SSA of 27 m^2/g which is consistent with its lack of porosity. In terms of oxidative pyrolysis, the porosity allows charcoal to burn on all surfaces (i.e. from inside-out as well as outside-in), so that as the external surface area declines during burning, the internal surface enlarges to maintain the overall surface area and maintain a near constant burn rate (Chapter 5). The surface area of charcoal during combustion therefore depends on the mass remaining.

8.4 Impregnation of catalysts on charcoal

Previous studies attempting to minimise CO emissions have focused either on improving cook stove designs [129], [141], or the oxidation of CO using a catalyst in a fixed bed or by channeling post-combustion CO through a catalyst [88], [92], [142]–[148]. These studies have not focused on the root

cause. The findings of this study regarding the mechanical impregnation of charcoal with Pd-Sn/alumina and Cu-Mn/graphite (Chapter 6) and treatment of briquettes with Pd-Sn/alumina provide an alternative method for the effective management of CO and other dangerous combustion emissions from solid fuels. The SSA of solid fuels discussed in Chapter 7 and its relation to burning rate in Chapter 5 was exploited during the mechanical impregnation of charcoal with catalysts. Small-scale laboratory mortar-and-pestle batches were prepared by mixing charcoal particles (< 210 μm) with different quantities of Pd-Sn/alumina and Cu-Mn/graphite until a homogeneous product was obtained. These were burnt in a tube furnace isothermally and the residual CO was recorded as a function of temperature (Chapter 6). Non-isothermal combustion with real-time emission analysis was also conducted on Pd-Sn/alumina treated and untreated briquetted in Chapter 7.

Initial characterisation of the catalysts by thermogravimetric analysis and differential scanning calorimetry (Chapter 6) showed that Pd-Sn/alumina progressively loses moisture bound on the alumina support until the most stable phase (Al_2O_3) is formed at ~ 470 °C. The concentration of the active ingredients (Pd-Sn) within the alumina support was low, so the behaviour of Pd-Sn during heating was masked by the alumina transitions. On the other hand, the Cu-Mn/graphite quickly lost moisture at 114 °C and subsequent changes were due to transitions in oxidation states to more stable states at high temperatures. The Cu^{2+} will have changed to Cu^{+} at 450 °C and finally to Cu metal at 660 °C. Similarly, $Mn^{2.7+}$ will have changed to $Mn^{3.2+}$ at 500 °C and finally to a more stable Mn^{3+} at 550 °C. These transitions were supported by X-ray diffraction analysis of the catalysts as-received and after oxidative pyrolysis in air at 600 °C (Chapter 6). The as-received Pd-Sn/alumina catalyst featured the phases AlO(OH), $Al_2O_3.3H_2O$ and Al_2O_3. After heat treatment at 600 °C, Al_2O_3 and PdO were identified, as reported elsewhere [149]. On the other hand, the as-received Cu-Mn/graphite catalyst featured the phases MnO_2, $CuMn_2O_4$ and graphite. After heat treatment at 600 °C, $Cu_{1.5}Mn_{1.5}O_4$, Mn_5O_8, Mn_2O_3 and

graphite were identified, as reported elsewhere [150]. However, as discussed below, the more stable phases show less CO oxidation activity. Heat treatment was implemented to observe the behaviour of the catalysts under high-temperature conditions. The rapid oxidation of CO during combustion of catalyst treated samples was attributed to CO & O_2 adsorption on the catalyst surfaces. At high temperatures > 500 ^{o}C, catalyst sintering, or thermal deactivation was responsible for the decreased activity of the catalysts (Chapter 6 &7).

At the time of this study, a kilogram of Cu-Mn/graphite cost £65. This implies that a 5 wt% catalyst impregnation would add £3.25 per kilogram to the price of lump charcoal already on the market. However, this concentration reduced the amounts of emitted CO from 100 % to 16.7 % at 300 °C and to 41.7 % at 600 °C. Although our product would be safer (in terms of CO emissions) it would not be very competitive on the market with a 5 wt% catalyst concentration. Reduction of the Cu-Mn/graphite catalyst concentration to 2 wt% resulted in residual CO levels of 15.6 – 25.3 %, similar to the 5 wt% catalyst. In terms of costs, the 2 % catalyst would add only £1.30 per kilogram to the cost of the final product, which is much more likely to be competitive.

The cost of one kilogram of Pd-Sn/alumina at the time of this study was £650. Pd-Sn/alumina is a better catalyst for CO oxidation than Cu-Mn/graphite, and a loading of only 1 wt% therefore reduced the CO emissions from 100 % to 3.5 % at 350 °C and to 31.6 % at 600 °C. In economic terms, 1 wt% Pd-Sn/alumina would add £6.50 per kilogram to the cost of charcoal (making it commercially unfeasible for this application, except for a wealthy few!). However, 0.2 wt% Pd-Sn/alumina reduced CO emissions from 100 % to 26.9 % at 350 °C and to 44.4 % at 600 °C (Chapter 6). This would add only £1.3 per kilogram to the final product cost. With non-isothermal oxidation (Chapter 7), 1 wt% Pd-Sn/alumina catalyst treatment reduced CO emissions by more than 87 % compared to coal, 62 % compared to untreated charcoal briquettes and 50 % compared

to commercial untreated charcoal all values computed at 100 mL/min airflow. The enhanced activity with catalyst loading is consistent with previous observations [149]. Increasing the amount of catalyst impregnated onto the charcoal increases the number of active sites for the adsorption of CO and O_2 leading to more efficient CO oxidation [24].

8.4.1 Investment worthiness of the product

From the above discussion, the cost of charcoal/briquettes would increase by the same amount if impregnated with a 2 wt% Cu-Mn/graphite or 0.2 wt% Pd-Sn/alumina catalyst. However, the residual CO is lower with the 2wt% Cu-Mn/graphite catalyst (15.6 % residual CO at 350 °C and 25.3 % at 600 °C) than the 0.2 wt% Pd-Sn/alumina catalyst (26.9 % at 350 °C and 44.4 % at 600 °C). There are many other considerations from the health and product manufacturing perspectives that would also dictate the final pricing.

8.4.1.1 The health perspective

- The quantity of the catalyst would end up on the food during cooking from the briquette dust, material transfer via contact, and sparks should be established
- Whether such amounts are within the recommended daily intake as per local and international health standards
- The management of the residual ash from the briquettes after cooking – whether the ash be environmentally friendly if discharged without caution

8.4.1.2 The manufacturing perspective

- Making charcoal briquettes would involve more than just the addition of the catalysts.
- It may involve accelerants for quick start-up,
- white ash to show that the briquettes are hot enough and ready to cook food,
- binders for holding together all the briquette ingredients,
- press release for easy removal of briquettes from the mould during production, and
- fillers that add mass to the briquettes.

All the above parameters would add costs to the final product. However, the author asserts that a safe briquette is always less expensive than a life. Lobbying governments to subsidise these safe briquette products is an important strategy to ensure affordability of the products. Importantly, this study tested only two commercial catalysts. There are many catalysts that are known to facilitate CO oxidation (some of which are discussed in Chapter 2, 6 & 7) and other combinations that have never been tested before. These are some of the issues that will be investigated in the next phase before the product goes on the market as well as continuous research and development.

8.4.1.3 Recycling the residual ash

The residual ash left after cooking food would contain all the chemicals (catalysts) used to treat the solid fuels in addition to the inherent trace elements that the raw materials could have picked from their original locations. Consumers would then be supplied with appropriate disposable bags as they buy the catalyst treated solid fuels to keep the cooled residual ash after cooking/heating. This would then be bought back at an appropriate

fee or simply collected at no charge by the solid fuel manufacturing companies for recycling the catalysts. This would mean that (i) the residual ash would have a monetary value and (ii) we would not have issues with potential contamination of the environment with metal catalysts (iii) we would have a possibility of extracting the trace elements that came along with the raw materials for other added uses.

8.5 Practicalities for the implementation and application of the work

Previous research has identified several metal/metal oxide catalysts for the oxidation of CO [50], [87], [104], [109], [151]–[159] and has shown how such catalysts can be impregnated on charcoal as a support for catalyst systems [160]–[173] among other applications. Here we provided laboratory data that could be used for pilot-scale and full-scale applications aiming to minimise CO emissions in domestic and industrial settings. Combining the reported catalyst systems and catalyst impregnation technologies will facilitate the creation of different recipes suitable for briquettes prepared from carbonaceous materials. This technology is simple to use and can be applied to any carbonaceous material. The application of this technology to municipal solid waste, wood waste, vegetable waste, sludge and others will help local councils and national governments to alleviate the challenge of sanitation arising from carbonaceous wastes by converting the waste into useful energy while reducing emissions – ultimately limiting the amount of waste sent for landfill. This will help to achieve sanitation, reduce greenhouse gas emissions and create jobs in communities.

8.6 Limitations

In chapter 3, there are many materials that could have been used but due to time and resource constraints, I could only use ash (fraxinus) to represent the different biomass materials whose energy potential has not yet been evaluated. Secondly, there are many different methods for analysis and interpretation of thermal data from TGA/DSC but I chose to use master plots for reaction mechanism elucidation since master plots give clear, reproducible and near accurate prediction of reaction mechanisms.

Combustion experiments with commercial samples revealed that the obtained data was not consistent. This could have been due to mixtures of different tree species in the commercial sample batches. I therefore decided to make my own samples from known tree species (chapter 4). I then chose Lilac tree sample to represent other since their proximate and ultimate analysis results were comparable.

Reproduction of the peryxyl radical spectra (chapter 4) was challenging since these spectra had low intensities and were superimposed on another bigger spectrum. This meant that interpretation was difficult. I overcame this using a simulation software JEOL v2000.

In chapter 5, I could not easily get a real house for demonstrating CO accumulation in confined spaces. I therefore used a metallic ISO container. This has its own internal conditions that were different from a real house: it had no windows (only a double door), the internal temperatures were colder during non-sunny periods and hotter during sunny hours.

In chapter 6 and 7, I used only Pd-Sn/alumina and Cu-Mn/graphite as commercial test catalysts for impregnation on charcoal to minimize CO during combustion yet there are other catalysts. At the time of this work, these two

catalysts had been synthesized in our laboratory a few months back and commercial samples that had been used for comparison were available. To avoid incurring a further cost, I decided to use these samples. Secondly, this work was about the application of catalysts for CO oxidation (when impregnated on solid fuels), so these were good representatives.

Chapter 9: CONCLUSIONS

The conclusions below reflect the objectives listed in the introduction, section 1.4.

Objective 1: To review the analysis and processing of solid fuels

From previous literature covered in chapter two, I observed that direct catalytic oxidations of post-combustion pollutants are highly efficient and can achieve up to 100 % CO conversion at ambient temperatures. They can be used in conjunction with other systems like cooking and heating. There are various combinations of catalysts available commercially and many more to be synthesised in the future. Their success is attributed to their high affinity for oxygen and toxic pollutants onto their surfaces. However, they are usually poisoned by moisture, SO_2, CO_2 and high temperatures > 600 ^{o}C. They are also affected by PH: low values reduce their active sites leading to reduced adsorption capabilities for CO and O_2. Effective systems also require high catalyst loading, specific preparation methods, and material properties. Failure to achieve the stringent requirements means that the prepared catalyst system will not perform to expectations.

Altering the composition of the solid fuels by impregnation of chemical catalysts has been used to trigger desired reactions and achieve target products. Using such an approach (while applying better chemical catalysts) on solid fuels used for cooking and heating systems would mean that the solid fuel would release minimal amounts of CO. Hence, the amounts of CO released would be rendered none lethal acutely. This coupled with other technologies like well-designed cookstoves, improved boilers, and sensors/detectors would ensure a safer environment for solid fuel users.

Objective 2: To understand the principles of biomass pyrolysis

In chapter 3, I described and demonstrated that there are several materials which could be used for energy generation yet their potential has not yet been evaluated. I chose one example to demonstrate this: Ash (Fraxinus) sawdust biomass materials were studied in detail by TGA/DSC to determine kinetic and thermodynamic parameters (in pyrolysis reactions), which are used to determine the energy potential of biomass materials. In this work the Friedman and Starink methods were used for kinetic analysis because these methods are more accurate than similar methods. From the results, the E_α values were 180 – 350 kJ/mol. Pyrolysis reactions involved several mechanisms, including diffusion, geometrical contraction, reaction-order models and/or nucleation. The pre-exponential factors were between 10^{12} and 10^{19} s^{-1}. The change in entropy values remained negative up to α = 0.75, but became positive at higher conversions, implying greater disorder among the final products compared to the reactants. The calorific value of the ash wood sawdust was 18.3 MJ/kg which is comparable to other sources of biomass used for energy generation. The knowledge and skills obtained from the pyrolysis of milligram-sized samples of ash were scaled up and customised to prepare laboratory charcoal samples for subsequent experiments.

Objective 3: To investigate the combustion and surface chemistry of charcoal

Chapter 4 describes how laboratory scale charcoal samples were prepared from five different tree species by pyrolysis. Lilac charcoal was chosen to represent the other biomass materials for in-depth analysis. Lilac was highly reactive, igniting at low temperatures of 250 – 290 °C. The high reactivity was shown to be due to the presence of oxygenated or aliphatic functional groups, the presence of active sites, the H/C ratio, the presence of free radicals, and the bonding between each unit. The high reactivity could also be due to the

presence of many exposed carbon atoms on the surface and between the pores, which are susceptible to oxidation.

Carbonisation of lilac wood formed charcoal with free radicals on its surface, including •C-C and C-O• as identified with ESR. Oxidation of lilac char with pressurised air formed persistent peroxyl radicals (-O-O•). The free radicals with oxygen heteroatoms are believed to be the source of CO during combustion. The pyrolysis of lilac charcoal in N_2 removed the free radicals. The same effect was observed when the charcoal was acid washed using 1 M hydrochloric acid. This was due to the removal of oxygen functional groups and rearrangement of the free radicals to form non-radical groups [135], [132].

Objective 4: To investigate the parameters responsible for the release of CO

The results in chapter 5 demonstrate that sawdust and charcoal both emit high amounts of CO during incomplete combustion. However, charcoal emitted almost twice as much CO as sawdust. The CO emissions were influenced by temperature and airflow. In a confined environment, the amounts of CO emissions recorded in the ISO container increased with decrease in airflow within the container. Higher amounts of CO were recorded at the upper parts of the container compared to the lower parts.

Objective 5: To investigate the effect of impregnating charcoal with catalysts on the emissions released during combustion.

Chapter 6 describes how charcoal dust was impregnated with Pd-Sn/alumina and Cu-Mn/graphite. This led to the reduction in the amounts of CO released when the catalyst treated sampled were heated isothermally in a tube furnace. In this case, addition of only 1 wt% Pd-Sn/alumina to charcoal dust led to the reduction of CO to as low as 3.5 % of the total. Additionally, increasing the amount of catalyst impregnated onto the charcoal increased the number of active sites for the adsorption of CO and O_2 and therefore

achieved more efficient CO oxidation [24]. However, CO oxidation activity of the catalysts decreased at higher temperatures due to the formation of less active phases [174].

In chapter 7, I describe how catalyst treated, and untreated charcoal briquettes which I prepared compare to commercial charcoal and coal for emission of CO, NO_x, CH_4 and CO/CO_2. Catalyst treated samples exhibited a higher combustion efficiency, by up to 20 %, compared to other samples. The CO/CO_2 was reduced by up to 7-fold while the temperature for the emission of NO_x was reduced though the amounts emitted were not impacted upon.

APPENDICES

10.1 Appendix A: Extended Peroxyl Radical Spectra

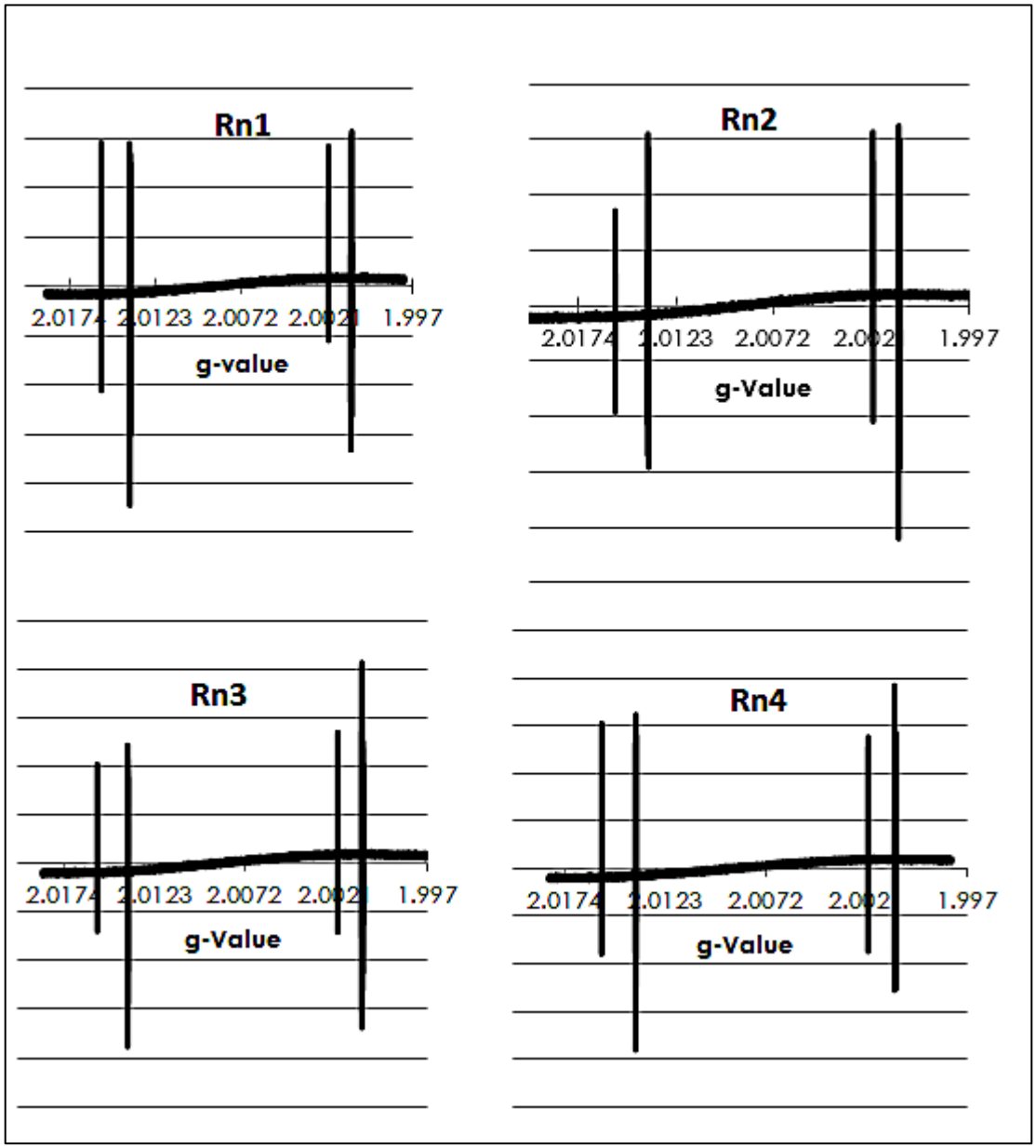

Figure A- 1: Spectra of the peroxyl radicals recorded at the same conditions

Figure A- 2: Expanded radical spectrum, g-value – 2.00067, center field – 320.679 mT

Figure A- 3: Expanded radical spectrum, g-value – 2.002, center field – 319.984 mT

Figure A- 4: Expanded radical spectrum, g-value – 2.0138, center field – 318.105 mT

Figure A- 5: Expanded radical spectrum, g-value – 2.0155, center field – 317.369 mT

10.2 Appendix B: Kinetic and Emission Data for Solid Fuel Combustion

10.2.1 Mass loss and CO emissions

10.2.1.1 Mass loss and CO emissions at 20 °C/min

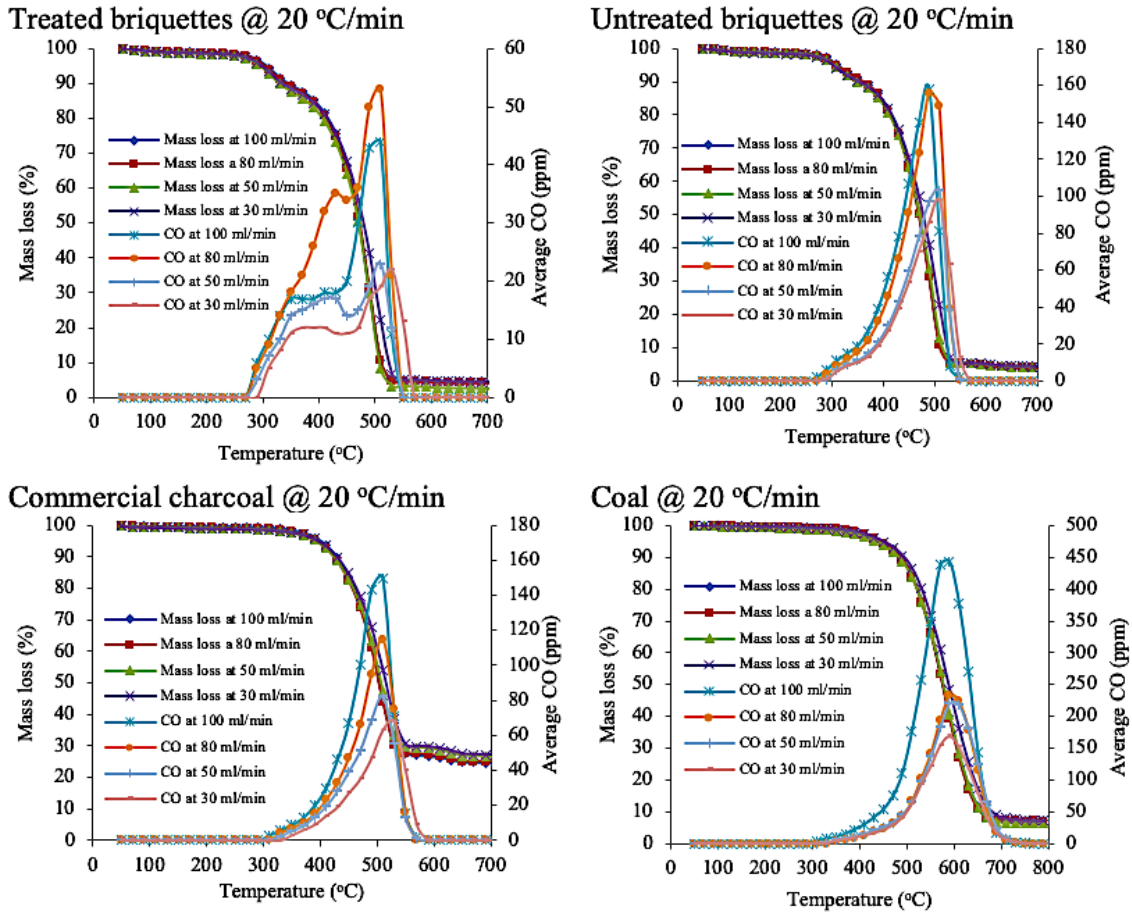

Figure B-1: Mass loss and CO emissions at different airflows and 20 °C/min heating rate for CTCB, UTCB, ComC, and coal

10.2.1.2 Mass loss and CO emissions at 30 °C/min

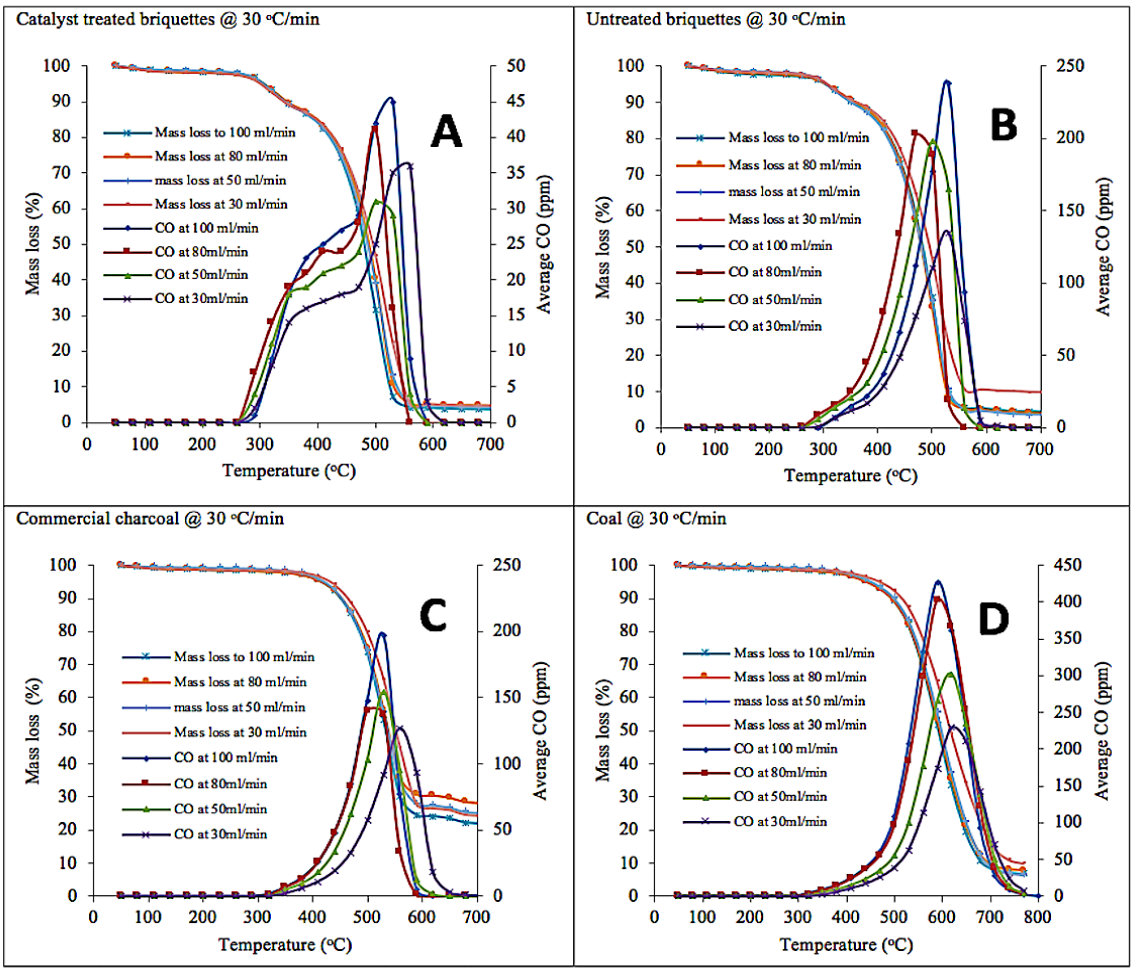

Figure B-2: Mass loss and CO emissions at different airflows and 30 °C/min heating rate. A – CTCB; B – UTCB; C – ComC; and D – Commercial coal

10.2.1.3 Mass loss and CO emissions at 40 °C/min

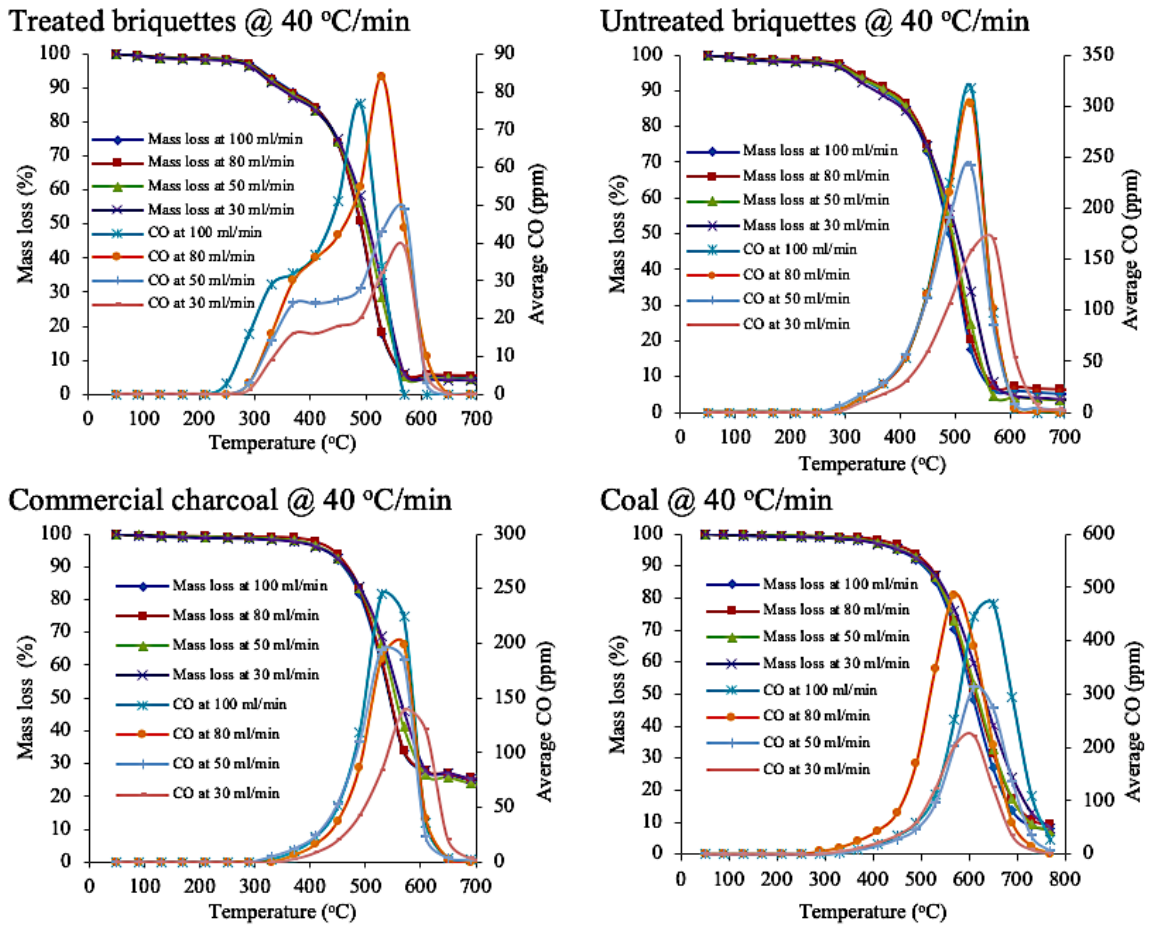

Figure B-3: Mass loss and CO emissions at different airflows and 40 °C/min heating rate for CTCB, UTCB, ComC, and coal

10.2.2 CO/CO_2 ratio

10.2.2.1 CO/CO_2 at 20 °C/min

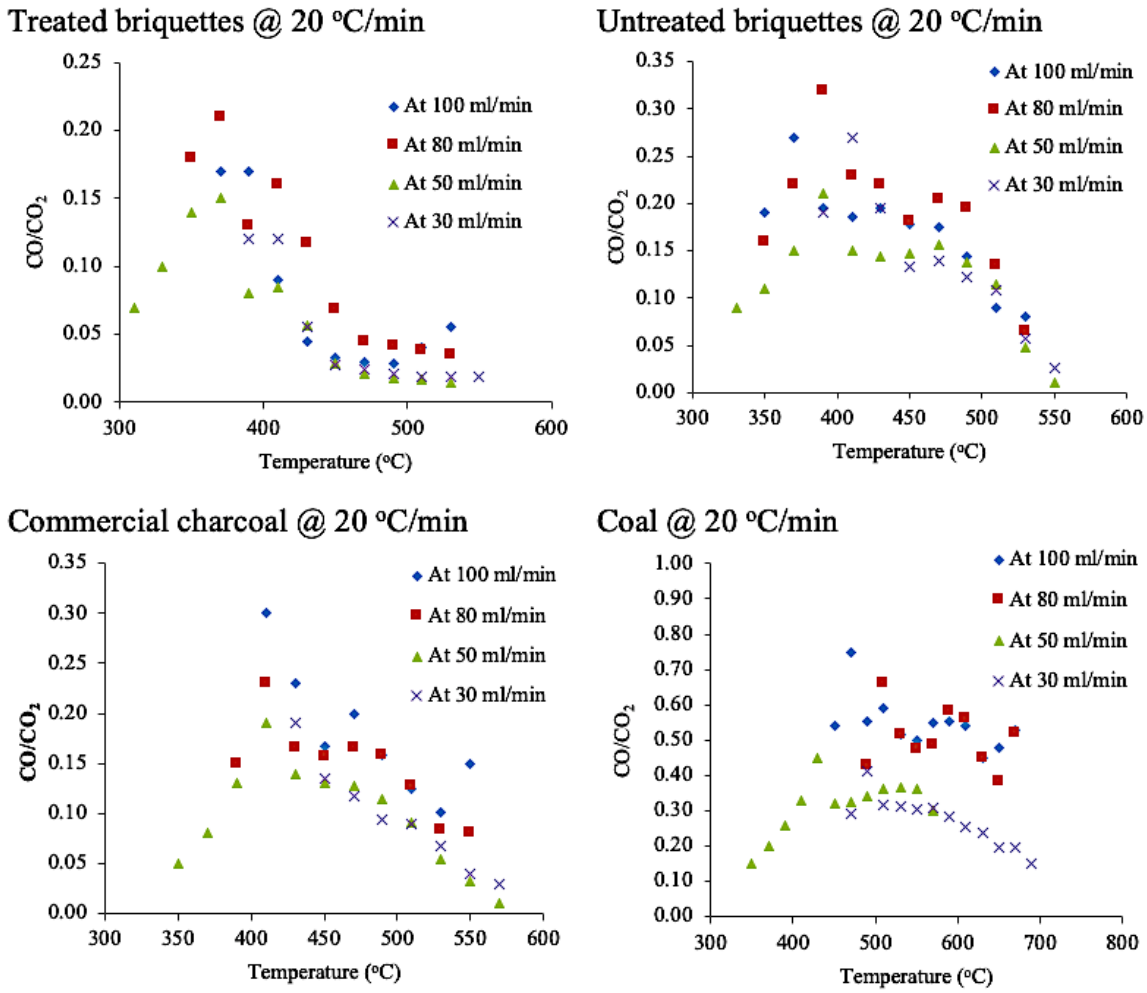

Figure B-4: CO/CO2 ratio for CTCB, UTCB, ComC, and coal at 20 °C/min

10.2.2.2 CO/CO_2 at 30 °C/min

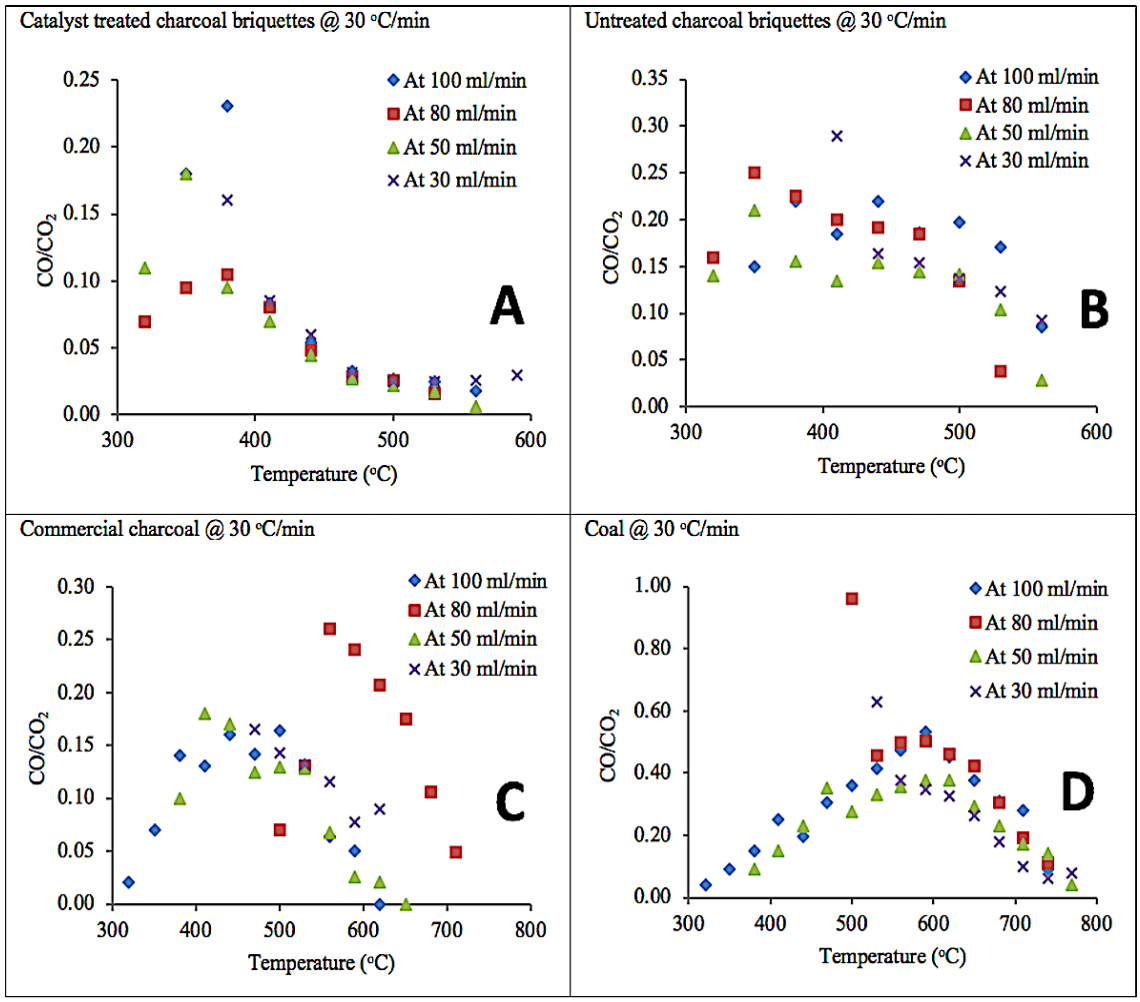

Figure B-5: CO/CO2 ratio at different airflows and 30 °C/min heating rate. A – CTCB; B – UTCB; C – ComC; and D – Commercial coal

10.2.2.3 CO/CO_2 at 40 °C/min

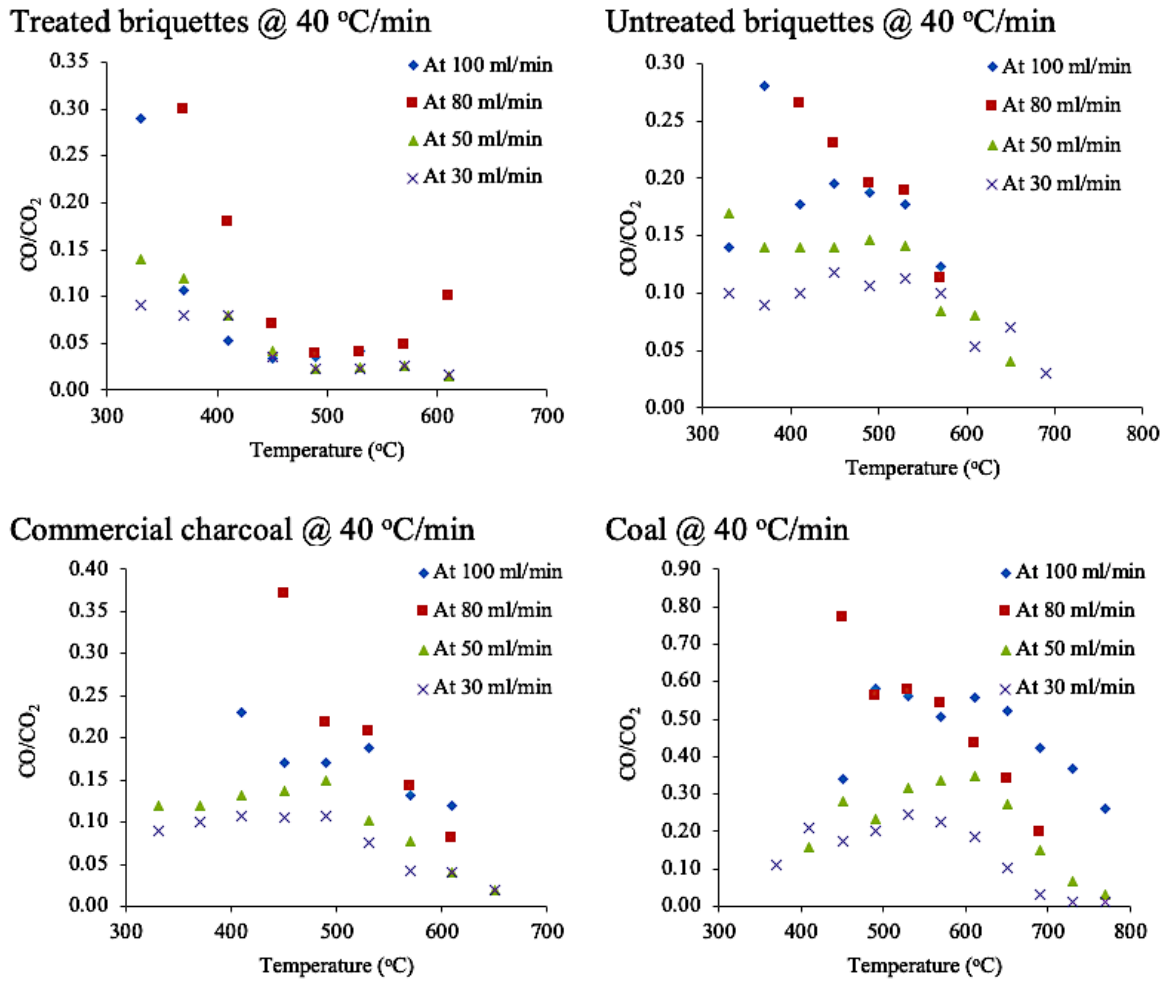

Figure B-6: CO/CO2 ratio for CTCB, UTCB, ComC, and coal at 40 °C/min

Appendix B - Table 1: The E_α analogous parameter B, pre-exponential factor related parameter A and the regression coefficients obtained from plots of CO/CO2 ratio function at different heating rates and conversions for CTCB

	100 mL/min			80 mL/min			50 mL/min			30 mL/min		
α	B	A	R^2	B	A	R^2	B	A	R^2	B	A	R^2
0.069	-	-	-	-	-	-	0.024	2.20×10^{18}	0.98	-	-	-
0.109	0.005	7.06×10^{3}	0.78	0.002	1.52×10^{2}	0.01	0.002	6.17×10^{1}	0.05	-	-	-
0.160	-0.009	2.83×10^{-6}	0.83	0.011	2.37×10^{7}	0.20	0.011	2.30×10^{7}	0.64	0.004	9.19×10^{2}	0.44
0.285	0.008	4.70×10^{4}	0.91	0.004	1.16×10^{3}	0.07	0.010	1.25×10^{6}	0.98	0.007	2.36×10^{4}	0.35
0.527	0.017	4.49×10^{9}	0.96	0.017	5.56×10^{9}	0.99	0.013	3.10×10^{7}	0.43	0.008	2.42×10^{4}	0.18
0.870	0.008	2.60×10^{4}	0.78	0.001	2.29×10^{0}	0.00	0.011	4.86×10^{5}	0.63	0.010	2.78×10^{5}	0.94
0.988	-	-	-	-	-	-	0.006	8.18×10^{2}	0.13	0.010	2.38×10^{5}	0.98
0.989	-	-	-	-	-	-	-	-	-	0.007	1.39×10^{3}	0.72

Appendix B - Table 2: The E_α analogous parameter B, pre-exponential factor related parameter A and the regression coefficients obtained from plots of CO/CO_2 ratios at different heating rates and conversions for UTCB

	100 mL/min			80 mL/min			50 mL/min			30 mL/min		
α	B	A	R^2	B	A	R^2	B	A	R^2	B	A	R^2
0.104	0.009	7.71×10^{6}	0.89	-	-	-	0.006	1.07×10^{5}	0.61	-	-	-
0.140	0.005	1.61×10^{4}	0.73	0.007	4.67×10^{5}	0.82	0.003	6.40×10^{2}	0.58	-	-	-
0.319	0.013	3.75×10^{8}	0.67	0.019	1.56×10^{12}	0.97	0.017	1.02×10^{11}	0.95	0.005	4.22×10^{3}	0.62
0.488	0.015	2.92×10^{9}	0.63	0.014	7.65×10^{8}	0.78	0.013	1.87×10^{8}	0.73	0.005	1.92×10^{3}	0.13
0.732	0.012	1.81×10^{7}	0.69	0.011	5.03×10^{6}	0.96	0.010	1.29×10^{6}	0.86	0.008	6.13×10^{4}	0.63
0.965	0.012	8.75×10^{6}	0.81	0.008	4.19×10^{4}	0.27	0.004	4.08×10^{2}	0.80	0.006	5.43×10^{3}	0.71
0.987	0.005	6.12×10^{2}	0.69	-	-	-	0.011	1.22×10^{6}	0.78	0.005	6.30×10^{2}	0.37

10.2.3 Mass loss rate

10.2.3.1 Mass loss rate at 20 °C/min

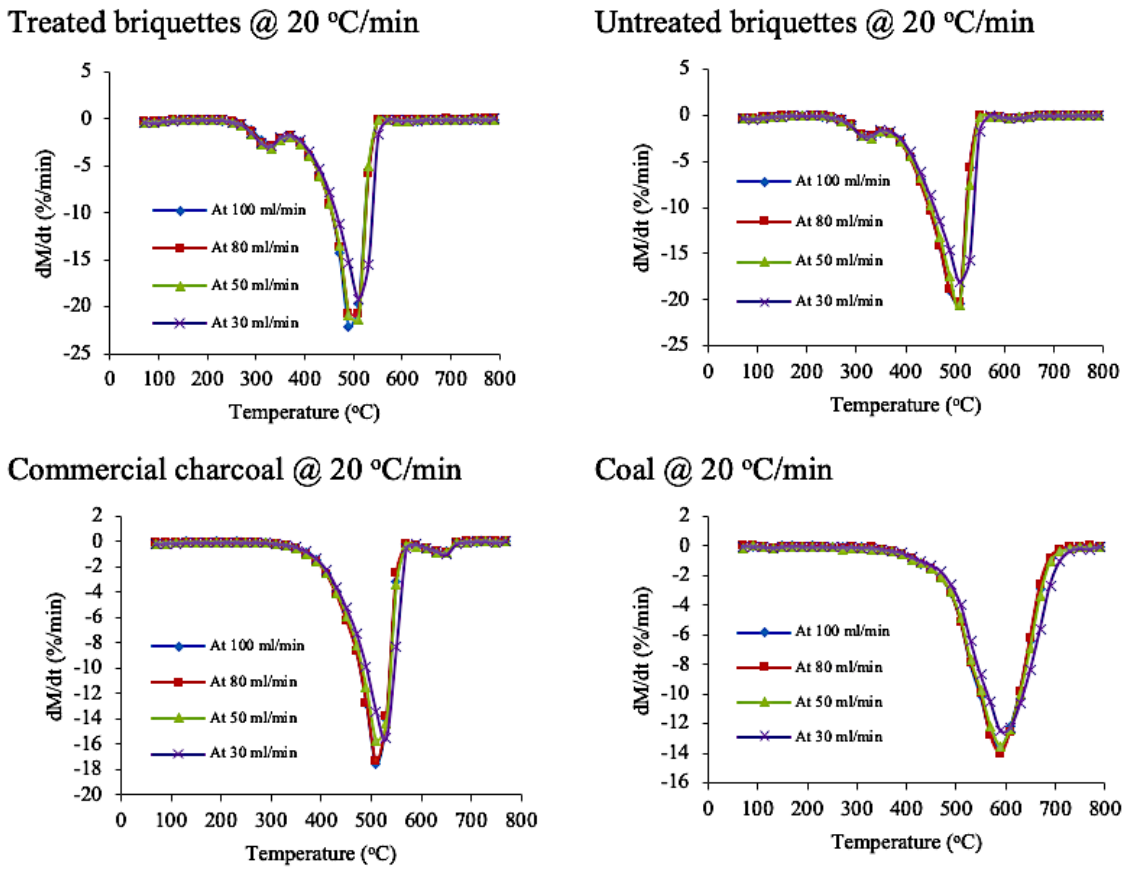

Figure B-7: Mass loss rate for CTCB, UTCB, ComC, and coal at 20 °C/min

10.2.3.2 Mass loss rate at 30 °C/min

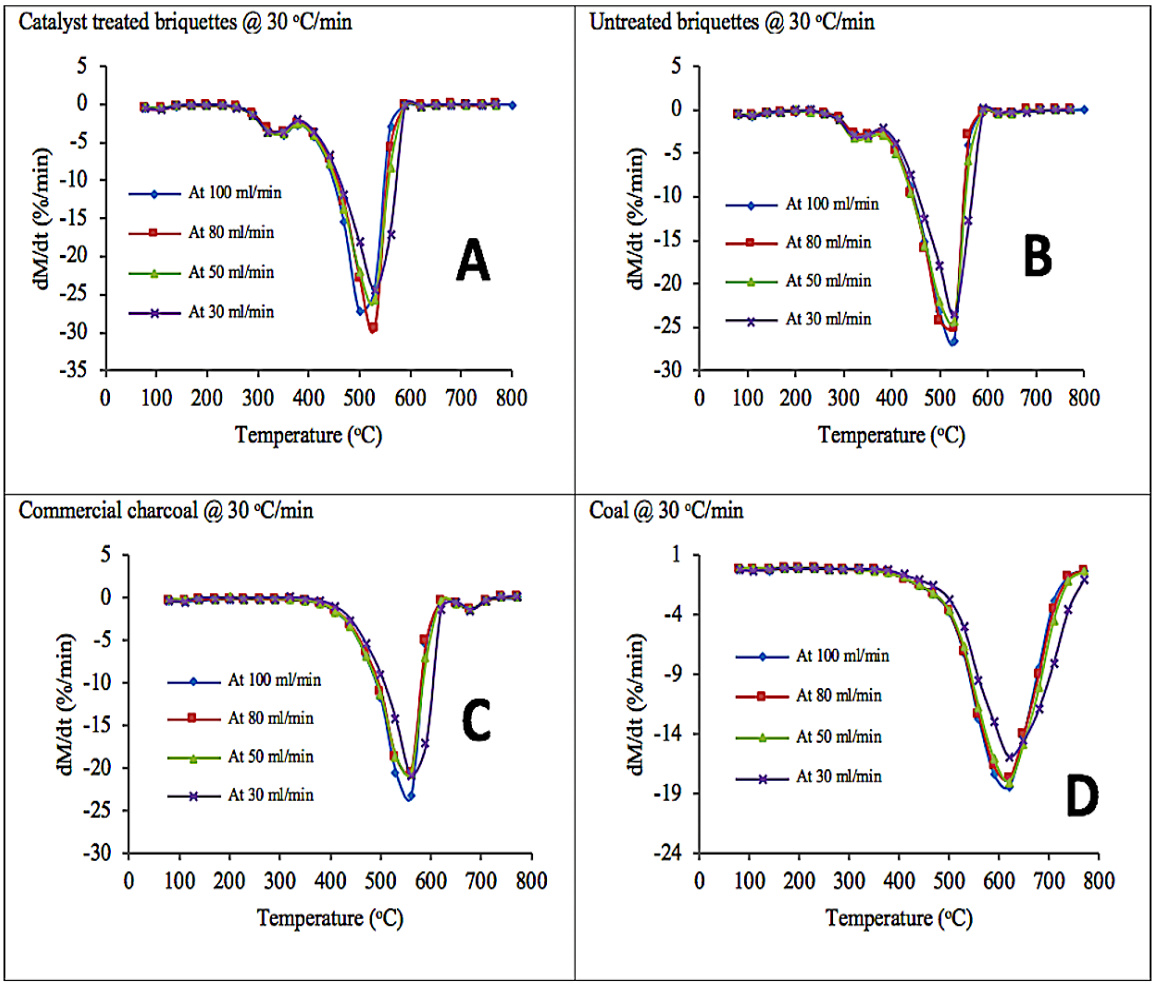

Figure B-8: Mass loss rate for CTCB, UTCB, ComC, and coal at 30 °C/min

10.2.3.3 Mass loss rate at 40 °C/min

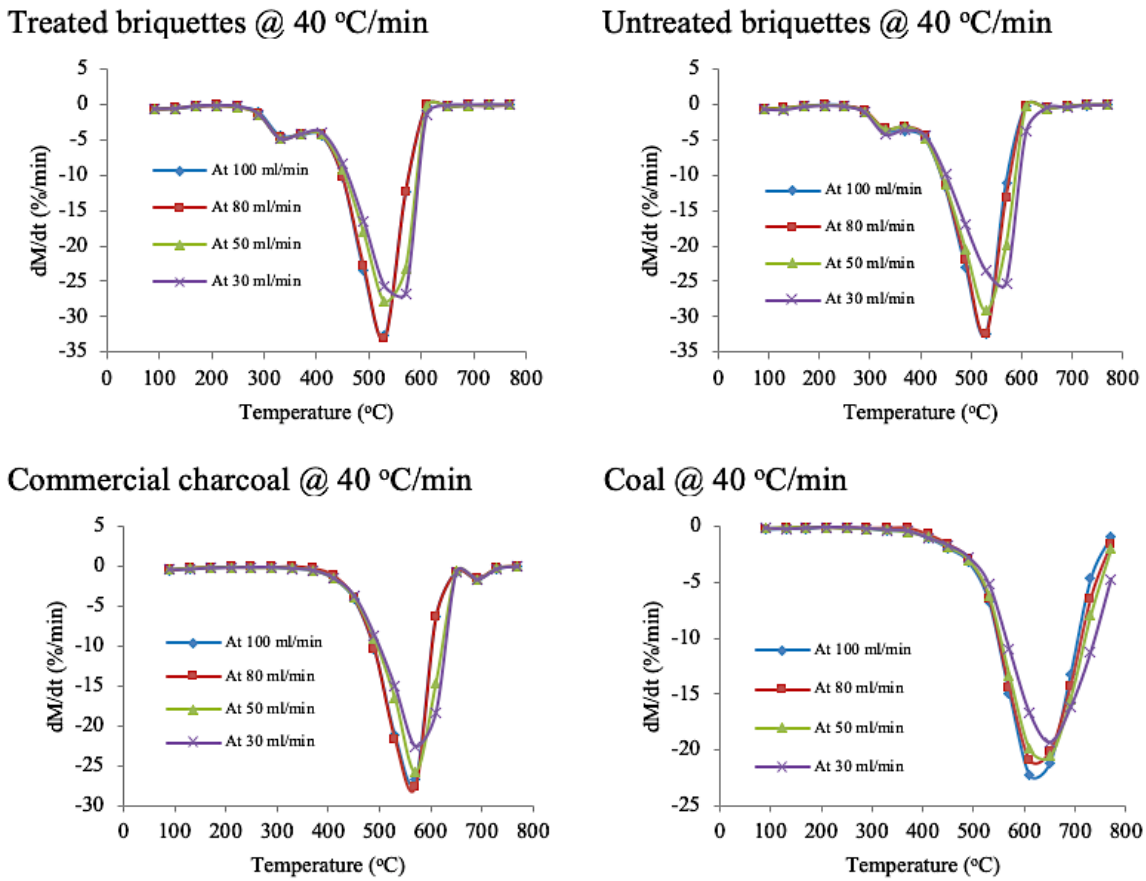

Figure B-9: Mass loss rate for CTCB, UTCB, ComC, and coal at 40 °C/min

10.3 Appendix C: Designs of Specialised Equipment Components

10.3.1 The design of the two-in-one CO-CO_2 sensor

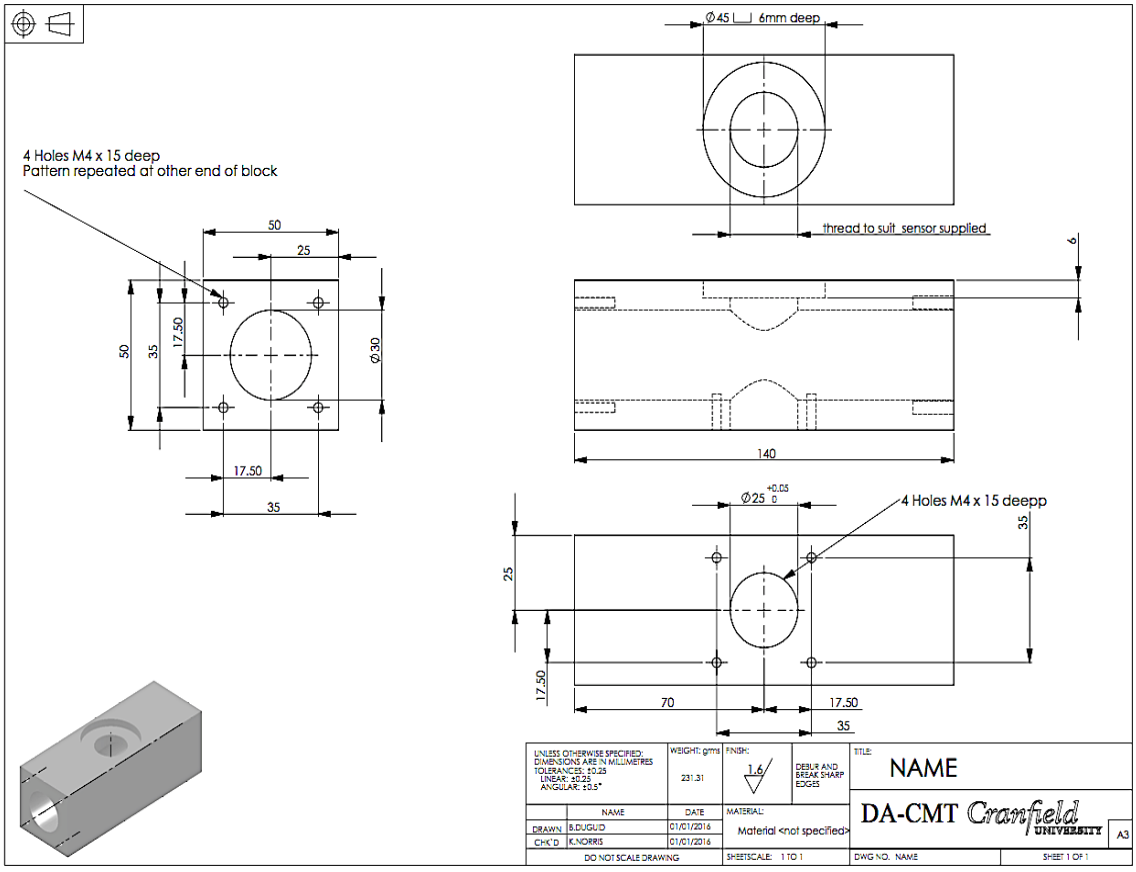

Figure C-1: The tube assembly

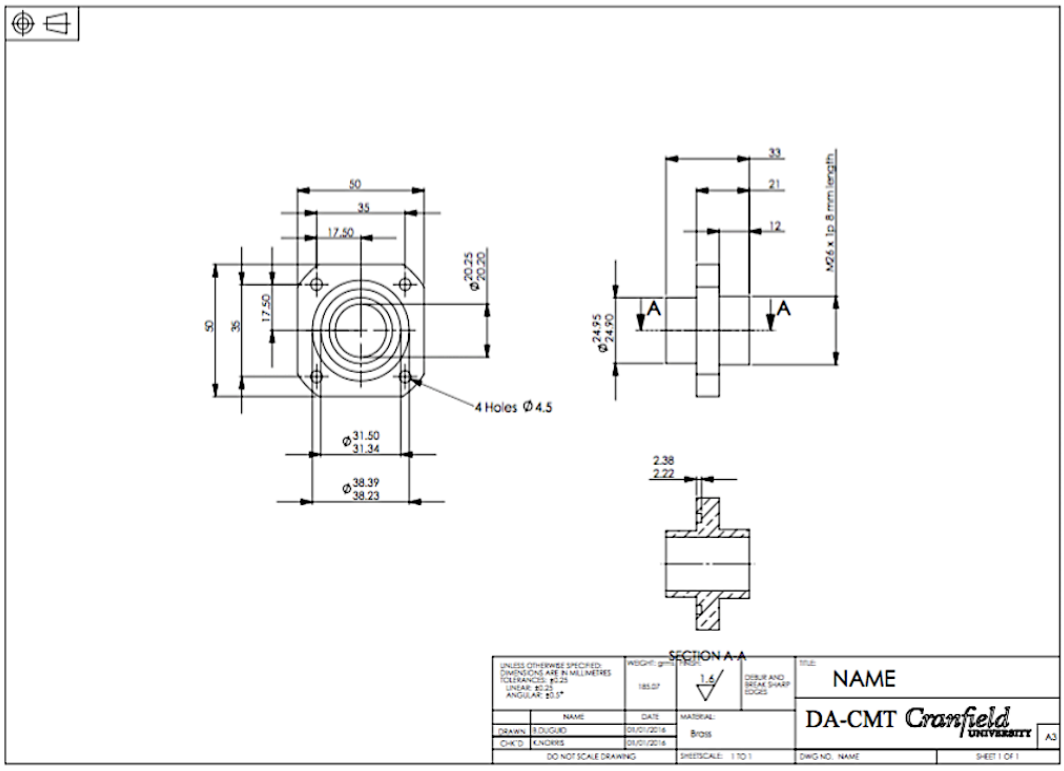

Figure C-2: Side A-the CO sensor port

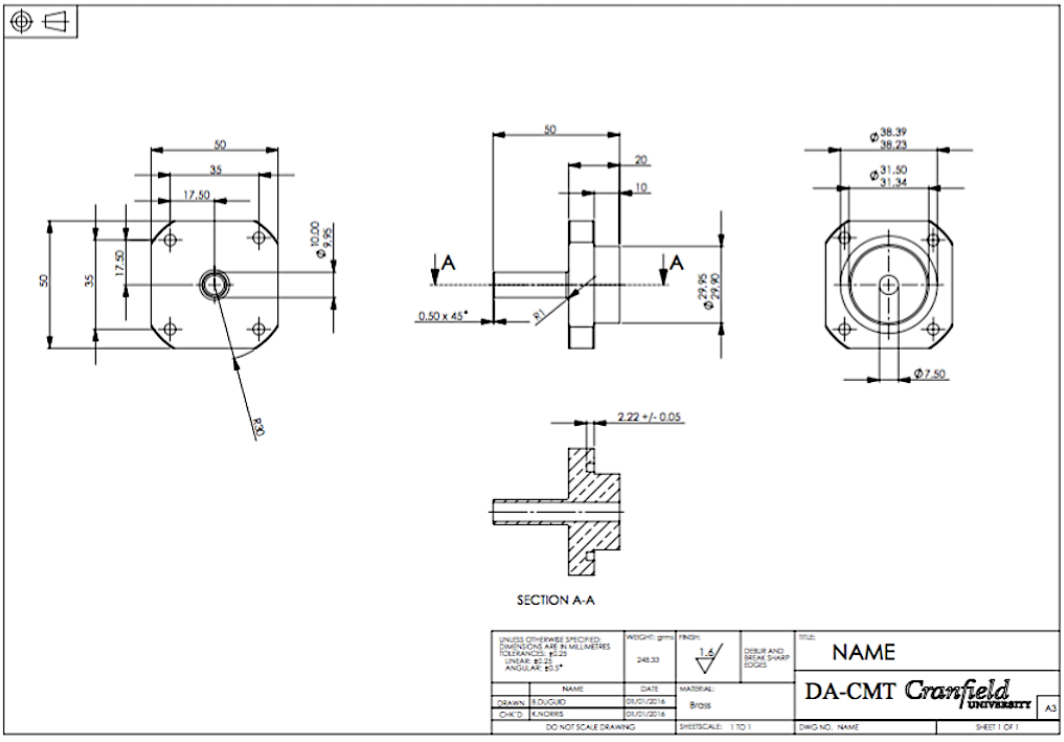

Figure C-3: Side B- the CO_2 sensor port

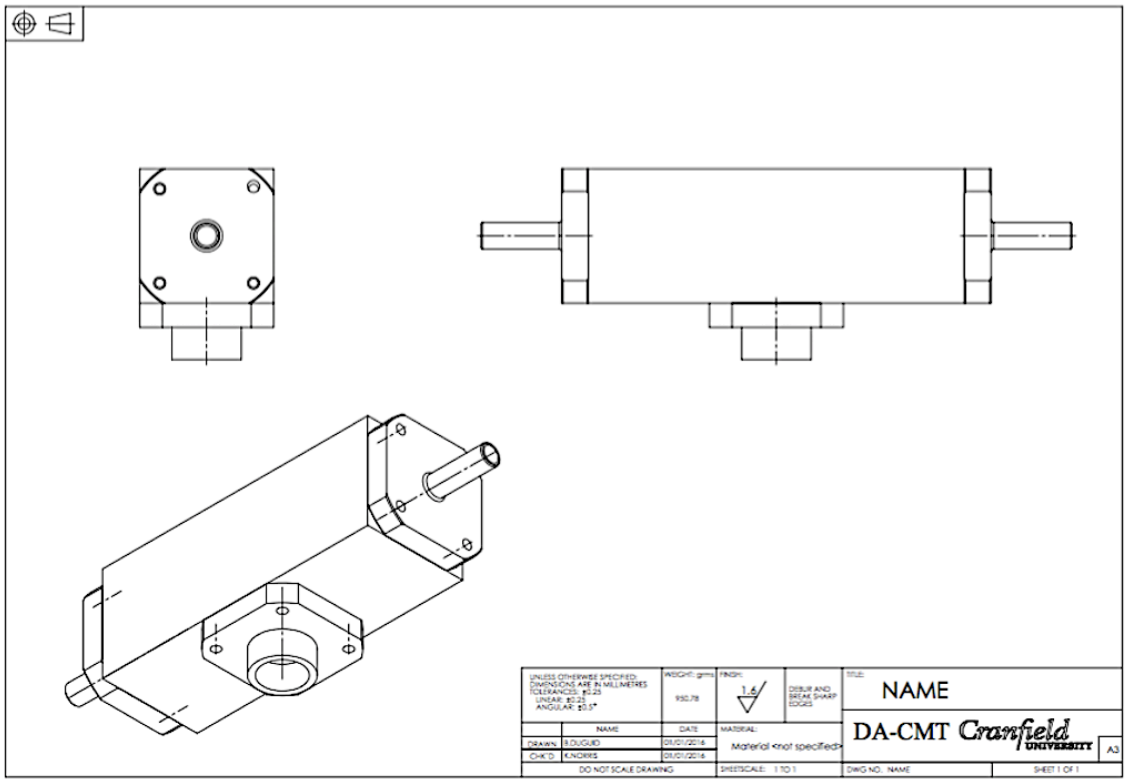

Figure C-4: The whole CO-CO_2 unit cell assembly

10.3.2 The design of the laboratory vibratory pulveriser

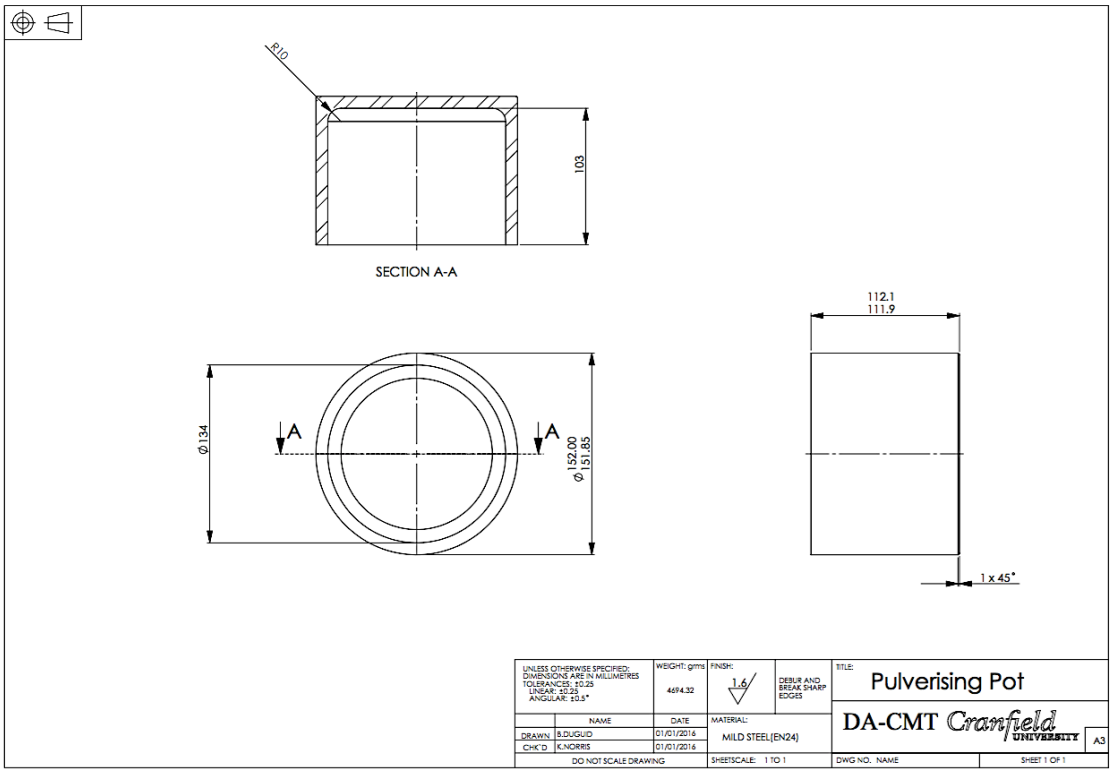

Figure C-5: The pulveriser pot

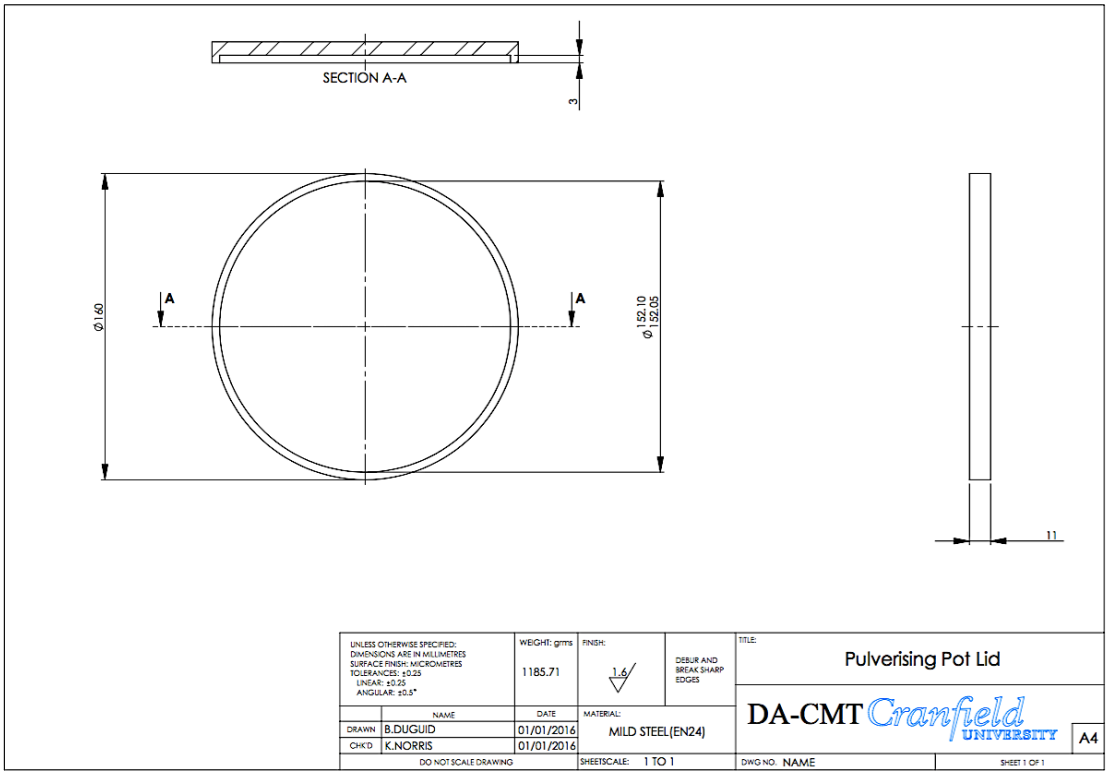

Figure C-6: The pulveriser lid

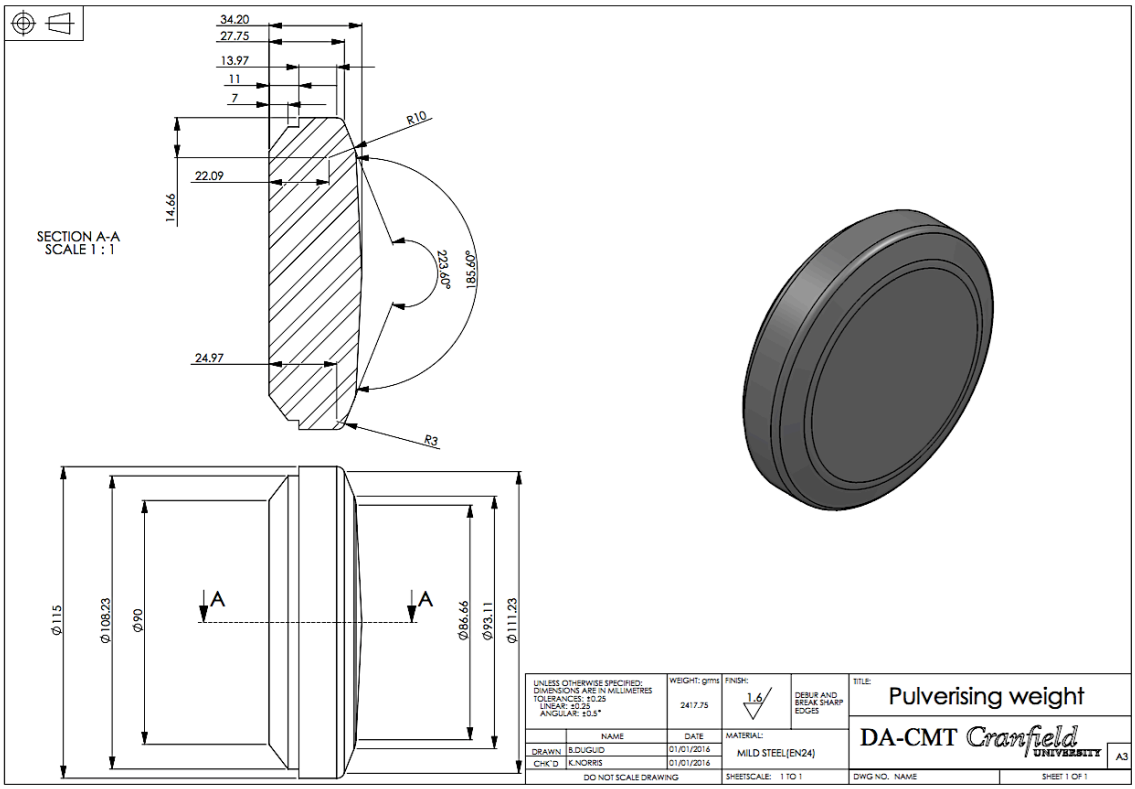

Figure C-7: The pulverising weight

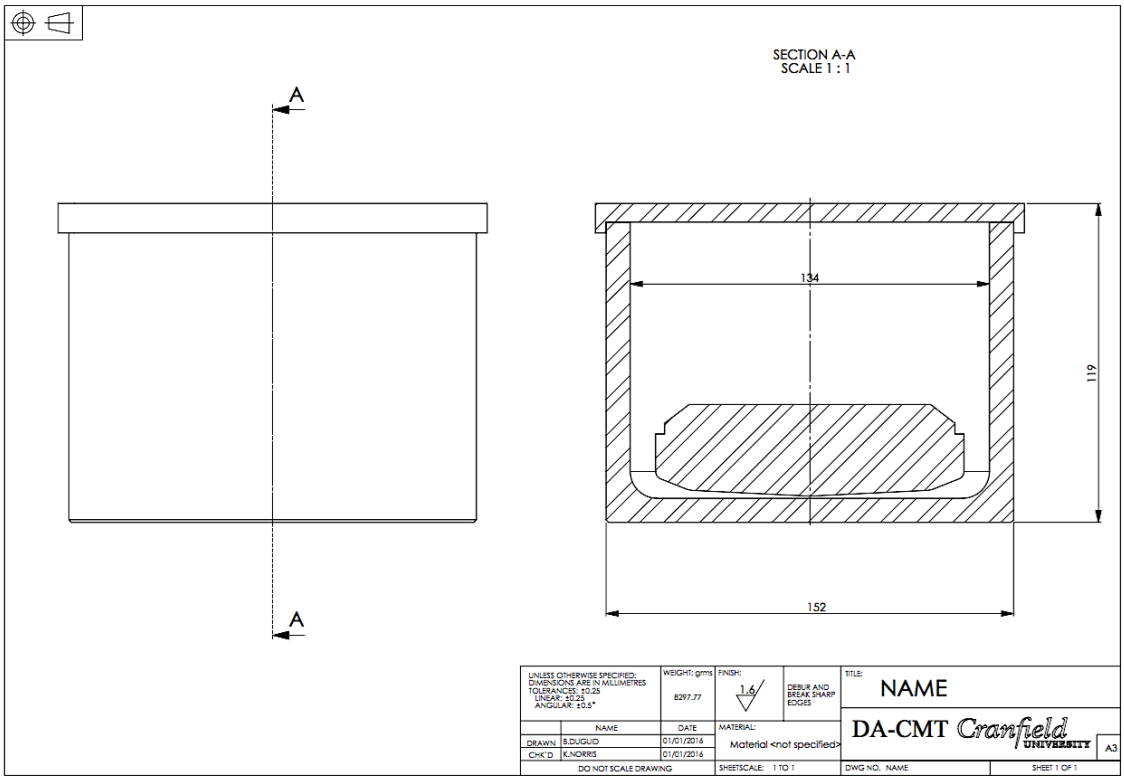

Figure C-8: The whole pulveriser assembly

10.4 Appendix D: The ISO container experimental set-up

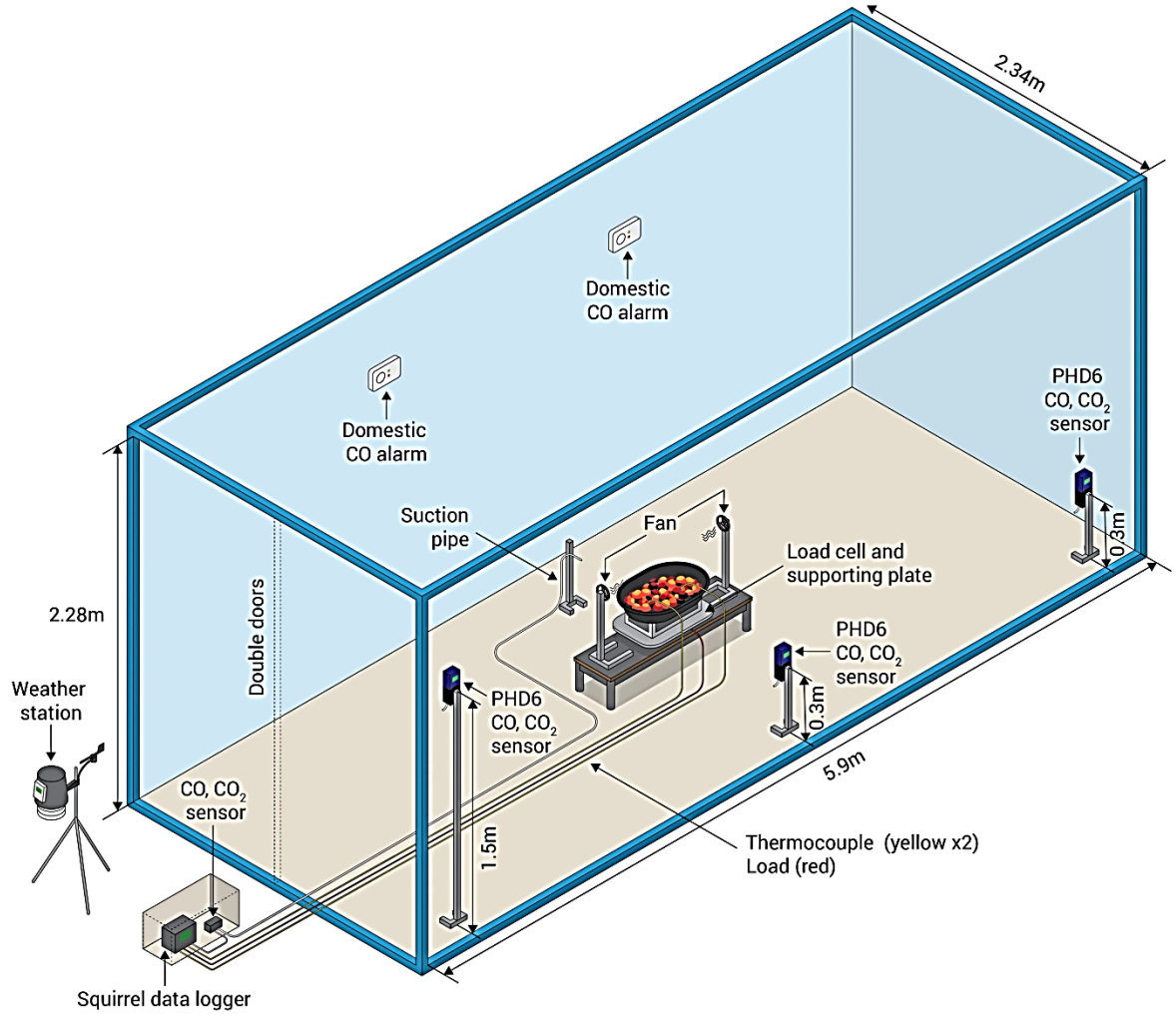

Figure D-1: ISO container experimental set-up

GLOSSARY

Activated complex	"A collection of intermediate structures in a chemical reaction that persist while bonds are breaking and new bonds are forming. It therefore represents not one defined state, but rather a range of transient configurations that a collection of atoms passes through in between clearly defined products and reactants" [175]
Activation energy	The minimum quantity of energy which the reacting species must possess in order to undergo a specified reaction
Adsorption	The process by which a solid holds molecule of a gas or liquid or solute as a thin film.
Air excess	Is a percentage of the theoretical air required to ensure complete combustion
Air staging	The introduction of over-fire air into the furnace
Air-fuel ratio	The mass ratio of air to a solid, liquid, or gaseous fuel present in a combustion process
Amorphous material	A solid that lacks the long-range order that is characteristic of a crystal
Anisotropy of a paramagnetic system	This describes how an object's *magnetic* properties can be different depending on direction. In the simplest case, there is no preferential direction for an object's *magnetic* moment
Asphyxiant	A substance that can cause unconsciousness or death by suffocation (asphyxiation)
Biochar	Charcoal produced from plant matter
Bioenergy potential	Renewable energy made available from materials derived from biological sources
Biomass	Organic matter used as a fuel
Calorific value	The amount of energy produced by the complete combustion of a material or fuel
Catalyst	A substance that increases the rate of a chemical reaction without itself undergoing any permanent chemical change
Chemisorption	Adsorption in which the adsorbed substance is held by chemical bonds.

Co-firing	The combustion of two (or more) different types of materials at the same time [176]
CO+Impact project	A project that investigated the impact of CO in England and Wales
Combustion	Rapid chemical combination of a substance with oxygen, involving the production of heat and light.
Combustion efficiency/selectivity to CO_2	a measurement of how well the fuel being burned is being utilized in the combustion process
Continuous wave (cw) - ESR/EPR	The application of a constant microwave field of constant frequency on a sample while sweeping a magnetic field (B_0) until the resonance condition is met. This results in a cw-EPR spectrum which is the reflected microwave radiation as a function of the magnetic field. An amplitude modulation typically with a frequency of 100 kHz of the magnetic field is carried out to obtain better signal to noise. This additional modulation leads to the characteristic first derivative line shapes observed in cw-EPR. There are three parameters that can be readily obtained upon analysis of cw-EPR spectra: (a) field position, (b) hyperfine interactions, and (c) linewidth. The field positions can be used to calculate the g-factor values for the electron spin, which reveals the nature of the radical species formed and can be considered analogous of the chemical shift in NMR spectroscopy.
Crystalline	Property of a crystal. A solid material whose constituents (such as atoms, molecules, or ions) are arranged in a highly ordered microscopic structure, forming a crystal lattice that extends in all directions
Differential scanning calorimetry	Is a thermo-analytical technique in which the difference in the amount of heat required to increase the temperature of a sample and reference is measured as a function of temperature [177]
Diffuse reflectance infrared Fourier transform	Diffuse Reflectance Infrared Fourier Transform Spectroscopy (DRIFTS) is a technique that collects and analyzes scattered IR energy. It is used for measurement of fine particles and

	powders, as well as rough surface (e.g., the interaction of a surfactant with the inner particle, the adsorption of molecules on the particle surface). Sampling is fast and easy because little or no sample preparation is required [178]
Electron spin resonance	
Emission factor	Is a representative value that attempts to relate the quantity of a pollutant released to the atmosphere with an activity associated with the release of that pollutant
Endothermic	(Of a reaction or process) accompanied by or requiring the absorption of heat.
Enthalpy	A thermodynamic quantity equivalent to the total heat content of a system. It is equal to the internal energy of the system plus the product of pressure and volume
Entropy	A thermodynamic quantity representing the unavailability of a system's thermal energy for conversion into mechanical work, often interpreted as the degree of disorder or randomness in the system
Exothermic	(Of a reaction or process) accompanied by the release of heat.
Fossil fuel	A natural fuel such as coal or gas, formed in the geological past from the remains of living organisms.
Fractional conversion	The ratio of the amount reacted to the amount fed
Free radical	An uncharged molecule (typically highly reactive and short-lived) having an unpaired valence electron.
Fuel-lean-condition	Meaning too much air for the amount of fuel or as not enough fuel for the amount of air
Fuel-rich-condition	Meaning too much fuel for the amount of air supplied or as not enough air for the amount of fuel available
g-factor	In the absence of nuclear hyperfine interactions, B and ν are related by: $h\nu = g\mu_B B$, where h is the Planck constant, ν is the microwave frequency, μ_B is the Bohr magneton $eh/(4\pi m_e)$, and the dimensionless scalar g is called g-factor. This

	dimensionless value determines the position of the ESR/EPR signal.
Gasification	A process that converts organic or fossil fuel-based carbonaceous materials into carbon monoxide, hydrogen and carbon dioxide
Gibbs free energy	A thermodynamic potential that can be used to calculate the maximum of reversible work that may be performed by a thermodynamic system at a constant temperature and pressure
Heating rate	The amount of heat supplied per unit time
Heating value	The amount of heat released during the combustion of a specified amount of a substance
Hydrophobic	Tending to repel or fail to mix with water.
Hyperfine coupling constant	Is directly related to the distance between peaks in a spectrum and its magnitude indicates the extent of delocalization of the unpaired electron over the molecule.
Hyperfine line splitting	Is a special feature of ESR caused by the interaction of electron spins with the magnetic nuclei in the sample. I.e. a magnetic nucleus with quantum number I will split a single ESR line (peak) into 2I+1 lines (peaks).
Iso-conversional	The principal applies on two assumptions: (*i*) Rate of the processes in condensed state is generally a function of temperature and conversion and (*ii*) The activation parameters are obtained from a set of kinetic runs from the dependences of time *vs*. temperature (for isothermal measurements), temperature *vs*. heating rate (for integral and incremental methods with linear heating rate) or from reaction rate *vs*. temperature (for the differential Friedman method). The evaluation is carried out at the fixed conversion [179]
Isothermal	Involving or possessing a constant temperature.
Lamella constituent molecules	These are molecules with strong covalent bonds between atoms but the interplanar bonds are weak. Like in graphite, the C-C bonds are strong but interplanar bonds are composed of weak van der waal forces

Lattice parameter	The physical dimension of unit cells in a crystal lattice.
Lewis acid	A chemical species that contains an empty orbital which is capable of accepting an electron pair from a Lewis base to form a Lewis adduct.
Municipal solid waste	Commonly known as trash or garbage or rubbish, is a waste type consisting of everyday items that are discarded by the public.
Non-isothermal	Involving or possessing temperatures that are not constant.
Nuclear magnetic resonance	Involves the immersion of nuclei in a magnetic field, and then matching the frequency at which they are processing with electromagnetic radiation of exactly the same frequency so that energy absorption can occur.
Physiochemical	Pertaining to both physical and chemical properties, changes, and reactions. of or according to physical chemistry
Physisorption	Also called physical adsorption, is a process in which the electronic structure of the atom or molecule is barely perturbed upon adsorption
Polycyclic aromatic hydrocarbon	Are hydrocarbons – organic compounds containing only carbon and hydrogen— that are composed of multiple aromatic rings (organic rings in which the electrons are delocalized)
Pyrolysis	Thermal decomposition of materials at elevated temperatures in an inert atmosphere. It involves a change of chemical composition and is irreversible.
Residual CO	The amount of carbon monoxide left relative to the total amount emitted
Slow pyrolysis	The slow heating of organic material in absence of oxygen. Instead of combusting, the volatiles from the organic material evaporate partly, and a product (charcoal) remains, consisting for a large part (normally 80%) of carbon.
Smouldering	Smoldering is a low-temperature, slow, flameless combustion maintained by heat from reaction of oxygen with fuel components [180]. It involves both pyrolysis

	of the original fuel and oxidation of the resulting char. Since smoldering usually occurs in limited oxygen supply, the rate of reaction is directly proportional to the oxygen mass flux. At above 35% oxygen supply, smoldering may transition to flaming [181]. For sawdust and charcoal, smoldering is affected by temperature, ash content, volatile matter content, and particle size oxygen supply and heat loss. With sawdust, temperature increases while during charcoal smoldering, temperature decreases. Low ash content allows oxygen diffusion leading to increased smoldering front propagation. High volatile content fuels produce much smoke during smoldering compared to low volatile content fuels [182].
Specific surface area	Is a property of solids defined as the total *surface area* of a material per unit of mass, (with units of m^2/kg or m^2/g) or solid or bulk volume (units of m^2/m^3 or m^{-1}). It is a physical value that can be used to determine the type and properties of a material (e.g. soil or snow).
Thermogravimetric analysis	Is a method of thermal analysis in which the mass of a sample is measured over time as a function of temperature.
Torrefaction	Torrefaction [183] is a low temperature (200–300 °C) process in an inert environment in which moisture, carbon oxides (CO &CO_2), and oxygen are removed from biomass materials including depolymerisation of long chain polysaccharide forming a solid product with low H/C and O/C ratios. The properties of the final product (weight loss, thermophysical and chemical) are influenced mainly by torrefaction temperature. Torrefaction is aimed at improving the thermochemical properties of final biomass product for application in co-firing with coal, gasification and combustion [184] [185], [186].
X-band of the microwave frequency	Is a frequency range from 8 to 12 GHz

REFERENCES

[1] Office-for-National-Statistics-UK, "Number of deaths from accidental poisoning by carbon monoxide, England and Wales, deaths registered in 2011-2015," London, 2016.

[2] D. Gunnell *et al.*, "Suicide by gases in England and Wales 2001-2011: Evidence of the emergence of new methods of suicide," *Affect. Disord.*, vol. 170, pp. 190-195., 2015.

[3] C. Safety, "FUEL type relating to UK Deaths from unintentional carbon APPLIANCE type relating to UK Deaths from unintentional carbon," 2015.

[4] CO-Gas Safety, "UK deaths caused by accidental Carbon Monoxide (CO) poisoning," Isle of Wight, 2017.

[5] Gas Safety trust, "CO - Death and injuries," 2015.

[6] U. Gas-Safety, "Carbon monoxide Gas Safety Statistics on death and Injuries," 2019.

[7] U. Gas-Safety-Trust, "Notes relating to the compilation of CO-Gas Safety statistics and graphic representations: Fuel Type relating to UK deaths from unintentional CO poisoning from 1995 to 2018," 2018.

[8] R. C. Flagan and J. H. Seinfeld, "Combustion fundamentals," in *Fundamentals of Air pollution engineering*, no. 1–2, Prentice Hall: Englewood Cliffs, NJ, 1988, pp. 59–163.

[9] J. M. Dasch, "Particulate and gaseous emissions from wood-burning fireplaces," *Environ. Sci. Technol.*, vol. 16, no. 10, pp. 639–645, 1982.

[10] T. Salthammer, T. Schripp, S. Wientzek, and M. Wensing, "Impact of operating wood-burning fireplace ovens on indoor air quality," *Chemosphere*, vol. 103, pp. 205–211, 2014.

[11] A. T. Simpson, M. A. Hemingway, and C. Seymour, "Dangerous (toxic) atmospheres in UK wood pellet and wood chip fuel storage.," *J. Occup. Environ. Hyg.*, vol. 13, no. 9, pp. 699–707, 2016.

[12] S. Gauthier, H. Grass, M. Lory, M. Thali, and C. Bartsch, "Lethal Carbon Monoxide Poisoning in Wood Pellet Storerooms — Two Cases and a Review of the Literature," *Ann. Occup. Hyg.*, vol. 56, no. 7, pp. 755–763, 2012.

[13] M. J. Serapiglia, C. A. Mullen, L. B. Smart, and A. A. Boateng, "Variability in pyrolysis product yield from novel shrub willow genotypes," *Biomass and Bioenergy*, vol. 72, pp. 74–84, 2015.

[14] F. Ferrara, A. Orsini, A. Plaisant, and A. Pettinau, "Pyrolysis of coal, biomass and their blends: Performance assessment by thermogravimetric analysis," *Bioresour. Technol.*, vol. 171, pp. 433–441, 2014.

[15] S. S. Idris, N. A. Rahman, K. Ismail, A. B. Alias, Z. A. Rashid, and M. J. Aris, "Investigation on thermochemical behaviour of low rank Malaysian coal, oil palm biomass and their blends during pyrolysis via thermogravimetric analysis (TGA)," *Bioresour. Technol.*, vol. 101, no. 12, pp. 4584–4592, 2010.

[16] P. A. Campbell and R. E. Mitchell, "The impact of the distributions of surface oxides and their migration on characterization of the heterogeneous carbon-oxygen reaction," *Combust. Flame*, vol. 154, no. 1–2, pp. 47–66, 2008.

[17] S. Ahmed and M. H. Back, "The role of the surface complex in the kinetics of the reaction of oxygen with carbon," *Carbon N. Y.*, vol. 23, no. 5, pp. 513–524, 1985.
[18] J. Dollimore, C. M. Freedman, B. H. Harrison, and D. F. Quinn, "Surface complexes on carbon-I. A preliminary investigation of surface oxygen complex on a non-graphitic carbon," *Carbon N. Y.*, vol. 8, no. 5, pp. 587–596, 1970.
[19] R. Anderson and E. P. H, "Surface Complexes on Charcoal: Gas Evolution as a Function of Vapor Adsortion and of High-Temperature Evacuation," in *Adsorption of Gases - 110th Meeting of the American Chemical Society*, 1947, pp. 1308–1329.
[20] F. J. Vastola, P. J. Hart, and P. . Walker, "A study of carbon-oxygen surface complexes using O18 as a tracer," *Carbon N. Y.*, vol. 2, no. 1, pp. 65–71, 1964.
[21] R. C. Bansal, F. J. Vastola, and P. L. Walker, "Studies on ultra-clean carbon surfaces-IV. Decomposition of carbon-oxygen surface complexes," *Carbon N. Y.*, vol. 8, no. 4, pp. 443–448, 1970.
[22] J. Hrdlička, P. Skopec, T. Dlouhý, and F. Hrdlička, "Emission factors of gaseous pollutants from small scale combustion of biofuels," *Fuel*, vol. 165, pp. 68–74, 2016.
[23] M. F. Demirbas and T. Demirbas, "Hazardous Emissions from Combustion of Biomass," *Energy Sources, Part A Recover. Util. Environ. Eff.*, vol. 31, no. February 2015, pp. 527–534, 2009.
[24] S. Royer and D. Duprez, "Catalytic Oxidation of Carbon Monoxide over Transition Metal Oxides," *ChemCatChem*, vol. 3, no. 1, pp. 24–65, 2011.
[25] A. Nyombi, M. R. Williams, and R. Wessling, "Determination of Kinetic Parameters and Thermodynamic properties of Ash (fraxiuns) sawdust slow pyrolysis using Thermogravimetric Analysis," *Energy Sources, Part A Recover. Util. Environ. Eff.*, vol. 40, no. 22, pp. 2660–2670, 2018.
[26] R. W. A. Nyombi, M. Williams, "Reactivity and Free Radical Chemistry of Lilac (Syringa) Charcoal," *Energy & Fuels*, 2019.
[27] A. Nyombi, M. R. Williams, and R. Wessling, "Toxic emissions from smouldering combustion of woody biomass and derived char with a case study of CO build-up in an ISO container," *Energy Sources, Part A Recover. Util. Environ. Eff.*, 2019.
[28] A. Nyombi, M. R. R. Williams, and R. Wessling, "Mechanical impregnation of Pd-Sn/alumina and Cu-Mn/graphite on charcoal to minimise carbon monoxide emissions," *Chem. Phys. Lett.*, vol. 715, pp. 181–185, Jan. 2019.
[29] A. Nyombi, M. Williams, and R. Wessling, "Catalytic effects on the non-isothermal oxidation of solid fuels by oxygen: An experimental study," *Energy & Fuels*, 2019.
[30] R. Ots *et al.*, "Modelling carbonaceous aerosol from residential solid fuel burning with different assumptions for emissions," pp. 4497–4518, 2018.
[31] C. Char and N. Graphite, "Experimental Model Development of Oxygen-Enriched Combustion Kinetics on Porous Coal Char and Non-Porous Graphite," 2017.
[32] G. Shen *et al.*, "Comparison of carbonaceous particulate matter

emission factors among different solid fuels burned in residential stoves," *Atmos. Environ.*, vol. 89, pp. 337–345, 2014.
[33] G. Q. A. Anderson and M. J. Fergusson, "Energy from biomass in the UK : sources , processes and biodiversity implications," in *Ibis*, 2006, vol. 148, pp. 180–183.
[34] K. Y. Lisandy, G. Kim, J. Kim, G. Kim, and C. Jeon, "Enhanced Accuracy of the Reaction Rate Prediction Model for Carbonaceous Solid Fuel Combustion," 2017.
[35] P. Wang and B. H. Howard, "Impact of thermal pretreatment temperatures on woody biomass chemical composition, physical properties and microstructure," *Energies*, vol. 11, no. 1, p. 25, 2018.
[36] M. S. Ahmad *et al.*, "Thermogravimetric analyses revealed the bioenergy potential of Eulaliopsis binata," *Therm. Anal. Calorim.*, vol. 130, no. 3, pp. 1237–1247, 2017.
[37] X. J. Lee, L. Y. Lee, S. Gan, S. Thangalazhy-Gopakumar, and H. K. Ng, "Biochar potential evaluation of palm oil wastes through slow pyrolysis: Thermochemical characterization and pyrolytic kinetic studies," *Bioresour. Technol.*, vol. 236, p. 236, pp. 155–163, 2017.
[38] R. Muktham, A. S. Ball, S. K. Bhargava, and S. Bankupalli, "Study of thermal behavior of deoiled karanja seed cake biomass: Thermogravimetric analysis and pyrolysis kinetics," *Energy Sci. Eng.*, vol. 4, no. 1, pp. 86–95, 2016.
[39] A. Malika, N. Jacques, E. F. Jaafar, B. Fatima, and A. Mohammed, "Pyrolysis investigation of food wastes by TG-MS-DSC technique," *Biomass Convers. Biorefinery*, vol. 6, no. 2, pp. 161–172, 2016.
[40] G. Özsin and A. E. Pütün, "Kinetics and evolved gas analysis for pyrolysis of food processing wastes using TGA/MS/FT-IR," *Waste Manag.*, vol. 64, pp. 315-326., 2017.
[41] A. G. Borrego, L. Garavaglia, and W. D. Kalkreuth, "Characteristics of high heating rate biomass chars prepared under N2 and CO2 atmospheres," *Int. J. Coal Geol.*, vol. 77, no. 3–4, pp. 409-415., 2009.
[42] S. Sadaka, H. Liechty, M. Pelkki, and M. Blazier, "Pyrolysis and combustion kinetics of raw and carbonized cottonwood and switchgrass agroforest," vol. 10, no. 3. pp. 4498–4518, 2015.
[43] B. Adrian, "Coal fire emissions curb children's growth," *Environ. Health Perspect.*, vol. 119, no. 6, p. A245, 2011.
[44] E. Borsos, L. Makra, R. Beczib, B. Vitanyi, and M. Szentpeteri, "Anthropogenic Air pollution in ancient times," *Acta Climatol. Chorol.*, vol. 36–37, pp. 5–15, 2003.
[45] J. B. Russell and J. L. Jeraci, "Effect of Carbon Monoxide on Fermentation of Fiber, Starch, and Amino Acids by Mixed Rumen Microorganisms In Vitro," *Appl. Environ. Microbiol.*, vol. 48, no. 1, pp. 211–217, 1984.
[46] P. Capros *et al.*, "European decarbonisation pathways under alternative technological and policy choices : A multi-model analysis q," *Energy Strateg. Rev.*, vol. 2, no. 3–4, pp. 231–245, 2020.
[47] T. Nandy, J. Ronald A. Coutu, and C. Ababei, "Carbon Monoxide Sensing Technologies for Next-Generation Cyber-Physical Systems," *Sensors*, vol.

18, no. 3443, pp. 1–29, 2018.
[48] K. Lucarelli, K. Wyne, J. E. Svenson, K. Lucarelli, K. Wyne, and J. E. Svenson, "Improved cookstoves and their effect on carbon monoxide levels in San Lucas Tolimán , Guatemala," *Int. J. Environ. Health Res.*, vol. 3123, pp. 1–7, 2018.
[49] F. Ozil, V. Tschamber, F. Haas, and G. Trouvé, "Efficiency of catalytic processes for the reduction of CO and VOC emissions from wood combustion in domestic fireplaces," *Fuel Process. Technol.*, vol. 90, no. 9, pp. 1053–1061, 2009.
[50] M. Carltonbird, S. Eaimsumang, S. Pongstabodee, S. Boonyuen, S. M. Smith, and A. Luengnaruemitchai, "Effect of the exposed ceria morphology on the catalytic activity of gold/ceria catalysts for the preferential oxidation of carbon monoxide," *Chemical Engineering Journal*, vol. 344. pp. 545–555, 2018.
[51] X. Hong and Y. Sun, "Effect of Preparation Methods on the Performance of Pt/CeO2 Catalysts for the Catalytic Oxidation of Carbon Monoxide," *Catalysis Letters*, vol. 146, no. 10. pp. 2001–2008, 2016.
[52] JEOL ltd, "ESR instrumentation," *JEOL Company*, 2020. [Online]. Available: https://www.jeol.co.jp/en/products/esr/basics.html. [Accessed: 28-Feb-2020].
[53] J. Zhang, "Electrodeposition of novel nanostructured and porous materials for advanced applications: synthesis, structural characterization and physical/chemical performance," Universitat Autonoma de Barcelona, 2016.
[54] B. Debjani, "Experimental Techniques in Thermal Analysis Thermogravimetry (TG) & Differential Scanning Calorimetry (DSC)," 2017.
[55] S. Vyazovkin, "Model-free Kinetics: Staying free of multiplying entities without necessity," *J. Therm. Anal. Calorim.*, vol. 83, no. 1, pp. 45–51, 2006.
[56] Y. Ding, O. A. Ezekoye, S. Lu, and C. Wang, "Thermal degradation of beech wood with thermogravimetry/Fourier transform infrared analysis," *Energy Convers. Manag.*, vol. 120, pp. 370–377, Jul. 2016.
[57] J. A. Conesa, J. Caballero, A. Marcilla, and R. Font, "Analysis of different kinetic models in the dynamic pyrolysis of cellulose," *Thermochim. Acta*, vol. 254, no. C, pp. 175–192, 1995.
[58] W. Jin, K. Singh, and J. Zondlo, "Pyrolysis Kinetics of Physical Components of Wood and Wood-Polymers Using Isoconversion Method," *Agriculture*, vol. 3, no. 1, pp. 12–32, 2013.
[59] P. Rantuch and B. Nagypál, "Investigation of activation energy of polypropylene composite thermooxidation by model-free methods," *Eur. J. Environ. Saf. Sci.*, vol. 2, no. 1, pp. 12–18, 2014.
[60] M. Heydari, M. Rahman, and R. Gupta, "Kinetic study and thermal decomposition behavior of lignite coal," *Int. J. Chem. Eng.*, vol. 2015, 2015.
[61] F. H. Joseph and W. A. Leo, "A quick, direct method for the determination of activation energy from thermogravimetric data," *Polym. Lett.*, vol. 4, no. 5, pp. 323–328, 1966.
[62] T. Ozawa, "A New Method of Analyzing Thermogravimetric Data," *Bull.*

Chem. Soc. Jpn., vol. 38, no. 11, pp. 1881–1886, 1965.
[63] C. D. Doyle, "Kinetic analysis of thermogravimetric data," *J. Appl. Polym. Sci.*, vol. 5, no. 15, pp. 285–292, May 1961.
[64] S. Mallakpour and M. Taghavi, "The Accuracy of Approximation Equations in the Study of Thermal Decomposition Behaviour of Some Synthesized Optically Active Polyamides," *Iran. Polym. J. (English Ed.*, vol. 18, no. 11, pp. 857–872, 2009.
[65] G. I. Senum and R. . Yang, "Rational approximations of the intergral of the Arrhenius function," *Therm. Anal.*, no. 1, pp. 445–447, 1977.
[66] H. E. Kissinger, "Variation of peak temperature with heating rate in differential thermal analysis," *J. Res. Natl. Bur. Stand. (1934).*, vol. 57, no. 4, p. 217, 1956.
[67] H. Ishida and D. J. Allen, "Gelation behavior of near-zero shrinkage polybenzoxazines," *J. Appl. Polym. Sci.*, vol. 79, no. 3, pp. 406–417, 2001.
[68] M. J. Starink, "The determination of activation energy from linear heating rate experiments: A comparison of the accuracy of isoconversion methods," *Thermochim. Acta*, vol. 404, no. 1–2, pp. 163–176, 2003.
[69] L. Fedunik-hofman, A. Bayon, J. Hinkley, and W. Lipin, "Friedman method kinetic analysis of CaO-based sorbent for high-temperature thermochemical energy storage," *Chem. Eng. Sci.*, vol. 200, pp. 236–247, 2019.
[70] A. K. Gupta, A. K. Jena, and M. C. Chaturvedi, "A differential technique for the determination of the activation energy of precipitation reactions from differential scanning calorimetric data," *Scr. Metall.*, vol. 22, pp. 369–371, 1988.
[71] A. Jerez, "A modification to the freeman and carroll method for the analysis of the kinetics of non-isothermal processes," *J. Therm. Anal.*, vol. 26, pp. 315–318, 1983.
[72] C. Danvirutai and P. Noisong, "Combined facile methods of the DSC and origin lab program to study the dehydration kinetics of KMnPO4.H2O," *Therm. Anal. Calorim.*, pp. 2249–2255, 2015.
[73] P. G. Boswell, "On the calculation of activation energies using a modified Kissinger method," *J. Therm. Anal.*, vol. 18, no. 2, pp. 353–358, 1980.
[74] M. Sajjad, M. Aamer, S. Taha, and H. Taqvi, "Pyrolysis, kinetics analysis, thermodynamics parameters and reaction mechanism of Typha latifolia to evaluate its bioenergy potential Bioresource Technology," *Bioresour. Technol.*, vol. 245, no. September, pp. 491–501, 2017.
[75] A. I. Osman, A. Abdelkader, C. R. Johnston, K. Morgan, and D. W. Rooney, "Thermal Investigation and Kinetic Modeling of Lignocellulosic Biomass Combustion for Energy Production and Other Applications," *Ind. Eng. Chem. Res.*, vol. 56, no. October, pp. 12119–12130, 2017.
[76] A. Fernandez, G. Mazza, and R. Rodriguez, "Thermal decomposition under oxidative atmosphere of lignocellulosic wastes : Different kinetic methods application," *J. Environ. Chem. Eng.*, vol. 6, no. September, pp. 404–415, 2017.
[77] G. Wang, J. Zhang, J. Shao, H. Sun, and H. Zuo, "Thermogravimetric Analysis of Coal Char Combustion Kinetics," *J. Iron Steel Res. Int.*, vol. 21,

no. 10, pp. 897–904, 2014.
[78] L. A. Pérez-Maqueda and J. M. Criado, "Accuracy of Senum and Yang's approximations to the Arrhenius integral," *J. Therm. Anal. Calorim.*, vol. 60, no. 3, pp. 909–915, 2000.
[79] S. Vyazovkin and C. Wight, A, "Isothermal and non-isothermal kinetics of thermally stimulated reactions of solids," *Int. Rev. s Phys. Chem.*, vol. 17, no. 3, pp. 407–433, 1998.
[80] R. L. Blaine and H. E. Kissinger, "Homer Kissinger and the Kissinger equation," *Thermochim. Acta*, vol. 540, pp. 1–6, 2012.
[81] L. Vlaev, N. Nedelchev, K. Gyurova, and M. Zagorcheva, "A comparative study of non-isothermal kinetics of decomposition of calcium oxalate monohydrate," *J. Anal. Appl. Pyrolysis*, vol. 81, no. 2, pp. 253–262, 2008.
[82] S. Vyazovkin, A. K. Burnham, J. M. Criado, L. A. Pérez-Maqueda, C. Popescu, and N. Sbirrazzuoli, "ICTAC Kinetics Committee recommendations for performing kinetic computations on thermal analysis data," *Thermochim. Acta*, vol. 520, no. 1–2, pp. 1–19, 2011.
[83] S. V Chaparala and A. Raj, "Reaction mechanism for the oxidation of zigzag site on polycyclic aromatic hydrocarbons in soot by O2," *Combust. Flame*, vol. 165, pp. 21–33, 2016.
[84] A. Raj, G. Robert, and S. Ho, "Reaction mechanism for the free-edge oxidation of soot by O2," *Combust. Flame*, vol. 159, no. 11, pp. 3423–3436, 2012.
[85] A. Raj, S. Y. Yang, D. Cha, R. Tayouo, and S. H. Chung, "Structural effects on the oxidation of soot particles by O2: Experimental and theoretical study," *Combust. Flame*, vol. 160, no. 9, pp. 1812–1826, 2013.
[86] D. S. N. Parker, R. I. Kaiser, T. P. Troy, O. Kostko, M. Ahmed, and A. M. Mebel, "Toward the Oxidation of the Phenyl Radical and Prevention of PAH Formation in Combustion Systems," 2015.
[87] R. Zhang *et al.*, "Control synthesis of CeO2 nanomaterials supported gold for catalytic oxidation of carbon monoxide," *Molecular Catalysis*, vol. 442. pp. 173–180, 2017.
[88] P. Sudarsanam, P. R. Selvakannan, S. K. Soni, S. K. Bhargava, and B. M. Reddy, "Structural evaluation and catalytic performance of nano-Au supported on nanocrystalline Ce0.9Fe0.1O2-δ solid solution for oxidation of carbon monoxide and benzylamine," vol. 4, no. 82. pp. 43460–43469, 2014.
[89] I. Lee and F. Zaera, "Catalytic oxidation of carbon monoxide at cryogenic temperatures," vol. 319. pp. 155–162, 2014.
[90] Y. Song, X. Chu, Y. Lin, and X. Yang, "Pyrrolidone Modifying Gold Nanocatalysts for Enhanced Catalytic Activities in Aerobic Oxidation of Alcohols and Carbon Monoxide," *Journal of Chemistry*, vol. 2017. 2017.
[91] L. Mokoena, G. Pattrick, and M. S. Scurrell, "Catalytic activity of gold-perovskite catalysts in the oxidation of carbon monoxide," *Gold Bulletin*, vol. 49, no. 1–2. pp. 35–44, 2016.
[92] S. Xie *et al.*, "Preparation and high catalytic performance of Au/3DOM Mn2O3 for the oxidation of carbon monoxide and toluene," vol. 279. pp. 392–401, 2014.

[93] K. Koizumi, K. Nobusada, and M. Boero, "Reaction Pathway and Free Energy Landscape of Catalytic Oxidation of Carbon Monoxide Operated by a Novel Supported Gold-Copper Alloy Cluster," vol. 119, no. 27. pp. 15421–15427, 2015.
[94] X. Bai *et al.*, "Insight into Copper Oxide-Tin Oxide Catalysts for the Catalytic Oxidation of Carbon Monoxide: Identification of Active Copper Species and a Reaction Mechanism," *ChemCatChem*, vol. 9, no. 16. pp. 3226–3235, 2017.
[95] D. A. Svintsitskiy, I. Y. Pakharukov, E. M. Slavinskaya, T. Y. Kardash, V. N. Parmon, and A. I. Boronin, "Influence of the Copper(II) Oxide Dispersion on its Catalytic Properties in Carbon Monoxide Oxidation: A Comparative Study by Using Two Types of Catalytic Reactors," *ChemCatChem*, vol. 8, no. 22. pp. 3546–3555, 2016.
[96] Z.-P. Hu *et al.*, "CuO catalysts supported on activated red mud for efficient catalytic carbon monoxide oxidation," *Chemical Engineering Journal*, vol. 302. pp. 23–32, 2016.
[97] T. Biemelt *et al.*, "Hopcalite nanoparticle catalysts with high water vapour stability for catalytic oxidation of carbon monoxide," vol. 184. pp. 208–215, 2016.
[98] P.-P. Du *et al.*, "Synthesis and metal-support interaction of subnanometer copper-palladium bimetallic oxide clusters for catalytic oxidation of carbon monoxide," *Inorganic Chemistry Frontiers*, vol. 4, no. 4. pp. 668–674, 2017.
[99] W. Zhang, F. Wu, J. Li, and Z. You, "Dispersion–precipitation synthesis of highly active nanosized Co3O4 for catalytic oxidation of carbon monoxide and propane," vol. 411. pp. 136–143, 2017.
[100] W. Ahmad, T. Noor, and M. Zeeshan, "Effect of synthesis route on catalytic properties and performance of Co3O4/TiO2 for carbon monoxide and hydrocarbon oxidation under real engine operating conditions," *Catalysis Communications*, vol. 89. pp. 19–24, 2017.
[101] T. Umegaki, T. Inoue, and Y. Kojima, "Fabrication of hollow spheres of Co3O4 for catalytic oxidation of carbon monoxide," vol. 663. pp. 68–76, 2016.
[102] J.-L. Cao *et al.*, "Mesoporous Co-Fe-O nanocatalysts: Preparation, characterization and catalytic carbon monoxide oxidation," vol. 2, no. 1. pp. 477–483, 2014.
[103] B. Kucharczyk, "Catalytic Oxidation of Carbon Monoxide on Pd-Containing LaMnO3 Perovskites," vol. 145, no. 6. pp. 1237–1245, 2015.
[104] T. L. Rakitskaya, T. A. Kiose, A. A. Ennan, K. O. Golubchik, L. P. Oleksenko, and V. G. Gerasiova, "Effect the conditions of the acid–thermal modification of clinoptilolite have on the catalytic properties of palladium–copper complexes anchored on it in the reaction of carbon monoxide oxidation," *Russian Journal of Physical Chemistry A*, vol. 90, no. 6. pp. 1120–1127, 2016.
[105] M. Wilklow-Marnell and W. D. Jones, "Catalytic oxidation of carbon monoxide by A-alumina supported 3 nm cerium dioxide nanoparticles," *Molecular Catalysis*, vol. 439. pp. 9–14, 2017.

[106] L. P. dos Santos Xavier, V. Rico-Pérez, A. M. Hernández-Giménez, D. Lozano-Castelló, and A. Bueno-López, "Simultaneous catalytic oxidation of carbon monoxide, hydrocarbons and soot with Ce-Zr-Nd mixed oxides in simulated diesel exhaust conditions," vol. 162. pp. 412–419, 2015.
[107] A. Mohajeri and N. Hassani, "Catalytic activity of corrole complexes with post-transition elements for the oxidation of carbon monoxide: A first-principles study," *New Journal of Chemistry*, vol. 42, no. 15. pp. 12632–12643, 2018.
[108] H. A. Lara-García, E. Vera, J. A. Mendoza-Nieto, J. F. Gómez-García, Y. Duan, and H. Pfeiffer, "Bifunctional application of lithium ferrites (Li5FeO4 and LiFeO2) during carbon monoxide (CO) oxidation and chemisorption processes. A catalytic, thermogravimetric and theoretical analysis," *Chemical Engineering Journal*, vol. 327. pp. 783–791, 2017.
[109] J.-Y. Tang *et al.*, "Investigation of carbon monoxide catalytic oxidation on vanadium-embedded graphene," *Monatshefte fur Chemie*, vol. 149, no. 8. pp. 1349–1356, 2018.
[110] G. Dai, L. Chen, and X. Zhao, "Catalytic oxidation mechanisms of carbon monoxide over single and double vacancy Cr-embedded graphene." 2018.
[111] A.-S. Rola Mohammad, M. S. Khaled, and D. Joydeep, "Critical Review of Low-Temperature CO Oxidation and Hysteresis Phenomenon on Heterogeneous Catalysts," *Catal. Today*, vol. 8, no. 660, pp. 1–19, 2018.
[112] A. Anca-Couce, A. Dieguez-Alonso, N. Zobel, A. Berger, N. Kienzl, and F. Behrendt, "Influence of Heterogeneous Secondary Reactions during Slow Pyrolysis on Char Oxidation Reactivity of Woody Biomass," *Energy and Fuels*, vol. 31, no. 3, pp. 2335-2344., 2017.
[113] K. Kirtania, J. Axelsson, L. Matsakas, P. Christakopoulos, K. Umeki, and E. Furusjö, "Kinetic study of catalytic gasification of wood char impregnated with different alkali salts," vol. 118. pp. 1055–1065, 2017.
[114] L. Jiang *et al.*, "Catalytic effects of inherent alkali and alkaline earth metallic species on steam gasification of biomass," *Int. J. Hydrog. Energy*, vol. 40, pp. 15460–15469, 2015.
[115] H. A. Baloch *et al.*, "Parametric study of pyrolysis and steam gasification of rice straw in presence of K2CO3," *Korean J. Chem. Eng.*, vol. 33, no. 9, pp. 2567–2574, 2016.
[116] F.-X. Collard, A. Bensakhria, M. Drobek, G. Volle, and J. Blin, "Influence of impregnated iron and nickel on the pyrolysis of cellulose," vol. 80. pp. 52–62, 2015.
[117] I. K. M. Yu *et al.*, "Catalytic valorization of starch-rich food waste into hydroxymethylfurfural (HMF): Controlling relative kinetics for high productivity," vol. 237. pp. 222–230, 2017.
[118] M. A. Martín-Lara, G. Blázquez, A. Ronda, and M. Calero, "Kinetic study of the pyrolysis of pine cone shell through non-isothermal thermogravimetry: Effect of heavy metals incorporated by biosorption," *Renew. Energy*, vol. 96, pp. 613–624, 2016.
[119] M. A. Martín-Lara, A. Ronda, G. Blázquez, A. Pérez, and M. Calero, "Pyrolysis kinetics of the lead-impregnated olive stone by non-isothermal

thermogravimetry," *Process Saf. Environ. Prot.*, vol. 113, pp. 448–458, 2018.
[120] A. Trubetskaya *et al.*, "Comparison of high temperature chars of wheat straw and rice husk with respect to chemistry, morphology and reactivity," vol. 86. pp. 76–87, 2016.
[121] S. Fan and C. Sheng, "Impact of Inorganic Matter on the Low-Temperature Oxidation of Cornstalk and Cellulose Chars," *Energy and Fuels*, vol. 30, no. 3, pp. 1783–1791, 2016.
[122] Y. Liao *et al.*, "Charcoal-supported catalyst with enhanced thermal-stability for the catalytic combustion of volatile organic compounds," vol. 522. pp. 32–39, 2016.
[123] B. Zhou *et al.*, "Adsorption and oxidation of SO2 in a fixed-bed reactor using activated carbon produced from oxytetracycline bacterial residue and impregnated with copper," vol. 65, no. 2. pp. 165–170, 2015.
[124] S. Wan, J. Wu, S. Zhou, R. Wang, B. Gao, and F. He, "Enhanced lead and cadmium removal using biochar-supported hydrated manganese oxide (HMO) nanoparticles: Behavior and mechanism," vol. 616–617. pp. 1298–1306, 2018.
[125] J.-H. Park, J. J. Wang, R. Xiao, N. Tafti, R. D. DeLaune, and D.-C. Seo, "Degradation of Orange G by Fenton-like reaction with Fe-impregnated biochar catalyst," vol. 249. pp. 368–376, 2018.
[126] H. M. Alayan *et al.*, "The formation of hybrid carbon nanomaterial by chemical vapor deposition: An efficient adsorbent for enhanced removal of methylene blue from aqueous solution," vol. 77, no. 6. pp. 1714–1723, 2018.
[127] S. Bourahla, C. Harrats, H. Belayachi, F. Nemchi, and M. Belhakem, "Grape marc activated carbon/TiO2 hybrid degradation of RB5 azo dye: FT-IR and UV-visible analysis," vol. 104. pp. 324–329, 2018.
[128] L. A. Poggi and K. Singh, "Thermal degradation capabilities of modified bio-chars and fluid cracking catalyst (FCC) for acetic acid," vol. 90. pp. 243–251, 2016.
[129] J. Jetter *et al.*, "Pollutant emissions and energy efficiency under controlled conditions for household biomass cookstoves and implications for metrics useful in setting international test standards," *Environ. Sci. Technol.*, vol. 46, no. 19, pp. 10827-10834., 2012.
[130] P. Lu, Q. Huang, A. C. (Thanos) Bourtsalas, Y. Chi, and J. Yan, "Synergistic effects on char and oil produced by the co-pyrolysis of pine wood, polyethylene and polyvinyl chloride," *Fuel*, vol. 230, pp. 359–367, 2018.
[131] E. Apaydin-Varol and A. E. Pütün, "Preparation and characterization of pyrolytic chars from different biomass samples," *J. Anal. Appl. Pyrolysis*, vol. 98, pp. 29–36, 2012.
[132] A. Trubetskaya, P. A. Jensen, A. D. Jensen, P. Glarborg, F. H. Larsen, and M. L. Andersen, "Characterization of free radicals by electron spin resonance spectroscopy in biochars from pyrolysis at high heating rates and at high temperatures," *Biomass and Bioenergy*, vol. 94, pp. 117–129, 2016.
[133] T. Urbanski, S. Benbenek, S. Bedynski, and A. Wasilewski, "Free radicals in charcoal and the combustion of compositions containing charcoal,"

Explosivstoffe, vol. 1, pp. 9–11, 1970.
[134] A. Nyombi, M. Williams, and R. Wessling, "Determination of kinetic parameters and thermodynamic properties for ash (Fraxinus) wood sawdust slow pyrolysis by thermogravimetric analysis," *Energy Sources, Part A Recover. Util. Environ. Eff.*, vol. 40, no. 22, pp. 2660–2670, Aug. 2018.
[135] E. P. Fanning and M. A. Vannice, "A Drifts Study of the Formation of Surface Groups on Carbon By Oxidation," *Carbon N. Y.*, vol. 31, no. 5, pp. 721–730, 1991.
[136] P. Nowicki, "The effect of mineral matter on the physicochemical and sorption properties of brown coal-based activated carbons," *Adsorption*, vol. 22, no. 4–6, pp. 561–569, 2016.
[137] L. Tognotti, J. . Longwell, and F. Sarofim, "The products of the high temperature oxidation of a single char particle in an electrodynamic balance," in *Twenty-Third Symposium (International) on Combustion/The Combustion Institute*, 1990, pp. 1207–1213.
[138] J. H. Pohl, "Influence of Mineral Matter on the Rate of Coal Char Combustion," in *Mineral Matter and Ash in Coal*, 1986, pp. 430–436.
[139] D. P. Mccollor, M. L. Jones, S. A. Benson, and B. . Young, "Promotion of char oxidation by inorganic constituents," in *Twenty-second Symposium (international) on combustion/The Combustion Institute*, 1988, pp. 59–67.
[140] L. Zhigang, "Characteristics of Byoyancy Driven Natural Ventilation Through Horizontal Openings," Aalborg University, 2006.
[141] S. C. Bhattacharya, D. O. Albina, and P. A. Salam, "Emission factors of wood and charcoal-fired cookstoves," *Biomass and Bioenergy*, vol. 23, pp. 453–469, 2002.
[142] M.-Y. Kim *et al.*, "Platinum catalysts supported on silicas: Effect of silica characteristics on their catalytic activity in carbon monoxide oxidation," vol. 103, no. 2. pp. 463–479, 2011.
[143] A. A. Shutilov, G. A. Zenkovets, S. V Tsybulya, V. Y. Gavrilov, and G. N. Kryukov, "Effect of the microstructure of the supported catalysts Cuo/TiO 2 and Cuo/(Ceo 2-Tio 2) on their catalytic properties in carbon monoxide oxidation," vol. 53, no. 3. pp. 409–418, 2012.
[144] P. V Gosavi and R. B. Biniwale, "Catalytic preferential oxidation of carbon monoxide over platinum supported on lanthanum ferriteeceria catalysts for cleaning of hydrogen," vol. 222. pp. 1–9, 2013.
[145] P. Kaminski *et al.*, "Zeolite MCM-22 modified with Au and Cu for catalytic total oxidation of methanol and carbon monoxide," vol. 117, no. 5. pp. 2147–2159, 2013.
[146] D. Gu *et al.*, "Highly Ordered Mesoporous Cobalt-Containing Oxides: Structure, Catalytic Properties, and Active Sites in Oxidation of Carbon Monoxide," vol. 137, no. 35. pp. 11407–11418, 2015.
[147] L.-W. Guo *et al.*, "Contributions of distinct gold species to catalytic reactivity for carbon monoxide oxidation," vol. 7. 2016.
[148] H. A. Elazab, "The catalytic activity of copper oxide nanoparticles towards carbon monoxide oxidation catalysis: microwave – assisted synthesis approach," vol. 8, no. 3. pp. 3278–3281, 2018.
[149] Y. Bi and G. Lu, "Catalytic CO oxidation over palladium supported

NaZSM-5 catalysts," *Appl. Catal. B Environ.*, vol. 41, no. 3, pp. 279–286, 2003.
[150] M. Augustin *et al.*, "Manganese oxide phases and morphologies: A study on calcination temperature and atmospheric dependence," *Beilstein J. Nanotechnol.*, vol. 6, no. 1, pp. 47–59, 2015.
[151] E. Y. Liberman *et al.*, "Synthesis, structure, and properties of a Au/MnOx–CeO2 nanocatalyst for low-temperature oxidation of carbon monoxide," *Inorganic Materials*, vol. 53, no. 4. pp. 406–412, 2017.
[152] S. Wannakao, T. Maihom, M. Probst, J. Limtrakul, and K. Kongpatpanich, "Porous Materials as a Platform for Highly Uniform Single-Atom Catalysts: Tuning the Electronic Structure for the Low-Temperature Oxidation of Carbon Monoxide," *Journal of Physical Chemistry C*, vol. 120, no. 35. pp. 19686–19697, 2016.
[153] Y.-X. Miao, L. Shi, Q. Sun, and W.-C. Li, "A highly efficient potassium-treated Au-Cu/Al2O3 catalyst for the preferential oxidation of carbon monoxide," *RSC Advances*, vol. 6, no. 29. pp. 24603–24609, 2016.
[154] X. Gong *et al.*, "Metal-organic-framework derived controllable synthesis of mesoporous copper-cerium oxide composite catalysts for the preferential oxidation of carbon monoxide," *Fuel*, vol. 229. pp. 217–226, 2018.
[155] M. C. Figueiredo, D. Hiltrop, R. Sundararaman, K. A. Schwarz, and M. T. M. Koper, "Absence of diffuse double layer effect on the vibrational properties and oxidation of chemisorbed carbon monoxide on a Pt(111) electrode," *Electrochimica Acta*, vol. 281. pp. 127–132, 2018.
[156] E. Y. Liberman *et al.*, "Influence of Ionizing Radiation on the Properties of a Nanodispersed PdO/CeO2 Catalyst in the Reaction of Low-Temperature Carbon Monoxide Oxidation," *High Energy Chemistry*, vol. 52, no. 4. pp. 307–311, 2018.
[157] E. M. Slavinskaya *et al.*, "Transformation of a Pt–CeO2 Mechanical Mixture of Pulsed-Laser-Ablated Nanoparticles to a Highly Active Catalyst for Carbon Monoxide Oxidation," *ChemCatChem*, vol. 10, no. 10. pp. 2232–2247, 2018.
[158] S. Chong and T. C.-K. Yang, "Optimization of the photo-deposition parameters for carbon monoxide oxidation over gold–titania," *Chemical Engineering Communications*, vol. 205, no. 5. pp. 647–656, 2018.
[159] V. Nemec, H. Kaper, G. Pétaud, M. Ivanda, and G. Štefanić, "Impact of Mg2+ ion incorporation on the phase development of ZrO2-type solid solutions and their application in the catalytic oxidation of carbon monoxide," *Journal of Molecular Structure*, vol. 1140. pp. 127–141, 2017.
[160] S.-H. Chai *et al.*, "Graphitic mesoporous carbon-supported molybdenum carbides for catalytic hydrogenation of carbon monoxide to mixed alcohols," vol. 170. pp. 141–149, 2013.
[161] C.-A. Ma, C. Xu, M. Shi, G. Song, and X. Lang, "The high performance of tungsten carbides/porous bamboo charcoals supported Pt catalysts for methanol electrooxidation," vol. 242. pp. 273–279, 2013.
[162] J. Wu, Y. Yi, Y. Li, Z. Fang, and E. P. Tsang, "Excellently reactive Ni/Fe bimetallic catalyst supported by biochar for the remediation of

decabromodiphenyl contaminated soil: Reactivity, mechanism, pathways and reducing secondary risks," vol. 320. pp. 341–349, 2016.
[163] N. Tafreshi, S. Sharifnia, and S. Moradi Dehaghi, "Box–Behnken experimental design for optimization of ammonia photocatalytic degradation by ZnO/Oak charcoal composite," vol. 106. pp. 203–210, 2017.
[164] B. O. Otieno, S. O. Apollo, B. E. Naidoo, and A. Ochieng, "Photodecolorisation of melanoidins in vinasse with illuminated TiO2-ZnO/activated carbon composite," vol. 52, no. 7. pp. 616–623, 2017.
[165] M. Hu, M. Laghari, B. Cui, B. Xiao, B. Zhang, and D. Guo, "Catalytic cracking of biomass tar over char supported nickel catalyst," vol. 145. pp. 228–237, 2018.
[166] G.-H. Song, M.-Q. Shi, Y.-Q. Chu, and C.-A. Ma, "Synthesis and characterization of highly dispersed Pt-TiO2|WC/BC as anode catalyst for methanol oxidation," vol. 112. pp. 53–58, 2013.
[167] S. Wang, H. Wang, Q. Yin, L. Zhu, and S. Yin, "Methanation of bio-syngas over a biochar supported catalyst," vol. 38, no. 9. pp. 4471–4477, 2014.
[168] Y. Qin *et al.*, "Carbon-supported molybdenum-based catalysts for the hydrodeoxygenation of maize oil," vol. 6, no. 9. pp. 2698–2705, 2014.
[169] Y. Shen, P. Zhao, Q. Shao, F. Takahashi, and K. Yoshikawa, "In situ catalytic conversion of tar using rice husk char/ash supported nickel-iron catalysts for biomass pyrolytic gasification combined with the mixing-simulation in fluidized-bed gasifier," vol. 160. pp. 808–819, 2015.
[170] Y. Sun, F. Tao, L. Liu, X. Zeng, and W. Wang, "Influence of activated-carbon-supported transition metals on the decomposition of polychlorobiphenyls. Part I: Catalytic decomposition and kinetic analysis," vol. 159. pp. 659–667, 2016.
[171] Y. Sun, L. Liu, K. Oshita, X. Zeng, W. Wang, and Y. Zhang, "Influence of activated-carbon-supported transition metals on the decomposition of polychlorobiphenyls. Part II: Chemical and physical characterization and mechanistic study," vol. 159. pp. 668–675, 2016.
[172] D. Yao *et al.*, "Hydrogen production from biomass gasification using biochar as a catalyst/support," vol. 216. pp. 159–164, 2016.
[173] J. R. Kim and E. Kan, "Heterogeneous photocatalytic degradation of sulfamethoxazole in water using a biochar-supported TiO2 photocatalyst," vol. 180. pp. 94–101, 2016.
[174] M. Argyle and C. Bartholomew, "Heterogeneous Catalyst Deactivation and Regeneration: A Review," *Catalysts*, vol. 5, no. 1, pp. 145–269, 2015.
[175] Wikipedia, "Activated complex," 2018. [Online]. Available: https://en.wikipedia.org/wiki/Activated_complex. [Accessed: 28-Oct-2019].
[176] National Renewable Energy Laboratory, "Biomass Cofiring: A Renewable Alternative for Utilities," 2000.
[177] P. Gill, T. T. Moghadam, and B. Ranjbar, "Differential scanning calorimetry techniques: Applications in biology and nanoscience," *J. Biomol. Tech.*, vol. 21, no. 4, pp. 167–193, 2010.
[178] Naunce-Northwest, "Diffuse Reflectance Infrared Fourier Transform

Spectroscopy," 2018. [Online]. Available: http://www.nuance.northwestern.edu/docs/keckii-pdf/what-is-diffuse-reflectance-spectroscopy.pdf. [Accessed: 28-Oct-2019].
[179] P. Šimon, "Isoconversional methods: Fundamentals, meaning and application," *J. Therm. Anal. Calorim.*, vol. 76, no. 1, pp. 123–132, 2004.
[180] G. Rein, "Smoldering Combustion," in *SFPE Handbook of Fire Protection Engineering*, M. J. Hurley, D. Gottuk, J. R. Hall, K. Harada, E. Kuligowski, M. Puchovsky, J. Torero, J. M. Watts, and C. Wieczorek, Eds. New York, NY: Springer New York, 2016, pp. 581–603.
[181] R. M. Hadden, G. Rein, and C. M. Belcher, "Study of the competing chemical reactions in the initiation and spread of smouldering combustion in peat," *Proc. Combust. Inst.*, vol. 34, no. 2, pp. 2547–2553, 2013.
[182] F. He, W. Yi, Y. Li, J. Zha, and B. Luo, "Effects of fuel properties on the natural downward smoldering of piled biomass powder: Experimental investigation," *Biomass and Bioenergy*, vol. 67, pp. 288–296, 2014.
[183] D. Chen, Z. Zheng, K. Fu, Z. Zeng, J. Wang, and M. Lu, "Torrefaction of biomass stalk and its effect on the yield and quality of pyrolysis products," *Fuel*, vol. 159, pp. 27–32, 2015.
[184] J. Sun *et al.*, "Production and utilization of biochar : A review," *J. Ind. Eng. Chem.*, vol. 40, pp. 1–15, 2016.
[185] K. Weber and P. Quicker, "Properties of biochar," *Fuel*, vol. 217, no. September, pp. 240–261, 2017.
[186] S. Varjani, G. Kumar, and E. R. Rene, "Developments in biochar application for pesticide remediation : Current knowledge and future research directions," *J. Environ. Manage.*, vol. 232, no. November, pp. 505–513, 2018.